

Development of the $^{10}\text{Be}(\text{meteoric})/^9\text{Be}$ isotope system to quantify Earth surface processes in small headwater catchments with different lithologies

Dissertation

zur Erlangung des Grades
Doktorin der Naturwissenschaften
(Dr. rer. nat.)

am Fachbereich Geowissenschaften
der Freien Universität Berlin



Vorgelegt von
Nadine Dannhaus

Berlin 2016

Erstgutachter: Prof. Dr. Friedhelm von Blanckenburg

Zweitgutachter: Dr. Jean L. Dixon

Tag der Disputation: 24. Juni 2016

Eidesstattliche Erklärung

Hiermit versichere ich, die vorliegende Dissertation selbstständig und ohne unerlaubte Hilfe angefertigt zu haben. Bei der Verfassung der Dissertation wurden keine anderen als die im Text aufgeführten Hilfsmittel und Quellen verwendet. Ein Promotionsverfahren zu einem früheren Zeitpunkt an einer anderen Hochschule oder bei einem anderen Fachbereich wurde nicht beantragt.

Berlin, 16. April 2016

Nadine Dannhaus

Danksagung

An erster Stelle möchte ich hier meinem Doktorvater Prof. Dr. Friedhelm von Blanckenburg danken. Sein fachlicher Rat sowie seine wissenschaftlichen Ideen und Kompetenz waren mir immer eine große Unterstützung. Ich danke ihm für sein Vertrauen, mich diese Arbeit selbstständig fertig stellen zu lassen.

Ein großer Dank geht an Dr. Hella Wittmann-Oelze, die mich über die ganze Zeit fachlich sowie persönlich gestärkt hat. Ich danke ihr für die fachlichen Diskussionen meiner Resultate sowie für ihre Unterstützung im Labor und vor allem auch für das intensive Korrekturlesen in der letzten Phase meiner Arbeit.

I am very grateful to Dr. Pavel Kram who introduced me to the Slavkov Forest field sites and assisted me during sampling in the field and at the CGS in Prague. He provided me further samples and a large data set that improved the interpretation of my data considerably. In diesem Zusammenhang möchte ich mich auch bei Dr. Jan Schüssler bedanken, der mich ins Feld begleitet hat und immer für Fragen zur Verfügung stand.

Ich danke Dr. Marcus Christl und Dr. Peter Kubik von der ETH Zürich sowie Dr. Stefan Heinze und Dr. Steven Binnie vom CologneAMS für die Messung meiner Proben am AMS und die zügige Bereitstellung meiner Ergebnisse. Ein weiterer Dank geht an unsere technischen Mitarbeiterinnen Cathrin Schulz, Jutta Bartel und Josefine Buhk, die im Labor eine große Hilfe waren. Rudolf Naumann und Andrea Gottsche vom GFZ Potsdam danke ich für die Durchführung und Unterstützung bei den XRF und XRD-Messungen. Heike Rothe vom GFZ Potsdam danke ich für die Unterstützung bei der Messung meiner Wasserproben mit dem HR-ICP-MS.

Meinen Kollegen in der Sektion „Geochemie der Erdoberfläche“ danke ich für die vielen lebhaften Diskussionen, Gespräche und Hilfestellungen, im Speziellen meinen Mit-Doktoranden Michael Tatzel, David Uhlig, Marcus Oelze und Ricarda Behrens. Besonders danken möchte ich hier Hanna Haedke, mit der ich vor allem in der letzten Phase viele hilfreiche Diskussionen geführt habe und die mich wieder aufgebaut hat. I want to thank also all my former colleagues who supported me and gave me new input during their stay at the GFZ Potsdam. Especially, Herdís Schopka and Jeannie Dixon, who helped me with scientific questions but more importantly reminded me that there is a life outside my office and the lab.

Abschließend danke ich meinen Eltern und meiner Schwester. Meine Eltern haben mir durch ihre finanzielle Unterstützung mein Studium ermöglicht und mich in meinen Entscheidungen und in schwierigen Phasen immer unterstützt. Ganz besonders dankbar bin ich auch meiner Schwester, die immer für mich da ist.

Summary

A new proxy to quantify denudation and chemical weathering, the cosmogenic meteoric beryllium-10 (^{10}Be) to beryllium-9 (^9Be) isotope ratio, was tested on the spatial scale of a small headwater catchment. The $^{10}\text{Be}/^9\text{Be}$ isotope ratio is an ideal proxy to quantify Earth's surface processes because it combines the stable trace metal ^9Be , whose release rate depends on weathering, with the cosmogenic meteoric isotope ^{10}Be produced in the atmosphere. In the Critical Zone (extending from the unweathered bedrock up to the top of the vegetation cover) these two isotopes mix to a characteristic ratio that is dependent on the denudation rate, the fraction of ^9Be released from primary minerals, and the ^9Be concentration of the parent bedrock. The $^{10}\text{Be}/^9\text{Be}$ ratio can be determined either on the reactive phase of sediment (adsorbed onto or precipitated in secondary minerals) that can be isolated from the residual mineral-bound phase by sequential chemical extractions, termed $(^{10}\text{Be}/^9\text{Be})_{\text{reac}}$, or on the dissolved phase in stream water, termed $(^{10}\text{Be}/^9\text{Be})_{\text{diss}}$. Dissolved cosmogenic ^{10}Be is co-precipitated from a water sample. Unlike *in situ*-produced cosmogenic ^{10}Be , denudation rates determined with the $^{10}\text{Be}(\text{meteoric})/^9\text{Be}$ isotope ratio do not depend on the presence of quartz.

I applied this new isotope proxy to three creek catchments in the Slavkov Forest, Czech Republic. Each of these catchments is composed of a different lithology, from felsic to ultramafic rocks. Geomorphic and climatic conditions, vegetation, and catchment size are similar. These settings are ideal to investigate the potential of the $^{10}\text{Be}(\text{meteoric})/^9\text{Be}$ isotope system under various geochemical conditions that result from the contrasting lithologies and anthropogenic acidification which impacted the area of the Slavkov Forest in the second half of the 20th century. The granitic catchment has a low acid neutralizing capacity, such that the resulting pH is acidic, whereas in the two (ultra)mafic catchments pH values of the stream waters reach from neutral to slightly alkaline. Since the distribution of beryllium is highly dependent on the pH of associated solutions, the retention behaviour of beryllium is primarily affected, as shown by e.g. elevated dissolved meteoric ^{10}Be and ^9Be fluxes exported from the acidic granitic catchment. Still, the long-term reactive pool of meteoric ^{10}Be is unaffected by this temporary disturbance of the system. In the case of the (ultra)mafic catchments, the meteoric ^{10}Be mass flux balance shows that these catchments are in steady state regarding their atmospheric ^{10}Be deposition and the sedimentary ^{10}Be export fluxes. $^{10}\text{Be}/^9\text{Be}$ ratios measured on the reactive phase of bedload sediment and on the dissolved phase in stream water, respectively, agree within a factor of two for each catchment. $^{10}\text{Be}/^9\text{Be}$ ratios of the dissolved phase seem to be affected by short-term changes in precipitation and consequent changes in water runoff composition. Due to this hydrological dependency of $(^{10}\text{Be}/^9\text{Be})_{\text{diss}}$, that could be utilized to trace short-term processes rather, I concluded that $(^{10}\text{Be}/^9\text{Be})_{\text{reac}}$ more suitably reflect the long-term denudational state of the catchments. I thus used these ratios that were measured on fine-grained

bedload sediment to calculate catchment-wide denudation rates. This calculation requires the exact knowledge of the parent bedrock concentration. In the case of the studied catchments the bedrock concentration could not be determined directly because of a high heterogeneity in the parent bedrock and was thus approached with a regression method. The denudation rates, calculated with $(^{10}\text{Be}/^9\text{Be})_{\text{reac}}$, turned out to be highest for the (ultra)mafic catchments (100 and $115 \text{ t km}^{-2} \text{ y}^{-1}$) and lower for the granitic catchment, being $65 \text{ t km}^{-2} \text{ y}^{-1}$. Due the presence of quartz in all three catchments, I could also determine *in situ* ^{10}Be -derived denudation rates on sand-sized bedload sediment for comparison. These *in situ* ^{10}Be -derived denudation rates are similar to the $^{10}\text{Be}(\text{meteoric})/^9\text{Be}$ derived rates and range from about 50 to $110 \text{ t km}^{-2} \text{ y}^{-1}$. Short-term chemical weathering rates (monitoring period about 10 to 20 y) derived from stream gauging data are relatively low when compared to the cosmogenic derived denudation rates (integration time scale about 14 to 60 ky). This observation is attributed to changes in environmental and climate conditions at the transition from the late Pleistocene into the Holocene.

In the Southern Sierra Critical Zone Observatory, Sierra Nevada, California (USA), I measured meteoric ^{10}Be concentrations and $^{10}\text{Be}/^9\text{Be}$ ratios throughout a soil and regolith depth profile, in bedload sediment, and in stream waters. Meteoric ^{10}Be concentrations and $^{10}\text{Be}/^9\text{Be}$ ratios measured throughout the regolith profile decrease with increasing profile depth. In contrast, in the soil profile both, ^{10}Be concentrations and $^{10}\text{Be}/^9\text{Be}$ ratios, are roughly constant with depth, but considerably higher than throughout the regolith profile. The ^9Be concentrations measured in the reactive and mineral-bound phase in the regolith profile markedly change at the transition from the saprolite into the overlying soil, potentially originating from e.g. changes in the occurrence of mineral phases in the soil or from external input of laterally transported soil material. I used the total inventory of meteoric ^{10}Be and the ^{10}Be surface concentration of the regolith profile to calculate a local soil erosion that is about $54 \text{ t km}^{-2} \text{ y}^{-1}$. When coupled to the chemical depletion fraction of the soil, a total denudation rate of about $112 \text{ t km}^{-2} \text{ y}^{-1}$ is derived for this regolith site. This rate is in good agreement with a catchment-wide denudation rate derived from the total $^{10}\text{Be}/^9\text{Be}$ ratio measured on stream bedload sediment, which is about $113 \text{ t km}^{-2} \text{ y}^{-1}$, and with published *in situ* ^{10}Be -derived denudation rates.

In conclusion, the $^{10}\text{Be}(\text{meteoric})/^9\text{Be}$ isotope system is well suited to quantify denudation processes on the hillslope scale and in headwater catchments. The results presented in this work are among the first ones using cosmogenic nuclides to quantify denudation rates in (ultra)mafic lithologies showing that this new approach can be applied to any lithology, provided that the bedrock ^9Be concentration is known. Given that mafic rocks cover a large area of the continental surface and generate a considerable weathering flux, this proxy yields great potential for future Earth's surface process studies.

Zusammenfassung

Für die vorliegende Doktorarbeit habe ich einen neuen Proxy zur Bestimmung von Denudationsraten und chemischer Verwitterung, nämlich das Verhältnis von meteorischem Beryllium-10 (^{10}Be) zu Beryllium-9 (^9Be), auf der räumlichen Skala von kleinen Quelleinzugsgebieten angewandt. Das $^{10}\text{Be}/^9\text{Be}$ -Isotopenverhältnis ist ein idealer Proxy, um Prozesse an der Erdoberfläche zu untersuchen, da es das stabile Spurenelement ^9Be , dessen Freisetzung durch die Verwitterungsrate bestimmt wird, mit dem kosmogenen meteorischen Nuklid ^{10}Be kombiniert, das in der Atmosphäre produziert wird. In der „Critical Zone“ (der Bereich vom unverwitterten Grundgestein bis zur Vegetation) mischen sich beide Isotope und bilden ein charakteristisches Verhältnis, das von der Denudationsrate, dem Anteil von bei der Verwitterung freigesetztem ^9Be und der ^9Be Konzentration im Grundgestein bestimmt wird. Dieses Verhältnis kann entweder in der reaktiven Phase in Sediment (adsorbiert an oder eingebaut in sekundäre Minerale; $(^{10}\text{Be}/^9\text{Be})_{\text{reac}}$) oder gelöst in Flusswasser ($(^{10}\text{Be}/^9\text{Be})_{\text{diss}}$) gemessen werden. Die Abtrennung der reaktiven Phase von der residualen, in Mineralen gebundenen Phase wird mit Hilfe einer sequenziellen Extraktionsmethode erreicht. Gelöstes kosmogenes ^{10}Be wird zusammen mit Eisen(III)-Oxid in einer Wasserprobe ausgefällt. Im Gegensatz zu der Anwendung von *in situ*-produziertem ^{10}Be können Denudationsraten mit dieser neuen Methode unabhängig vom Vorkommen des Minerals Quarz bestimmt werden.

Diesen neuen Proxy habe ich in drei kleinen Quelleinzugsgebieten im Kaiserwald (Slavkov Forest), Tschechische Republik, angewandt. Jedes dieser Einzugsgebiete ist geprägt von unterschiedlichen Lithologien, die von felsischen bis ultramafischen Gesteinen reichen. Die Einzugsgebiete weisen ähnliche geomorphologische und klimatische Bedingungen, eine ähnliche Vegetation und Größe auf. Die geochemisch stark unterschiedlichen Bedingungen dieser Einzugsgebiete, die aus den unterschiedlichen Lithologien und der anthropogenen Versauerung des Gebietes des Kaiserwalds in der zweiten Hälfte des 20. Jahrhunderts entstehen, bilden die ideale Umgebung, um das Potenzial des $^{10}\text{Be}/^9\text{Be}$ Systems zu testen. Das granitische Untersuchungsgebiet hat eine niedrige Säureneutralisierungskapazität und daraus resultierend einen sauren pH-Wert, wohingegen der pH-Wert in den beiden (ultra)mafischen Gebieten von neutral bis leicht alkalisch reicht. Die Verteilung von Beryllium zwischen sekundären und gelösten Phasen ist stark vom pH-Wert abhängig. Somit ist die Adsorption von Beryllium in dem sauren granitischen Einzugsgebiet reduziert. ^{10}Be -Massenbilanzen zeigen, dass die (ultra)mafischen Einzugsgebiete im stationären Gleichgewicht bezüglich der atmosphärischen ^{10}Be -Deposition und dem Export von ^{10}Be an Flusssediment sind. Das saure Einzugsgebiet weist jedoch einen deutlich erhöhten Massenfluss an gelöstem ^{10}Be aus dem System auf. Langfristig gesehen hat diese kurzzeitige Störung des Systems, bedingt durch die anthropogene Versauerung, das Reservoir an reaktivem ^{10}Be nicht beeinträchtigt. $^{10}\text{Be}/^9\text{Be}$ Verhältnisse, die an der

reaktiven Phase von Flusssediment und in der gelösten Phase in Flusswasser gemessenen wurden, stimmen innerhalb eines Faktors von zwei überein. Das $^{10}\text{Be}/^9\text{Be}$ -Verhältnis von gelöstem Beryllium schwankt jedoch mit temporären Änderungen im Niederschlag und den einhergehenden Änderungen in der Zusammensetzung des Gesamtabflusses. Aufgrund dieser hydrologischen Abhängigkeit von gelösten $^{10}\text{Be}/^9\text{Be}$ -Verhältnissen und der Annahme, dass die reaktiven $^{10}\text{Be}/^9\text{Be}$ Verhältnisse, gemessen an feinkörnigem Flusssediment, den langfristigen Zustand des Systems besser repräsentieren, habe ich anhand dieser Verhältnisse einzugsgebietsweite Denudationsraten berechnet. Die Berechnung von Denudationsraten mit $^{10}\text{Be}/^9\text{Be}$ -Verhältnissen erfordert, dass die ^9Be -Konzentration im Grundgestein bekannt ist. Aufgrund der hohen Heterogenität in den Grundgesteinen der Einzugsgebiete ist die Konzentration nicht direkt bestimmbar, sondern wurde mit einer Regressionsmethode abgeschätzt. Die resultierende Denudationsrate ist für das granitische Einzugsgebiet mit ca. $65 \text{ t km}^{-2} \text{ y}^{-1}$ am niedrigsten und liegt für die (ultra)mafischen Einzugsgebiete bei ca. 100 und $115 \text{ t km}^{-2} \text{ y}^{-1}$. Da in allen drei Einzugsgebieten Quarz vorkommt, konnten zusätzlich Denudationsraten anhand der Konzentration von *in situ*-produziertem ^{10}Be bestimmt werden. Diese Denudationsraten liegen in der gleichen Größenordnung wie die Raten, die aus dem $^{10}\text{Be}(\text{meteorisch})/^9\text{Be}$ Verhältnis bestimmt wurden, nämlich bei etwa 50 bis $110 \text{ t km}^{-2} \text{ y}^{-1}$. Kurzzeitige chemische Verwitterungsraten (Beobachtungszeitraum über ca. 10 bis 20 Jahren), die mit Hilfe von Abflussmessungen in den Bächen bestimmt wurden, sind im Vergleich mit den kosmogenen Langzeit-Denudationsraten (Integrationszeitraum von ca. 14 bis 60 ka) relativ niedrig. Diese Beobachtung wird auf veränderte ökologische und klimatische Bedingungen am Übergang vom späten Pleistozän ins Holozän zurückgeführt.

Im „Southern Sierra Critical Zone Observatory“ in der südlichen Sierra Nevada, Kalifornien (USA), habe ich meteorische ^{10}Be -Konzentrationen und $^{10}\text{Be}/^9\text{Be}$ -Verhältnisse entlang eines Boden- und Regolithprofils sowie an Flusssediment und -wasser gemessen. Entlang des Regolithprofils nehmen sowohl die meteorischen ^{10}Be Konzentrationen wie auch die $^{10}\text{Be}/^9\text{Be}$ Verhältnisse mit zunehmender Tiefe ab. Im Bodenprofil sind die ^{10}Be Konzentrationen sowie die $^{10}\text{Be}/^9\text{Be}$ -Verhältnisse konstant mit der Tiefe, aber deutlich höher als im Regolithprofil. Die ^9Be -Konzentrationen in der reaktiven und der mineral-gebundenen Phase ändern sich entlang des Regolithprofils deutlich am Übergang vom Saprolith in den aufliegenden Boden. Dieser Sprung in der Konzentration ist möglicherweise durch das Auftreten anderer Mineralphasen im Boden oder durch den Eintrag von lateral transportiertem Bodenmaterial bedingt. Anhand des gesamten Inventars an meteorischem ^{10}Be und der ^{10}Be -Konzentration an der Oberfläche des Regolithprofils konnte ich eine lokale Bodenerosionsrate berechnen, die bei ungefähr $54 \text{ t km}^{-2} \text{ y}^{-1}$ liegt. In Verbindung mit der chemischen Abreicherung im Boden kann eine Denudationsrate hergeleitet werden; diese beträgt ca. $112 \text{ t km}^{-2} \text{ y}^{-1}$. Diese Rate entspricht der Denudationsrate für das gesamte Einzugsgebiet (ca. $113 \text{ t km}^{-2} \text{ y}^{-1}$), die aus dem

gesamten $^{10}\text{Be}/^9\text{Be}$ Verhältnis, gemessen an Flusssediment, berechnet wurde sowie publizierten, mit *in situ* ^{10}Be Konzentrationen berechneten Denudationsraten.

Schlussfolgernd ist das $^{10}\text{Be}(\text{meteorisch})/^9\text{Be}$ Isotopensystem ein geeigneter Proxy um Denudationsprozesse in kleinen Einzugsgebieten zu quantifizieren. Die hier vorgestellten Ergebnisse gehören mit zu den ersten Denudationsraten, die mit Hilfe kosmogener Nuklide in (ultra)mafischen Gesteinen bestimmt wurden. Sie zeigen damit, dass dieser neue Ansatz - unter der Voraussetzung, dass die Berylliumkonzentration vom Grundgestein bekannt ist - in verschiedensten Lithologien angewandt werden kann. Angesichts der Tatsache, dass mafische Gesteine einen weiten Teil der Landoberfläche ausmachen und zu einem bedeutenden Anteil zu der globalen Verwitterung beitragen, werden zukünftige Studien das Potenzial des $^{10}\text{Be}/^9\text{Be}$ Proxys in der Quantifizierung von erdoberflächennahen Prozessen verdeutlichen.

Preface

In this PhD thesis I present my research work in the form of one introduction chapter and two main research chapters. Below I briefly summarise the individual chapters and indicate the contribution of colleagues that I collaborated with on these projects.

- **Chapter 1** is an introduction into the application of cosmogenic nuclides, in particular meteoric ^{10}Be , in the context of Earth surface studies. I introduce the meteoric ^{10}Be to ^9Be ratio system as a new proxy for the quantification of denudation and weathering. This method was developed parallel with my thesis in the section of “Earth Surface Geochemistry” at the GFZ German Research Centre for Geosciences (von Blanckenburg et al., 2012; Wittmann et al., 2015; Wittmann et al., 2012).
- In **Chapter 2** I explore the $^{10}\text{Be}(\text{meteoric})/^9\text{Be}$ isotope system in headwater catchments with contrasting lithologies and hydrogeochemical conditions in the Slavkov Forest, Czech Republic. Reactive phases were extracted from bedload sediment and one soil depth profile, and measured for meteoric ^{10}Be and stable ^9Be concentrations. Additionally dissolved concentrations were measured in stream water. The results show that the method can be applied to derive denudation rates from different lithologies, on small spatial scales, and also in environments that are affected by anthropogenic acidification. The main part of the stream water samples were sampled by Dr. Pavel Kram (*Czech Geological Survey*). He also provided a large data set of dissolved element concentrations and further hydrological parameters that I mainly used to describe the beryllium hydrochemistry in the catchments (Section 2.6) and to calculate chemical weathering fluxes (Section 2.8.3). The bedrock cores were taken within the European SoilTrEC Project (Banwart et al., 2011).
- In **Chapter 3** I consider the $^{10}\text{Be}(\text{meteoric})/^9\text{Be}$ isotope system in a small headwater catchment in the Southern Sierra Nevada, California, USA. ^{10}Be and ^9Be concentrations were measured on extracted phases and the residual fraction throughout a soil and a regolith depth profile, and in bedload sediment and stream water. The sampling of the Sierra Nevada samples and the production of the background data set (e.g. XRF bulk data) were carried out by several colleagues during an ongoing project of the Earth Surface Geochemistry group at the GFZ Potsdam. I processed soil, saprolite, bedload, and stream water samples to measure meteoric ^{10}Be and stable ^9Be concentrations. The four soil samples of the regolith profile were processed in 2015 by my colleague David Uhlig.

Table of Contents

1	Introduction into the $^{10}\text{Be}(\text{meteoric})/^{9}\text{Be}$ isotope system	1
1.1	The cosmogenic nuclide ^{10}Be	3
1.1.1	Production of cosmogenic nuclides	3
1.1.2	Depositional flux of meteoric ^{10}Be to the Earth's surface.....	5
1.1.3	Meteoritic ^{10}Be at the Earth's surface	7
1.2	Theoretical framework of the $^{10}\text{Be}(\text{meteoric})/^{9}\text{Be}$ isotope system.....	9
1.2.1	Meteoritic ^{10}Be and stable ^{9}Be in the Critical Zone	9
1.2.2	Mass balance of beryllium fluxes	11
1.2.3	Erosion rates based on meteoric [^{10}Be].....	13
1.2.4	Denudation rates based on $^{10}\text{Be}/^{9}\text{Be}$ ratios	14
1.3	Analytical methods	15
1.3.1	Sequential extraction method applied to sediment samples	15
1.3.2	Measurement of dissolved beryllium concentrations.....	17
1.3.3	Sample preparation for AMS measurement.....	19
2	Quantification of denudation and chemical weathering in creek catchments with different lithologies in the Slavkov Forest, Czech Republic	21
2.1	Introduction.....	21
2.2	Study site and sampling	22
2.2.1	Study site.....	22
2.2.2	Sampling	24
2.3	Methods	26
2.3.1	Stream bedload and borehole core samples	26
2.3.2	Treatment of water samples.....	26
2.3.3	<i>In situ</i> ^{10}Be method.....	27
2.3.4	Additional methods	27
2.4	Measured concentrations of beryllium	28
2.4.1	Bedload Samples.....	28
2.4.2	Depth profile at Lysina.....	34

2.4.3	Parent bedrock ^9Be concentration.....	36
2.5	Denudation rates from <i>in situ</i> -produced ^{10}Be	40
2.6	Beryllium hydrochemistry of the catchments.....	42
2.6.1	Beryllium concentrations and $^{10}\text{Be}/^9\text{Be}$ ratios in the stream waters	42
2.6.2	Hydrological behaviour of dissolved [^9Be], [^{10}Be], and ($^{10}\text{Be}/^9\text{Be}$)	45
2.6.3	Concentration-discharge characteristics	49
2.6.4	Comparison of ($^{10}\text{Be}/^9\text{Be}$) _{diss} to ($^{10}\text{Be}/^9\text{Be}$) _{reac}	51
2.6.5	Partition coefficient of beryllium	53
2.7	Testing of steady state assumption for the studied catchments.....	54
2.7.1	Balance of meteoric ^{10}Be input and output fluxes	54
2.7.2	Fraction of ^9Be weathered and ^9Be fluxes	58
2.8	Weathering, erosion, and denudation rates.....	60
2.8.1	Erosion rates from meteoric [^{10}Be] _{reac}	61
2.8.2	Denudation rates from $^{10}\text{Be}(\text{meteoric})/^9\text{Be}$ ratios	64
2.8.3	Independent chemical weathering rates from gauging data	65
2.8.4	Comparison of derived denudation and weathering rates	66
2.9	Conclusion Slavkov Forest	70
3	$^{10}\text{Be}(\text{meteoric})/^9\text{Be}$ isotope ratios and denudation rates measured in a small headwater catchment in the Southern Sierra Nevada, California.....	73
3.1	Introduction.....	73
3.2	Study Sites and Samples	74
3.3	Methods	78
3.3.1	Soil, saprolite, and bedload sediment samples.....	78
3.3.2	Stream water samples.....	78
3.3.3	Bedrock samples	78
3.3.4	Chemical depletion fraction and elemental loss	79
3.4	Results	80
3.4.1	[^9Be], [^{10}Be], and ($^{10}\text{Be}/^9\text{Be}$) measured on the Balsam Profile (BP)	80
3.4.2	[^9Be], [^{10}Be], and ($^{10}\text{Be}/^9\text{Be}$) measured on the soil profile P301	82
3.4.3	[^9Be], [^{10}Be], and ($^{10}\text{Be}/^9\text{Be}$) measured on stream bedload sediment.....	87
3.4.4	San Joaquin Soil (Reference Material)	87
3.4.5	[^9Be], [^{10}Be], and ($^{10}\text{Be}/^9\text{Be}$) measured on stream water.....	87

3.4.6	$[^9\text{Be}]_{\text{parent}}$ in the bedrock	88
3.5	Discussion.....	88
3.5.1	Weathering indices (Balsam Profile).....	88
3.5.2	Characterisation of the extracted phases.....	89
3.5.3	$(^{10}\text{Be})_{\text{meteoric}}$ in the mineral-bound phase	93
3.5.4	Equilibrium between dissolved and reactive phases	94
3.5.5	Balance of meteoric ^{10}Be input and output fluxes	95
3.5.6	Denudation and erosion rates	96
3.6	Conclusion Sierra Nevada.....	99
Bibliography		101
A Appendix		117

1 Introduction into the $^{10}\text{Be}(\text{meteoric})/{}^9\text{Be}$ isotope system

Over time scales of 10^3 to 10^5 years the Earth's land surface is shaped by processes like soil formation and hillslope erosion. Through chemical weathering and physical erosion (together denoted as denudation) nutrients are liberated and supplied to ecosystems. Denudation delivers solutes and sediment to streams, and silicate weathering leads to the withdrawal of CO_2 from the atmosphere. It is thus critical to quantify these rates over a wide range of spatial and temporal scales. Cosmogenic nuclides can be used to quantify terrigenous fluxes on time scales that are relevant for the influence of external forcing like climate and tectonics governing soil formation and hillslope erosion. The cosmogenic nuclide beryllium-10 (^{10}Be) has a half-life of 1.39 My (Chmeleff et al., 2010; Korschinek et al., 2010); it is thus an ideal proxy to quantify long-term Earth surface processes (von Blanckenburg and Willenbring, 2014). In the last years the development of a new method using the cosmogenic fallout nuclide meteoric ^{10}Be in combination with its stable counterpart beryllium-9 (${}^9\text{Be}$) was introduced by von Blanckenburg et al. (2012). While meteoric ^{10}Be is produced at a roughly constant rate in the atmosphere and accumulates at the Earth's surface (Willenbring and von Blanckenburg, 2010b), the stable isotope ${}^9\text{Be}$ is released from mineral lattices during weathering. von Blanckenburg et al. (2012) developed steady state mass balance equations that describe this $^{10}\text{Be}(\text{meteoric})/{}^9\text{Be}$ isotope system serving to quantify denudation and weathering from the spatial scale of a soil column up to an entire river catchment.

In the last decades the scientific effort was focused on the *in situ*-produced nuclide ^{10}Be (Lal, 1991) that is nowadays routinely applied to determine soil erosion and production rates, spatially averaged catchment-wide denudation rates, and exposure dates in quartz bearing lithologies (Bierman and Nichols, 2004; Dixon and Riebe, 2014; Granger and Riebe, 2007; Granger and Schaller, 2014; von Blanckenburg, 2005; von Blanckenburg and Willenbring, 2014). One disadvantage of *in situ* ^{10}Be is that it can be only measured on quartz-bearing lithologies or their erosion products, whereas meteoric ^{10}Be can be measured on any lithology and small amounts of fine-grained sediment independent of the presence of quartz. This advantage of meteoric ^{10}Be and the fact that, due to its high production rates, concentrations were high enough to be detected by accelerator mass spectrometry early on, studies using this nuclide were pursued since the early 1980's, following the landmark publication by Lal and Peters (1967). In 2010, the application of meteoric ^{10}Be in Earth surface studies was reviewed by two independent groups (Graly et al., 2010; Willenbring and von Blanckenburg, 2010b) drawing renewed attention to this nuclide. It is now being used again in Earth surface studies to trace sediment transport, to constrain soil ages and soil erosion in e.g. saprolite, till, or river terraces, or to date

deposits (Brown, 1987; Ebert et al., 2012; Foster et al., 2015; Graly et al., 2010; Jagercikova et al., 2015; Jungers et al., 2009; Lebatard et al., 2010; Pavich et al., 1986; Pavich et al., 1984; Reusser et al., 2010; West et al., 2013). Similar to *in situ* ^{10}Be , adsorbed concentrations of meteoric ^{10}Be measured on stream sediment were used to quantify catchment-wide erosion rates (Brown et al., 1988; You et al., 1988). Because of the variable retention behaviour of beryllium, which led to its sidelining with respect to *in situ* ^{10}Be , the single meteoric ^{10}Be isotope can only be applied in settings where it is fully retentive in the weathering zone and where no riverine particle sorting occurs (Willenbring and von Blanckenburg, 2010b). An ideal way to circumvent retentivity and grain size issues is to normalise meteoric ^{10}Be over stable ^9Be , an isotope with identical chemical properties. Two pioneering studies in this field were done by Barg et al. (1997), who evaluate $^{10}\text{Be}/^9\text{Be}$ ratios in authigenic minerals in soils with regard to soil ages, and by Brown et al. (1992), who examined the distributions of ^{10}Be and ^9Be in dissolved and suspended loads in tropical river basins. In a recent study performed by Wittmann et al. (2012) in the Amazon Basin these authors showed that normalising meteoric ^{10}Be over reactive ^9Be cancels out grain size effects and that a $^{10}\text{Be}/^9\text{Be}$ ratio representative for bulk sediment can be determined. This finding yielded the precondition for the new concept developed by von Blanckenburg et al. (2012) to quantify denudation and weathering with the $^{10}\text{Be}(\text{meteoric})/^9\text{Be}$ ratio. This framework was recently applied by Wittmann et al. (2015) to bedload sediment, suspended sediment, and stream water on the large scale of the Amazon Basin. Besides these studies focusing on processes of the terrestrial Earth surface, the $^{10}\text{Be}/^9\text{Be}$ ratio is commonly applied to sea water and authigenic phases of marine sediments, suggesting that this ratio records sedimentation rates and global denudation (Bourlès et al., 1989; Frank et al., 2008; von Blanckenburg and Bouchez, 2014; von Blanckenburg et al., 1996b; Willenbring and von Blanckenburg, 2010a). In a very recent study von Blanckenburg et al. (2015) explored $^{10}\text{Be}/^9\text{Be}$ ratios in marine records to trace relative changes in weathering fluxes over Quaternary climate cycles.

For the first part of this study I applied the $^{10}\text{Be}(\text{meteoric})/^9\text{Be}$ isotope system as a proxy for denudation in creek scale headwater catchments ($< 1 \text{ km}^2$) with contrasting lithologies. The catchments are located in the Slavkov Forest, Czech Republic, and comprise bedrocks that differ from granitic rocks to mafic (e.g. amphibolite) and ultramafic rocks (serpentine). Depending on the lithology each catchment exhibits various hydrogeochemical conditions, e.g. the stream water pH varies between these catchments from acidic to slightly alkaline. In these catchments, I calculated denudation rates from reactive $^{10}\text{Be}/^9\text{Be}$ ratios and compared these with rates derived by techniques that are routinely used to infer weathering and denudation rates; these are river load gauging integrating over short decadal time scales ($10^0 - 10^2$ years) and cosmogenic *in situ* ^{10}Be in quartz in river sediment on Quaternary time scales ($10^2 - 10^5$ years). In the second part of this study I explored the potential of the $^{10}\text{Be}(\text{meteoric})/^9\text{Be}$ isotope system from the soil column scale to a small headwater catchment in a granitic, forested ecosystem in the Southern Sierra Nevada in California.

1.1 The cosmogenic nuclide ^{10}Be

Beryllium is a rare but widely distributed alkaline earth metal having eight isotopes. Of these isotopes only beryllium-9 (^9Be) is stable with a mean upper continental crust concentration of about 2.5 ppm (Rudnick et al., 2003). Beryllium-10 (^{10}Be) and beryllium-7 (^7Be) are naturally occurring cosmogenic nuclides that are present at the Earth's surface (Faure and Mensing, 2004), and are used to trace geological and environmental processes. Cosmogenic ^{10}Be is a very rare radioactive nuclide that is only accumulated in natural materials when these materials are exposed to cosmic rays. It is the most long-living unstable beryllium nuclide and decays by β^- emission to stable Bor-10 (^{10}B). Thanks to its relative long half-life of 1.387 ± 0.012 My (Chmeleff et al., 2010; Korschinek et al., 2010) ^{10}Be is suited to study geological and geomorphological processes, for example erosion or soil production.

1.1.1 Production of cosmogenic nuclides

Cosmic rays arriving at the top of Earth's atmosphere can be separated into a solar and a galactic component (Lal and Peters, 1967). The solar part consists mainly of protons and of variable amounts of α -particles and some heavy particles. The galactic radiation is made up of high energetic nuclei of H (hydrogen) and He (helium; Faure and Mensing (2004)). About 90% are protons, 9% are α -particles, and the remaining 1% are heavy particles. Because of their high energy of some billion electron volts (GeV), the particles are able to interact with nuclei of atoms they impinge on (Dickin, 2005). Once cosmic rays enter the Earth's atmosphere, spallation reactions take place producing a cascade of secondary particles like neutrons, protons, or muons. These secondary cosmogenic particles undergo further nuclear reactions. Cosmogenic ^{10}Be that is produced by spallation reactions with target nuclides, e.g. oxygen (O) and nitrogen (N), in the atmosphere is called meteoric ^{10}Be (see Figure 1.1). A smaller part of the secondary cosmic rays reaches the Earth's surface where *in situ* ^{10}Be nuclides are produced by nuclear interactions in mineral lattices (Faure and Mensing, 2004; Lal and Peters, 1967). *In situ* ^{10}Be is produced at a rate that is magnitudes lower than the depositional flux of meteoric ^{10}Be reaching the Earth's surface (production rate of *in situ* ^{10}Be $\sim 4 \text{ atoms g}_{(\text{qtz})}^{-1} \text{ y}^{-1}$ at SLHL; Dunai (2000); Gosse and Phillips (2001); Muzikar et al. (2003); Phillips et al. (2016)).

The intensity of the cosmic rays reaching the Earth's surface is influenced by the intensity of the primary cosmic rays, the solar modulation, the geomagnetic modulation and changes in the intensity and orientation of the geomagnetic field (Lal and Peters, 1967). Therefore, the cosmic radiation follows variations and the production of cosmogenic nuclides varies. The charged particles of the cosmic rays interact with the Earth's magnetic field that induces latitudinal variations in the irradiation because of its geometry. The magnetic deflection towards the poles leads to a stronger irradiance at higher latitudes (Masarik and Beer, 2009). Besides, the nuclide production is higher in

the stratosphere than in the troposphere (Lal and Peters, 1967). At low elevations secondary cosmogenic particles have lower energies and thus less nuclear reaction takes place resulting in lower cosmogenic nuclide production rates at sea level compared to higher altitudes. About 99% of the atmospheric nuclide production takes place at elevations above three kilometers. This insensitivity to altitude (< 3 km) simplifies the application of meteoric cosmogenic ^{10}Be because in this altitude range no scaling of the depositional flux is required (Willenbring and von Blanckenburg, 2010b).

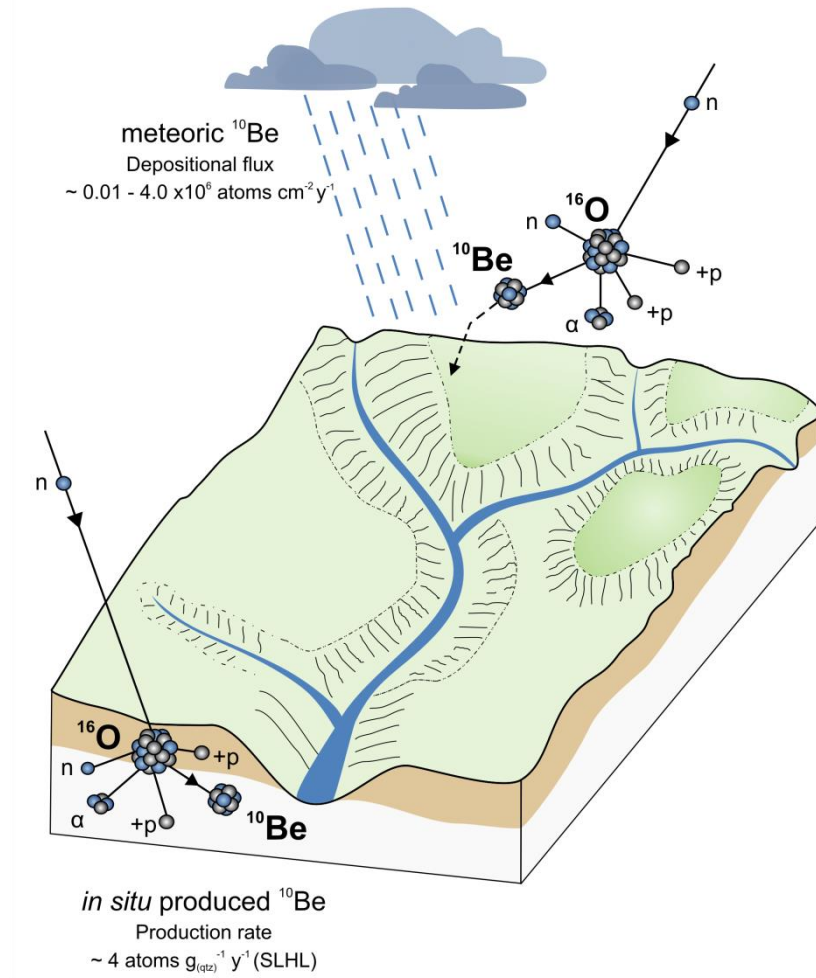


Figure 1.1: Production of meteoric ^{10}Be and *in situ* ^{10}Be by spallation with target nuclides in the atmosphere or in mineral lattices, respectively. The depositional flux of meteoric ^{10}Be to the Earth's surface varies between about $0.01 - 4.0 \times 10^6 \text{ atoms cm}^{-2} \text{ y}^{-1}$ (Heikkilä and von Blanckenburg, 2015); compared to a production rate of *in situ* ^{10}Be at the Earth's surface of only about $4 \text{ atoms g}_{(\text{qtz})}^{-1} \text{ y}^{-1}$ at sea level and high latitude (SLHL; Phillips et al. (2016)).

The effect of temporal changes resulting from the solar modulation is assumed to average out at time scales of soil accumulation (Willenbring and von Blanckenburg, 2010b). ^{10}Be depositional flux records from GRIP ice cores (*Greenland Ice Core Project*) over the past 10,000 years show short-term fluctuations but the long-term integrated flux is not affected (Vonmoos et al., 2006; Willenbring and von Blanckenburg, 2010b). Since ^{10}Be is accumulated in soils over similar long time scales, it is

assumed that studies of soils and sediments are not affected by short-term fluctuations. Longer-term variations in meteoric ^{10}Be flux resulting from changes in Earth's magnetic field, in contrast, have to be corrected for (von Blanckenburg et al., 2015).

1.1.2 Depositional flux of meteoric ^{10}Be to the Earth's surface

After its production by spallation in the atmosphere, meteoric ^{10}Be is present in the form of reactive molecules like ^{10}BeO or $^{10}\text{Be}(\text{OH})_2$ that are attached to aerosols. The residence time of ^{10}Be in the atmosphere depends on the atmospheric export, the troposphere/stratosphere exchange, and the inner tropospheric mixing (McHargue and Damon, 1991). The average residence time of ^{10}Be in the lower stratosphere is about one to two years (Raisbeck et al., 1981). In the troposphere ^{10}Be is scavenged to aerosols and thus enters the hydrological cycle. The aerosols are precipitated both by dry (turbulent) or wet (precipitation-related) processes (Field et al., 2006). The residence time of meteoric ^{10}Be in the troposphere is only about a few weeks until it is precipitated to the Earth's surface. Meteoric ^{10}Be deposited at the Earth's surface consists of ^{10}Be produced in the atmosphere and precipitated directly, and so-called recycled ^{10}Be that is transported with dust or soil particles (aeolian component, MchHargue and Damon (1991), Heikkilä and Smith (2013)). Because of the strong dependence of atmospheric ^{10}Be scavenging on precipitation, the ^{10}Be delivery to the Earth's surface is highly dependent on atmospheric circulation in the atmosphere and hence on climate.

The depositional flux of cosmogenic meteoric ^{10}Be to the Earth's surface ($F_{\text{met}}^{10\text{Be}}$, in $\text{atoms cm}^{-2} \text{y}^{-1}$) is reviewed in detail in Willenbring and von Blanckenburg (2010b) but what governs its variation is highly discussed. Willenbring and von Blanckenburg (2010b) argue that the flux of ^{10}Be delivery to the Earth's surface is independent of the precipitation rate in settings where the atmospheric transport time is fast ("dilution effect"). In contrast, Graly et al. (2011) suggest that the deposition of ^{10}Be is primarily a function of the amount of precipitation ("additive effect"). At the current state of research one way to estimate the depositional flux is measuring long-term meteoric ^{10}Be inventories in independently dated soils and correlate these with short-term ^{10}Be concentrations measured in precipitation (Graly et al., 2011). In doing so, one derives first-order estimates of primary ^{10}Be fallout for a given precipitation rate at a certain mid- or low-latitude. A second way is using three-dimensional general circulation models of the atmosphere (GCM; Field et al. (2006); Heikkilä (2007); Heikkilä et al. (2013a); Heikkilä and Smith (2013)). These GCMs are combined with physical models that simulate cosmic ray particle interactions with the Earth's atmosphere and subsequent production and transport of secondary particles (Masarik and Beer, 2009). These modelled ^{10}Be fluxes average over large spatial scales and agree well with fluxes derived from ^{10}Be concentration measurement in ice cores (Finkel and Nishiizumi, 1997; Muscheler et al., 2004), and also recent measured ^{10}Be flux

estimates from e.g. rainfall (Willenbring and von Blanckenburg, 2010b). However, the meteoric ^{10}Be depositional flux to the Earth's surface remains still a large unknown in Earth surface studies as it is required when using this isotope for quantification of ages and rates.

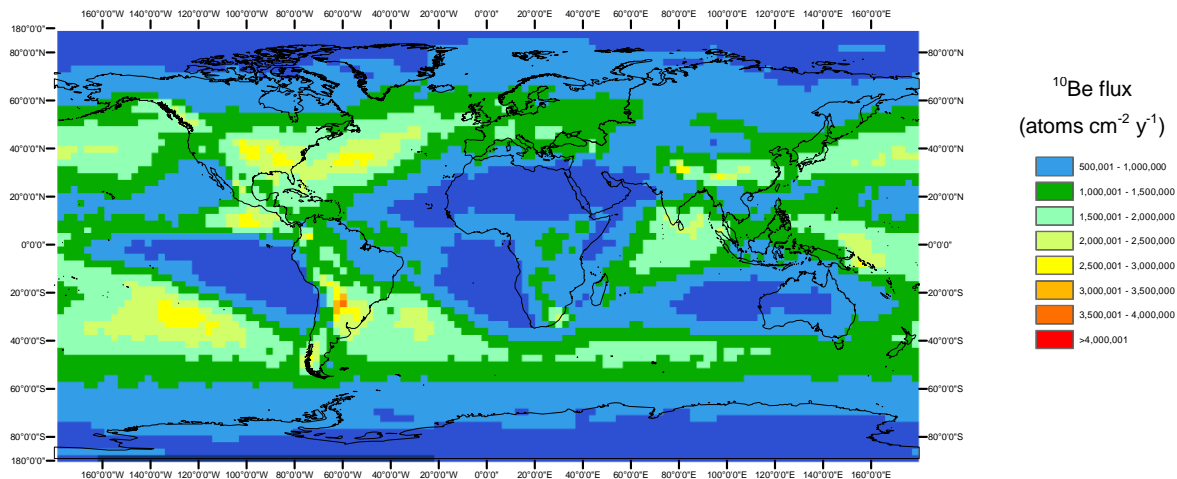


Figure 1.2: Average Holocene distribution of the depositional ^{10}Be flux (in $\text{atoms cm}^{-2} \text{y}^{-1}$) from the average of a “pre-industrial” GCM model run representing early Holocene conditions and an modern “industrial” model run (Heikkilä and von Blanckenburg, 2015). Figure from Heikkilä and von Blanckenburg (2015).

In this study the depositional flux of ^{10}Be is assessed from a modern “industrial” and an early Holocene “pre-industrial” model run that were combined by Heikkilä and von Blanckenburg (2015). Being representative of Holocene ^{10}Be deposition two ECHAM5-HAM GCM (European Centre for Medium-Range Weather Forecasts Hamburg Model 5) models were applied (see Figure 1.2), one describing modern atmospheric transport and meteoric ^{10}Be deposition (“industrial”; Heikkilä et al. (2013a)) and the other one simulating late deglacial climate conditions in the early Holocene (“pre-industrial”; Heikkilä et al. (2013b)). For the “industrial” model the direct output from the ECHAM5-HAM run (30 year time slice, resolution 2.8° by 2.8°) with modern atmosphere and aerosol loading was used to derive depositional ^{10}Be fluxes. In the case of the “pre-industrial” early Holocene model, ECHAM5-HAM was run with pre-industrial aerosol and greenhouse gas concentrations (30 year climatological simulation). Both models were run with an average “modern” solar modulation Φ of 501.76 MeV (averaged over three 11-year solar cycles). Steinhilber et al. (2012) derived an average Φ of 280.94 MeV for the Holocene from cosmogenic radionuclide studies in polar ice cores and tree rings, including changes in the geomagnetic field and in Φ . Hence, production rates for pre-industrial times should be higher than the ones considered in the model from Heikkilä et al. (2013b). For that reason modern ^{10}Be fluxes were corrected by a factor of 1.2315 (Heikkilä and von Blanckenburg, 2015), representing the combined solar modulation and geomagnetic field during the Holocene. However, these models provide only estimates at two different times, providing two “end member scenarios”. Nevertheless, over the long time scales investigated with cosmogenic ^{10}Be , short-term

temporal variations in the depositional flux are likely smoothed. For larger spatial scales, such as the Amazon basin, Wittmann et al. (2015) suggested that the GCM-derived depositional fluxes should be accurate. For smaller spatial scales, however, the values of the depositional ^{10}Be flux may be not accurately representing the actual ones due to the coarse-resolution of the global circulation model. For example, $F_{\text{met}}^{10\text{Be}}$ could – on the small scale considered in both studies presented here – deviate locally due to e.g. orographic effects that affect local precipitation patterns and the additive effect might play a role (Willenbring and von Blanckenburg, 2010b).

For the studied catchments in the Slavkov Forest an averaged depositional flux $F_{\text{met}}^{10\text{Be}}$ of $1.46 \times 10^6 \text{ atoms cm}^{-2} \text{ y}^{-1}$ results (see Figure 1.2). The difference between both models described above is $0.02 \times 10^6 \text{ atoms cm}^{-2} \text{ y}^{-1}$, resulting in a relative uncertainty of about 1%. As this uncertainty describes only the variability over time and not the uncertainty on the flux model itself an uncertainty of 1% is most likely underestimating the true uncertainty on $F_{\text{met}}^{10\text{Be}}$. Thus, I assume here an uncertainty of 10% that is assessed from the difference of the used pixel-read value to that of the adjacent cells read from the flux map (see Figure 1.2), accordingly providing a “spatial” uncertainty. In the case of the Sierra Nevada study site, a meteoric ^{10}Be flux $F_{\text{met}}^{10\text{Be}}$ of $1.20 \times 10^6 \text{ atoms cm}^{-2} \text{ y}^{-1}$ is read from Figure 1.2. In this case the uncertainty is $0.41 \times 10^6 \text{ atoms cm}^{-2} \text{ y}^{-1}$ resulting in an uncertainty of 34% that is propagated in following calculations.

1.1.3 Meteoric ^{10}Be at the Earth’s surface

At the Earth’s surface meteoric ^{10}Be is either adsorbed to or co-precipitated with amorphous and crystalline phases like Fe- and Al-(hydr)oxides and incorporated into secondary minerals (called “reactive” phase, $(^{10}\text{Be})_{\text{reac}}$) or it is transported in the dissolved form ($(^{10}\text{Be})_{\text{diss}}$). In the absence of humic acids and a corresponding pH value of above 5, ^{10}Be is mainly present in its hydrolyzed form (Takahashi et al., 1999). The high affinity of beryllium in natural environments to adsorb to solid soil particles is described by the partition coefficient (K_d value). The K_d value is defined as the reactive concentration over the dissolved concentration (in 1 kg^{-1}) and is a function of environmental conditions, like pH value, temperature, ionic strength of the solution, and equilibration time. Thus, the behaviour of beryllium in river sediment and soils is highly dependent on the hydrochemical conditions. Under neutral or alkaline conditions the K_d value of beryllium between solid particles and water is about 10^5 , but between a pH value of six and two the K_d value decreases rapidly by several magnitudes (You et al., 1989). In several laboratory studies the time-dependence of the partition of beryllium isotopes (^{10}Be and ^7Be) between dissolved and particulate phases was investigated showing that equilibrium is attained within several hours to weeks (Aldahan et al., 1999; Nyffeler et al., 1984;

You et al., 1989). As the adsorption of beryllium is fast but highly dependent on the pH value, acidification of aquatic systems affects the mobility and sorption of beryllium (Aldahan et al., 1999). Thus, beryllium is highly mobile in organic rich continental waters and the ^{10}Be concentration in such acidic streams is comparatively high being similar to ^{10}Be concentrations measured in rain (Brown et al., 1992).

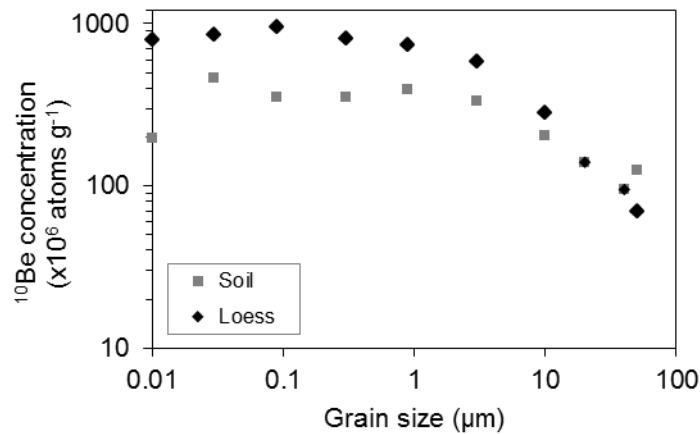


Figure 1.3: Grain size dependency of the ^{10}Be concentration in soil (grey squares) and loess deposits (black diamonds). The ^{10}Be concentration increases with decreasing grain size. Small clay-sized minerals ($< 3 \mu\text{m}$) have about the same concentrations. Data are from Shen et al. (2004) and figure is adapted from Willenbring and von Blanckenburg (2010b).

Due to the highly reactive character of beryllium hydroxides (BeOH^+ and $\text{Be}(\text{OH})_2$), beryllium is preferentially adsorbed to e.g. clay minerals, iron- or aluminum oxyhydroxides, or soil organic matter (Willenbring and von Blanckenburg, 2010b). Additionally, the retentivity of ^{10}Be is influenced by the grain size distribution. The smaller the grain size the higher the specific surface area (Helz and Valette-Silver, 1992) and the ion exchange capacity (Brown et al., 1992). The relation between the grain size and the beryllium concentration is illustrated in Figure 1.3. In this way, soils with a homogenous grain size distribution with depth have a maximum meteoric beryllium concentration at the soil surface; with depth the ^{10}Be concentration decreases exponentially (e.g. Pavich et al. (1986); Pavich et al. (1984); Willenbring and von Blanckenburg (2010b)). Differing concentration maxima in soil profiles (see Figure 1.4) often arise from a high occurrence of clays and clay-sized minerals (e.g. Graly et al. (2010)). Depending on the retentivity, meteoric ^{10}Be can percolate to depths of several meters. Bacon et al. (2012) and West et al. (2013) found in their studies significant meteoric ^{10}Be concentrations in saprolite at a depth of more than ten meters.

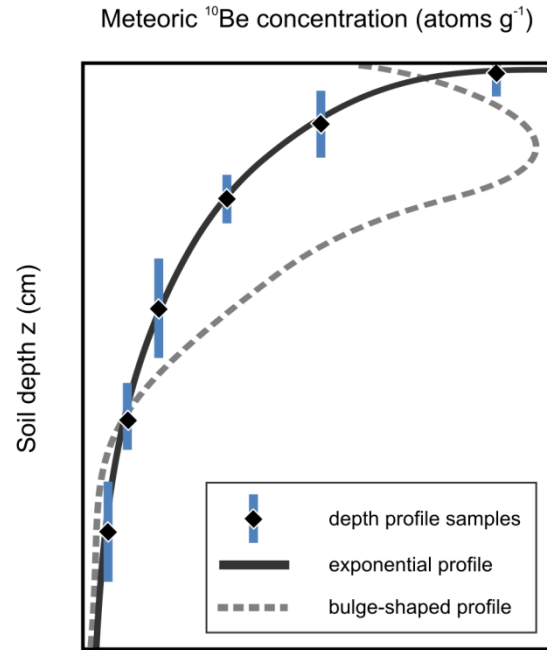


Figure 1.4: Conceptual meteoric ^{10}Be concentration depth profiles in soil based on published ^{10}Be depth profiles. The occurrence of clay rich soil horizons can lead to concentration maxima in these horizons that reflect grain size effects, indicated by a typical “bulge” shaped depth profile (Graly et al., 2010). In e.g. young soils and sediments the concentration simply decreases with soil depth, indicated by an exponential profile (Willenbring and von Blanckenburg, 2010b).

1.2 Theoretical framework of the $^{10}\text{Be}(\text{meteoric})/^{9}\text{Be}$ isotope system

1.2.1 Meteoric ^{10}Be and stable ^9Be in the Critical Zone

So far there are many studies using concentrations of the isotope meteoric ^{10}Be only ($[\text{}^{10}\text{Be}]$, in atoms g^{-1} ; concentrations are denoted in squared brackets hereafter) to quantify erosion rates or soil ages. However, the adsorption of ^{10}Be is highly dependent on the specific surface area (i.e. the grain size of sampled material) and the prevailing hydrogeochemical conditions (e.g. pH value of associated waters, see Section 1.1.3). Using meteoric ^{10}Be as proxy for erosion rates, taking a fine-grained sample and sand-dominated sample of the same catchment will yield different meteoric ^{10}Be concentrations and thus different erosion rate estimates. To correct for this grain size effect, ^{10}Be can be normalized over another metal with the following properties: (1) its chemical behavior should be similar to ^{10}Be , having about the same partition coefficient, (2) it should not generate new adsorption sites for ^{10}Be , (3) it should not limit the flux of ^{10}Be to the adsorption sites, (4) it should not be present in such a high amount that the adsorption sites are saturated (Willenbring and von Blanckenburg,

2010b). Considering all these properties, the best suitable metal is beryllium itself in its stable form (^9Be). Recently, von Blanckenburg et al. (2012) provide a set of mass balances to quantify denudation using meteoric ^{10}Be combined with its stable counterpart ^9Be that are summarized in Section 1.2.2.

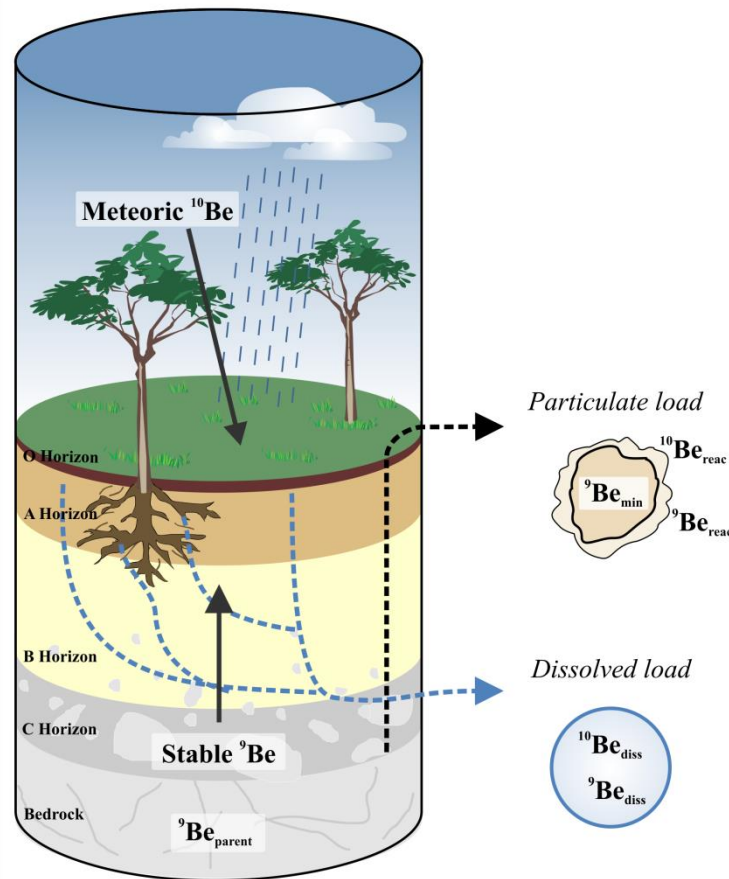


Figure 1.5: The meteoric ^{10}Be and stable ^9Be system shown for the Critical Zone. Meteoric ^{10}Be enters the weathering zone only through atmospheric deposition. Stable ^9Be is released from primary by weathering processes. In the Critical Zone ^{10}Be and ^9Be mix to a characteristic ratio that can be measured either in the dissolved load ($(\text{Be})_{\text{diss}}$) leaving the system by groundwater discharge or water runoff, or in the particulate form adsorbed to eroding sediment (e.g. secondary minerals; $(\text{Be})_{\text{reac}}$). The initial ^9Be concentration in the parent bedrock concentration is named $(^9\text{Be})_{\text{parent}}$, whereas the beryllium that is still locked in primary minerals that are exported by erosion is named $(^9\text{Be})_{\text{min}}$.

Stable ^9Be occurs at the Earth's surface by being present in parent bedrock material ($(^9\text{Be})_{\text{parent}}$). The advance of the weathering front leads to the release of ^9Be from primary minerals by weathering (see Figure 1.5). This ^9Be can either be reactive ($(^9\text{Be})_{\text{reac}}$) or it remains in the dissolved form in soil and stream waters ($(^9\text{Be})_{\text{diss}}$). The distribution of ^9Be is dependent on the weathering intensity and the formation of secondary minerals. Incongruent weathering leads to a fraction of ^9Be that stays locked in primary minerals (mineral-bound phase; $(^9\text{Be})_{\text{min}}$). In the Critical Zone ^{10}Be and ^9Be mix to a characteristic ratio that is dependent on the denudation rate, the depositional ^{10}Be flux, the fraction of ^9Be released from primary minerals, and the beryllium concentration of the parent bedrock (von Blanckenburg et al., 2012). The Critical Zone is the zone from the unweathered bedrock up to the

vegetation cover, within this interface meteoric waters and atmospheric gases interact with soil and rocks, and weathering takes place (Anderson et al., 2007). The ratio of ^{10}Be to ^9Be can be either determined in bulk sediment, in the reactive phase only (adsorbed onto mineral surfaces or precipitated in secondary/pedogenic minerals), or on the dissolved phase in stream waters yielding the denudation rate and the degree of weathering of an entire river basin (von Blanckenburg et al., 2012). One prerequisite to apply this method is that both beryllium isotopes equilibrate between the fluids decomposing primary minerals and the secondary and clay minerals formed during weathering.

1.2.2 Mass balance of beryllium fluxes

Using the framework presented by von Blanckenburg et al. (2012) requires that the ingoing depositional flux of meteoric ^{10}Be into a system (e.g. Critical Zone, stream catchment) is in steady state with the outgoing ^{10}Be flux in the reactive or dissolved form in streams. The catchment-wide ^{10}Be flux $J_{\text{atm}}^{10\text{Be}}$ (atoms y^{-1}) deposited at the Earth's surface, according to Wittmann et al. (2015), is:

$$J_{\text{atm}}^{10\text{Be}} = A_{\text{catch}} * F_{\text{met}}^{10\text{Be}} \quad \text{Equation 1.1}$$

where A_{catch} is the catchment area (m^2) that is exposed to the depositional flux of meteoric ^{10}Be ($F_{\text{met}}^{10\text{Be}}$; atoms $\text{m}^{-2} \text{y}^{-1}$). The flux of ^{10}Be that is exported from the catchment via streams is described by:

$$J_{\text{stream}}^{10\text{Be}} = J_{\text{reac}}^{10\text{Be}} + J_{\text{diss}}^{10\text{Be}} \quad \text{Equation 1.2}$$

Here, the total ^{10}Be flux $J_{\text{stream}}^{10\text{Be}}$ (atoms y^{-1}) carried by a stream is the sum of reactive ^{10}Be ($[^{10}\text{Be}]_{\text{reac}}$ in atoms kg^{-1}) carried by the sediment that is eroded (E in $\text{kg} \text{m}^{-2} \text{y}^{-1}$) and dissolved ^{10}Be ($[^{10}\text{Be}]_{\text{diss}}$ in atoms l^{-1}) measured in stream water runoff q ($\text{l} \text{m}^{-2} \text{y}^{-1}$):

$$J_{\text{stream}}^{10\text{Be}} = A_{\text{catch}} * (E * [^{10}\text{Be}]_{\text{reac}} + q * [^{10}\text{Be}]_{\text{diss}}) \quad \text{Equation 1.3}$$

At steady state $J_{\text{stream}}^{10\text{Be}}$ equals $J_{\text{atm}}^{10\text{Be}}$ (Wittmann et al., 2015) such that combining Equation 1.1 and Equation 1.3 results in the following Equation 1.4:

$$F_{\text{met}}^{10\text{Be}} = E * [^{10}\text{Be}]_{\text{reac}} + q * [^{10}\text{Be}]_{\text{diss}} \quad \text{Equation 1.4}$$

The total ^9Be stream output flux $J_{\text{stream}}^{^9\text{Be}}$ (atoms y^{-1}) is the sum of mineral-bound ^9Be ($[^9\text{Be}]_{\text{min}}$ in atoms kg^{-1}) and reactive ^9Be ($[^9\text{Be}]_{\text{reac}}$ in atoms kg^{-1}) carried by the eroded sediment plus dissolved ^9Be ($[^9\text{Be}]_{\text{diss}}$ in atoms l^{-1}) measured in water runoff q ($\text{l m}^{-2} \text{y}^{-1}$):

$$J_{\text{stream}}^{^9\text{Be}} = A_{\text{catch}} * (E * [^9\text{Be}]_{\text{min}} + E * [^9\text{Be}]_{\text{reac}} + q * [^9\text{Be}]_{\text{diss}}) \quad \text{Equation 1.5}$$

^9Be enters the system by the advance of the weathering front. It follows that for the ^9Be system the mass balance is (von Blanckenburg et al., 2012):

$$D * [^9\text{Be}]_{\text{parent}} = E * ([^9\text{Be}]_{\text{min}} + [^9\text{Be}]_{\text{reac}}) + q * [^9\text{Be}]_{\text{diss}} \quad \text{Equation 1.6}$$

with D being the denudation rate ($\text{kg m}^{-2} \text{y}^{-1}$) and $[^9\text{Be}]_{\text{parent}}$ the beryllium concentration of the parent bedrock material (atoms kg^{-1}). Expressed in non-dimensional ^9Be fractional fluxes (derived by dividing Equation 1.6 by $D * [^9\text{Be}]_{\text{parent}}$):

$$1 = f_{\text{min}}^{^9\text{Be}} + f_{\text{reac}}^{^9\text{Be}} + f_{\text{diss}}^{^9\text{Be}} \quad \text{Equation 1.7}$$

The term $f_{\text{reac}}^{^9\text{Be}} + f_{\text{diss}}^{^9\text{Be}}$ describes the fraction of ^9Be that is released upon weathering from primary minerals and is thus a measure for the degree of weathering of Be-bearing minerals (von Blanckenburg et al., 2012). Only this component of ^9Be that is partitioned between the dissolved phase and the reactive phase mixes with meteoric ^{10}Be in the Critical Zone. It can be calculated from measured concentrations of $(^9\text{Be})_{\text{reac}}$ and $(^9\text{Be})_{\text{min}}$ by:

$$(f_{\text{reac}}^{^9\text{Be}} + f_{\text{diss}}^{^9\text{Be}})_{\text{min/reac}} = \frac{1}{\left(\frac{[^9\text{Be}]_{\text{min}}}{[^9\text{Be}]_{\text{reac}}} + 1\right)} \quad \text{Equation 1.8}$$

This equation is likely to be applicable with moderate bias for soil samples, whereas in cases where sorting occurs, e.g. in river sediment, $[^9\text{Be}]_{\text{reac}}$ can be enriched over $[^9\text{Be}]_{\text{min}}$ when measuring fine-grained sediment. If the individual fluxes of ^9Be are known, the degree of ^9Be weathering can alternatively be derived from dissolved and sediment fluxes of ^9Be (atoms y^{-1} ; Wittmann et al. (2015)):

$$J_{\text{stream}}^{^9\text{Be}} = J_{\text{min}}^{^9\text{Be}} + J_{\text{reac}}^{^9\text{Be}} + J_{\text{diss}}^{^9\text{Be}} \quad \text{Equation 1.9}$$

The non-dimensional fraction of $f_{\text{reac}}^{9\text{Be}} + f_{\text{diss}}^{9\text{Be}}$ can be calculated by dividing the individual fluxes by the total riverine flux:

$$\left(f_{\text{reac}}^{9\text{Be}} + f_{\text{diss}}^{9\text{Be}}\right)_{\text{fluxes}} = \frac{J_{\text{reac}}^{9\text{Be}}}{J_{\text{stream}}^{9\text{Be}}} + \frac{J_{\text{diss}}^{9\text{Be}}}{J_{\text{stream}}^{9\text{Be}}} \quad \text{Equation 1.10}$$

1.2.3 Erosion rates based on meteoric [^{10}Be]

Beryllium concentrations in the dissolved phase and in the reactive phase are linked by the partition coefficient K_d that describes the partition of an element between the particulate and the dissolved phase (kg^{-1}):

$$K_d = \frac{[\text{Be}]_{\text{reac}}}{[\text{Be}]_{\text{diss}}} \quad \text{Equation 1.11}$$

Substituting Equation 1.11 in Equation 1.4 allows calculating a steady state erosion rate E ($\text{kg m}^{-2} \text{y}^{-1}$) from a reactive ^{10}Be concentration:

$$E = \frac{F_{\text{met}}^{10\text{Be}}}{[^{10}\text{Be}]_{\text{reac}}} - \frac{q}{K_d} \quad \text{Equation 1.12}$$

This equation shows that an accurate erosion rate can only be determined if the water runoff q and the K_d value are known over the residence time of meteoric ^{10}Be in the weathering zone (von Blanckenburg et al., 2012). Ignoring the q/K_d -term is only valid in settings with a high retentivity for beryllium (most beryllium is adsorbed or precipitated as reactive beryllium; high K_d), a very low water runoff q , or a high erosion rate E , corresponding to $E \gg q/K_d$:

$$E = \frac{F_{\text{met}}^{10\text{Be}}}{[^{10}\text{Be}]_{\text{reac}}} \quad \text{Equation 1.13}$$

Note that $[^{10}\text{Be}]_{\text{reac}}$ is dependent on the specific surface area of the sampled material and therefore a grain size effect has to be considered evaluating erosion rates.

1.2.4 Denudation rates based on $^{10}\text{Be}/^9\text{Be}$ ratios

Linking the mass balances for meteoric ^{10}Be and stable ^9Be leads to Equation 1.14, which underlines that the reactive or dissolved ratio between ^{10}Be and ^9Be is the ratio between the flux of meteoric ^{10}Be precipitated at the Earth's surface and the flux of ^9Be dissolved by weathering processes in the Critical Zone (von Blanckenburg et al., 2012):

$$\left(\frac{^{10}\text{Be}}{^9\text{Be}}\right)_{\text{reac}} = \left(\frac{^{10}\text{Be}}{^9\text{Be}}\right)_{\text{diss}} = \frac{F_{\text{met}}^{^{10}\text{Be}}}{D * [^9\text{Be}]_{\text{parent}} - E * [^9\text{Be}]_{\text{min}}} \quad \text{Equation 1.14}$$

Ignoring any mass-dependent isotope fractionation $(^{10}\text{Be}/^9\text{Be})_{\text{reac}}$ equals $(^{10}\text{Be}/^9\text{Be})_{\text{diss}}$ at equilibrium. This equation is valid in a system that is at steady state regarding denudational and isotopic fluxes provided that ^{10}Be and ^9Be are mixed to a characteristic ratio that integrates over all fluxes of beryllium isotopes into and out of the weathering zone. As stable ^9Be serves as a weathering proxy, taking the isotope ratios of $(^{10}\text{Be}/^9\text{Be})_{\text{reac}}$ or $(^{10}\text{Be}/^9\text{Be})_{\text{diss}}$ provides information about the total denudation and a denudation rate D ($\text{kg m}^{-2} \text{y}^{-1}$) can be calculated (von Blanckenburg et al., 2012):

$$D = \frac{F_{\text{met}}^{^{10}\text{Be}}}{\left(\frac{^{10}\text{Be}}{^9\text{Be}}\right)_{\text{reac/diss}} * [^9\text{Be}]_{\text{parent}}} \left(\frac{[^9\text{Be}]_{\text{min}}}{[^9\text{Be}]_{\text{reac}}} + 1 \right) - \frac{q}{K_d} * \frac{[^9\text{Be}]_{\text{min}}}{[^9\text{Be}]_{\text{parent}}} \quad \text{Equation 1.15}$$

Although $(^{10}\text{Be}/^9\text{Be})_{\text{reac}}$ and $(^{10}\text{Be}/^9\text{Be})_{\text{diss}}$ are independent of water runoff or retentivity, calculating D still requires knowing q/K_d (von Blanckenburg et al., 2012). Equation 1.15 can be simplified if $K_d \gg \frac{q * [^9\text{Be}]_{\text{min}}}{D * [^9\text{Be}]_{\text{parent}}}$:

$$D = \frac{F_{\text{met}}^{^{10}\text{Be}}}{\left(\frac{^{10}\text{Be}}{^9\text{Be}}\right)_{\text{reac/diss}} * [^9\text{Be}]_{\text{parent}}} \left(\frac{[^9\text{Be}]_{\text{min}}}{[^9\text{Be}]_{\text{reac}}} + 1 \right) \quad \text{Equation 1.16}$$

If the fractional fluxes of ^9Be are known (Equation 1.7), a denudation rate can also be calculated with:

$$D = \frac{F_{\text{met}}^{^{10}\text{Be}}}{\left(\frac{^{10}\text{Be}}{^9\text{Be}}\right)_{\text{reac}} * [^9\text{Be}]_{\text{parent}}} * \frac{1}{\left(f_{\text{reac}}^{^9\text{Be}} + f_{\text{diss}}^{^9\text{Be}}\right)} \quad \text{Equation 1.17}$$

In contrast to the single isotope system $[^{10}\text{Be}]_{\text{reac}}$, where the concentration of reactive ^{10}Be depends linearly on the loss of ^{10}Be into solution, $(^{10}\text{Be}/^9\text{Be})_{\text{reac}}$ and $(^{10}\text{Be}/^9\text{Be})_{\text{diss}}$ are independent of whether the ^9Be was portioned into the dissolved or reactive phase, but rather depends on $f_{\text{reac}}^{^9\text{Be}} + f_{\text{diss}}^{^9\text{Be}}$ (von Blanckenburg et al., 2012).

Additionally, a denudation rate can be calculated with the total beryllium ratio $((^{10}\text{Be}/^9\text{Be})_{\text{total}})$ using total beryllium concentrations measured in bulk sediment (von Blanckenburg et al., 2012):

$$D = \frac{F_{\text{met}}^{^{10}\text{Be}}}{\left(\frac{^{10}\text{Be}}{^9\text{Be}}\right)_{\text{total}} * [^9\text{Be}]_{\text{parent}}} \quad \text{Equation 1.18}$$

In this equation $(^{10}\text{Be}/^9\text{Be})_{\text{total}}$ is defined as the ratio that is exported as bulk solid material from the system. In most systems, $[^{10}\text{Be}]_{\text{total}}$ equals $[^{10}\text{Be}]_{\text{reac}}$ and $[^9\text{Be}]_{\text{total}}$ is calculated by the sum of $[^9\text{Be}]_{\text{reac}}$ and $[^9\text{Be}]_{\text{min}}$.

1.3 Analytical methods

1.3.1 Sequential extraction method applied to sediment samples

Meteoric ^{10}Be delivered to the Earth's surface and stable ^9Be released through weathering reactions adsorb to the surfaces of secondary minerals or are incorporated into Fe- and Al-(hydr)oxides, amorphous alumina silicates or clays. In the case of ^9Be , isolating those parts of ^9Be that have participated in weathering reactions from the remaining mineral-bound beryllium still present in primary minerals is necessary. To extract this reactive phase of beryllium $(\text{Be})_{\text{reac}}$ from the remaining mineral-bound phase $(\text{Be})_{\text{min}}$, sediment and soil samples were treated with a sequential extraction method (Bourlès et al., 1989; Guelke et al., 2010; Tessier et al., 1979) described in detail in Wittmann et al. (2012) (see also Appendix A.1.1). For most of the samples processed in this study, I adapted the sequential leaching procedure by only extracting amorphous oxides $(\text{Be})_{\text{am-ox}}$ and crystalline oxides $(\text{Be})_{\text{x-ox}}$ (see Figure 1.6) because in most cases beryllium measured in the exchangeable phase $(\text{Be})_{\text{ex}}$ and organic-bound phase $(\text{Be})_{\text{org}}$ is negligible (Wittmann et al. (2012); see Appendix A.2.1).

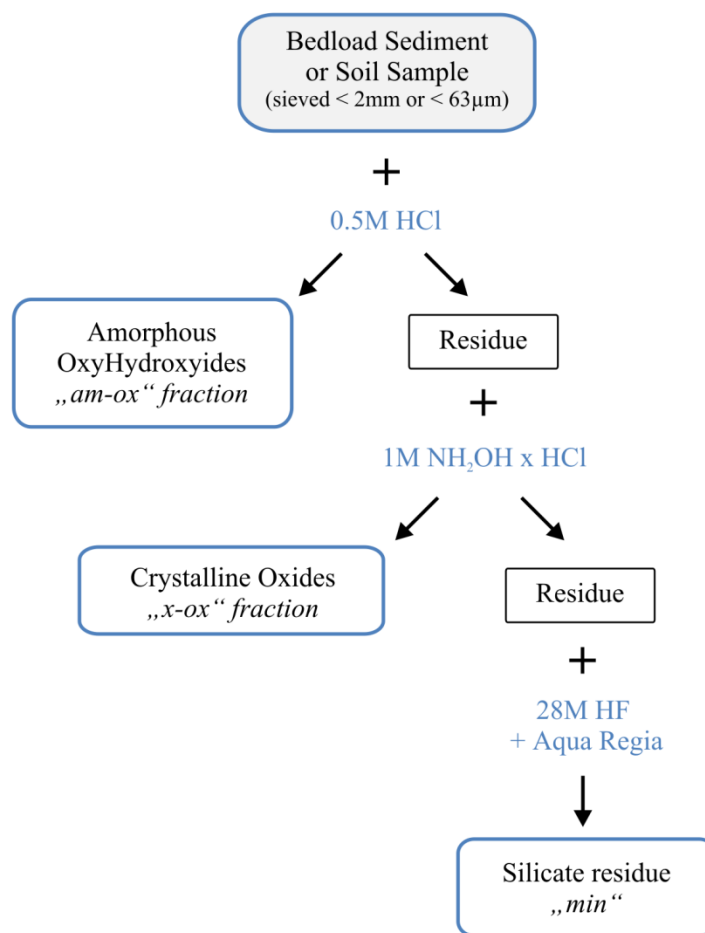


Figure 1.6: Sequential extraction procedure to separate the reactive phase of beryllium ((Be)_{rac}) from mineral-bound beryllium ((Be)_{min}). See text for description. Figure modified from Wittmann *et al.* (2012).

About 0.5 to 1 g of sediment was used for extraction. In a first step amorphous oxy(hydro)oxides (called “am-ox”) were attacked with 0.5M HCl (hydrochloric acid) under mild shaking at room temperature for 24 hours. Afterwards the crystalline oxides (called “x-ox”) were dissolved by using a 1M hydroxylamine-hydrochloride solution (NH₂OH*HCl). The samples were placed in an ultrasonic bath, heated up to about 70°C and manually shaken repeatedly every ten minutes. The solutions were then treated with concentrated H₂O₂ (hydrogen peroxide) and concentrated HNO₃ (nitric acid) to destroy potential hydroxylamine complexes. In case of high amounts of hydroxylamine complexes I destroyed these in a microwave application run (see Appendix A.1.1). In some cases an insoluble residue emerged after the single dissolution steps, which was then treated with a mixture of HF (hydrofluoric acid) and HNO₃. The solid residue material (called “min”) that remains after these extraction steps was dissolved either by digestion on a hotplate or in a microwave run with concentrated HNO₃ and HF and an additional aqua regia step. After each extraction or dissolution step the samples were evaporated and redissolved in 3M HNO₃. One aliquot was taken for natural ⁹Be and major element concentration measurements with ICP-OES (Inductively coupled plasma optical

emission spectroscopy, *Varian 720-ES*, axial optics) and a second aliquot was taken for cosmogenic ^{10}Be measurements. For measurements of the cosmogenic ^{10}Be , the samples were spiked with 150 to 500 μg ^9Be (in-house “phenakite” ^9Be Carrier – *Phenakite Batch 2Q2P*), depending on the amount of ^{10}Be expected, and homogenized. The samples were evaporated and the method of a “fluoride cake” was applied to samples with high cation loads (> 2 meq) to remove e.g. Al (Stone, 1998) by adding 1 ml of HF. The HF was evaporated, the step repeated, and then 10 ml of MilliQ[®]-H₂O were added and the samples were heated at temperatures of ~ 75 °C. After this water leach, where water soluble BeF_2 is dissolved whereas other cations stay in their fluoride form (Stone, 1998), the samples were evaporated and in the following prepared for the measurement with accelerator mass spectrometry (AMS) as described in Section 1.3.3.

The accuracy of stable ^9Be concentration measurements on the ICP-OES was verified by routinely measuring reference materials with an element matrix comparable to the measured samples. These are two reference materials, a granite (“Geostandard GA”, *Centre de Recherches Pétrographiques et Géochimiques* CRPG – CNRS; published Be concentration 3.6 ± 0.3 ppm (95 % confidence limit, (Govindaraju, 1995)) and a rhyolite (“RGM-1”, *United States Geological Survey* USGS, published Be concentration 2.4 ± 0.2 ppm (1SD; Govindaraju (1994)) that were dissolved and diluted for measurement on the ICP-OES. Average concentration values measured were 3.1 ± 0.2 ppm Be in the GA solution and 2.1 ± 0.1 ppm Be in the RGM-1 solution (see Appendix A.1.3.2). The long-term repeatability propagated with ICP-OES concentration results is 5%.

Together with the soil and sediment samples of the Sierra Nevada I also performed sequential extractions on a soil reference material (San Joaquin Soil, “SRM 2709”, *National Institute of Standards & Technology* NIST). In the case of the first extraction step using HCl a good repeatability is achieved. An average ^9Be concentration of 0.325 ± 0.021 ppm (1SD, $n = 6$; see Appendix A.3.2) is measured. For the second step (extraction with $\text{NH}_2\text{OH}\cdot\text{HCl}$) only two ^9Be measurements were performed that give a ^9Be concentration of 0.165 ± 0.067 ppm (1SD, $n = 2$). The median published value given for the leachable phases with this reference material is 0.61 ppm (range 0.5 - 0.72 ppm; leached after USEPA methods 200.7 and 3050B). In that case the soil was leached with HCl, HNO_3 , and H_2O_2 with temperatures of about 95°C. The different extraction procedures applied can explain the difference in the published ^9Be concentration compared to the total reactive ^9Be concentration of 0.49 ± 0.09 (1SD) ppm measured here.

1.3.2 Measurement of dissolved beryllium concentrations

Because of its low natural concentrations, ^{10}Be is pre-concentrated from water samples. Dissolved cosmogenic ^{10}Be can be concentrated from a water sample by co-precipitation with iron(III)-

hydroxide (see Figure 1.7) as the concentration of beryllium in water is otherwise too low to coagulate. The preparation of the stream water samples for cosmogenic ^{10}Be measurements followed an adapted method of Jeandel (1993) and Frank et al. (2009), who measured neodymium isotopes and dissolved $^{10}\text{Be}/^9\text{Be}$ ratios, respectively, in sea water samples.

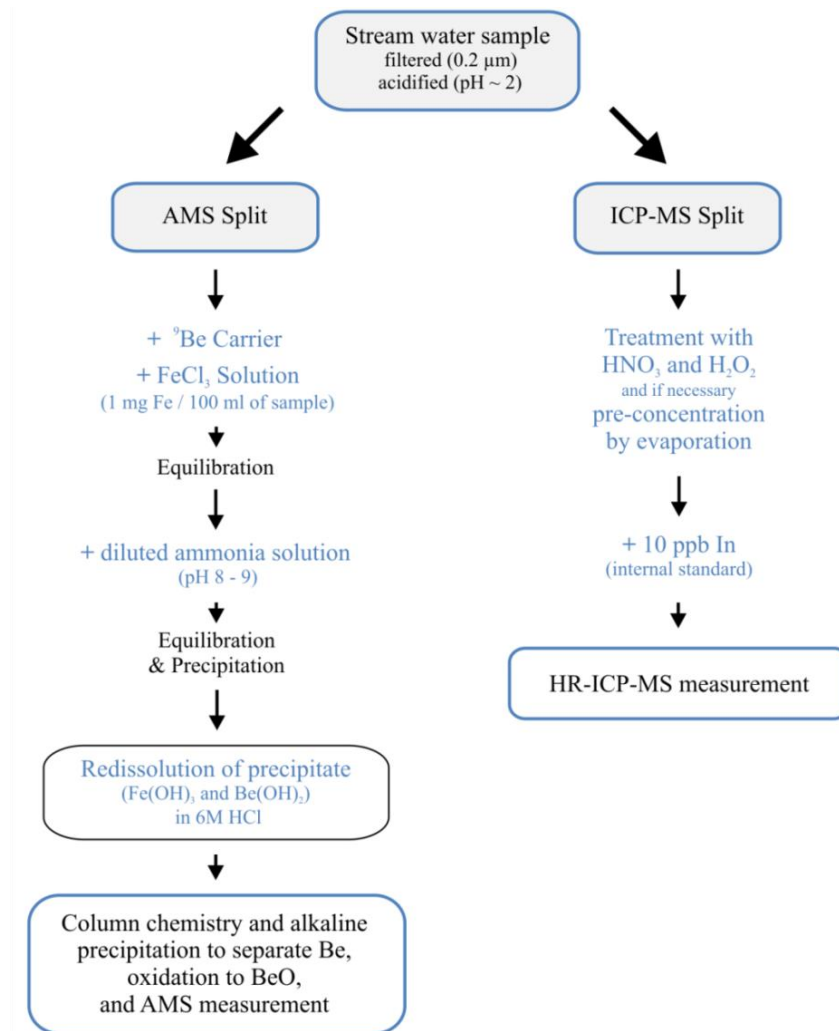


Figure 1.7: Treatment of water samples. The method for meteoric ^{10}Be is adapted from Jeandel (1993) and Frank et al. (2009). Figure modified from Wittmann et al. (2015).

I used about 200 to 600 ml of stream water, depending on the expected amount of cosmogenic ^{10}Be in the samples. Between 150 and 400 μg ^9Be carrier were added to each sample. After carrier addition, the samples were spiked with iron in the form of FeCl_3 solution (in 1M HCl). About 1 mg iron per 100 ml sample was added. After about 12 hours of equilibration time beryllium was precipitated with Fe(OH)_3 by bringing up the pH to 8 - 9 using diluted ammonia solution. In the case of high organic content in the samples, I added a few 100 μl of concentrated H_2O_2 to enhance the precipitation of Fe(OH)_3 and Be(OH)_2 . Afterwards the samples were filtered through a 0.2 μm membrane filter or centrifuged to separate the precipitate, followed by the redissolution of the hydroxides in 6M HCl.

The beryllium was then separated prepared for AMS measurement (as summarized in Section 1.3.3). The recovery of this method was tested to be about 90% (see Appendix A.1.3.3) by adding a known amount of ^9Be to five artificial samples. Two artificial samples were additionally spiked with oxalic acid to mirror an organic-rich water sample. In this case the recovery of ^9Be is about 85%, which I regard as sufficient recovery because at the AMS facility $^{10}\text{Be}/^9\text{Be}$ ratios will be measured and it is assumed that ^{10}Be and ^9Be are partitioned in the same way.

The natural ^9Be concentration in stream water was measured directly on a high-resolution mass spectrometer (HR-ICP-MS, *Element XR Thermo Fischer*), but spiked beforehand with 10 ppb indium (In) for internal standard correction. Expecting relatively low natural ^9Be concentration in a sample, I pre-concentrated samples before measurement by evaporation. For validation of the measurements and reproducibility assessment, I measured a natural water (acidified spring water, “SRM 1640a”, *National Institute of Standards & Technology NIST*, published $[\text{Be}] = 3.002 \pm 0.027 \mu\text{g kg}^{-1}$). For ^9Be the long-term reproducibility is 7.4 % (in total 14 measurements in 2 ½ years; see Appendix A.1.3.1), which was propagated as uncertainty to the individual stream water samples.

1.3.3 Sample preparation for AMS measurement

For measurement of the cosmogenic ^{10}Be , beryllium has to be separated from the remaining sample. This beryllium separation was done by ion exchange chromatography and subsequent alkaline precipitation as described in von Blanckenburg et al. (1996a) and von Blanckenburg et al. (2004). The samples were first taken up in 6 M HCl for anion column chemistry to separate iron (Fe). The resin (Bio-Rad AG 1-X8, mesh 100-200) was conditioned also with 6M HCl such that Be is eluted immediately while Fe is retained on the resin (see Appendix A.1.2 for detailed description). This step was followed by a chromatographic separation of Be on a cation exchange column (Bio-Rad AG 50W-X12 resin, mesh 200-400). The samples were evaporated, taken up in 0.4M oxalic acid, and loaded on the column. Trivalent cations like Al or Fe were eluted directly. Beryllium was eluted in 1M HNO_3 and then precipitated as $\text{Be}(\text{OH})_2$ at pH ~ 9 using diluted ammonia solution (NH_4OH) that was added to the 1M HNO_3 solution. The beryllium precipitate was redissolved in 5M HNO_3 and evaporated in small quartz crucibles.

The measurements of most of the Slavkov Forest samples were performed at the Tandem AMS facility at the ETH Zurich relative to standard S2007N ($^{10}\text{Be}/^9\text{Be} = 28.1 \times 10^{-12}$) with an associated half-life of $1.39 \pm 0.012 \text{ My}$ (Kubik and Christl, 2010). The beryllium was mixed with AgNO_3 (Be : Ag = 1 : 20), oxidized to BeO, the BeO was then powdered and mixed with copper, and finally pressed into mass spectrometer targets. Some samples were measured on the 0.5MV Tandy facility at the ETH Zurich. In this case beryllium was oxidized first to BeO and then mixed with niobium (Nb).

The samples from the Sierra Nevada project were measured at the CologneAMS facility of the University of Cologne. Measurements were carried out relative to the standards of Nishiizumi (KN01-6-2 ($^{10}\text{Be}/^9\text{Be} = 5.35 \times 10^{-13}$) and KN01-5-1 ($^{10}\text{Be}/^9\text{Be} = 2.709 \times 10^{-11}$)) which assume a half-life for ^{10}Be of 1.36 ± 0.07 My (Nishiizumi et al., 2007). For measurement, BeO is oxidized, afterwards mixed with Nb (Nb : BeO = 6 : 1), and then pressed into mass spectrometer targets. Blanks yielded an average $^{10}\text{Be}/^9\text{Be}$ ratio ($\pm 1\text{SD}$) of $4.93 \pm 5.90 \times 10^{-15}$ ($n = 14$) for the AMS facility at ETH Zurich, $6.506 \pm 0.075 \times 10^{-15}$ ($n = 2$) for the Tandem at ETH Zurich, and $1.28 \pm 1.11 \times 10^{-15}$ ($n = 15$) for the CologneAMS. These blanks were subtracted, respectively, and the standard deviation of their mean propagated together with analytical uncertainties into the given ^{10}Be concentration uncertainties. In the case of the soil and sediment samples, ^{10}Be concentrations were corrected for natural ^9Be concentrations and for the amount of the ^9Be split for ICP-OES measurement.

2 Quantification of denudation and chemical weathering in creek catchments with different lithologies in the Slavkov Forest, Czech Republic

2.1 Introduction

In this study, I applied the $^{10}\text{Be}(\text{meteoric})/^9\text{Be}$ system on the small spatial scale in creek catchments that differ in their lithology. Three small first-order stream catchments that are located in the Slavkov Forest, Czech Republic, were selected. The lithology of these upland catchments differs from felsic (granite) to mafic (amphibolite) and ultramafic (serpentinite) rocks. The catchments exhibit highly variable hydrogeochemical conditions, e.g. stream water pH values vary from acidic to slightly alkaline between these catchments, displaying the ability of the (ultra)mafic catchments to buffer the acidification caused by e.g. acid rain, while the felsic catchment is a highly acidic catchment with a low acid-buffering capability. In the second half of the 20th century, atmospheric anthropogenic acid deposition highly affected European terrestrial and aquatic ecosystems, being visible through e.g. soil acidification and local acidification of surface waters (Drever, 1997; Paces, 1985; Reuss et al., 1987). Many forested landscapes like the studied area of the Slavkov Forest slowly recover ever since (Hruška and Kram, 2003; Navrátil et al., 2007). The major acidifying anion in the granitic catchment is sulphate (SO_4) which can be only derived from acidic precipitation as there is no source of sulfur in the granitic bedrock (Hruška and Kram, 2003). This acidic catchment (Lysina) and the ultramafic catchment (Pluhův Bor) have been established as research catchments in 1989 and 1991, respectively, to study the impact of acidic precipitation on forest systems (Krám and Hruška, 1994).

I studied the behaviour of ^{10}Be and $^{10}\text{Be}/^9\text{Be}$ ratios in the catchments by (1) testing whether the depositional flux of ^{10}Be is in balance with the ^{10}Be flux exported in the sedimentary and dissolved form and hence a steady state is established, (2) exploring whether the dissolved phase is in equilibrium with the reactive phase, and (3) considering the dependence of the $^{10}\text{Be}/^9\text{Be}$ ratio in bedload sediment and stream water on the depth distribution and fluid flow paths in the catchments. I calculated erosion and denudation rates from meteoric ^{10}Be only and the $^{10}\text{Be}(\text{meteoric})/^9\text{Be}$ ratio, respectively, and compared these rates with *in situ* ^{10}Be -derived denudation rates and chemical weathering rates based on dissolved loads in streams. In the context of decade-spanning records of stream water chemistry and pH values plus diverse catchment lithologies the settings in the Slavkov Forest offer unique conditions to test the potential of the $^{10}\text{Be}(\text{meteoric})/^9\text{Be}$ system.

2.2 Study site and sampling

2.2.1 Study site

The Slavkov Forest is a mountainous Protected Landscape Area (CHKO Slavkovský les) located in western Bohemia in the northwest of the Czech Republic (see Figure 2.1). Geologically the area of the Slavkov Forest is dominated by the Karlovy Vary Massif, a Late Variscan granite body (Blecha and Stemprok, 2012). In the south of the Slavkov Forest mafic rocks of the Mariánské Lázně Complex, a high-grade ophiolitic complex, and the Kladská Unit occur (Jelínek et al., 1997).

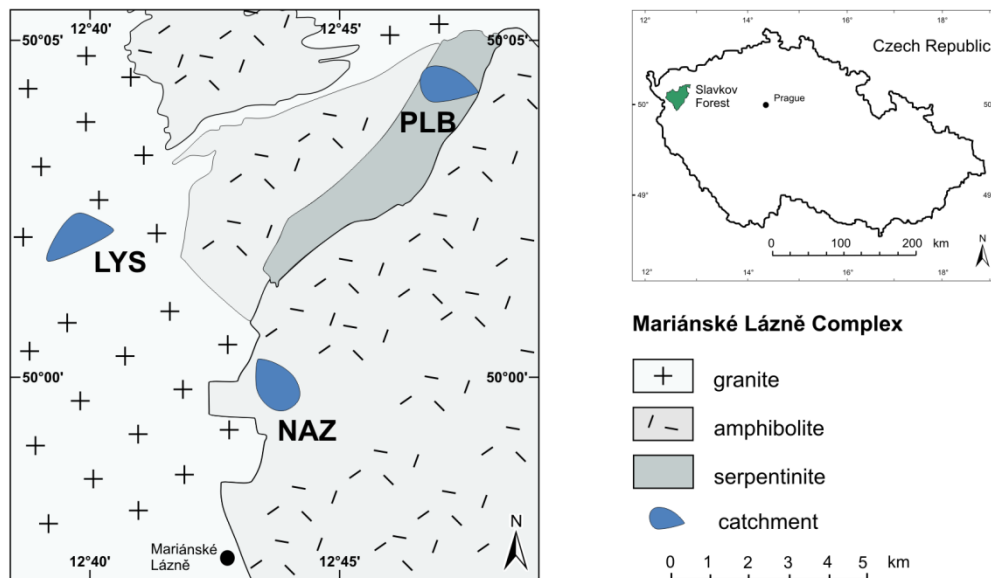


Figure 2.1: Simplified map of a part of the Mariánské Lázně Complex with the prevailing bedrock types (modified after Jelínek and Štědrá (1997)). In blue the three catchments are shown (not true scale; LYS Lysina, NAZ Na Zeleném, and PLB Pluhův Bor). The small map shows the location of the Slavkov Forest in the Czech Republic.

The acidic Lysina catchment (LYS) is underlain by leucocratic granite comprising orthoclase, quartz, albite and a lithium mica as main minerals (Navrátil, 2000). In the other catchments that are located in the direct vicinity of Lysina mafic and ultramafic rocks of the Mariánské Lázně Complex crop out. The mafic Na Zeleném catchment (NAZ) exhibits mainly retrogressed garnetiferous amphibolite with intrusions of Mg-rich metadorite (Štědrá et al., 2014). The amphibolite predominantly consists of tremolite and plagioclase. The ultramafic Pluhův Bor catchment (PLB) is dominated by serpentinite, tremolite schist and actinolitic schist, and amphibolites (Krám et al., 2009). The predominant mineral in the serpentinite is antigorite with trace amounts of opaque minerals and talc (Krám and Hruška,

1994; Krám et al., 2012). The granite at Lysina is weathered primarily by dissolution of plagioclase, orthoclase and mica, resulting in formation of secondary clay minerals (Krám and Hruška, 1994). In amphibolite rocks the predominant weathering processes are the dissolution of plagioclase, hornblende (Ca amphibole, tremolite) and biotite (Velbel, 1992). The release of Al and SiO₂ allows the formation of secondary clay minerals. In ultramafic serpentinite the most important weathering process is the dissolution of antigorite (Krám and Hruška, 1994). In the early stages of serpentinite weathering, MgO and SiO₂ are leached and a large proportion goes into solution and is removed from the catchment in the dissolved form (Caillaud et al., 2004). During pedogenesis of ultramafic rocks, Fe is transferred from silicate minerals to Fe-oxides and hydroxides (Caillaud et al., 2006), and serpentine and chlorite alter to Fe- and Al- clay minerals like vermiculite and smectite (Bulmer and Lavkulich, 1994).

Table 2.1: Location and characteristics of the three studied catchments in the Slavkov Forest, Czech Republic

Catchment	Lysina (LYS)	Na Zeleném (NAZ)	Pluhův Bor (PLB)
Coordinates of catchment outlet	50°2.069'N, 12°40.149'E	49°59.896'N, 12°42.563'E	50°3.389'N, 12°47.309'E
Area (km ²)	0.273	0.550	0.216
Altitude (m.a.s.l.)	829 - 949	736 - 802	690 - 804
Mean discharge (mm y ⁻¹)	432	338	253
Mean stream water pH	4.2	6.9	7.6
Underlying bedrock	felsic (granite)	mafic rocks (e.g. amphibolite)	(ultra-)mafic rocks (serpentinite, amphibolite)
Soil type	Podzol, Gleysol	Cambisol	Stagnosol
Vegetation cover	Norway Spruce	Norway Spruce	Norway Spruce, Scots pine

All catchments have similar topography, altitude, catchment size (see Table 2.1), mean annual air temperature (5-6 °C), and a mean precipitation of about 950 mm (Mariánské Lázně). The altitude varies between 690 m a.s.l. (the lowest point at Pluhův Bor) and 949 m a.s.l. (the highest point at Lysina). The highest peaks in the Slavkov Forest are Mount Lesný (983 m asl) and Mount Lysina (982 m asl). The catchments are covered mainly by Norway spruce (*Picea abies*) monocultures, and are 0.22 - 0.55 km² in size with perennial streams of less than one kilometer length. The water runoff, averaged over the time since installation of the monitoring sites, is about 430 mm y⁻¹ in Lysina, 340 mm y⁻¹ in Na Zeleném, and 250 mm y⁻¹ in Pluhův Bor (Hruška and Kram (2003); Krám et al. (2012); P. Kram, unpublished data). Due to the different bedrock types the stream waters reveal highly contrasting hydrochemical characteristics and highly differentiated stream chemistry regarding their cation load (Krám et al., 2012). In Lysina, the impact of anthropogenic acidification to the ecosystems

of the catchments results in acidic soil waters (Krám et al., 2013). The soil water pH in the (ultra)mafic catchments is slightly acidic in the uppermost organic and mineral horizons but neutral to alkaline in C horizon and stream water (Krám et al., 2013). Also, the stream water in Lysina is characterized by a very low mean pH value of 4.2 and a negative alkalinity. Its chemistry is dominated by Ca-Na-SO₄-organic acids and elevated Al concentrations, characteristic for acidic waters. The stream water in the mafic Na Zeleném catchment is neutral (pH ~ 6.9), has a moderate acid neutralizing capacity (ANC) and a solute composition that is characterized by Ca-Mg-SO₄-HCO₃. Stream water in the ultramafic Pluhův Bor catchment has the highest pH values (~ 7.6) and alkalinity. The predominant components are by Mg-HCO₃-SO₄-organic acids and elevated concentrations of SiO₂, Ni and Cr are apparent (Krám et al., 2012). The prevailing soils are Podzol and Gleysol (Lysina), Cambisol (Na Zeleném) and Stagnosol (Pluhův Bor). The soil depth is about 1.5 m in the Lysina catchment, about 0.9 m in Na Zeleném and 1.2 m in the Pluhův Bor catchment (at borehole sites). The soils are underlain by a mixture of sandy residuum and bedrock boulders, followed by highly weathered bedrock featuring many joints. The overall thickness of the regolith is a few meters. There is no evidence for glaciation in the studied area during the Late Pleistocene and Holocene. The upland catchments (elevation > 500 m), though influenced by periglacial processes, are not covered by loess (Haase et al., 2007) and thus no external cosmogenic nuclide signal has to be considered.

The Lysina and Pluhův Bor catchments belong to the Czech GEOMON network of small forested watersheds (Oulehle et al., 2008) and the Czech LTER network (Czech Long-term Ecological Research). All three catchments form further a Critical Zone Observatory (CZO) in the framework of the European Commission project SoilTrEC (Menon et al., 2014; Regelink et al., 2015). Observation of the Lysina and Pluhův Bor catchments began in 1989 and 1991, respectively. The Na Zeleném catchment is being observed since 2001. The main objective of monitoring is to study the effects of anthropogenic atmospheric deposition on stream water chemistry. In the framework of the monitoring programs, stream water discharge has been monitored continuously by using V-notch weirs and mechanical water level recorders. Collection of stream water is performed weekly for the Lysina and Pluhův Bor catchment and less intensive (mostly monthly) sampling is carried out for the Na Zeleném catchment. In addition bulk precipitation is sampled and measured monthly.

2.2.2 Sampling

I sampled bedload sediment and stream water at the outflow of each catchment (see Figure 2.2) in August 2011. The instantaneous discharge in all three catchments at the time of sampling was relatively low (0.42 l s⁻¹ at Lysina, 0.23 l s⁻¹ at Na Zeleném, 0.17 l s⁻¹ at Pluhův Bor). For the Lysina

catchment I additionally sampled groundwater from a shallow well called “Lenka” located at the border of the catchment. In addition to the samples taken in August 2011, I received stream water sampled over a time span of nine month in 2012 and 2013 from *P. Kram* (Czech Geological Survey, Prague). In this period there were only minor high discharge events and the samples I measured were almost all taken at base flow (instantaneous discharge $< 1 \text{ l s}^{-1}$).

In August/September 2012 one bedrock core was taken within the framework of the SoilTrEC project in each catchment with a final depth of 30 m at Lysina, 26 m at Na Zeleném, and 28 m at Pluhův Bor. Bedrock was sampled at various depths of the cores at the Czech Geological Survey in Prague. Additionally, I received soil and sediment samples from the top part of the Lysina core, except the very top horizon that was very organic rich material.

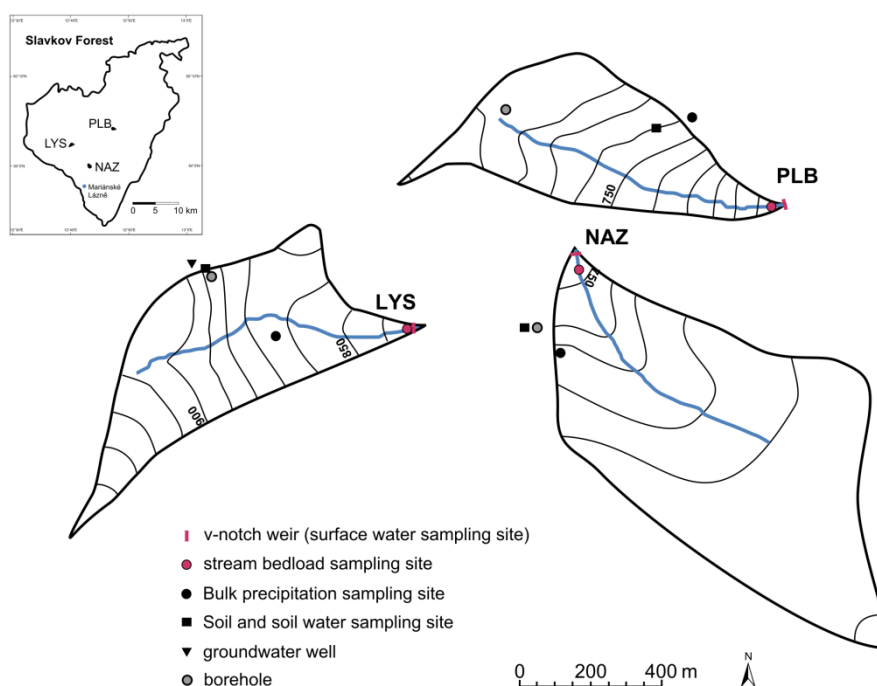


Figure 2.2: Detailed scheme of each catchment with 10m elevation contours and sampling sites drawn at arbitrary geographic positions. Inset map shows the location of the single catchments within the Slavkov Forest.

2.3 Methods

2.3.1 Stream bedload and borehole core samples

I determined the reactive $^{10}\text{Be}/^9\text{Be}$ ratio ($(^{10}\text{Be}/^9\text{Be})_{\text{reac}}$) on bedload sediment by measuring the single ^{10}Be and ^9Be concentrations separately on the individually extracted fractions and then calculating an isotope ratio. The bedload sediment samples taken at the outlet of each catchment were manually dry-sieved into a fraction smaller than 63 μm that was used for chemical extraction (for description of the sequential extraction method see Section 1.3.1). In the case of these bedload samples, I applied the complete sequential extraction procedure described in Appendix A.1.1 with an ahead step using 1 M MgCl_2 to extract the exchangeable phase and an additional organic leach step. Additionally, the concentrations of beryllium that is still bound in the primary minerals (Be_{min}) of the bedload sediment after chemical extraction were measured.

In order to explore the dependence of beryllium concentrations and $^{10}\text{Be}/^9\text{Be}$ ratios on the grain size, I further determined $[^9\text{Be}]_{\text{reac}}$ on coarser grain size fractions (62-125 μm , 125-250 μm , and 250-500 μm) on the bedload sediments. Reactive ^{10}Be measurements were carried out on the 125-250 μm grain size fraction to calculate a $(^{10}\text{Be}/^9\text{Be})_{\text{reac}}$ ratio in order to test whether $(^{10}\text{Be}/^9\text{Be})_{\text{reac}}$ ratios are uniform with grain size on the small catchment scale.

In the case of the core taken in the acidic Lysina catchment, soils were sampled to a depth of 3.4 m where the sediment to bedrock interface is located. The reactive phase of five bulk soil samples was analyzed to estimate the depth percolation of meteoric ^{10}Be . Additionally, at a depth of 4.40 m where the core comprises weathered fragments of broken bedrock a sample was taken, pulverized, and processed. Regarding these core samples, I cannot exclude any vertical mixing of sediment in the uppermost meters of the soil. The core sediment and bedrock samples have been pulverized at the Czech Geological Survey. The sequential leaching was done in the same way as described in Section 1.3.1, but for these samples, I determined only the reactive phase of ^{10}Be and ^9Be .

2.3.2 Treatment of water samples

All water samples were filtered through a 0.2 μm membrane filter and acidified with nitric acid to a pH of about 2. The dissolved $^{10}\text{Be}/^9\text{Be}$ ratio ($(^{10}\text{Be}/^9\text{Be})_{\text{diss}}$) in these waters was calculated from individually measured ^{10}Be and ^9Be concentrations. For the measurement of the dissolved meteoric ^{10}Be concentration, I applied the method described in Section 1.3.2 by using about 200 to 600 ml of stream water, spiked with 250 to 400 μg ^9Be carrier. To measure the natural ^9Be concentration of the

stream water (see Section 1.3.2), the samples of the two mafic catchments exhibit too low ^9Be concentrations and had to be pre-concentrated. On this, about 50 ml of water were evaporated and taken up again in 0.3M HNO_3 . In case of visible high dissolved organic carbon content, the samples were treated with concentrated H_2O_2 and HNO_3 before measurement.

2.3.3 *In situ* ^{10}Be method

To compare the meteoric-derived denudation rates with an independent estimate, I also determined *in situ*-derived denudation rates on the same bedload sediment. Based on the results of the mineral composition measurements, showing marked amounts of quartz also in the mafic catchments (Table 2.5 in Section 2.4.1), I also measured *in situ*-produced ^{10}Be concentrations in the bedload of these catchments. In case of Lysina, the 250-500 μm and 500-800 μm fractions were used for mineral separation, using magnetic and chemical separation techniques to separate quartz from other minerals. In the cases of Na Zeleném and Pluhův Bor, the composite 125-800 μm fraction was taken due to very low amounts of quartz in these samples. Final dissolution of pure quartz was done using hydrofluoric acid. After complete dissolution, the samples were spiked with ^9Be carrier and the beryllium was separated by ion exchange chromatography and hydroxide precipitation and prepared for measurement at the AMS at ETH Zurich (see 1.3.3).

The measured surface concentration of *in situ*-produced ^{10}Be ($[^{10}\text{Be}]_{in situ}$) is inversely proportional to the denudation rate $D_{in situ}$ (cm y^{-1} ; von Blanckenburg (2005)):

$$[^{10}\text{Be}]_{in situ} = \frac{P(0)}{\lambda + \frac{D_{in situ}}{z^*}} \quad \text{Equation 2.1}$$

$P(0)$ is the production rate of *in situ* ^{10}Be in a mineral at the Earth's surface ($\text{atoms g}^{-1} \text{y}^{-1}$), λ is the decay constant (y^{-1}), and z^* is the absorption path length (cm). The cosmic ray absorption mean free path Λ (g cm^{-2}) describes the depth at which the intensity of cosmic rays is reduced by a factor of e . In silicate rocks this depth correspond to an absorption depth z^* of typically 60 cm. I used in this study a *in situ* ^{10}Be production rate of $4.00 \text{ atoms g}_{(\text{qtz})}^{-1} \text{y}^{-1}$ at sea level and high latitudes ($> 60^\circ$; SLHL; Phillips et al. (2016)). For conversion of units a density of 2.6 g cm^{-3} was used.

2.3.4 Additional methods

Additionally, qualitative X-ray diffractometry (XRD) and X-ray fluorescence (XRF) analyses were carried out to determine the mineralogical composition and major and trace element concentrations of

the sampled bedload sediment and bedrock samples. For analysis the samples were crushed (bedrock) and powdered, followed by preparation of fusion tablets using a flux for XRF analysis. The XRD analyses were performed on a Bruker-axs D5000 Diffractometer and the XRF analysis on a PANalytical Advance machine at the *GFZ German Research Centre of Geosciences Potsdam*.

Parent beryllium concentrations were determined in bedrock samples of each bedrock type (sampled hand pieces and pieces from the bedrock cores). The mafic bedrock samples were dissolved with a HF and aqua regia digestion procedure, using 100 - 200 mg of crushed and grinded sample material. Most of the granitic samples were digested by a flux fusion method. In the latter case, I applied a fusion procedure described in Georg et al. (2006) with solid sodium hydroxide (NaOH) as flux. About 20 mg of powdered bedrock was weighed, circa 400 mg solid NaOH were added, and the mixture was heated in a Pt-crucible at temperature at 750°C for one hour. The formed “fusion cake” was then stepwise dissolved with MilliQ[®]-H₂O and a weak HCl solution. The pH of the solution was adapted to a value of 9 to precipitate beryllium whereas the excess sodium remained in solution. This step was repeated twice and the samples then diluted for measurement. The bedrock beryllium concentration measurements were performed with an ICP-OES for all bedrock types. Concerning the ultramafic samples, the beryllium concentration was in some cases below the detection limit of the ICP-OES, which is ca. 10 ppb Be.

2.4 Measured concentrations of beryllium

2.4.1 Bedload Samples

First, I measured concentrations of ⁹Be ([⁹Be]) and meteoric ¹⁰Be ([¹⁰Be]) in the fine-grained fraction (< 63µm) of the bedload sediments. The granitic catchment Lysina exhibits the highest concentration of total ⁹Be (total = reac + min; 5.49 ± 0.49 ppm, analytical uncertainty; see Table 2.2). In the catchments draining mafic and ultramafic rocks lower [⁹Be]_{total} are observed; these are 3.4 ± 1.4 ppm in case of Na Zeleném and only 0.58 ± 0.02 ppm at Pluhův Bor (see Table 2.2). The reactive ⁹Be concentration (reac = am-ox + x-ox) is with 2.09 ± 0.08 ppm highest in the bedload of the Na Zeleném. [⁹Be]_{reac} at Lysina is 1.12 ± 0.06 ppm and the ultramafic Pluhův Bor catchment has the lowest [⁹Be]_{reac} of 0.31 ± 0.01 ppm (see Figure 2.3 A and Table 2.2). All three catchments exhibit higher [⁹Be] in the amorphous oxide fraction (HCl-leachable) by a factor of two to four than in the crystalline oxide fraction (NH₂OH * HCl leach; see Figure 2.3 A). With regard to the mineral-bound ⁹Be, the sediment sampled at Lysina has an about four times higher [⁹Be]_{min} in the residual mineral

phase than in the reactive phase ($[^9\text{Be}]_{\text{reac}} \sim 26\%$ of $[^9\text{Be}]_{\text{total}}$). In contrast, the sediments of the other catchments have higher ^9Be concentrations in the reactive phase (NAZ: $[^9\text{Be}]_{\text{reac}} \sim 63\%$ of $[^9\text{Be}]_{\text{total}}$; PLB: $[^9\text{Be}]_{\text{reac}} \sim 54\%$ of $[^9\text{Be}]_{\text{total}}$; Table 2.2).

The reactive meteoric ^{10}Be concentrations measured in the bedload sediment of Na Zeleném and Pluhův Bor are similar with $400 \pm 11 \times 10^6 \text{ atoms g}^{-1}$ and $403 \pm 11 \times 10^6 \text{ atoms g}^{-1}$, respectively (see Table 2.2 and Figure 2.3 B). $[^{10}\text{Be}]_{\text{reac}}$ determined in the granitic Lysina catchment is about $177 \pm 5 \times 10^6 \text{ atoms g}^{-1}$, and hence low in comparison to the mafic catchments. When considering the extracted fractions separately, $[^{10}\text{Be}]_{\text{am-ox}}$ is higher by a factor of six to eight than $[^{10}\text{Be}]_{\text{x-ox}}$ (see Figure 2.3 B).

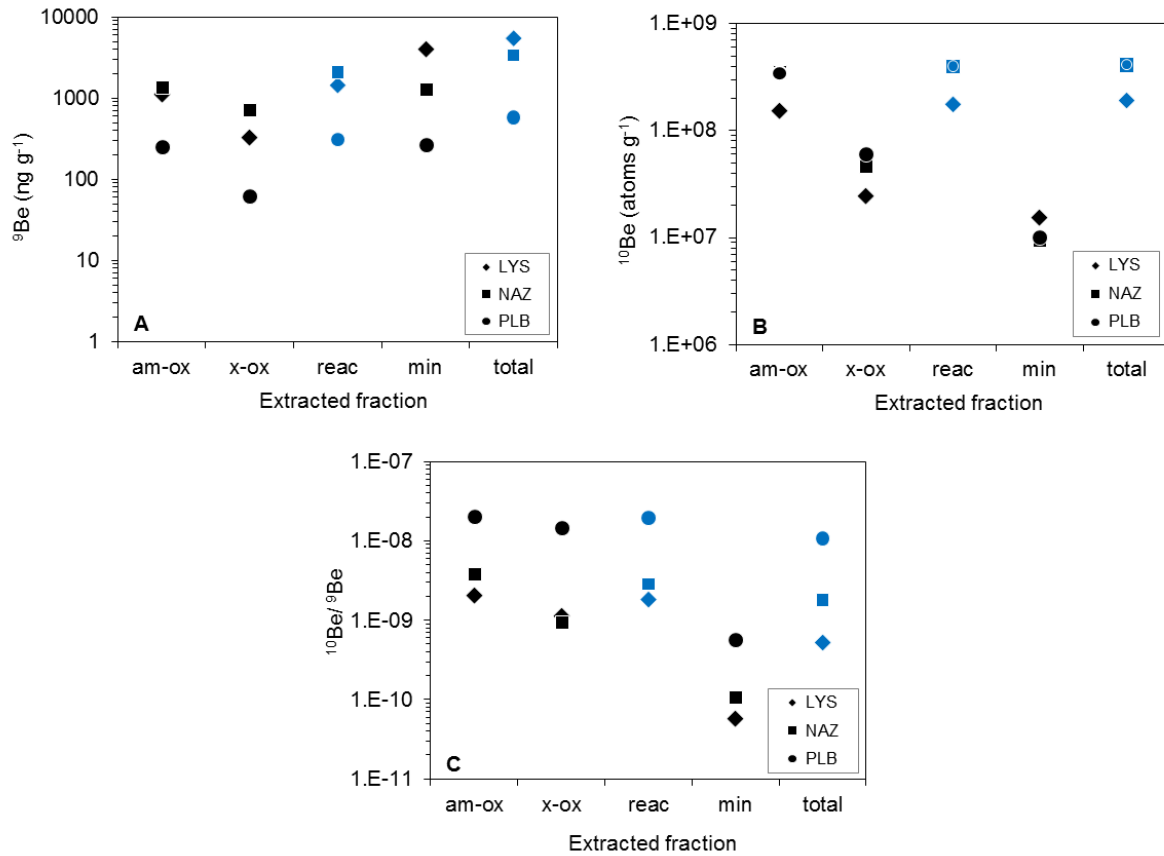


Figure 2.3: Concentrations of ^9Be and ^{10}Be and resulting $^{10}\text{Be}/^9\text{Be}$ ratios for the sequentially extracted fractions. Measured extracted fractions - in black - are “am-ox” (amorphous oxides) and “x-ox” (crystalline oxides); “min” represents the amount of beryllium that is still locked in the silicate residue. Blue symbols show calculated fractions: “reac” is the total reactive fraction (am-ox + x-ox) and “total” is the sum of all measured Be concentrations (am-ox + x-ox + min). Error bars are smaller than displayed symbols. **A** ^9Be concentration (ng g^{-1}), calculated relative to initial solid sample weight. **B** ^{10}Be concentration (atoms g^{-1}). **C** $^{10}\text{Be}/^9\text{Be}$ ratios calculated from individual Be concentrations.

Regarding the beryllium ratios, Lysina and Na Zeleném both yield low reactive ratios of $18 \pm 1 \times 10^{-10}$ and $28 \pm 1 \times 10^{-10}$, respectively (see Table 2.2 and Figure 2.3 C). $(^{10}\text{Be}/^9\text{Be})_{\text{reac}}$ measured at Pluhův Bor

is with $194 \pm 10 \times 10^{-10}$ comparably high, due to very low ^9Be concentrations. All three catchments reveal lower $(^{10}\text{Be}/^9\text{Be})_{\text{x-ox}}$, determined on the crystalline oxide fraction, than $(^{10}\text{Be}/^9\text{Be})_{\text{am-ox}}$ (see Figure 2.3 C).

Table 2.2: Concentrations of ^9Be and ^{10}Be and calculated $^{10}\text{Be}/^9\text{Be}$ ratios for the sequentially extracted fractions and residuals measured on the fine-grained bedload sediment ($< 63 \mu\text{m}$) and calculated sums of reactive and total beryllium

Sample name ¹	Extracted fraction ²	Initial Sample Weight (g)	$[^{10}\text{Be}]$ ³ ($\times 10^6$ atoms g^{-1})	$[^9\text{Be}]$ ⁴ ($\mu\text{g g}^{-1}$)	$^{10}\text{Be}/^9\text{Be}$ ($\times 10^{-10}$)
LYS	am-ox	0.5069	151.9 ± 5.2	1124 ± 58	20.2 ± 1.3
	x-ox	0.5069	24.6 ± 1.1	325 ± 17	11.33 ± 0.77
	reac	0.5069	176.5 ± 5.4	1449 ± 61	18.2 ± 1.0
	min	0.5069	15.31 ± 0.75	4040 ± 210	0.567 ± 0.040
	total	0.5069	191.9 ± 5.4	5490 ± 220	5.23 ± 0.26
NAZ	am-ox	0.5092	354 ± 11	1395 ± 72	38.0 ± 2.3
	x-ox	0.5092	45.5 ± 1.8	759 ± 39	8.96 ± 0.59
	reac	0.5092	400 ± 11	2154 ± 83	27.8 ± 1.3
	min	0.5092	8.46 ± 0.46	1294 ± 67	0.978 ± 0.073
	total	0.5092	408 ± 11	3450 ± 110	17.71 ± 0.74
NAZ (1)	am-ox	0.5220	351 ± 11	1327 ± 66	39.6 ± 2.4
	x-ox	0.5220	47.1 ± 1.8	693 ± 35	10.18 ± 0.65
	reac	0.5220	398 ± 11	2020 ± 74	29.5 ± 1.4
	min	0.5220	10.43 ± 0.76	1312 ± 66	1.19 ± 0.11
	total	0.5220	409 ± 11	3330 ± 100	18.36 ± 0.76
PLB	am-ox	0.5649	343 ± 11	249 ± 13	206 ± 13
	x-ox	0.5649	60.3 ± 2.3	62.1 ± 3.2	145.5 ± 9.4
	reac	0.5649	403 ± 11	311 ± 13	194 ± 10
	min	0.5649	10.12 ± 0.50	267 ± 14	5.66 ± 0.41
	total	0.5649	413 ± 11	579 ± 19	106.9 ± 4.6

¹ NAZ and NAZ(1) are two independently processed sample aliquots (newly weighted).

² "am-ox" = amorphous oxide phase, "x-ox" = crystalline oxide phase, "min" = mineral-bound phase,

"reac" = reactive phase (sum of "am-ox" and "x-ox"), "total" = sum of all phases (am-ox + x-ox + min).

³ Calculated from AMS ratio using the sum of ^9Be carrier and natural ^9Be content (value given in column $[^9\text{Be}]$ of this table), with combined analytical and blank error (all uncertainties 1SD), relative to initial solid sample weight.

⁴ For stable ^9Be measurements a 5% uncertainty is given that represents the long-term repeatability.

Highest $[^9\text{Be}]_{\text{total}}$ in the granitic Lysina catchment is expected as beryllium is incompatible during crystallization processes and is thus concentrated in highly differentiated igneous rocks (Ryan and Langmuir, 1988). Although in Lysina $[^9\text{Be}]_{\text{total}}$ is highest, the reactive concentration is significantly higher at Na Zeleném. This could point to higher weathering of beryllium containing minerals or a higher beryllium retentivity at Na Zeleném. In all three samples a minor concentration of ^{10}Be in the

“min” fraction is detected (2 to 8% of total ^{10}Be). One explanation could be that the extraction was not complete, or that potentially some meteoric beryllium is incorporated into clay minerals during formation of secondary weathering products since beryllium tends to be retained in and adsorbed onto clay minerals (Brown et al., 1992). These clay minerals would not have been attacked during the leaching procedure. The *in situ* ^{10}Be concentration can be neglected in this case since it is much smaller ($\sim 10^5$ atoms g^{-1} , see Table 2.9 in Section 2.5) than the meteoric ^{10}Be concentrations.

Investigation of potential grain size effects in the ^{10}Be system is carried out by comparing the $< 63 \mu\text{m}$ to the 125-250 μm size fraction, which shows that the single $[^{10}\text{Be}]_{\text{reac}}$ and $[^9\text{Be}]_{\text{reac}}$ decrease markedly with increasing grain size (see Table 2.3). In contrast, calculated $(^{10}\text{Be}/^9\text{Be})_{\text{reac}}$ for these two grain size fractions are identical within the analytical uncertainty.

Table 2.3: $[^9\text{Be}]_{\text{reac}}$ and where determined $[^{10}\text{Be}]_{\text{reac}}$ and calculated $(^{10}\text{Be}/^9\text{Be})_{\text{reac}}$ for the sum of sequentially extracted fractions for different grain sizes

Sample name	Grain size (μm)	Extracted fraction ¹	Initial Sample Weight (g)	$[^{10}\text{Be}]_{\text{reac}}$ ^{2, 3} ($\times 10^6$ atoms g^{-1})	$[^9\text{Be}]_{\text{reac}}$ (ppb)	$(^{10}\text{Be}/^9\text{Be})_{\text{reac}}$ ² ($\times 10^{-10}$)
LYS	< 63	am-ox + x-ox	0.5069	191.9 ± 5.4	1449 ± 61	19.8 ± 1.0
LYS 63	63-125	reac	0.5050		1067 ± 41	
LYS 125	125-250	reac	0.7531	50.3 ± 1.6	387 ± 15	19.4 ± 1.0
LYS 250	250-500	reac	1.0067		320 ± 13	
NAZ	< 63	am-ox + x-ox	0.5092	408 ± 11	2154 ± 83	28.3 ± 1.3
NAZ 63	63-125	reac	0.5031		1696 ± 67	
NAZ 125	125-250	reac	0.7533	310.4 ± 5.1	1403 ± 55	33.1 ± 1.4
NAZ 250	250-500	reac	1.0043		1055 ± 42	
PLB	< 63	am-ox + x-ox	0.5649	413 ± 11	311 ± 13	199 ± 10
PLB 63	63-125	reac	0.7552		216.7 ± 9.3	
PLB 125	125-250	reac	1.0059	242.1 ± 4.4	157.8 ± 6.8	230 ± 11
PLB 250	250-500	reac	1.0256		141.5 ± 6.0	

¹ "am-ox + x-ox": both phases measured separately for ^{10}Be and ^9Be concentrations;

"reac": am-ox and x-ox were extracted separately but then combined to one "reac" phase for measurement

² ^{10}Be concentrations were only measured on $< 63 \mu\text{m}$ and 125-250 μm grain size fractions

³ Calculated from AMS ratio using the sum of ^9Be carrier and natural ^9Be content (value given in column $[^9\text{Be}]_{\text{reac}}$ of this table), with combined analytical and blank error (all uncertainties 1SD), relative to initial solid sample weight.

Next, I present a characterisation of the chemical composition of the extracted phase (see Figure 2.4). This characterisation was done by normalizing the major element concentrations in the reactive phase to the total element concentration (obtained through ICP-OES; see Table 2.4). The first observation is that the element compositions of the mafic and ultramafic catchment show roughly identical pattern

whereas the pattern for the granitic catchment slightly differs from the other ones (see Figure 2.4 D). However, the distribution of most elements is comparable for all three lithologies, indicating that the applied sequential extraction method extracts similar phases for all types of bedrock. Iron (Fe) and manganese (Mn) are mainly concentrated in the reactive phase and so is beryllium. Most of the extracted beryllium is contained in the amorphous oxide phase (65-80 %). These proportions show that in principle authigenic phases such as Fe- and Mn- (hydro)oxides that are dissolved during sequential leaching contain a notable amount of reactive Be. The reactive fraction in the Lysina sediment contains an exceptional high amount of calcium (Ca) with most of this Ca being present in the HCl-leachable phase. In the absence of carbonates, feldspars are potentially etched to a low degree by the leaching reagents (Wittmann et al., 2012). In the case of Na Zeleném a relatively high amount of potassium was leached by the hydroxylamine extraction step (see Figure 2.4 B). As the prevalent amphibole is a tremolite that is a Ca-amphibole and can be excluded due to small amounts of Ca in this phase, probably small amounts of muscovite were etched during the extraction procedure.

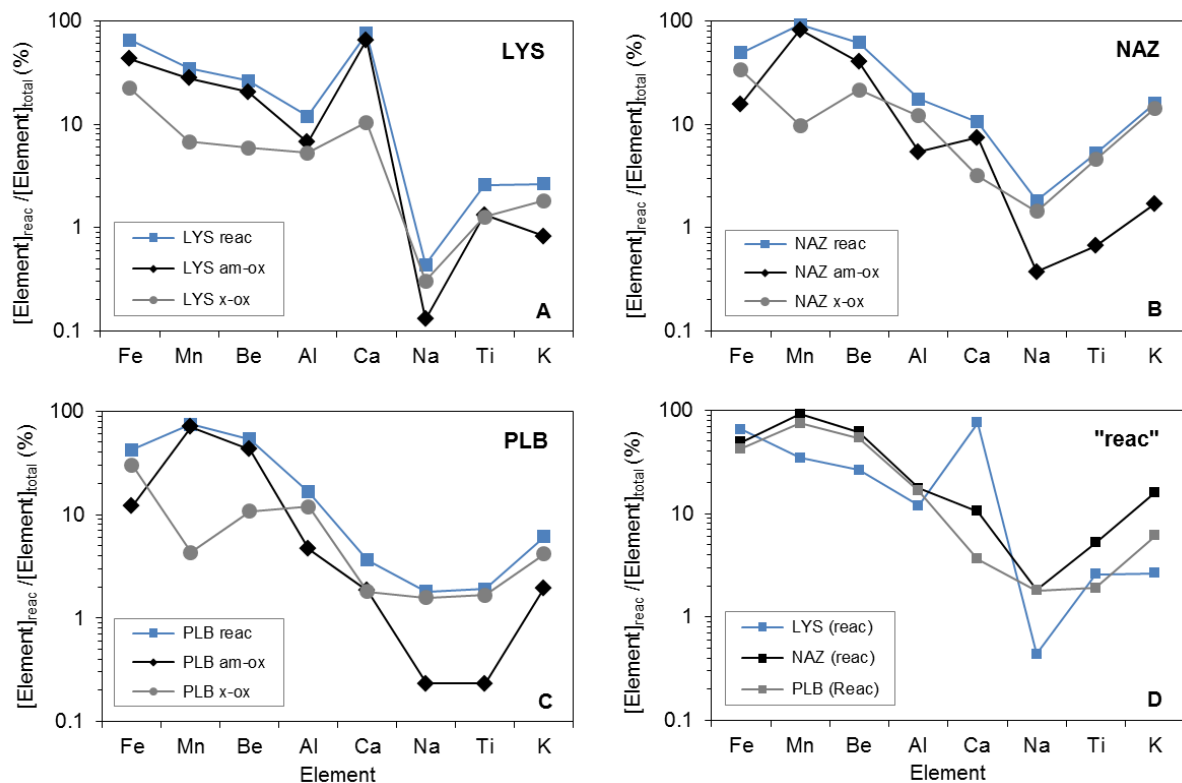


Figure 2.4: A-C: Element concentrations measured in the amorphous oxide phase (am-ox), crystalline oxide phase (x-ox) and total reactive element concentrations (reac = am-ox + x-ox) relative to total (am-ox + x-ox + min) element concentrations ($[\text{Element}]_{\text{reac}} / [\text{Element}]_{\text{total}}$ in %), determined on the fine-grained sediment fraction ($< 63 \mu\text{m}$) of each catchment. D: Reactive element concentrations relative to total element concentrations for all three catchments. Results for Mg were not included, as an additional exchangeable step is applied on these samples, which is using 1M MgCl_2 that is potentially carried over into the following extraction steps.

Table 2.4: Element concentration measured in the single extracted compartments and the residual fraction of the bedload sediment (in $\mu\text{g g}^{-1}$, except Be that is in ng g^{-1})

Sample name	Fraction	Al ($\mu\text{g g}^{-1}$)	Ba ($\mu\text{g g}^{-1}$)	Be (ng g^{-1})	Ca ($\mu\text{g g}^{-1}$)	Cd ($\mu\text{g g}^{-1}$)	Co ($\mu\text{g g}^{-1}$)	Cr ($\mu\text{g g}^{-1}$)	Cu ($\mu\text{g g}^{-1}$)	Fe ($\mu\text{g g}^{-1}$)	K ($\mu\text{g g}^{-1}$)
LYS	am-ox	3605 \pm 187	16.92 \pm 0.88	1124 \pm 58	2771 \pm 144	0.400 \pm 0.021	n.d.	3.99 \pm 0.21	6.0 \pm 0.31	6617 \pm 344	84.0 \pm 21.0
	x-ox	2850 \pm 148	6.32 \pm 0.33	325 \pm 17	442 \pm 23	0.067 \pm 0.003	n.d.	6.17 \pm 0.32	1.4 \pm 0.07	3431 \pm 178	186.8 \pm 46.8
	min	47403 \pm 2463	105.2 \pm 5.5	4039 \pm 210	1036 \pm 54	0.081 \pm 0.004	n.d.	16.86 \pm 0.88	3.8 \pm 0.20	5353 \pm 278	9950 \pm 2492
NAZ	am-ox	4272 \pm 222	228 \pm 12	1395 \pm 72	1128 \pm 59	1.273 \pm 0.066	12.0 \pm 0.62	5.92 \pm 0.31	15.5 \pm 0.80	7653 \pm 398	119.0 \pm 29.8
	x-ox	9486 \pm 493	70.2 \pm 3.6	759 \pm 39	526 \pm 27	0.329 \pm 0.017	n.d.	27.1 \pm 1.4	11.9 \pm 0.62	16249 \pm 844	984 \pm 246
	min	63785 \pm 3314	236 \pm 12	1294 \pm 67	13031 \pm 677	0.361 \pm 0.019	n.d.	55.6 \pm 2.9	5.7 \pm 0.30	24263 \pm 1261	5432 \pm 1360
NAZ (1)	am-ox	4071 \pm 212	201 \pm 10	1327 \pm 69	1160 \pm 60	1.055 \pm 0.055	11.22 \pm 0.58	5.06 \pm 0.26	15.63 \pm 0.81	7276 \pm 378	90 \pm 22
	x-ox	9158 \pm 476	66.1 \pm 3.4	693 \pm 36	462 \pm 24	0.301 \pm 0.016	1.513 \pm 0.079	25.7 \pm 1.3	12.96 \pm 0.67	15669 \pm 814	783 \pm 196
	min	n.d.	205 \pm 11	1312 \pm 68	14697 \pm 764	0.358 \pm 0.019	n.d.	57.4 \pm 3.0	6.95 \pm 0.36	n.d.	4886 \pm 1223
PLB	am-ox	1985 \pm 103	53.3 \pm 2.8	249 \pm 13	479 \pm 25	0.470 \pm 0.024	19.6 \pm 1.02	43.4 \pm 2.3	10.8 \pm 0.56	6989 \pm 363	49.5 \pm 12.4
	x-ox	5104 \pm 265	6.03 \pm 0.31	62.1 \pm 3.2	470 \pm 24	0.328 \pm 0.017	0.4 \pm 0.02	ND \pm ND	6.2 \pm 0.32	17473 \pm 908	106.0 \pm 26.5
	min	35535 \pm 1846	70.7 \pm 3.7	267 \pm 14	25125 \pm 1306	0.484 \pm 0.025	0.4 \pm 0.02	1778 \pm 92	3.2 \pm 0.16	33303 \pm 1730	2379 \pm 596

Sample name	Fraction	Mg ¹ ($\mu\text{g g}^{-1}$)	Mn ($\mu\text{g g}^{-1}$)	Na ($\mu\text{g g}^{-1}$)	Ni ($\mu\text{g g}^{-1}$)	Pb ($\mu\text{g g}^{-1}$)	Sr ($\mu\text{g g}^{-1}$)	Ti ($\mu\text{g g}^{-1}$)	Zn ($\mu\text{g g}^{-1}$)	Zr ² ($\mu\text{g g}^{-1}$)
LYS	am-ox	n.d.	68.9 \pm 3.6	18.18 \pm 4.55	1.89 \pm 0.10	27.5 \pm 1.4	2.33 \pm 0.12	25.0 \pm 1.3	31.0 \pm 1.6	3.31 \pm 0.17
	x-ox	430 \pm 22	16.8 \pm 0.9	42.4 \pm 10.6	3.57 \pm 0.19	3.84 \pm 0.20	1.568 \pm 0.081	24.1 \pm 1.3	9.37 \pm 0.49	0.532 \pm 0.028
	min	1021 \pm 53	161.7 \pm 8.4	13843 \pm 3466	3.51 \pm 0.18	3.38 \pm 0.18	16.66 \pm 0.87	1842 \pm 96	48.2 \pm 2.5	200 \pm 10
NAZ	am-ox	n.d.	4475 \pm 233	35.2 \pm 8.8	19.7 \pm 1.0	22.6 \pm 1.2	6.27 \pm 0.33	28.7 \pm 1.5	94.2 \pm 4.9	1.332 \pm 0.069
	x-ox	4442 \pm 231	418 \pm 22	128.7 \pm 32.2	19.8 \pm 1.0	8.62 \pm 0.45	14.08 \pm 0.73	197 \pm 10	74.0 \pm 3.8	0.758 \pm 0.039
	min	10675 \pm 555	413 \pm 21	7141 \pm 1788	16.89 \pm 0.88	4.47 \pm 0.23	69.4 \pm 3.6	4106 \pm 213	61.1 \pm 3.2	117.1 \pm 6.1
NAZ (1)	am-ox	4775 \pm 248	4424 \pm 230	23.9 \pm 6.0	16.49 \pm 0.86	27.9 \pm 1.5	7.92 \pm 0.41	n.d.	78.2 \pm 4.1	n.d.
	x-ox	4174 \pm 217	642 \pm 33	98 \pm 25	17.42 \pm 0.91	33.9 \pm 1.8	17.35 \pm 0.90	n.d.	64.9 \pm 3.4	n.d.
	min	11442 \pm 595	491 \pm 26	8363 \pm 2094	16.15 \pm 0.84	45.7 \pm 2.4	94.1 \pm 4.9	n.d.	48.0 \pm 2.5	n.d.
PLB	am-ox	n.d.	1574 \pm 82	12.13 \pm 3.04	475 \pm 25	100.6 \pm 5.2	1.07 \pm 0.06	7.91 \pm 0.41	35.9 \pm 1.9	1.778 \pm 0.092
	x-ox	9149 \pm 475	95.7 \pm 5.0	82.3 \pm 20.6	305 \pm 16	9.03 \pm 0.47	0.991 \pm 0.052	56.6 \pm 2.9	26.3 \pm 1.4	1.218 \pm 0.063
	min	72035 \pm 3743	552 \pm 29	5155 \pm 1291	446 \pm 23	2.43 \pm 0.13	35.6 \pm 1.8	3336 \pm 173	43.7 \pm 2.3	109.6 \pm 5.7

n.d.: not determined (above or below calibration); Si could not be measured due to HF decomposition.

¹ Mg concentration might be biased from MgCl_2 leach (step 1, results not shown).

² Potentially, some zircon minerals were not completely dissolved during digestion.

Table 2.5 summarizes the results from the XRD measurement of the bedload samples on the $< 63\mu\text{m}$ fraction. The resulting mineral compositions confirm the highly heterogeneous lithology of the mafic catchments. For example, the serpentinite dominated catchment shows distinct amounts of hornblende, an amphibolite mineral, and quartz in the bedload. The highly heterogeneous underlying bedrock types are confirmed by drilled bedrock cores (see Appendix A.2.6 for detailed data set).

Table 2.5: Mineral composition of the stream bedload sediment that is used for sequential extraction ($< 63\mu\text{m}$)

Catchment	Main Lithology	Minerals ¹
LYS	granite	quartz, plagioclase, muskovite, illite, orthoclase, kaolinite
NAZ	mafic rocks like amphibolite	quartz, hornblende, plagioclase, muscovite, chlorite, rutile, magnetite
PLB	(ultra)mafic rocks like serpentinite and amphibolite	hornblende, quartz, serpentine, talc, chlorite, plagioclase, vermiculite, magnesite

¹ In order from highest to lowest amount (no absolute amounts are given because only qualitative XRD analysis were performed).

2.4.2 Depth profile at Lysina

In order to investigate to which depth the meteoric ^{10}Be percolates in low-pH environments, I determined reactive beryllium concentrations on bulk samples taken from the borehole core in the Lysina catchment (see Figure 2.5).

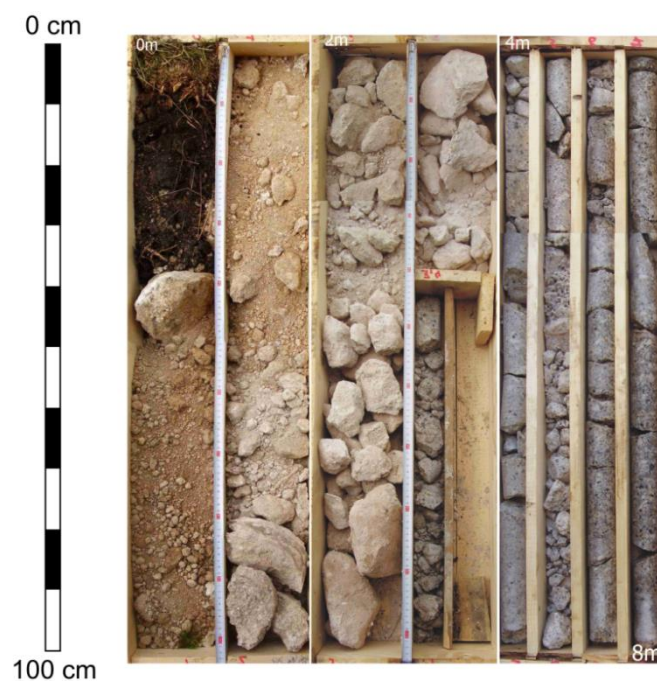


Figure 2.5: Photo of the upper 8 m of the core taken at Lysina. *Photo courtesy of P. Kram.*

The general trend shows that $[^{10}\text{Be}]_{\text{reac}}$ is decreasing with increasing depth whereas $[^9\text{Be}]_{\text{reac}}$ is increasing in the soil (see Figure 2.6 A). The maximum $[^{10}\text{Be}]_{\text{reac}}$ of 97×10^6 atoms g^{-1} is measured in the middle part of the profile (see Table 2.6). The sample taken from highly fractured and weathered bedrock has with about 17×10^6 atoms g^{-1} a $[^{10}\text{Be}]_{\text{reac}}$ that is still about 20% of the concentration measured in the uppermost sample of the core. $[^9\text{Be}]_{\text{reac}}$ ranges from between 480 ppb in the uppermost samples and 730 ppb. $(^{10}\text{Be}/^9\text{Be})_{\text{reac}}$ decreases throughout the profile. The ratio determined from the uppermost sample is about 22×10^{-10} and decreases with depth to a ratio of ca. 5×10^{-10} .

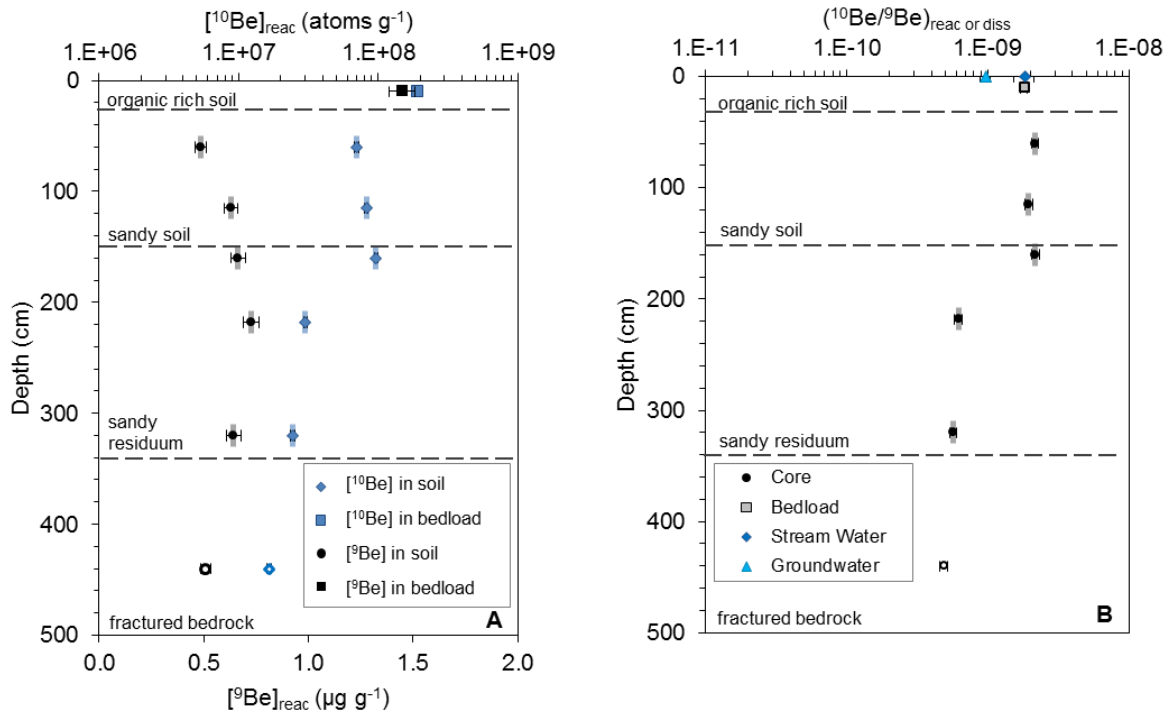


Figure 2.6: Results from a depth profile on bulk sediment samples (< 2 mm) taken from the drilled core at Lysina **A:** $[^{10}\text{Be}]_{\text{reac}}$ (atoms g^{-1} ; blue diamonds) and $[^9\text{Be}]_{\text{reac}}$ ($\mu\text{g g}^{-1}$; black dots) and **B:** $(^{10}\text{Be}/^9\text{Be})_{\text{reac}}$. The small gray and light blue bars display the uncertainty in depth derived from sampling. Note that the lowest sample represents a highly weathered fragment of fractured bedrock that was ground before chemical leaching (open symbols). For comparison are plotted in **A** $[^{10}\text{Be}]_{\text{reac}}$ and $[^9\text{Be}]_{\text{reac}}$, and in **B** $(^{10}\text{Be}/^9\text{Be})_{\text{reac}}$ determined on fine-grained bedload ($< 63\mu\text{m}$), $(^{10}\text{Be}/^9\text{Be})_{\text{diss}}$ measured in stream water, and $(^{10}\text{Be}/^9\text{Be})_{\text{diss}}$ measured in groundwater. Where not visible, the displayed symbols are larger than the error bars. The concentrations of dissolved ^{10}Be ($\sim 10^4$ atoms g^{-1}) and ^9Be (ng l^{-1}) are not shown as they are much lower than the reactive ones.

In the core samples, beryllium concentrations were measured on bulk samples (< 2 mm). To enable comparison with the bedload data, I recalculated a “bulk concentration” for the bedload samples by weighting different grain size fractions (see Appendix A.2.4). For $[^9\text{Be}]_{\text{reac}}$ a value of about 450 ppb results and for $[^{10}\text{Be}]_{\text{reac}}$ a value of approximately 60×10^6 atoms g^{-1} is derived. These concentration estimates are in the order of the ones measured in the profile.

Table 2.6: Concentrations of ^9Be and ^{10}Be and calculated $^{10}\text{Be}/^9\text{Be}$ ratios for the sum of sequentially extracted fractions measured on different depth samples from the core taken in Lysina

Sample name	sample description	Sampled depth (cm)	Extracted fraction ¹	Initial Sample Weight (g)	$[^{10}\text{Be}]_{\text{reac}}^2$ ($\times 10^6$ atoms g^{-1})	$[^9\text{Be}]_{\text{reac}}$ (ng g^{-1})	$(^{10}\text{Be}/^9\text{Be})_{\text{reac}}$ ($\times 10^{-10}$)
LYS C	sandy soil	60	reac	0.7577	70.3 ± 2.3	484 ± 25	21.7 ± 1.3
LYS 1	sandy soil	115	reac	0.7503	82.3 ± 2.7	630 ± 33	19.6 ± 1.2
LYS 2	sandy residuum	160	reac	0.7525	97.0 ± 3.2	664 ± 35	21.8 ± 1.3
LYS 4	sandy residuum	218	reac	0.7562	30.2 ± 1.0	726 ± 38	6.22 ± 0.39
LYS 6	sandy residuum	320	reac	0.7528	24.59 ± 0.87	644 ± 33	5.72 ± 0.36
LYS 8	weathered rock	440	reac	0.7762	16.69 ± 0.62	509 ± 26	4.90 ± 0.31

¹ HCl-leachable fraction (am-ox) and hydroxylamine- hydrochloride leachable fraction (x-ox) were extracted separately and then combined to one reactive fraction for AMS measurement.

² Calculated from AMS ratio using the sum of ^9Be carrier and natural ^9Be content (value given in column $[^9\text{Be}]_{\text{reac}}$ of this table), with combined analytical and blank uncertainty (all uncertainties 1SD), relative to the initial solid sample weight.

2.4.3 Parent bedrock ^9Be concentration

To determine $[^9\text{Be}]_{\text{parent}}$, I measured bedrock samples from different depths in the bedrock core of each catchment. As already mentioned the underlying bedrock of each catchment is very heterogeneous regarding lithology and main element composition and so is the beryllium concentration among individual bedrock types (see Figure 2.7 and Appendix A.2.6 for bedrock description and individual $[^9\text{Be}]$ measurements). This natural heterogeneity results in high standard deviations of $[^9\text{Be}]_{\text{parent}}$ for each catchment (see Figure 2.7 and Table 2.7).

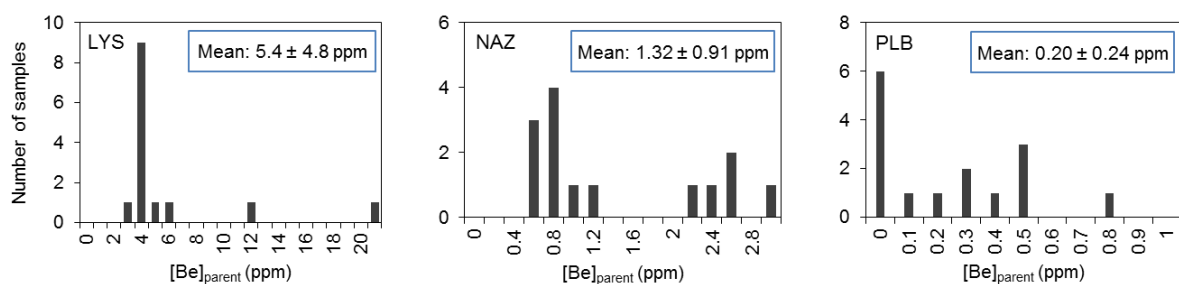


Figure 2.7: Histograms showing the distribution of the beryllium bedrock concentration (in ppm) in the individual catchments (no classification of single bedrock types is displayed here). The mean beryllium concentration is given with a 1 SD, which corresponds to the natural variability in each catchment.

In Lysina the beryllium concentration of the granitic bedrock varies by an order of magnitude (from 2.8 ppm up to about 20 ppm Be; Table 2.7). The average $[^9\text{Be}]$ of the granite is about 5.4 ppm and the median value is 3.5 ppm. At Na Zeleném amphibolites with an average beryllium concentration of

about 0.69 ppm (see Table 2.7) are the predominant bedrock type. The metabasites and –dolerites found in this catchments yield, with on average 2.5 ppm, markedly higher [^9Be]. The ultramafic serpentinite at Pluhův Bor has low [^9Be] of less than 10 ppb (see Table 2.7). In contrast, the amphibolites and metabasites prevailing in Pluhův Bor yield, relative to the ultramafic rocks, higher concentrations of 0.5 ppm and 0.2 ppm Be, respectively (see Table 2.7).

Table 2.7: [^9Be]_{parent} of the different bedrock types prevailing in the catchments

Bedrock type	Average [Be] ¹ (ppm)	Median [Be] (ppm)	Min [Be] ² (ppm)	Max [Be] ² (ppm)	n ³
<i><u>Lysina</u></i>					
Granite	5.4 ± 4.8	3.5	2.83 ± 0.14	20.3 ± 1.0	14
Catchment-wide estimate ^{4,5}	5.5				
<i><u>Na Zeleném</u></i>					
Amphibolite	0.69 ± 0.23	0.63	0.426 ± 0.021	1.174 ± 0.059	9
Metadolerite/-basite	2.43 ± 0.27	2.47	2.08 ± 0.10	2.89 ± 0.14	5
Whole bedrock	1.32 ± 0.91	0.87	0.426 ± 0.021	2.89 ± 0.14	14
Catchment-wide estimate ^{4,5}	1.21				
<i><u>Pluhův Bor</u></i>					
Serpentinite	< 0.01 ⁶				6
Amphibolite	0.495 ± 0.042	0.452	0.368 ± 0.018	0.727 ± 0.036	5
Ultra-/Metabasite	0.163 ± 0.064	0.225	0.102 ± 0.005	0.249 ± 0.012	3
Shist	0.249				1
Whole bedrock	0.205 ± 0.238	0.102	< 0.01 ⁷	0.727 ± 0.036	15
Catchment-wide estimate ^{4,5}	0.18				

¹ Average value given with 1SD uncertainty (natural range).

² Concentration value given with 5% uncertainty of ICP-OES measurement.

³ Number of measured bedrock samples.

⁴ Catchment-wide beryllium concentration derived from [^9Be] measured in bedload sediment (LYS) or from linear regression approach (NAZ and PLB; see text for detailed explanation). Value is given without an uncertainty as the total uncertainty on this bedrock beryllium concentration value cannot be assessed reliably.

⁵ This average [Be] is used for further calculations of the denudation rate.

⁶ The detection limit of measurements is 10 ppb of Be in the bedrock.

The average and median values in the granite are within the typical range of measured beryllium concentrations in granitic rocks (Gao et al., 1998). Granites often have specifically high [^9Be], whereas mafic rocks exhibit much lower [^9Be] than the average upper crust which has a mean value of 2.2 ± 0.5 ppm (Grigor'yev, 1986a; Grigor'yev, 1986b; Rudnick et al., 2003; von Blanckenburg et al., 2012). The high heterogeneity in [^9Be] in granites of the Czech Republic is also found by other authors (Navrátil, 2000; Navrátil et al., 2002). It could be due to a “nugget effect” caused by beryllium minerals like beryl. Further, in the Jelení granite type present at Lysina a beryllium rich

lithium mica (Zinwaldite) with concentration of about 13 ppm Be occurs (Navrátil, 2000). If incongruent weathering takes place these more weathering resistant minerals - high in Be - could be enriched compared to other minerals in the rock. Published concentration data of mafic bedrock types are comparable to the measured data and also the low concentrations for ultramafic rocks are confirmed by other authors (see Table 2.8).

Table 2.8: Published beryllium concentrations measured in mafic and ultramafic rock types and serpentine minerals

Bedrock type / Mineral Specification	Locality	Beryllium concentration (ppm)	Reference
Amphibolite	Catalina Shist, California	0.41 - 1.10	Bebout et al. (1993)
Greenschist-amphibolite facies	Ural Mountains	0.5 - 8.0	Grew (2002)
Metapelites (amphibolite facies)	Kinzigite formation, NW Italy		Bea and Montero (1999)
Metabasite	Swiss-Italian Alps	0.79 - 0.86	Pelletier et al. (2008)
Serpentinite (whole rock)	Swiss-Italian Alps	0.01 - 0.04	Pelletier et al. (2008)
Serpentine minerals (serpentinized peridotites)		0.00013 - 0.016	Vils et al. (2008)

In the case of the mafic and the ultramafic catchment methodological complications arise due to different lithologies with distinctly different $[^9\text{Be}]$ that comprise the geological basement of each catchment. Due to this large variability in beryllium concentrations between individual rock types and in the absence of knowledge of the areal distribution of these rocks within the catchments, I cannot calculate a meaningful average bedrock value that would be representative for an entire catchment. However, such a parent bedrock concentration is required to calculate a denudation rate. Thus, to derive a catchment-wide parent bedrock beryllium concentration, I used the concentration of a reliable major element in river sediment and calculated the beryllium concentration in bedrock from linear regression of the concentration of this element in bedrock against the concentration of beryllium in bedrock. The method comprises two steps. First, I identified a reliable element by plotting averaged major element and beryllium concentrations measured in the bedrock ($[X]_{\text{bedrock}}$) versus major element and beryllium concentrations measured in the bedload sediment of each catchment ($[X]_{\text{bedload sediment}}$; see Figure 2.8). Assuming that bedload sediment is averaging over the entire catchment area (von Blanckenburg, 2005) and thus represents the total bedrock composition, an element that plots on a 1:1 line in these plots should not be affected by any loss or river bed particle sorting. For Lysina, I observe a good agreement between the average $[^9\text{Be}]_{\text{bedrock}}$ and $[^9\text{Be}]_{\text{bedload sediment}}$ (see Figure 2.8). Hence, I assumed that $[^9\text{Be}]_{\text{bedload sediment}}$ represents the catchment-wide bedrock concentration. The resulting $[^9\text{Be}]_{\text{parent}}$ for Lysina is then 5.5 ppm.

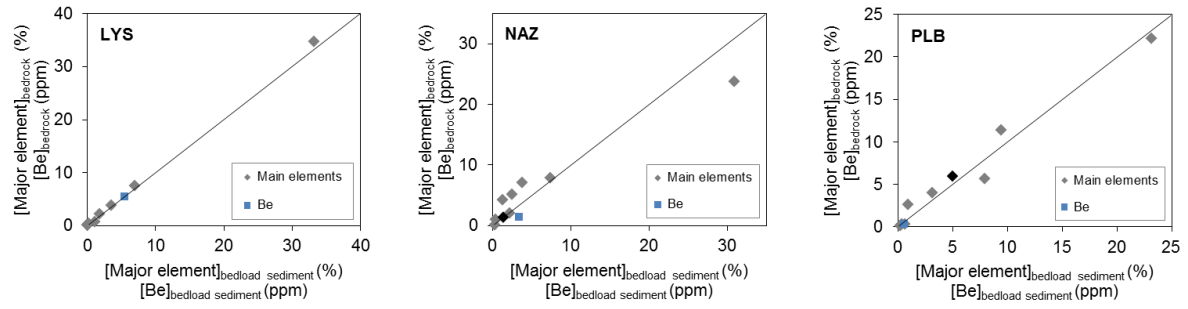
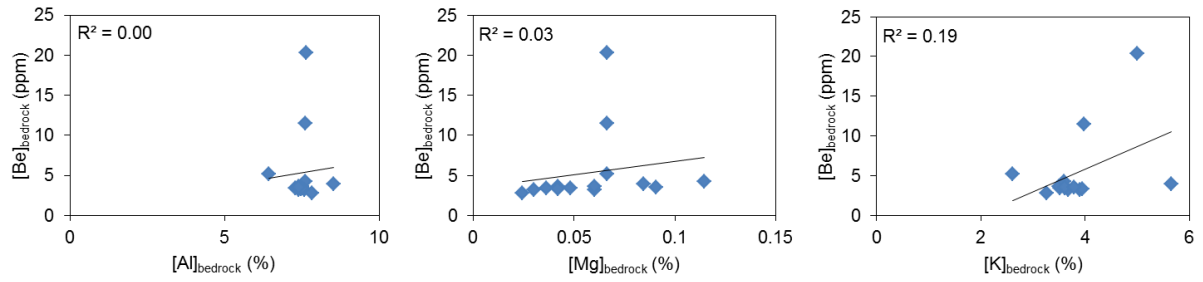


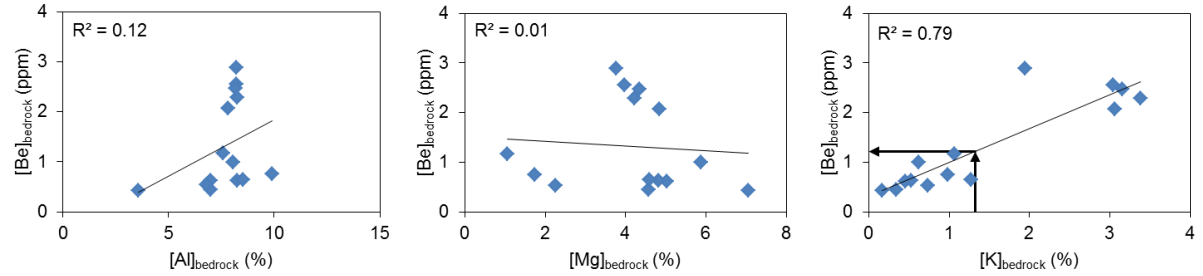
Figure 2.8: Average major element (Si, Ti, Al, Fe, Mn, Mg, Ca, Na, K) and average Be concentrations of the bedrock ($[X]_{bedrock}$) plotted versus the major element and Be concentration determined in the bedload sediment ($[X]_{bedload\ sediment}$) of each catchment. [Major element] in % were measured with XRF (shown in grey), and [Be] in ppm with ICP-OES (shown in blue). In black is shown the element chosen for calculation of $[^9Be]_{parent}$ in the case of the mafic and ultramafic catchment. (K at NAZ and Al at PLB). The black line represents a 1:1 line.

The second step was applied in the case of the mafic and ultramafic catchment where $[^9Be]_{bedload\ sediment}$ is much higher than $[^9Be]_{bedrock}$. I used a linear regression method, derived from plotting $[^9Be]$ measured in individual bedrock samples versus the concentration of a second element measured on these bedrock samples (in Figure 2.9 I show plots for Al, Mg, and K versus Be). Assuming that the bedload sediment concentration of the respective second element that correlates reasonably well with Be (K at NAZ and Al at PLB) represents the catchment-wide bedrock concentration, and was considered as reliable by plotting on the 1:1 line (see black symbols in Figure 2.8), I can calculate a representative $[^9Be]$ from the intersection of the major element's bedload sediment concentration with the slope of the linear trend in Figure 2.9. Applying this approach to K versus Be in the case of the mafic catchment, a $[^9Be]_{parent}$ of 1.21 ppm is derived for Na Zeleném. At the ultramafic catchment Pluhův Bor a $[^9Be]_{parent}$ of 0.18 ppm results from the slope of fitting Al versus Be (see Figure 2.9). These $[^9Be]_{parent}$ are reasonable as they are in the order of the average $[^9Be]$ determined on the bedrock core samples (see Table 2.7). For comparison, I can estimate the $[^9Be]_{parent}$ for the Pluhův Bor catchment from the distribution of the bedrock that is known from point counting of bedrock outcrops (Krám et al., 2009). The bedrock composition is composed of 51% serpentinite, 28% tremolite (shist) and actinolite (shist), 13% amphibolite and 8% other rocks. Weighting these rock type percentages with the corresponding $[^9Be]$ yields a $[^9Be]_{parent}$ of 0.15 ppm that is similar to the $[^9Be]_{parent}$ derived with the linear regression approach.

LYS



NAZ



PLB

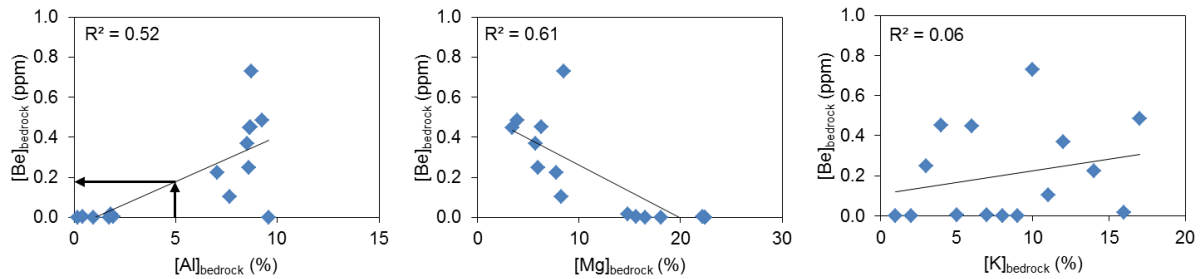


Figure 2.9: Linear regression to estimate a catchment-wide averaged $[^9Be]_{parent} - [^9Be]_{bedrock}$ measured in individual bedrock samples of the bedrock core are plotted versus major element $[X]_{bedrock}$ (Al, Mg, and K) concentrations measured in the same bedrock samples. The black line is the linear fit line through all individual data points (blue diamonds). Black arrows show how a $[^9Be]_{parent}$ is derived from the bedload sediment concentration of K (1.3 %) at NAZ and Al (5.0 %) at PLB, respectively, which are the only elements that correlate reasonably well with Be. Note that although Mg also correlates with Be in the case of PLB, it is not used here as it is likely underestimated in bedload sediment because it is lost into the dissolved fraction (see Figure 2.8). The overall poor correlation in the (ultra)mafic catchments is likely due to the chemically highly heterogeneous bedrock types.

2.5 Denudation rates from *in situ*-produced ^{10}Be

To compare the meteoric derived denudation rates with an independent estimate, I also determined *in situ* ^{10}Be denudation rates ($D_{in situ}$). The *in situ*-produced ^{10}Be concentration is uniform for the two analyzed grain sizes of the granitic Lysina catchment (17.7×10^4 atoms g^{-1} ; see Table 2.9). The mafic catchments yield *in situ*-produced ^{10}Be concentrations of 17.9×10^4 atoms g^{-1} (NAZ) and

33.8×10^4 atoms g^{-1} (PLB). Using Equation 2.1, for the quartz-bearing granitic Lysina catchment a denudation rate ($D_{in situ}$) of $108 \pm 11 \text{ t km}^{-2} \text{ y}^{-1}$ results (see Table 2.9). The mafic Na Zeleném catchment has a denudation rate of $97 \pm 11 \text{ t km}^{-2} \text{ y}^{-1}$, and Pluhův Bor exhibits a lower denudation rate of $49 \pm 5 \text{ t km}^{-2} \text{ y}^{-1}$. *In situ*-derived denudation rates integrate over the time it takes to erode one attenuation path length that is the depth at which $1/e$ of the incoming cosmic rays are attenuated. The integration time scales for the studied catchments are about 14 ky in Lysina, 16 ky in Na Zeleném, and 32 ky in Pluhův Bor (see Table 2.9).

$D_{in situ}$ for the granitic and mafic catchment are in the range of *in situ*-derived denudation rates for (granitic) catchments in middle Europe. Schaller et al. (2001) measured *in situ* ^{10}Be denudation rates in river basins of Middle Europe with a vegetation cover and precipitation rates being similar to the ones of the catchments studied here. For example, the crystalline Regen catchment exhibits denudation rates of 65 to $105 \text{ t km}^{-2} \text{ y}^{-1}$, these rates being equivalent to an integration time scale of 10 to 40 ky (recalculated in Schaller et al. (2002b)). Morel et al. (2003) who studied catchments in an unglaciated area with granitic lithology in the Black Forest, Germany, obtained *in situ* ^{10}Be rates of about $90 \text{ t km}^{-2} \text{ y}^{-1}$.

Table 2.9: *In situ*-produced ^{10}Be concentrations and calculated denudation rates in $\text{t km}^{-2} \text{ y}^{-1}$ and mm ky^{-1}

Sample name	ETH Code	Grain Size (μm)	^{10}Be concentration ($\times 10^4$ atoms g^{-1})	Total production rate ² (atoms $\text{g}_{(\text{qtz})}^{-1} \text{ y}^{-1}$)	Denudation rate ($\text{t km}^{-2} \text{ y}^{-1}$)	Denudation rate ³ (mm ky^{-1})	Integration time scale (ky)
LYS 250 ¹	ZB8705	250-500	17.6 ± 1.4	8.82	108 ± 12	41.5 ± 4.5	14.4 ± 1.6
LYS 500 ¹	ZB8706	500-800	17.69 ± 0.94	8.82	107.5 ± 9.5	41.3 ± 3.6	14.5 ± 1.3
NAZ	ZB9468	125-800	17.9 ± 1.5	7.95	97 ± 11	37.4 ± 4.0	16.0 ± 1.7
PLB	ZB9469	125-800	33.8 ± 2.6	7.81	48.6 ± 5.3	18.7 ± 2.0	32.1 ± 3.5

¹ Two grain sizes from same sample; LYS 250: grain size 250-500 μm , LYS 500: grain size 500-800 μm

² Total production rate scaled after Dunai (2000) using a total SLHL production rate of $4.00 \text{ atoms g}_{(\text{qtz})}^{-1} \text{ y}^{-1}$ (Phillips et al., 2016)

³ For conversion of units ($\text{t km}^{-2} \text{ y}^{-1}$ to mm ky^{-1}), a density of 2.6 g cm^{-3} was used.

The denudation rate of the ultramafic catchment Pluhův Bor is distinctly lower than the rates of the other two catchments. In this catchment quartz occurs in veins that are intersecting the bedrock. These veins are commonly formed in serpentinite due to weathering and alteration of antigorite and the subsequent release of SiO_2 that is re-precipitated as joint fillings (Cleaves et al., 1974). These quartz veins could potentially erode slower by episodic erosion events than the surrounding bedrock and thus exhibit higher cosmogenic nuclide concentrations (Codilean et al., 2014).

2.6 Beryllium hydrochemistry of the catchments

2.6.1 Beryllium concentrations and $^{10}\text{Be}/^9\text{Be}$ ratios in the stream waters

I measured dissolved ^9Be ($[^9\text{Be}]_{\text{diss}}$) and meteoric ^{10}Be concentrations ($[^{10}\text{Be}]_{\text{diss}}$) in stream water samples of the three catchments. When evaluating these stream water data measured over a short time series of several months, seasonal variability in the dissolved beryllium concentrations is observed (see Figure 2.10). Generally, the ^9Be chemistry of stream waters is primarily influenced by the abundance of beryllium in the parent bedrock of the drainage basin and the pH of the stream water. Meteoric ^{10}Be concentrations are controlled by atmospheric input and pH value of associated solutions.

The dissolved cosmogenic ^{10}Be concentrations are highest in the acidic granitic catchment (on average $[^{10}\text{Be}]_{\text{diss}} = 11.8 \pm 1.7 \times 10^4$ atoms g^{-1} , 1SD uncertainty, $n = 10$; see Table 2.10). $[^{10}\text{Be}]_{\text{diss}}$ measured in the groundwater of the Lysina catchment is with $13.4 \pm 0.4 \times 10^4$ atoms g^{-1} similar to the stream water. The average $[^{10}\text{Be}]_{\text{diss}}$ in the neutral Na Zeleném catchment is $1.02 \pm 0.75 \times 10^4$ atoms g^{-1} and in the slightly alkaline catchment Pluhův Bor $[^{10}\text{Be}]_{\text{diss}}$ averages to $2.1 \pm 1.8 \times 10^4$ atoms g^{-1} . For these two catchments no $[^{10}\text{Be}]_{\text{diss}}$ in groundwater is available. Dissolved $[^9\text{Be}]$ are highest for the stream water of the felsic Lysina catchment (for time period of sampling on average 969 ± 82 ng l^{-1} , 1SD uncertainty, $n = 10$; see Table 2.10). $[^9\text{Be}]_{\text{diss}}$ in the groundwater of the Lysina catchment is distinctly higher (2075 ± 161 ng l^{-1} ; see Table 2.10) than in the stream water. In the neutral to alkaline catchments, Na Zeleném and Pluhův Bor, stream water $[^9\text{Be}]_{\text{diss}}$ are almost two orders of magnitude lower compared to the acidic catchment (on average $[^9\text{Be}]_{\text{diss}} = 25 \pm 14$ ng l^{-1} for NAZ and 17 ± 11 ng l^{-1} for PLB; 1SD uncertainty, $n = 10$; see Table 2.10). In these catchments where pH values in the streams are near-neutral, ^{10}Be and ^9Be show identical pattern (see Figure 2.10). In contrast, during a relatively dry period in the Lysina catchment (instantaneous discharge < 0.25 l s^{-1}) ^{10}Be and ^9Be behave in opposite ways.

The $^{10}\text{Be}/^9\text{Be}$ ratio of dissolved beryllium is in Lysina on average $18.4 \pm 3.0 \times 10^{-10}$ (range from 14.2 to 23.1×10^{-10}), in Na Zeleném $57 \pm 11 \times 10^{-10}$ (range from 42 to 77×10^{-10}), and Pluhův Bor reveals the highest ratio of $168 \pm 50 \times 10^{-10}$ (range from 88 to 230×10^{-10}). $(^{10}\text{Be}/^9\text{Be})_{\text{diss}}$ of the groundwater in Lysina is $9.64 \pm 0.82 \times 10^{-10}$.

Table 2.10: Discharge, pH value, ^{10}Be (in 10^4 atoms g^{-1}) and ^9Be (in ng l^{-1}) concentrations, and calculated dissolved ratios for a time series of stream water samples

Catchment	Sample ID ¹	Sampling date	Discharge (l s^{-1})	pH	^{10}Be (10^4 atoms g^{-1})	^9Be (ng l^{-1})	$^{10}\text{Be}/^9\text{Be}$ ($\times 10^{-10}$)
Lysina	1108 ²	03/08/2011	0.5	4.4	11.82 ± 0.51	911 ± 71	19.4 ± 1.7
	1204	30/04/2012	0.9	4.3	12.35 ± 0.49	899 ± 70	20.6 ± 1.8
	1206	27/06/2012	0.3	4.8	10.32 ± 0.47	1075 ± 84	14.4 ± 1.3
	1207	01/08/2012	0.2	4.8	10.42 ± 0.36	1084 ± 84	14.4 ± 1.2
	1208	29/08/2012	0.2	5.1	10.13 ± 0.42	1064 ± 83	14.2 ± 1.3
	1209	01/10/2012	0.2	5.0	9.80 ± 0.68	826 ± 64	17.8 ± 1.8
	1210	01/11/2012	0.4	5.1	13.52 ± 0.89	943 ± 73	21.5 ± 2.2
	1211	28/11/2012	3.4	4.1	15.6 ± 1.0	1016 ± 79	23.1 ± 2.4
	1301	08/01/2013	13.5	4.1	11.98 ± 0.48	944 ± 73	19.0 ± 1.7
	1302	05/02/2013	12.0	4.1	11.91 ± 0.37	924 ± 72	19.3 ± 1.6
	Average ³			4.6	11.8 ± 1.7	969 ± 82	18.4 ± 3.0
	"flood"	02/06/2013	112	4.0	-	574 ± 45	-
	Groundwater	03/08/2011	no value	-	13.36 ± 0.40	2075 ± 161	9.64 ± 0.80
Catchment	Sample ID ¹	Sample date	Discharge (l s^{-1})	pH	^{10}Be (10^4 atoms g^{-1})	^9Be (ng l^{-1})	$^{10}\text{Be}/^9\text{Be}$ ($\times 10^{-10}$)
Na Zeleném	1108 ²	03/08/2011	0.2	7.5	0.579 ± 0.046	14.8 ± 1.2	58.5 ± 6.5
	1204	30/04/2012	0.6	7.0	1.410 ± 0.089	32.7 ± 2.5	64.5 ± 6.4
	1206	27/06/2012	<0.1 ⁵	7.5	0.574 ± 0.060	16.2 ± 1.3	53.1 ± 6.9
	1207	01/08/2012	<0.1 ⁵	7.6	0.537 ± 0.056	17.0 ± 1.3	47.4 ± 6.1
	1208	29/08/2012	<0.1 ⁵	7.7	0.473 ± 0.046	13.9 ± 1.1	50.9 ± 6.4
	1209	01/10/2012	<i>no value</i> ⁵	7.5	0.358 ± 0.050	12.8 ± 1.0	41.8 ± 6.7
	1210	01/11/2012	3.9	7.0	0.761 ± 0.072	18.0 ± 1.4	63.3 ± 7.7
	1211	28/11/2012	1.0	7.2	0.706 ± 0.062	23.3 ± 1.8	45.3 ± 5.3
	1301	07/01/2013	26.6	6.3	2.633 ± 0.092	58.1 ± 4.5	67.9 ± 5.8
	1302	05/02/2013	12.2	6.5	2.15 ± 0.11	41.9 ± 3.3	76.8 ± 7.1
	Average ³			7.2	1.02 ± 0.75	25 ± 14	57 ± 11
	"flood"	02/06/2013	153	6.2	-	78.8 ± 6.1	-
Catchment	Sample ID ¹	Sample date	Discharge (l s^{-1})	pH	^{10}Be (10^4 atoms g^{-1})	^9Be (ng l^{-1})	$^{10}\text{Be}/^9\text{Be}$ ($\times 10^{-10}$)
Pluhův Bor	1108 ²	03/08/2011	0.2	8.0	1.274 ± 0.054	8.31 ± 0.65	229 ± 20
	1204	30/04/2012	0.3	7.8	1.635 ± 0.099	12.07 ± 0.94	203 ± 20
	1206	27/06/2012	0.1	8.1	0.567 ± 0.080	6.12 ± 0.48	139 ± 22
	1207	01/08/2012	0.2	8.1	1.91 ± 0.17	17.00 ± 1.32	168 ± 20
	1208	29/08/2012	0.1	8.1	0.418 ± 0.058	7.12 ± 0.55	88 ± 14
	1209	01/10/2012	0.1	8.2	0.258 ± 0.043	4.27 ± 0.33	90 ± 17
	1210	01/11/2012	1.2	7.8	2.32 ± 0.15	22.0 ± 1.7	158 ± 16
	1211	28/11/2012	0.5	7.9	2.03 ± 0.18	19.5 ± 1.5	156 ± 18
	1301	07/01/2013	6.1	7.3	5.21 ± 0.15	33.9 ± 2.6	230 ± 19
	1302	06/02/2013	7.0	7.3	5.60 ± 0.20	39.1 ± 3.0	214 ± 18
	Average ³			7.8	2.1 ± 1.8	17 ± 11	168 ± 50
	"flood"	02/06/2013	69	6.9	-	71.9 ± 5.6	-

¹ Sample ID, being composed of year and month.² Sample ID 1108: samples taken at the same date as bedload.³ Average values given with 1SD uncertainty. The natural variability in each catchment (given 1SD uncertainty) is larger than the uncertainty of the ICP-MS (^9Be) or AMS (^{10}Be) measurement for individual samples.⁴ ETH code: ZB: ^{10}Be measurement with the 6MV Tandem AMS at ETH Zurich;TB: ^{10}Be measurement with the Tandy AMS at ETH Zurich.⁵ In *italics*: only estimated values for discharge, because of damaged v-notch weir.

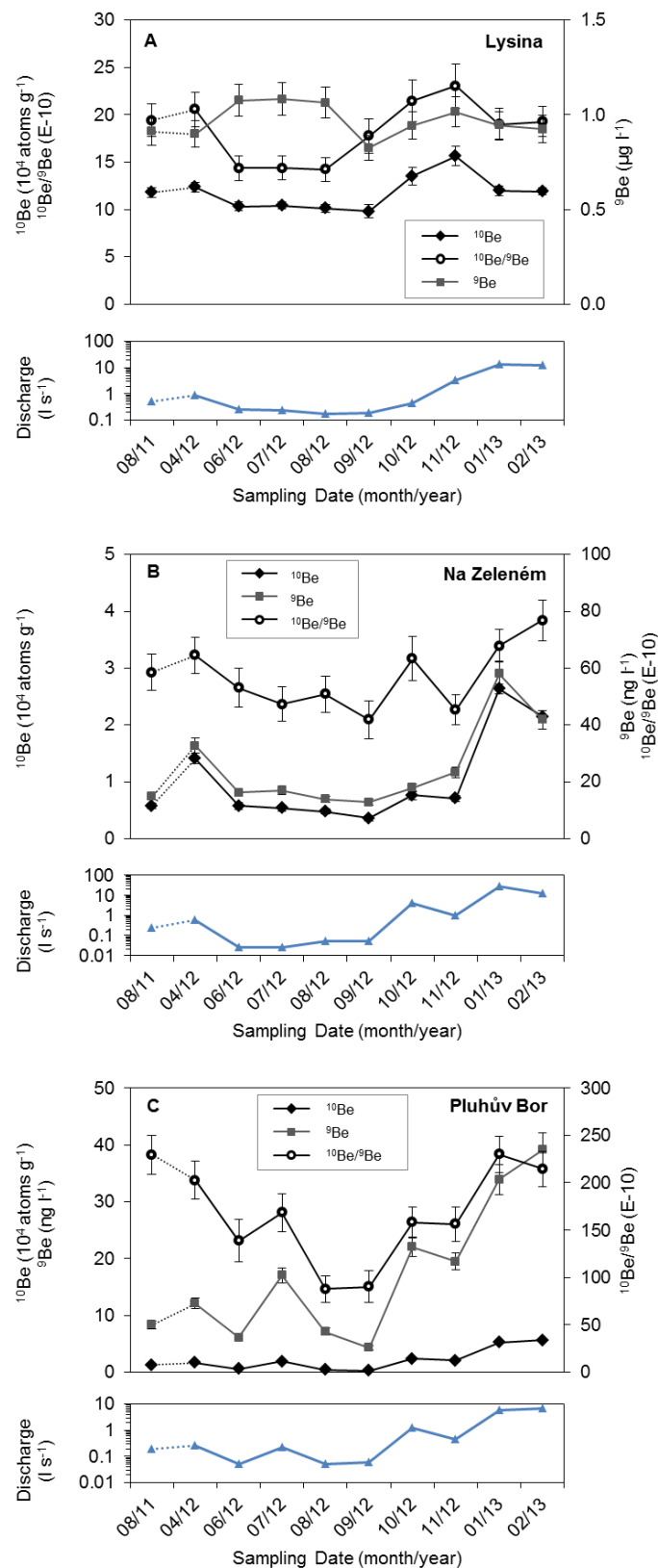


Figure 2.10: ^{10}Be (in 10^4 atoms g^{-1}) and ^9Be (in $\mu\text{g l}^{-1}$ for LYS and ng l^{-1} for NAZ and PLB) concentrations, and calculated dissolved ratios (in $\times 10^{-10}$) for a time series of stream water samples. **A:** Lysina, **B:** Na Zeleném, and **C:** Pluhův Bor. Note the different axes for each catchment. In each lower panel, the instantaneous discharge in l s^{-1} is displayed on a logarithmic scale (in blue).

2.6.2 Hydrological behaviour of dissolved [^9Be], [^{10}Be], and ($^{10}\text{Be}/^9\text{Be}$)

In Figure 2.11 and Figure 2.12, I consider the relation between dissolved beryllium concentrations, ($^{10}\text{Be}/^9\text{Be}$)_{diss}, and hydrological parameters (instantaneous discharge, pH value) measured in the stream waters. At Lysina [^{10}Be]_{diss} generally increases with increasing discharge but at high discharge conditions ($> 10 \text{ l s}^{-1}$) [^{10}Be]_{diss} is relatively lower. In comparison, [^9Be]_{diss} is relatively constant over a large range of discharge and pH values, except one data point measured during a flood event with a discharge of above 100 l s^{-1} that is markedly lower than the average [^9Be]_{diss} (see Figure 2.12). In the case of Na Zeleném and Pluhův Bor both [^{10}Be]_{diss} and [^9Be]_{diss} in general increase with increasing discharge (see Figure 2.12). In these catchments the beryllium concentration decreases with increasing pH value (see Figure 2.11). In the case of Lysina no relation between [^9Be]_{diss} and [^{10}Be]_{diss} with the pH value is observed (see Figure 2.11). Krám et al. (1998) also found this lack in correlation between [^9Be]_{diss} and pH value based on a much larger data set. In the neutral and slightly alkaline stream waters (NAZ and PLB) the pH value decreases noticeably with increasing discharge (see Figure 2.12), showing a dilution by more acidic precipitation. The acidic Lysina catchment shows a slightly different pattern. Only at very low discharge ($< 1 \text{ l s}^{-1}$), the pH value decreases markedly as discharge increases but at higher discharge this decrease in pH is moderated (see Figure 2.12).

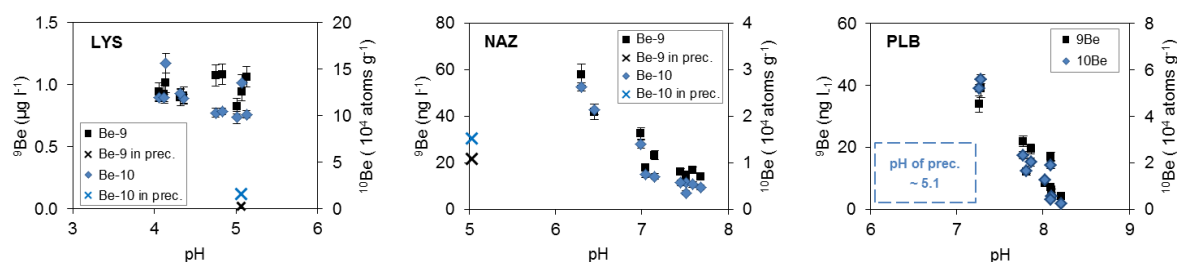


Figure 2.11: Dissolved ^9Be concentrations (in $\mu\text{g l}^{-1}$ (LYS) or ng l^{-1} (NAZ and PLB), and ^{10}Be concentrations (in $10^4 \text{ atoms g}^{-1}$) plotted against pH for Lysina (LYS), Na Zeleném (NAZ), and Pluhův Bor (PLB). Note the different scales in the diagrams. Additionally are plotted ^9Be (black cross) and ^{10}Be (blue cross) in precipitation. [^{10}Be] in precipitation ($1.54 \times 10^4 \text{ atoms g}^{-1} \pm 10\%$) is calculated from a mean annual precipitation of 950 mm and depositional ^{10}Be flux of $1.46 \times 10^6 \text{ atoms cm}^{-2} \text{ y}^{-1}$, and [^9Be] ($22 \pm 25 \text{ ng l}^{-1}$) was measured directly in the rain water (data from *P. Kram, Czech Geological Survey*). The pH value in precipitation is about 5.1. At Pluhův Bor, precipitation values do not plot in the displayed range.

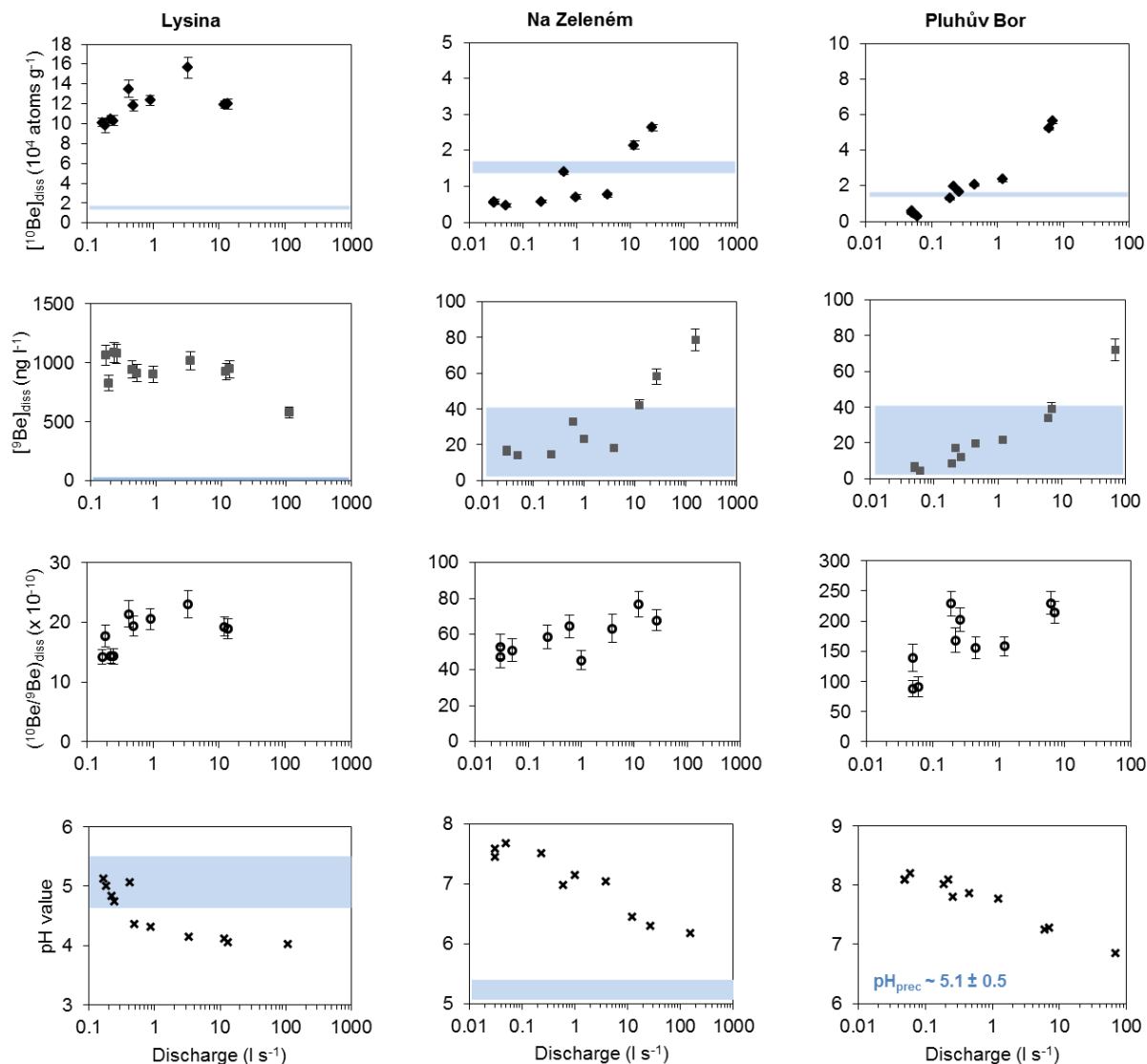


Figure 2.12: $[^{10}\text{Be}]_{\text{diss}}$ (in 10^4 atoms g⁻¹) and $[^9\text{Be}]_{\text{diss}}$ (in ng l⁻¹), $(^{10}\text{Be}/^9\text{Be})_{\text{diss}}$ (in $\times 10^{-10}$), and pH values measured in stream water plotted against instantaneous discharge (in l s⁻¹) for LYS (first column), NAZ (second column), and PLB (third column). The blue bars represent the respective range in precipitation values. $[^{10}\text{Be}]$ in precipitation (1.54×10^4 atoms g⁻¹ \pm 10%) is calculated from a mean annual precipitation of 950 mm and depositional ^{10}Be flux of 1.46×10^6 atoms cm⁻² y⁻¹, and $[^9\text{Be}]$ (22 ± 25 ng l⁻¹) was measured directly in the rain water. pH values were measured in precipitation in the years 2011 to 2013. ^9Be concentration data and pH values (on average about 5.1) in precipitation are from P. Kram, Czech Geological Survey. Note the different axis scales for each catchment. The error bars include the uncertainty of the concentration measurements.

Regarding the described relationships between beryllium concentrations, instantaneous discharge, and pH, knowing the relative contributions of groundwater versus surficial water runoff may help to decipher the observed trends. I consider here modelled water runoff data from oxygen isotopes that exist for the acidic Lysina catchment (Buzek et al. (1995); see Figure 2.13). The main component to water runoff in this catchment is groundwater making up of about 55% of the total water runoff (in winter: 57-62 %, in summer: 41-49 %). The residence time of the groundwater at Lysina is about one

year (Buzek et al., 1995). Direct surface (or overland) flow and subsurface (or indirect) flow comprise the remaining water runoff components. Direct surface flow has a residence time of a few hours and contributes on yearly average between 5% and up to 20% during flood events to total water runoff (Buzek et al., 1995). The indirect water flow originates in the upper soil horizons with a residence time of several weeks. This topsoil component is closely related to discharge (Lischeid et al., 2010). On average its contribution to water runoff is about 40%. During flood events however this soil water component becomes the dominant indirect component with about 80% contribution, whereas at base flow its contribution is close to zero. Base flow conditions in the small catchments studied here dominate at water runoff of about less than 1 l s^{-1} whereas stormflow conditions occur at water runoff of about more than 10 l s^{-1} (Büttcher, 2001). Note that the model probably cannot be applied directly to the other catchments.

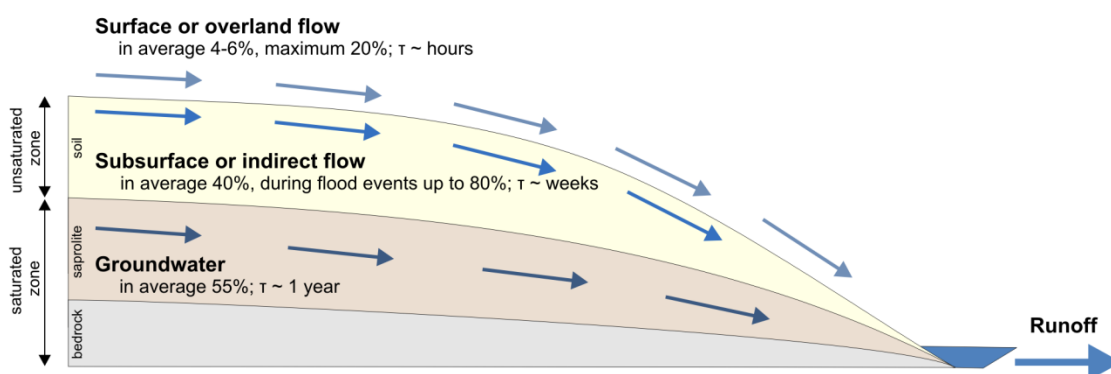


Figure 2.13: Sketch of the different water flow compartments at the Lysina catchment. τ is the residence of the water and in % are given the relative proportion to the total water runoff. Data from Buzek et al. (1995).

The negative trend between discharge and pH in the stream waters (see Figure 2.12) can be explained by differences in runoff generation depending on the contributions of base flow, subsurface, and overland flow. The pH value of soil water varies in the soil horizons from 3.5 to 4.4 at Lysina, from 4.0 to 5.8 at Na Zeleném, and from 4.9 to 7.7 at Pluhův Bor (Krám et al., 2013). The water component from the upper top soil horizons is more acidic due to acidic atmospheric deposition (in the case of NAZ and PLB) and from the presence of organic acids leached from the organic horizon. The pH value in precipitation in the vicinity of the studied sites is on average about 5 (data from P. Kram, Czech Geological Survey). Groundwater is usually less acidic than soil water due to pH buffering as a result of dissolution of minerals during weathering of bedrock (Chadwick and Chorover, 2001; Wilson, 2004). Lysina reveals a groundwater pH of around 5.9, Na Zeleném of circa 6.5, and Pluhův Bor of about 7.9 (data from P. Kram, Czech Geological Survey). During high discharge, runoff is generated in the upper soil parts of the catchment that are more acidic and penetration into the deeper soils is minor (Buzek et al., 1995). In contrast, at base flow water derived from the less acidic deep groundwater with deep flow paths dominates runoff.

The model further serves to explain the exceptional low $[^9\text{Be}]_{\text{diss}}$ in stream water during the flood event in Lysina. During this event there is a large input to water runoff from direct overland flow caused by high precipitation amounts with a markedly lower ^9Be concentration than the stream water. $[^9\text{Be}]_{\text{diss}}$ in precipitation is about $22 \pm 25 \text{ ng l}^{-1}$ (1SD uncertainty, $n = 91$) derived from a precipitation data set from the *Czech Geological Survey* (P. Kram, unpublished data). During lower flow groundwater that is high in ^9Be is the major runoff component. At the transition between bedrock and weathered material, the beryllium concentration is assumed to be high because “fresh” beryllium is released from primary minerals by chemical dissolution processes. Since the pH of the groundwater is still below 6, large amounts of this released beryllium are directly transported in the dissolved form. Likewise, the low $[^{10}\text{Be}]_{\text{diss}}$ during higher discharge in the stream water at Lysina can be explained. This pattern is attributed to dilution of the Lysina stream water at high discharge by precipitation that is low in ^{10}Be . The meteoric ^{10}Be concentration in precipitation is estimated to be about $1.5 \times 10^4 \text{ atoms g}^{-1}$, calculated from a mean annual precipitation of 950 mm and a depositional ^{10}Be flux of $1.46 \times 10^6 \text{ atoms cm}^{-2} \text{ y}^{-1}$ (see Section 1.1.2), and hence is a factor of ten lower than in the stream water of Lysina. In the neutral catchments I observe an opposite trend with exceptionally high $[^9\text{Be}]_{\text{diss}}$ and $[^{10}\text{Be}]_{\text{diss}}$ during the flood event. Due to the high pH values in the soil, stream, and ground waters, I assume that most of the beryllium is bound to adsorption sites, which is supported by very low dissolved ^9Be concentrations. However, as discharge increases, pH values drop because the runoff is generated mainly at the surface and in the upper soil horizons where pH values are lower. Thus, at lower pH values beryllium either stays in solution or is potentially leached from its adsorption sites for a short while and transported in the dissolved form as the K_d value decreases.

The high variability in $(^{10}\text{Be}/^9\text{Be})_{\text{diss}}$ (see Figure 2.10 and Figure 2.16) shows that the ratio of dissolved beryllium in small catchments is dependent on catchment flow paths and discharge. Apparently, small-term fluctuations in the concentrations of ^9Be and meteoric ^{10}Be are not averaged out on this small scale and variable $(^{10}\text{Be}/^9\text{Be})_{\text{diss}}$ are the consequence. The general increase in $(^{10}\text{Be}/^9\text{Be})_{\text{diss}}$ with higher discharge is supported by $(^{10}\text{Be}/^9\text{Be})_{\text{reac}}$ measured on the depth profile in Lysina that are higher in the top of the profile (see Section 2.4.2). During periods of high discharge, a large component of the water runoff is generated in the upper soil horizons (subsurface flow) where reactive $^{10}\text{Be}/^9\text{Be}$ ratios are about 20×10^{-10} at Lysina. This ratio equals the average ratio of dissolved beryllium in the stream water. However, as the uppermost centimetres of the depth profile were not sampled, it could potentially be that the ratio at the surface is even higher than 20×10^{-10} . The lower reactive beryllium ratios measured in the lower part of the profile were found again in a $(^{10}\text{Be}/^9\text{Be})_{\text{diss}}$ in the groundwater that is about 10×10^{-10} (see Figure 2.6 B). During the lowest runoff phases $(^{10}\text{Be}/^9\text{Be})_{\text{diss}}$ is about 14×10^{-10} in the stream water of Lysina. Given that the stream water consists of different water compartments, its beryllium ratio should reflect the contributions of these compartments.

2.6.3 Concentration-discharge characteristics

Chemical weathering and the transport of solute weathering products is coupled to the hydrology of a catchment as the fluid residence time and the physical flow path length control the chemical composition of streams. The ratio between the actual physical flow path length of a catchment and the flow path length that is effectively needed to reach chemical equilibrium is important as the maximum solute concentration and the silicate weathering flux are determined by the chemical equilibration between dissolving and precipitating phases (Maher, 2011). A chemical equilibrium state is achieved if the average fluid residence time and hence subsurface contact time of a catchment is long enough that the fluids reach equilibrium with the solids. The system is then characterised by only minor variation in solute concentrations despite highly variable discharge. Rates of solute production or mobilization are then nearly proportional to water fluxes. Such catchments exhibit “chemostatic behaviour” with the primary control on solute weathering fluxes being discharge (Godsey et al., 2009; Maher, 2011). In contrast, “complex dilution”, meaning decreasing solute concentrations with increasing discharge, occurs in a system that controls these solute concentrations by dilution of fixed weathering fluxes such that solutions get undersaturated (Godsey et al., 2009; Maher, 2011).

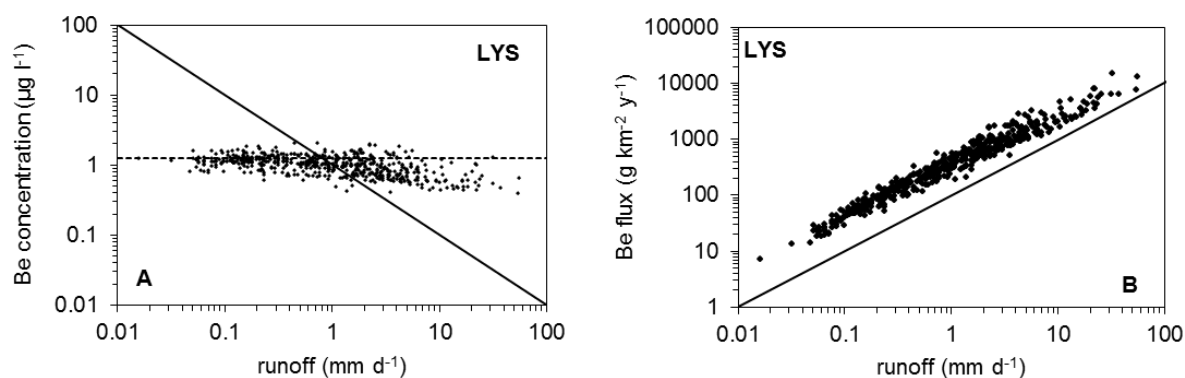


Figure 2.14 A: Concentration-runoff relationship for beryllium in Lysina (Data provided by *P. Kram, Czech Geological Survey, Prague*). The black line represents a log-log slope of -1, indicating concentrations set by dilution of fixed weathering fluxes (“complete dilution” hypothesis). A slope of zero would imply that the catchments behave “chemostatically” (dotted black line), meaning constant concentrations while the discharge varies. The beryllium data at Lysina show a “near-chemostatic” behaviour (log-log slope near zero, Godsey et al. (2009)). **B:** Beryllium flux (in $\text{g km}^{-2} \text{y}^{-1}$) as a function of water runoff (in mm d^{-1}). The black line represents a 1:1 relationship between solute fluxes and runoff, indicating constant concentration with variable runoff.

Long-term gauging data available from weekly sampling (data provided by *P. Kram, Czech Geological Survey*) show that beryllium concentrations at Lysina and most of the major weathering cations (Si, Mg, Ca, Na) at all three sites display near-chemostatic behaviour (see Figure 2.14 A and Figure 2.15). The cation concentration is constant until a certain threshold in water runoff is exceeded

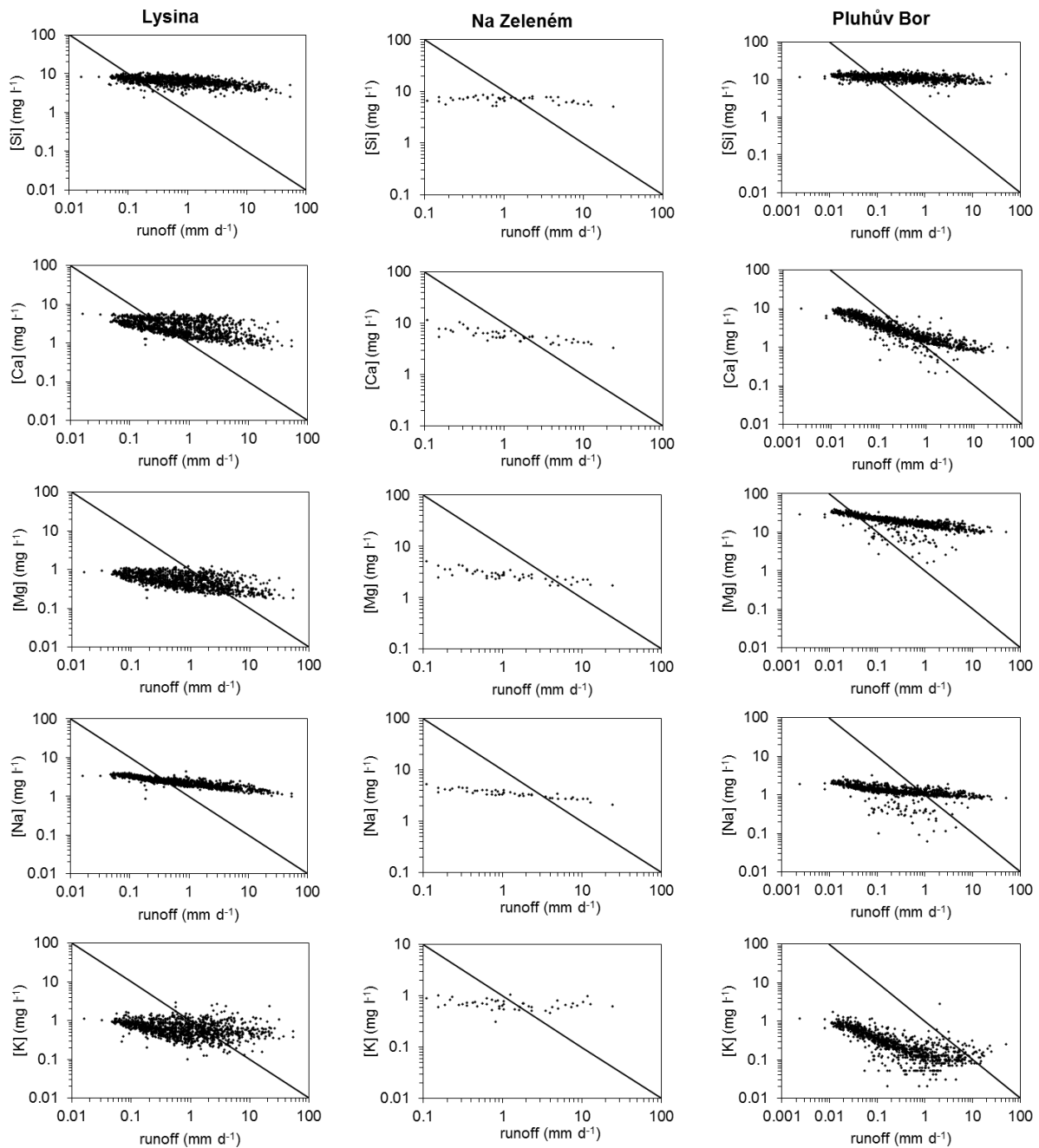


Figure 2.15: Concentration-discharge relationship of the major weathering cations (Si, Ca, Mg, Na, K) in the three catchments Lysina, Na Zeleném, and Pluhův Bor (Data set provided by *P. Kram, Czech Geological Survey, Prague*). On the x-axis is plotted the water runoff (in mm d^{-1}) and on the y-axis the concentrations of the major weathering elements (in mg l^{-1}). The black line represents a log-log slope of -1, indicating concentrations set by dilution of fixed weathering fluxes (“complete dilution”). A slope of zero would imply that the catchments behave “chemostatically”, meaning constant concentrations while the discharge varies. For the most part, the data of the three studied catchments show a “near-chemostatic” behaviour (log-log slope near zero, Godsey et al. (2009)).

and the concentration slightly decreases. In general, the dissolved concentrations of the weathering products decrease slightly with increasing runoff but vary only by a factor of less than 5 (except of K) whereas the runoff fluctuates by several orders of magnitude. Thus the fluxes of the weathering

solutes in the studied streams are, independent of lithologic differences, primarily controlled by water fluxes (Godsey et al., 2009) and so is the flux of beryllium at Lysina. At Pluhův Bor and Na Zeleném only very few data for beryllium exist that are limited by a measurement detection limit of $0.02 \mu\text{g l}^{-1}$, so that I am not able to do any further evaluation with respect to beryllium for these mafic catchments. The slight decrease in dissolved concentrations at high discharge can be explained by the heterogeneity in the flow path ways. For Lysina it is known that the groundwater component contributes a major amount to water runoff. A mean groundwater residence time in the order of one year (Buzek et al., 1995) suggests that the subsurface water contact time is long enough to reach chemical equilibrium. In contrast, water from the more shallow flow paths with shorter residence times of some hours to weeks is most likely not efficiently equilibrated.

2.6.4 Comparison of $(^{10}\text{Be}/^9\text{Be})_{\text{diss}}$ to $(^{10}\text{Be}/^9\text{Be})_{\text{reac}}$

In the following, I test whether the reactive phase of beryllium is in chemical equilibration with the dissolved phase in stream water. Although I do not know the residence time of phases containing reactive beryllium in the catchment, I can argue that it is in the order of several thousand years considering the determined denudation rates (see Section 2.8.2). Opposed to this, the residence time of the stream water is assessed to be about several hours to maximum one year (Buzek et al., 1995). That means that there is a large gap in the time it takes to form the reactive and the dissolved $^{10}\text{Be}/^9\text{Be}$ ratios, respectively.

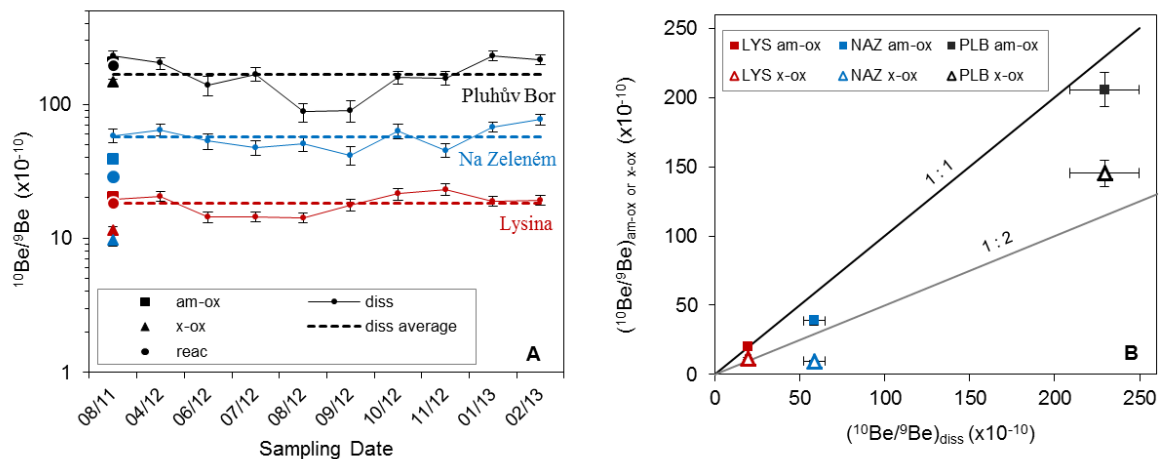


Figure 2.16: **A:** $^{10}\text{Be}/^9\text{Be}$ ratios (x10⁻¹⁰) determined on the total reactive phase (reac), HCl-leachable phase (am-ox) and $\text{NH}_2\text{OH}\cdot\text{HCl}$ -leachable phase (x-ox) of one individual bedload sample in each catchment, and dissolved $^{10}\text{Be}/^9\text{Be}$ ratios (diss) measured in stream water sampled over several months (average dissolved $^{10}\text{Be}/^9\text{Be}$ ratio value is also shown (dashed line)). **B:** Amorphous and crystalline oxide $^{10}\text{Be}/^9\text{Be}$ ratios versus dissolved $^{10}\text{Be}/^9\text{Be}$ ratios measured in stream water at time of coincident sampling (Aug. 2011). Error bars include the uncertainty of the concentration measurements.

In Lysina, $(^{10}\text{Be}/^9\text{Be})_{\text{diss}}$ is on average about 18.4×10^{-10} (see Table 2.10) and equals $(^{10}\text{Be}/^9\text{Be})_{\text{reac}}$ in stream bedload sediment (see Figure 2.16 A). In the ultramafic Pluhův Bor catchment $(^{10}\text{Be}/^9\text{Be})_{\text{reac}}$ and $(^{10}\text{Be}/^9\text{Be})_{\text{diss}}$ are within a factor of about two but the variability in $(^{10}\text{Be}/^9\text{Be})_{\text{diss}}$ is relatively high in this catchment, ranging from 88×10^{-10} to 230×10^{-10} . In Na Zeleném, however, $(^{10}\text{Be}/^9\text{Be})_{\text{diss}}$ is distinctly higher than $(^{10}\text{Be}/^9\text{Be})_{\text{reac}}$ (see Figure 2.16 A). Whereas in the catchments of Lysina and Pluhův Bor the residence time of waters in the catchments appears to be long enough in order to reach equilibrium with the reactive phase, in Na Zeleném the time to ensure sufficient mixing between water and sediment and thereby equilibration of the beryllium isotopes is presumably not attained.

At the time of paired sampling of bedload and stream water in August 2011 the $^{10}\text{Be}/^9\text{Be}$ ratios of dissolved beryllium are closer to those measured in the amorphous fraction as compared to those ratios determined on the crystalline oxide fraction (Figure 2.16 B). This would mean that at this stage the dissolved fraction most likely exchanges more readily with the amorphous oxide fraction. The same observation was made by Wittmann et al. (2015) on a much larger spatial scale in the Amazon River. On the small spatial scale considered here, this observation could be associated with diverse processes of oxide formation and different age or depth in the profile. Amorphous iron oxides (e.g. ferrihydrite) are formed in B-horizons of soils where rapid oxidation processes can take place and forming oxides are in regular exchange with Fe^{2+} -bearing soil solutions. Compared to crystalline structures these amorphous particles have large reactive surface areas and sorption and surface precipitation are rapid (Waychunas et al., 2005). Amorphous oxides convert into crystalline oxides (e.g. goethite or hematite) by crystallisation within the aggregate structure of the amorphous oxides (Schwertmann et al., 1999). The rate of crystalline oxide formation is slow, limited both by the conversion from amorphous Fe and by the supply of dissolved Fe(II) during weathering of mafic minerals. As the degree of crystallization increases with pedogenetic time (Cudennec and Lecerf, 2006), crystalline oxides could inherit a dissolved $^{10}\text{Be}/^9\text{Be}$ signal from the time of formation of the amorphous oxides and thus preserve the memory of a previous pedogenetic stage. In addition to the time of oxide formation, it may further matter where in the profile the crystalline oxides are formed. $(^{10}\text{Be}/^9\text{Be})_{\text{reac}}$ at deeper depths of a soil profile is expected to be lower and crystalline oxides formed at these depths will preserve ratios from variable depths during movement towards the surface as the soil is being eroded.

The prevailing soil type in Lysina is podzol where unstable amorphous iron oxides are formed (Regelink et al., 2015; Regelink et al., 2011). In this catchment the isotope ratio of beryllium between the dissolved and the amorphous phase is equilibrated. In the mafic catchment Na Zeleném crystalline oxides are formed that have been in regular exchange with Fe^{2+} -bearing solutions over long time scales and thus likely carry an inherited long-term reactive $^{10}\text{Be}/^9\text{Be}$ ration. In Pluhův Bor stagnosols occur that are characterized by temporary waterlogging. The soils at Pluhův Bor exhibit the highest content in clays like smectites that are characterized by recurring swelling leading to soils with low

permeability (Krám et al., 2012). In these soils reduction takes place and oxides are dissolved at their edges. These processes could be one probable explanation for the variability in dissolved $^{10}\text{Be}/^9\text{Be}$ ratios being highest at Pluhův Bor.

2.6.5 Partition coefficient of beryllium

Knowing the reactive and the dissolved beryllium concentration I am able to calculate K_d -values (see Equation 1.11) that are however based on the assumption that the reactive phase is in chemical equilibrium with the stream water regarding beryllium. As in the catchments studied here the dissolved phase is preferentially exchanging with the amorphous oxide phase (see Section 2.6.4), I calculated K_d values by means of $[\text{Be}]_{\text{am-ox}}$. The lowest K_d value for ^{10}Be with $1.3 \times 10^3 \text{ l kg}^{-1}$ is found in the Lysina catchment that exhibits the lowest pH value (see Figure 2.17 and Table 2.11). The ^{10}Be K_d values for the other catchments are $6.1 \times 10^4 \text{ l kg}^{-1}$ at Na Zeleném and $2.7 \times 10^4 \text{ l kg}^{-1}$ at Pluhův Bor, respectively. I can compare these measured K_d values to experimental data obtained under controlled laboratory conditions for river sediment and specific clay mineral phases (You et al. (1989); see Figure 2.17).

Table 2.11: K_d values for ^{10}Be and ^9Be (in l kg^{-1})

Catchment	pH value	K_d value (^{10}Be) - measured ¹ - (l kg^{-1})	K_d value (^9Be) - measured ¹ - (l kg^{-1})	K_d value - linear trend ² - (l kg^{-1})
Lysina	4.2	$1.3 \times 10^3 \pm 7.0 \times 10^1$	$1.2 \times 10^3 \pm 1.1 \times 10^2$	2.1×10^3
	5.5 (simulated) ³	-	-	1.5×10^4
Na Zeleném	6.9	$6.1 \times 10^4 \pm 5.1 \times 10^3$	$9.2 \times 10^4 \pm 8.5 \times 10^3$	1.2×10^5
Pluhův Bor	7.6	$2.7 \times 10^4 \pm 1.4 \times 10^3$	$3.0 \times 10^4 \pm 2.8 \times 10^3$	3.4×10^5

¹ K_d value calculated with measured values ((amorphous oxide-bound Be/g sediment)/(dissolved Be/ml water)).

² K_d value calculated from equation ($y = 0.65x + 0.59$) given in Figure 2.17.

³ Simulated, pre-industrial pH value of 5.5 from Hruška and Kram (2003)

I assume that reactive beryllium concentrations are established over pedogenetic time scales, whereas dissolved beryllium is affected on the short-term by stream water pH values that were lowered for a few decades in the last century. In the case of the acidic Lysina catchment that reveals a present-day pH value that is still too low compared to pre-industrial conditions and is not reflecting the long-term conditions in the catchment, I used a simulated pre-industrial pH value of 5.5 (Hruška and Kram, 2003) to calculate an empirical K_d value from the equation given in Figure 2.17 (linear fit plotted through the laboratory data from You et al. (1989), $R^2 = 0.93$; see Table 2.11). To be consistent, I also calculated theoretical values for the other two catchments and used these for calculation of the erosion and denudation rates.

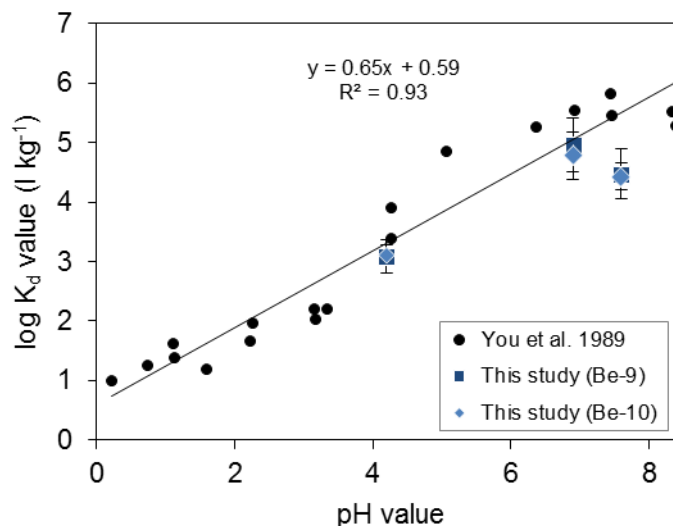


Figure 2.17: K_d values for ^{10}Be and ^9Be ((amorphous oxide-bound Be/g sediment)/(dissolved Be/ml water)) as a function of the pH value. Blue symbols show the calculated K_d values from this study (LYS pH = 4.2, NAZ pH = 6.9, and PLB pH = 7.6). Black dots are K_d values published in You et al. (1989), which are used for a linear trend line that is providing an empirical estimate of K_d for a given pH value.

2.7 Testing of steady state assumption for the studied catchments

2.7.1 Balance of meteoric ^{10}Be input and output fluxes

The studied catchments were affected by acidic precipitation in the second half of the 20th century. In contrast to the mafic and ultramafic catchments which were able to buffer the acid rain efficiently and to neutralize the acidic input, the felsic Lysina catchment exhibits a relatively low pH value and a negative acid-neutralization capacity. At Lysina, where the stream water pH dropped to about 3.9 (Hruška and Kram, 2003) due to the anthropogenic acidic input and where the soil water pH is acidic, it can be assumed that high amounts of beryllium were leached from adsorption sites and were delivered out of the system via runoff. It is likely that the system after its disturbance through the anthropogenic acidification has still not achieved a new steady state. The pH of the stream water and the beryllium concentration still seem to adapt to pre-anthropogenic conditions (see Figure 2.18). While the pH and the alkalinity in the surface waters is increasing (only slight but statistically significant increase ($p < 0.05$, seasonal Mann-Kendall test (Krám et al., 2012))), the dissolved beryllium concentration decreases. As dissolved beryllium shows near-chemostatic behaviour in Lysina (see Section 2.6.3), this implies that the observed decreasing trend in the beryllium concentration with time (see Figure 2.18) is an effect of the decreasing acidification in this catchment.

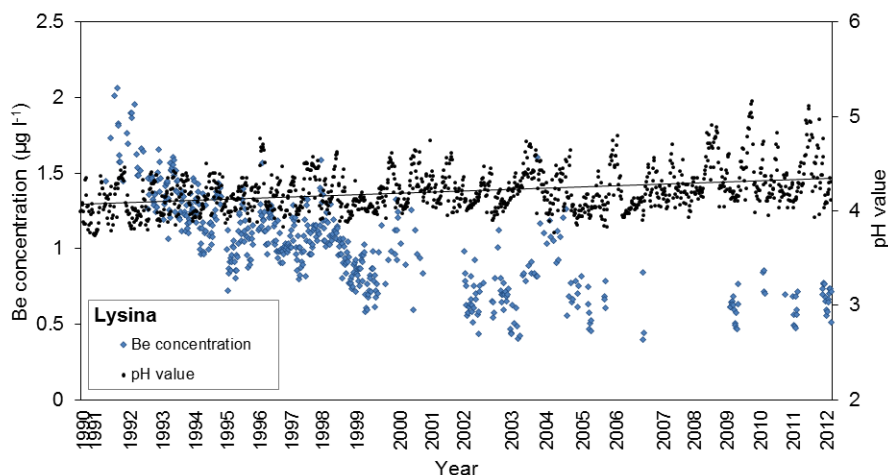


Figure 2.18: Beryllium concentration ($\mu\text{g l}^{-1}$, blue diamonds) and pH values (black dots with trend line) of the last 20 years measured in the stream water of the Lysina catchment. Stream water data were provided by P. Kram, Czech Geological Survey, Prague.

A first test whether steady state with respect to nuclide fluxes has been attained is to assess the balance of the atmospheric meteoric ^{10}Be deposited at the surface area of a catchment ($J_{\text{atm}}^{10\text{Be}}$) and the dissolved plus reactive meteoric ^{10}Be flux exported in the dissolved and particulate form, respectively, via streams ($J_{\text{stream}}^{10\text{Be}}$). For the studied catchments an averaged depositional flux $F_{\text{met}}^{10\text{Be}}$ of $1.46 \times 10^6 \text{ atoms cm}^{-2} \text{ y}^{-1}$ is assumed for all calculations (see Section 1.1.2). $J_{\text{atm}}^{10\text{Be}}$ is calculated using Equation 1.1 and the calculation of $J_{\text{stream}}^{10\text{Be}}$ is done by using Equation 1.2 (see Table 2.12). Note that $J_{\text{stream}}^{10\text{Be}}$ can be biased as the reactive ^{10}Be flux ($J_{\text{reac}}^{10\text{Be}}$) is calculated inferring a sediment flux from the *in situ* ^{10}Be -derived denudation rates. However, such $D_{\text{in situ}}$ is a measure of both weathering and erosion. I subtracted the weathering flux by assuming it is half of the total denudation ($E = D_{\text{in situ}} * \text{CDF}$). This estimate is justified as the chemical depletion factor (CDF) is 0.5 in most supply-limited weathering zones (Dixon and von Blanckenburg, 2012).

Table 2.12: ^{10}Be mass balance fluxes

Catchment	$J_{\text{atm}}^{10\text{Be}}$ ¹ ($10^{15} \text{ atoms y}^{-1}$)	$J_{\text{diss}}^{10\text{Be}}$ ² ($10^{15} \text{ atoms y}^{-1}$)	$J_{\text{reac}}^{10\text{Be}}$ ^{2, 3} ($10^{15} \text{ atoms y}^{-1}$)	$J_{\text{stream}}^{10\text{Be}}$ ⁴ ($10^{15} \text{ atoms y}^{-1}$)
Lysina	3.94 ± 0.05	13.8 ± 2.0	2.79 ± 0.63	16.5 ± 2.1
Na Zeleném	8.02 ± 0.09	1.9 ± 1.4	11.1 ± 2.5	12.9 ± 2.9
Pluhův Bor	3.21 ± 0.04	1.18 ± 0.99	2.18 ± 0.50	3.37 ± 1.11

¹ Depositional ^{10}Be flux to the surface area of each catchment calculated with Equation 1.1.

Given is a 10% uncertainty (see Section 1.1.2).

² Dissolved and particulate flux calculated with Equation 1.3.

³ Reactive ^{10}Be flux calculated using a sediment load derived from the *in situ* ^{10}Be denudation rate and a CDF of 0.5.

⁴ Total exported ^{10}Be flux calculated with Equation 1.2.

At Lysina steady state between depositional and exported ^{10}Be fluxes is not given, shown by $J_{\text{stream}}^{10}\text{Be}$ that is about four times higher than $J_{\text{atm}}^{10}\text{Be}$ (see Table 2.12 and Figure 2.19). This imbalance is mainly ascribed to a present-day $J_{\text{diss}}^{10}\text{Be}$ that is three to four times $J_{\text{atm}}^{10}\text{Be}$. For the (ultra-)mafic catchments Na Zeleném and Pluhův Bor, however, $J_{\text{stream}}^{10}\text{Be}$ is within a factor of less than two to $J_{\text{atm}}^{10}\text{Be}$. Based on the uncertainties of the method, I consider Na Zeleném and Pluhův Bor to be in steady state regarding their ^{10}Be fluxes as at steady state $J_{\text{stream}}^{10}\text{Be} / J_{\text{atm}}^{10}\text{Be} = 1$.

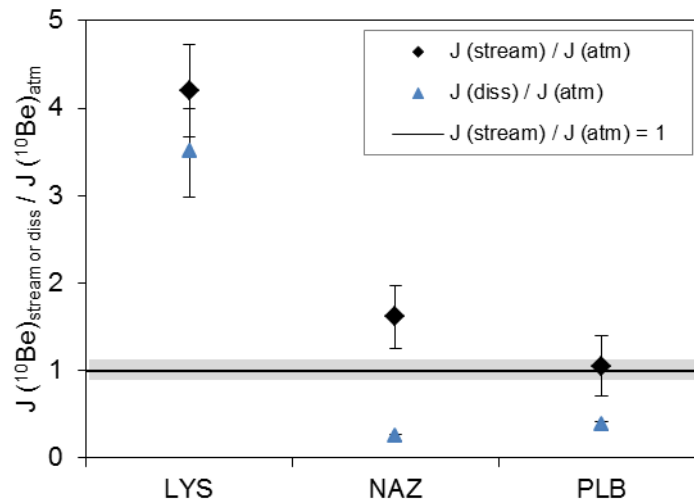


Figure 2.19: Flux ratio of ^{10}Be that enters the catchment via atmospheric deposition ($J_{\text{atm}}^{10}\text{Be}$) and ^{10}Be exported from the catchment ($J_{\text{stream}}^{10}\text{Be}$) either in the dissolved form ($J_{\text{diss}}^{10}\text{Be}$) only or in the dissolved plus reactive form ($J_{\text{stream}}^{10}\text{Be}$). Shown are $J_{\text{stream}}^{10}\text{Be} / J_{\text{atm}}^{10}\text{Be}$ (black diamonds) and $J_{\text{diss}}^{10}\text{Be} / J_{\text{atm}}^{10}\text{Be}$ (blue triangles). The reactive ^{10}Be flux is calculated inferring a sediment flux from the *in situ* ^{10}Be -derived denudation rates and assuming a CDF of 0.5. The black line displays a flux ratio of 1 that represents steady state. The gray bar represents an uncertainty of 10% on the depositional ^{10}Be flux (see Section 1.1.2). The error bars include the uncertainty of the ^{10}Be concentration measurement (AMS), the uncertainty on the calculated *in situ* denudation rates, and a 20% uncertainty on the assessed sediment flux.

The flux balance shows that at Lysina ^{10}Be is exported by far in excess of its atmospheric deposition. The question is whether this present-day excess loss of ^{10}Be has already affected the reactive ^{10}Be pool of this catchment in the long-term and thus compromises the use of reactive ^{10}Be to derive erosion and denudation rates. The inventory of reactive ^{10}Be in a soil column can be calculated by the following equation (Willenbring and von Blanckenburg, 2010b):

$$I_{10\text{Be}} = \int_{z=0}^z [^{10}\text{Be}]_{\text{reac}} * \rho * dz \quad \text{Equation 2.2}$$

where I is the inventory of reactive ^{10}Be (atoms cm^{-2}), $[^{10}\text{Be}]_{\text{reac}}$ the concentration (atoms g^{-1}), ρ the soil density (g cm^{-3}), and dz the soil depth (cm). An inventory can be calculated from $[^{10}\text{Be}]_{\text{reac}}$ measured on the depth profile from the Lysina core (see Section 2.4.2). The uppermost sample measured in this ^{10}Be depth profile was sampled at a depth of about 60 cm. To have an estimate of the ^{10}Be concentration at the surface of the profile, I use the concentration that is measured in bedload sediment at the outflow of the catchment (1.9×10^8 atoms g^{-1} ; see Section 2.4.1) that should represent the ^{10}Be concentration in the uppermost centimetres of the soils that are eroded. However, this concentration was measured on fine-grained sediment ($< 63 \mu\text{m}$) and is consequently not representative for bulk sediment. For that reason, I additionally calculated a weighted “bulk” ^{10}Be concentration that was derived by weighing $(^{10}\text{Be})_{\text{reac}}$ in the single grain size fractions (see Appendix A.2.4). This “bulk” surface concentration is estimated to be about 6×10^7 atoms g^{-1} . Both, (1) the measured ^{10}Be concentration ($< 63 \mu\text{m}$) and (2) the estimated “bulk” concentration, were used to quantify a ^{10}Be inventory at Lysina (see Appendix A.2.8). The inventory was calculated with a density assumed to be 1.8 g cm^{-3} in the regolith and 1.5 g cm^{-3} in the upper most 30 cm of the soil where a higher content of organic material leads to a lower soil density. The total ^{10}Be inventory, which is calculated over a total regolith depth of 3.4 m, ranges between (1) 4.2×10^{10} atoms cm^{-2} for the measured ^{10}Be concentration and (2) 3.6×10^{10} atoms cm^{-2} for a “bulk” ^{10}Be surface concentration, respectively.

To assess how much ^{10}Be is mobilized from this reactive ^{10}Be pool, I estimated the “inventory” of ^{10}Be (in atoms cm^{-2}) that is lost accumulated over the last 23 years (since beginning of catchment observation in 1990 to 2013). Because $[^{10}\text{Be}]_{\text{diss}}$ measurements cover only a short period of time, I used the average $^{10}\text{Be}/^9\text{Be}$ ratio of dissolved beryllium (18.4×10^{-10}) measured in this study (this ratio should be independent of any pH variations with time) and $[^9\text{Be}]_{\text{diss}}$ (measured over a time span of 23 years) provided by *P. Kram, Czech Geological Survey, Prague*, to calculate respective $[^{10}\text{Be}]_{\text{diss}}$ for the last decades:

$$[^{10}\text{Be}]_{\text{diss}} = \left(\frac{^{10}\text{Be}}{^9\text{Be}} \right)_{\text{diss}} * [^9\text{Be}]_{\text{diss}} \quad \text{Equation 2.3}$$

Using these $[^{10}\text{Be}]_{\text{diss}}$ and the available discharge data set from the *Czech Geological Survey*, I estimated a catchment-wide annual dissolved ^{10}Be flux that is exported in stream water ($F_{\text{diss}}^{^{10}\text{Be}}$ in atoms $\text{cm}^{-2} \text{ y}^{-1}$):

$$F_{\text{diss}}^{^{10}\text{Be}} = q * [^{10}\text{Be}]_{\text{diss}} \quad \text{Equation 2.4}$$

Adding these $F_{\text{diss}}^{10\text{Be}}$ up over the monitored 23 years yields a “lost inventory” of about 7×10^7 atoms cm^{-2} , which is $< 1\%$ of the total reactive pool. However, this estimate is assumed to be only a minimum loss as an distinct decrease in stream water pH is predicted already for the 1960s by the MAGIC model (Model of Acidification of Groundwater in Catchments; Hruška and Kram (2003). This model is a physically based lumped parameter dynamic model that reconstructs past and predict future catchment wide stream and soil water chemistry (Cosby et al., 2001; Cosby et al., 1985). Low stream water pH values are accompanied by high stream water base cation concentrations (see Figure 2.20). The lowest simulated pH value of 3.9 would lead to a K_d value that is by a factor of about ten lower than the pre-industrial value. Thus, I assessed a second, maximum estimate assuming a ten times elevated $F_{\text{diss}}^{10\text{Be}}$ over a period of 50 years, which results in a loss of ^{10}Be that is about 1×10^9 atoms cm^{-2} over this period. Even this amount is only max 4% of the total reactive ^{10}Be inventory. Taking the overall uncertainties of the applied methods into account, I can proceed with the assumption that the long-term reactive pool is not markedly affected by the relative short term anthropogenic acidification. The measured $[^{10}\text{Be}]_{\text{reac}}$ represents most likely a long-term state of denudational processes in the catchment.

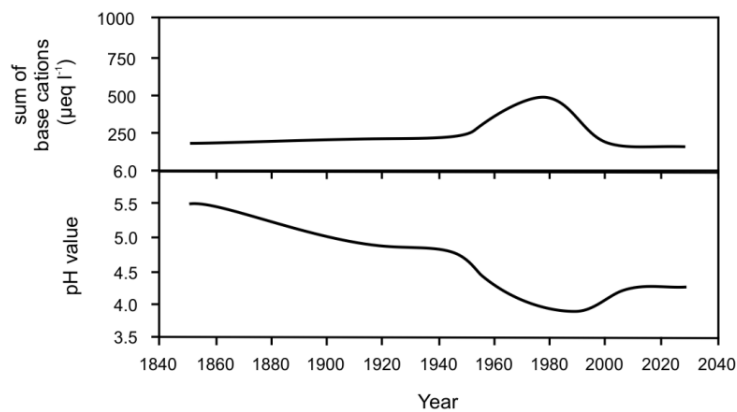


Figure 2.20: Simulated changes in stream water chemistry and pH value at Lysina (1851 – 2030) from Hruška and Kram (2003) who applied the MAGIC model. The minimum pH value is achieved around 1990; at this time instrumental observation of the catchment started. The sum of base cations includes Ca, Mg, K, and Na. Figure from Hruška and Kram (2003).

2.7.2 Fraction of ^9Be weathered and ^9Be fluxes

The fraction of ^9Be that is mobilized from primary minerals during weathering and that is now present in the dissolved or reactive fraction is expressed by $f_{\text{reac}}^{9\text{Be}} + f_{\text{diss}}^{9\text{Be}}$ (see Section 1.2.1). This non-dimensional fraction is proportional to the degree of beryllium weathering from primary minerals.

There are two different approaches to calculate this beryllium weathering degree: (1) Measuring the single concentrations of $(^9\text{Be})_{\text{reac}}$ and $(^9\text{Be})_{\text{min}}$ on sediment and calculate the fraction using Equation 1.8 - $\left(f_{\text{reac}}^{^9\text{Be}} + f_{\text{diss}}^{^9\text{Be}}\right)_{\text{min/reac}}$. (2) Estimating the sedimentary ^9Be fluxes and dissolved fluxes of ^9Be in the river following Equation 1.9 and Equation 1.10 - $\left(f_{\text{reac}}^{^9\text{Be}} + f_{\text{diss}}^{^9\text{Be}}\right)_{\text{fluxes}}$. For the second approach knowledge of the sediment and dissolved loads is required. In the studied catchments only the dissolved load is measured directly. To obtain an independent estimate, I calculated sediment loads from the *in situ* ^{10}Be -derived denudation rates and a CDF of 0.5. The different estimates of $(f_{\text{reac}}^{^9\text{Be}} + f_{\text{diss}}^{^9\text{Be}})$ are given in Table 2.13.

Table 2.13: Degree of ^9Be that is released by weathering $(f_{\text{reac}}^{^9\text{Be}} + f_{\text{diss}}^{^9\text{Be}})$

Catchment	$(f(^9\text{Be})_{\text{reac}} + f(^9\text{Be})_{\text{diss}})_{\text{min/reac}}^{1, 2}$	Estimating sediment load with $D_{\text{in situ}}^{3, 4}$			
		$f(^9\text{Be})_{\text{diss}}$	$f(^9\text{Be})_{\text{reac}}$	$f(^9\text{Be})_{\text{min}}$	$(f(^9\text{Be})_{\text{reac}} + f(^9\text{Be})_{\text{diss}})_{\text{fluxes}}$
Lysina	0.264 ± 0.014	0.571 ± 0.045	0.113 ± 0.013	0.316 ± 0.017	0.68 ± 0.14
Na Zeleném	0.616 ± 0.032	0.029 ± 0.002	0.607 ± 0.075	0.364 ± 0.019	0.64 ± 0.14
Pluhův Bor	0.538 ± 0.028	0.130 ± 0.010	0.468 ± 0.058	0.402 ± 0.023	0.60 ± 0.13

¹ Calculated with Equation 1.8 using measured concentrations: $[^9\text{Be}]_{\text{reac}}$ and $[^9\text{Be}]_{\text{min}}$

² Given uncertainty includes uncertainties from ICP-OES concentration measurements

³ Sediment load estimated using *in situ* ^{10}Be derived denudation rates and assuming a CDF of 0.5

⁴ Uncertainty include a measurement uncertainty on the ^9Be concentrations and the uncertainty on the *in situ* ^{10}Be -derived denudation rate

For illustration, I plotted $(f_{\text{reac}}^{^9\text{Be}} + f_{\text{diss}}^{^9\text{Be}})_{\text{min/reac}}$ versus $(f_{\text{reac}}^{^9\text{Be}} + f_{\text{diss}}^{^9\text{Be}})_{\text{fluxes}}$ in Figure 2.21. For the mafic catchments Na Zeleném and Pluhův Bor both estimates are similar. They reveal ^9Be weathering degrees of about 0.62 and 0.64 at Na Zeleném and 0.54 and 0.60 at Pluhův Bor, respectively, depending on the calculation mode. However, the weathering degrees of all three catchments might be biased by the sampled grain size for both methods. As I measured fine-grained sediment having a high specific surface area to adsorb more $(^9\text{Be})_{\text{reac}}$ the estimates given here might represent an upper limit.

At Lysina $(f_{\text{reac}}^{^9\text{Be}} + f_{\text{diss}}^{^9\text{Be}})_{\text{min/reac}}$ is much lower compared to $(f_{\text{reac}}^{^9\text{Be}} + f_{\text{diss}}^{^9\text{Be}})_{\text{fluxes}}$ using dissolved and sedimentary stream fluxes (see Figure 2.21). The reason for the observed difference at Lysina is that in this acidic catchment the dissolved flux ($f_{\text{diss}}^{^9\text{Be}} = 0.55$; Table 2.13) is highly overestimated at present time. Due to the low pH at Lysina the dissolved ^9Be flux leaving the system at present-day is increased compared to long-term steady state fluxes. Thus $(f_{\text{reac}}^{^9\text{Be}} + f_{\text{diss}}^{^9\text{Be}})_{\text{min/reac}}$ yields a more realistic ^9Be weathering fraction.

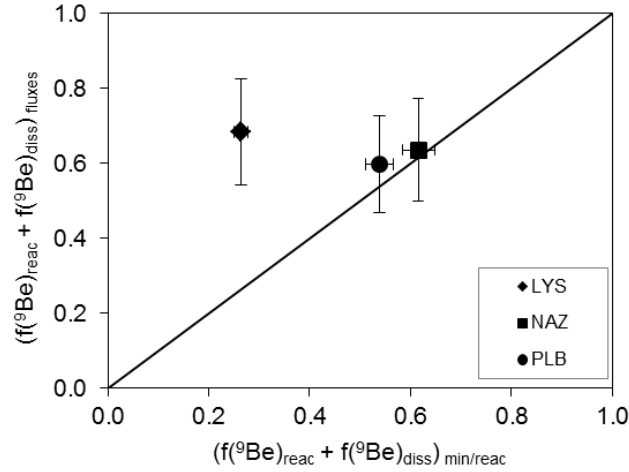


Figure 2.21: Fraction of ^9Be that is released by weathering $(f_{\text{reac}}^{^9\text{Be}} + f_{\text{diss}}^{^9\text{Be}})$. $(f_{\text{reac}}^{^9\text{Be}} + f_{\text{diss}}^{^9\text{Be}})_{\text{min/reac}}$ is derived from Equation 1.8 using measured concentrations of $[^9\text{Be}]_{\text{reac}}$ and $[^9\text{Be}]_{\text{min}}$. $(f_{\text{reac}}^{^9\text{Be}} + f_{\text{diss}}^{^9\text{Be}})_{\text{fluxes}}$ is derived using Equation 1.9 and Equation 1.10. The solid fluxes are calculated with estimating a sediment flux from the *in situ*-derived denudation rate and a CDF of 0.5. Uncertainties include the uncertainty of the concentration measurements and in case of the fluxes derived fraction the uncertainty on the *in situ* ^{10}Be -derived denudation rate D .

2.8 Weathering, erosion, and denudation rates

The $^{10}\text{Be}(\text{meteoric})/^9\text{Be}$ isotope ratio is a proxy to derive denudation rates D that comprises chemical weathering and physical erosion. In contrast, the meteoric ^{10}Be concentration only exclusively provides an erosion rate E . The “traditional” cosmogenic nuclide method to derive a denudation rate is using *in situ*-produced ^{10}Be in quartz. These cosmogenic nuclide approaches commonly integrate over time scales of 10^3 to 10^5 years. In this section, I will present meteoric ^{10}Be derived erosion rates and denudation rates derived from $^{10}\text{Be}(\text{meteoric})/^9\text{Be}$. To assess the reliability of the meteoric denudation rates, I interpret them in the context of the *in situ* ^{10}Be -derived denudation rates and independently derived chemical weathering rates. I used a short-term integrating method to derive chemical weathering rates from dissolved loads measured by gauging stations in streams (data were provided by *P. Kram, Czech Geological Survey*). Measuring total dissolved solids (TDS) in stream water provides information about the chemical weathering rate W ($\text{TDS} = W$). In the catchments studied here only these TDS data were obtained. If additionally available, the concentration of total suspended sediment (TSS) can be used to derive the sediment yield of a catchment that corresponds to an erosion rate E ($\text{TSS} = E$). The sum of both, TDS and TSS, represent the total mass loss and equals a denudation rate D ($\text{TDS} + \text{TSS} = D$).

2.8.1 Erosion rates from meteoric ^{10}Be _{reac}

Erosion rates were calculated using Equation 1.12 (see Section 1.2.3). The depositional flux of ^{10}Be is $1.46 \times 10^6 \text{ atoms cm}^{-2} \text{ y}^{-1}$; an uncertainty of 10% was assigned (see Section 1.1.2). I determined ^{10}Be _{reac} on the fine-grained sediment fraction (see Section 2.4.1) and I applied different K_d values in Equation 1.12 (for values see Table 2.11).

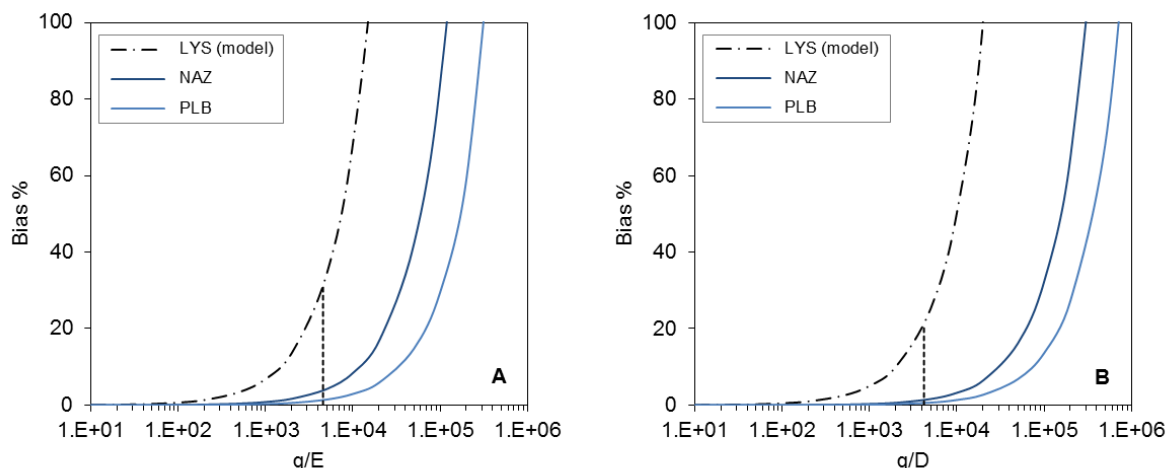


Figure 2.22: **A:** Bias (in %) on E calculated with the simplified Equation 1.13 that is ignoring the loss of ^{10}Be into solution (von Blanckenburg et al., 2012). The bias depends on the K_d value, the water runoff q , and the erosion rate itself. Plotted are the K_d values read from the linear trend in Figure 2.17 (1.2×10^5 for NAZ and 3.4×10^5 for PLB; solid curves). In the case of the acidic catchment LYS, the empirical K_d value is derived from a modelled pre-industrial pH value of 5.5 (1.5×10^4 ; intermittent curve). **B:** Bias (in %) on D calculated with the simplified Equation 1.16. The bias depends on $f\text{Be}_{\min}$ (and hence the weathering degree), the water runoff q , and the denudation rate itself. Curves are derived with the same K_d values as in A. $f\text{Be}_{\min}$ included in the calculation of the curves is 0.74 for LYS, 0.38 for NAZ, and 0.46 for PLB. The dotted vertical line represents the values for q/E and q/D , respectively, in the LYS catchment from which the bias can be read.

A prerequisite to calculate an erosion or denudation rate from the framework described in Section 1.2 (von Blanckenburg et al., 2012) is to know a valid steady state K_d value such that in naturally acidic environments one can correct for the loss of dissolved beryllium due to a low K_d value using the full Equation 1.12 or Equation 1.15. The biased induced by using the simplified Equation 1.13 and Equation 1.16 is shown in Figure 2.22. In the case of the acidic Lysina catchment that had already a naturally low pH before the European industrialization it is important to correct for the ^{10}Be that was exported from the system in the dissolved form. The low present-day K_d value at Lysina represents the period of acidification such that this value cannot be used to correct erosion or denudation rates based on long-term estimates of $[\text{Be}]_{\text{reac}}$. Hence I used the measured reactive concentrations of ^{10}Be and ^9Be but a pre-anthropogenic K_d value to correct E and D. Hruška and Kram (2003) simulated a pre-industrial stream water pH of 5.5 for the Lysina catchment applying the MAGIC model. This pH value is used for calculation of the erosion and denudation rate by reading a K_d value of

$1.5 \times 10^4 \text{ t km}^{-2} \text{ y}^{-1}$ from Figure 2.17 (see Section 2.6.5). In contrast, the mafic catchments are capable of buffering the acidic input. The MAGIC model shows for Pluhův Bor that the stream water pH at no period was below 6.8 (Hruška and Kram, 2003), meaning that the K_d value was always about 10^5 and only small quantities of beryllium were desorbed and transported in the dissolved form. However, to be consistent, I also calculated K_d values from the equation given in Figure 2.17 for Na Zeleném and Pluhův Bor (see Table 2.11) that were used to calculate K_d -corrected erosion and denudation rates.

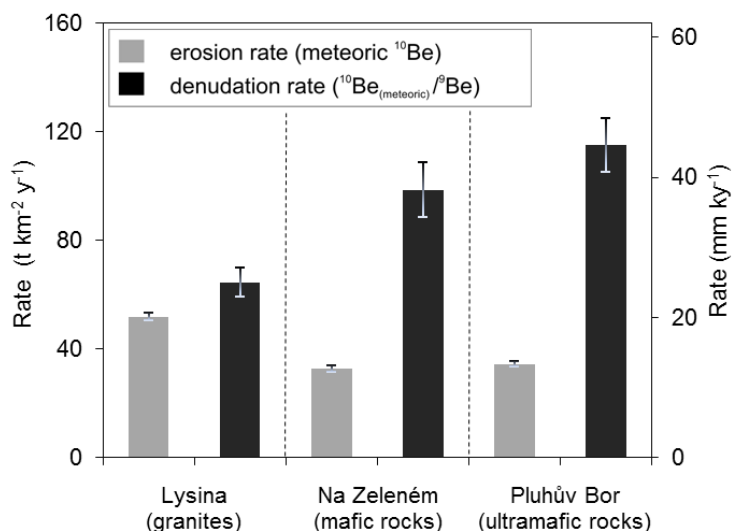


Figure 2.23: Erosion rates (in $\text{t km}^{-2} \text{ y}^{-1}$ and mm ky^{-1}) calculated from Equation 1.12 and denudation rates calculated from Equation 1.15 using empirical “linear” K_d values calculated from the equation given in Figure 2.17 (see also Table 2.11). For conversion of units ($\text{t km}^{-2} \text{ y}^{-1}$ to mm ky^{-1}), a density of 2.6 g cm^{-3} was used. The error bars include only an internal ^{10}Be AMS analytical uncertainty in the case of the erosion rates. In the case of the denudation rates, the analytical uncertainties from the ICP-OES and AMS concentration measurements are included. An uncertainty on $[^9\text{Be}]_{\text{parent}}$ (5.5 ppm for LYS, 1.2 ppm for NAZ, and 0.18 ppm for PLB) is not propagated because it cannot be assessed reliably.

The granitic Lysina catchment erodes at a rate of $52 \pm 5 \text{ t km}^{-2} \text{ y}^{-1}$ (see Table 2.14 and Figure 2.23). The erosion rates derived for the (ultra-)mafic catchments are similar, being $33 \pm 4 \text{ t km}^{-2} \text{ y}^{-1}$ at Na Zeleném and $35 \pm 4 \text{ t km}^{-2} \text{ y}^{-1}$ at Pluhův Bor, respectively. These erosion rates were calculated by means of the meteoric ^{10}Be concentration that is dependent on the sampled grain size. Here I measured these concentrations on fine-grained bedload sediment. This grain size may or may not be representative of the bulk of the eroded material such that these erosion rates could potentially be over- or underestimating the actual erosion rate. Nonetheless, the erosion rates are in the range of sediment yields observed in moderately eroding mountain upland areas and continental parts of Europe (Vanmaercke et al., 2011). These estimates are from river gauging stations (TSS) or are reservoir siltation rates and have thus much shorter integration time scales. Sediment yield estimates for catchments in the Czech Republic range from $7 - 30 \text{ t km}^{-2} \text{ y}^{-1}$ (Vanmaercke et al., 2010).

Table 2.14: Erosion rates (in $\text{t km}^{-2} \text{y}^{-1}$ and mm ky^{-1})

	Lysina		Na Zeleném		Pluhův Bor	
Depositional ^{10}Be flux ($10^6 \text{ atoms cm}^{-2} \text{y}^{-1}$)	1.46 ± 0.15		1.46 ± 0.15		1.46 ± 0.15	
$[^{10}\text{Be}]_{\text{reac}}$ ($10^6 \text{ atoms g}^{-1}$)	191.9 ± 5.4		408 ± 16		413 ± 11	
Erosion rate	$(\text{t km}^{-2} \text{y}^{-1})^4$	$(\text{mm ky}^{-1})^{4,5}$	$(\text{t km}^{-2} \text{y}^{-1})^4$	$(\text{mm ky}^{-1})^{4,5}$	$(\text{t km}^{-2} \text{y}^{-1})^4$	$(\text{mm ky}^{-1})^{4,5}$
- without correction ¹	76.0 ± 7.9	29.2 ± 3.0	35.7 ± 3.8	13.7 ± 1.5	35.3 ± 3.7	13.6 ± 1.4
- measured K_d ²	-	-	31.2 ± 3.3	12.0 ± 1.3	30.2 ± 3.1	11.6 ± 1.2
- K_d from linear trend line ³	52.3 ± 5.4	20.1 ± 2.1	33.1 ± 3.6	12.7 ± 1.4	34.8 ± 3.6	13.4 ± 1.4

¹ Calculated using the simplified Equation 1.13 (ignoring the correction term).

² Calculated using Equation 1.12 with a measured K_d value ((amorphous oxide-bound Be/g sediment)/(dissolved Be/ml water)).

³ Calculated using Equation 1.12 with an empirical K_d (from Figure 2.16, see also Table 2.11). Note that for Lysina a K_d value presumed for a modelled pre-industrial pH of 5.5 is applied.

⁴ The uncertainty (1SD) includes uncertainty of 10% on the depositional ^{10}Be flux and the uncertainty on the AMS ^{10}Be concentration measurements.

⁵ For conversion of units ($\text{t km}^{-2} \text{y}^{-1}$ to mm ky^{-1}), a density of 2.6 g cm^{-3} was used.

Table 2.15: Denudation rates (in $\text{t km}^{-2} \text{y}^{-1}$ and mm ky^{-1})

	Lysina		Na Zeleném		Pluhův Bor	
Depositional ^{10}Be flux ($10^6 \text{ atoms cm}^{-2} \text{y}^{-1}$)	1.46 ± 0.15		1.46 ± 0.15		1.46 ± 0.15	
$(^{10}\text{Be}/^9\text{Be})_{\text{reac}}$ ($\times 10^{10}$)	18.2 ± 1.0		28.6 ± 1.0		194 ± 10	
$[^9\text{Be}]_{\text{parent}}$ ($10^{16} \text{ atoms g}^{-1}$) ¹	36.7		8.1		1.20	
$[^9\text{Be}]_{\text{reac}}$ ($10^{16} \text{ atoms g}^{-1}$)	9.68 ± 0.41		13.95 ± 0.76		2.081 ± 0.089	
$[^9\text{Be}]_{\text{min}}$ ($10^{16} \text{ atoms g}^{-1}$)	27.0 ± 1.4		8.71 ± 0.45		1.786 ± 0.093	
Denudation rate	$(\text{t km}^{-2} \text{y}^{-1})^5$	$(\text{mm ky}^{-1})^{5,6}$	$(\text{t km}^{-2} \text{y}^{-1})^5$	$(\text{mm ky}^{-1})^{5,6}$	$(\text{t km}^{-2} \text{y}^{-1})^5$	$(\text{mm ky}^{-1})^{5,6}$
- without correction ²	83 ± 11	31.8 ± 4.2	102 ± 15	39.3 ± 6.0	117 ± 15	44.9 ± 5.9
- measured K_d ³	-	-	97 ± 14	37.5 ± 5.3	109 ± 14	42.0 ± 5.5
- K_d from linear trend line ⁴	65.2 ± 8.5	25.1 ± 3.3	99 ± 14	38.2 ± 5.4	116 ± 15	44.6 ± 5.8

¹ An uncertainty on $[^9\text{Be}]_{\text{parent}}$ (5.5 ppm for LYS, 1.2 ppm for NAZ, and 0.18 ppm for PLB) is not propagated because it cannot be assessed reliably.

² Calculated using the simplified Equation 1.16 (ignoring the correction term).

³ Calculated using Equation 1.15 with a measured K_d value ((amorphous oxide-bound Be/g sediment)/(dissolved Be/ml water)).

⁴ Calculated using Equation 1.15 with an empirical K_d (from Figure 2.16, see also Table 2.11). Note that for Lysina, a K_d value presumed for a modelled pre-industrial pH of 5.5 is applied.

⁵ The given uncertainty (1SD) includes a 10% uncertainty on the depositional ^{10}Be flux and the analytical uncertainty on the AMS and ICP-OES concentration measurements.

⁶ For conversion of units ($\text{t km}^{-2} \text{y}^{-1}$ to mm ky^{-1}), a density of 2.6 g cm^{-3} was used.

2.8.2 Denudation rates from $^{10}\text{Be}(\text{meteoric})/^9\text{Be}$ ratios

For calculation of the denudation rates using Equation 1.15 I used the $(^{10}\text{Be}/^9\text{Be})_{\text{reac}}$ and ^9Be concentrations determined on fine-grained sediment. The corrected denudation rate for the granitic Lysina catchment is $65 \pm 9 \text{ t km}^{-2} \text{ y}^{-1}$ and thus is the lowest one of the three studied catchments (see Figure 2.23 and Table 2.15; K_d value from linear trend). In Na Zeleném, dominated mainly by mafic rocks, the denudation rate is $99 \pm 14 \text{ t km}^{-2} \text{ y}^{-1}$. Considering Pluhův Bor, characterized by ultramafic serpentinite, the denudation rate is $116 \pm 15 \text{ t km}^{-2} \text{ y}^{-1}$.

The uncertainty reported includes the uncertainty of the depositional ^{10}Be flux and the analytical uncertainties but no uncertainty that results from the high heterogeneity of the parent bedrock material is propagated as this cannot be assessed reliably. However, the denudation rate is inversely proportional to the beryllium concentration of the parent bedrock. For example, in the case of the granitic Lysina catchment I used a beryllium concentration of 5.5 ppm that is measured on bedload sediment and that most likely equals the average bedrock concentration (see Figure 2.8). Should this value be overestimated because this high beryllium concentration was an artefact of incongruent weathering I would underestimate the denudation rate. For comparison, calculating a denudation rate with the median beryllium concentration of 3.5 ppm for Lysina results in a rate of about $111 \pm 14 \text{ t km}^{-2} \text{ y}^{-1}$.

Different depths of penetration of meteoric ^{10}Be lead to different integration time scales for this cosmogenic method. I cannot define the exact residence time of meteoric ^{10}Be as I did not determine the depth of ^{10}Be percolation or the total inventory of ^{10}Be in the soil column for all catchments. Still, I assess a residence time assuming beryllium adsorption over the whole soil depth (LYS: 150 cm; NAZ: 90 cm; PLB: 120 cm; *pers. comm. P. Kram*) that is supported by ^{10}Be concentration measurements in the core at Lysina. The residence time τ (in ky) is the ratio of the adsorption depth of ^{10}Be (z , in mm) divided by the denudation rate D (mm ky^{-1}):

$$\tau = \frac{z}{D} \quad \text{Equation 2.5}$$

The estimated residence time is about 60 ky for Lysina, 24 ky for Na Zeleném, and 27 ky for Pluhův Bor. Radioactive decay of ^{10}Be can be neglected as the half-life of ^{10}Be is long compared to its residence time in the weathering zone (Willenbring and von Blanckenburg, 2010b).

2.8.3 Independent chemical weathering rates from gauging data

In addition to the longer-term erosion and denudation rates from cosmogenic nuclides, I calculated short-term chemical weathering fluxes from gauging data (Table 2.16). I used silicate-derived total dissolved solids (TDS_{sil}) and discharge data measured in all three catchments over a monitoring period of about 20 years for Lysina and Pluhův Bor, respectively, and ten years for Na Zeleném (dissolved stream water and precipitation data are provided by *P. Kram, Czech Geological Survey, Prague*). These cation concentrations were corrected for atmospheric input with chlorine ratios (Galy and France-Lanord, 1999) using the precipitation record of the Lysina catchment. The chemical weathering fluxes are calculated by the sum of cations ($\text{Mg} + \text{Ca} + \text{K} + \text{Na}$) plus dissolved SiO_2 times water discharge. In order to obtain a weathering flux in $\text{t km}^{-2} \text{ y}^{-1}$, I divided by catchment area. Unfortunately, suspended material is not routinely sampled and thus no total suspended solid (TSS) estimates can be provided. The chemical weathering rate in the granitic catchment Lysina is about $6 \text{ t km}^{-2} \text{ y}^{-1}$. In Na Zeleném, dominated by mafic rocks, the chemical weathering rate is ca. $8 \text{ t km}^{-2} \text{ y}^{-1}$. The rate determined from the solute flux in Pluhův Bor, characterized by ultramafic rocks, appears to be the highest one of all three studied catchments with about $10 \text{ t km}^{-2} \text{ y}^{-1}$.

The major base cation concentrations ($\text{Na} + \text{K} + \text{Ca} + \text{Mg}$) measured in stream water can further be interpreted in the framework of the MAGIC model. As chemical weathering is one important parameter driving changes in stream water chemistry, Krám et al. (2012) modelled weathering rates (Table 2.16) for the studied catchments that however exclude the SiO_2 component. Thus, these estimates are lower than the rates calculated here.

For comparison, Paces (1986) published chemical weathering rates of 4 to $6 \text{ t km}^{-2} \text{ y}^{-1}$ for small forested upland catchments that are underlain by gneiss in the Bohemian massif. Overall low chemical weathering rates are supported by data published by Probst et al. (1990) and Viville et al. (2012) who evaluated dissolved fluxes in a declining spruce stand within a small granitic catchment in the Vosges Massif, France (atmosphere-corrected weathering flux of $2 \text{ t km}^{-2} \text{ y}^{-1}$). Oliva et al. (2003) and Schaller et al. (2001) obtained chemical weathering rates for small granitic catchments in Europe that range from 3 to $9 \text{ t km}^{-2} \text{ y}^{-1}$ and 6 to $10 \text{ t km}^{-2} \text{ y}^{-1}$, respectively. I assume that the relatively higher weathering rate at Pluhův Bor is due to the underlying ultramafic bedrock. Similarly high dissolved chemical fluxes were found for ultramafic and metamorphic rocks in catchments in French Guiana (about $12 \text{ t km}^{-2} \text{ y}^{-1}$, Freyssinet and Farah (2000)). Cleaves et al. (1974) who studied small watersheds in the U.S. underlain by serpentinite determined serpentinite chemical weathering rates of $6 \text{ t km}^{-2} \text{ y}^{-1}$. Meybeck (1987) found chemical weathering rates determined from river dissolved loads to be up to five times higher in serpentinite and amphibolite compared to granite. Accordingly, the chemical weathering flux at Lysina is the lowest and the serpentinite dominated catchment exhibits the highest weathering rate.

Table 2.16: Different estimates for chemical weathering rates in the studied catchments.

Catchment	Monitoring period	Chemical weathering rate (this study) ^{1,2} (t km ⁻² y ⁻¹)	Chemical weathering rate (from Kram 2012) ³ (t km ⁻² y ⁻¹)
Lysina	1989 - 2011	6.3 ± 2.0	1.3
Na Zeleném	2001 - 2011	7.8 ± 3.1	3.4
Pluhův Bor	1991 - 2011	10.3 ± 4.8	3.0

¹ Calculated in this study from TDS (Mg, Ca, K, Na, plus SiO₂) plus discharge; gauging data are provided by P. Kram, Czech Geological Survey, Prague

² Yearly average with 1SD uncertainty

³ From Krám et al. (2012); derived from the MAGIC model application (Mg, Ca, K, Na)

Higher weathering in the mafic and ultramafic catchment compared to the granitic catchment is also confirmed when considering the degree of beryllium that is released during weathering processes ($(f_{\text{reac}}^{9\text{Be}} + f_{\text{diss}}^{9\text{Be}})$; see Section 2.7.2). However, this value is a weathering degree for Be-containing minerals only and includes, in contrast to the dissolved fluxes derived from river gauging, also beryllium that is precipitated into secondary phases.

2.8.4 Comparison of derived denudation and weathering rates

In this section, I will compare the $^{10}\text{Be}(\text{meteoric})/^{9}\text{Be}$ derived denudation rates (D_{meteo} ; see Section 2.8.2) to the *in situ* ^{10}Be -derived denudation rates ($D_{\text{in situ}}$; see Section 2.5) and the chemical weathering rates (W_{gauging} ; see Section 2.8.3). The meteoric ^{10}Be derived erosion rates (E_{meteo}) are also shown in Figure 2.24 but not further discussed as they are potentially biased by grain size effects (see Section 2.8.1). *In situ* ^{10}Be is considered to be a robust tool for measuring rates of Earth's surface processes (e.g. Granger and Schaller (2014)) and can thus be considered as a benchmark.

Comparing the denudation rates derived from the $^{10}\text{Be}(\text{meteoric})/^{9}\text{Be}$ ratio with the *in situ*-derived denudation rates (see Figure 2.24) no consistent trend is evident. In the case of the granitic Lysina catchment D_{meteo} is distinctly lower than $D_{\text{in situ}}$. At the mafic Na Zeleném catchment both rates are equal whereas at the ultramafic Pluhův Bor catchment D_{meteo} is with a factor of more than two markedly higher than $D_{\text{in situ}}$. However, $D_{\text{in situ}}$ at Pluhův Bor is potentially biased by the occurrence of quartz veins such that in that case the actual rate could be underestimated (see Section 2.5). Altogether, all cosmogenic denudation rates cover the range of *in situ*-derived denudation rates for upland catchments in Europe (e.g. Schaller et al. (2001)).

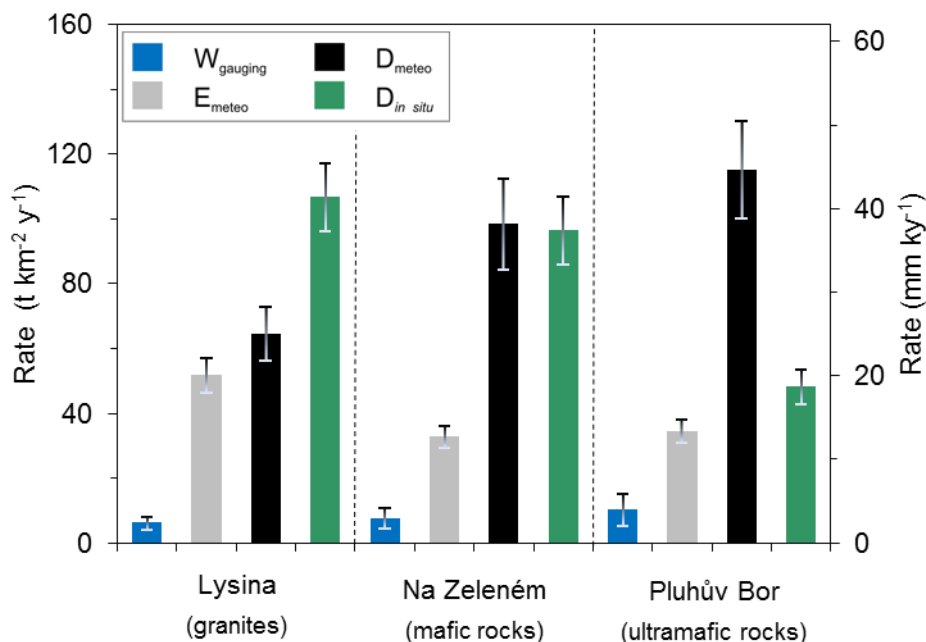


Figure 2.24: Summary of chemical weathering fluxes derived from gauging data (W_{gauging} , in blue), erosion rates calculated from meteoric ^{10}Be (E_{meteo} , in grey), denudation rates calculated from $^{10}\text{Be}(\text{meteoric})/^9\text{Be}$ ratios (D_{meteo} , in black), and *in situ* ^{10}Be -produced denudation rates ($D_{\text{in situ}}$, in green) for all three catchments in $\text{t km}^{-2} \text{ y}^{-1}$ and mm ky^{-1} . D_{meteo} are calculated with an estimated catchment-wide $[^9\text{Be}]_{\text{parent}}$ and with $[^9\text{Be}]$ measured on fine-grained sediment ($< 63\mu\text{m}$). The error bars include an analytical AMS uncertainty for the cosmogenic data, an uncertainty of 10% for the depositional flux of ^{10}Be for the meteoric rates, and an uncertainty on the production rate for $D_{\text{in situ}}$. Please note that in the case of D_{meteo} no uncertainty of the parent bedrock concentration is propagated as this cannot be reliably assessed. For W_{gauging} a 1SD uncertainty of the entire data set is shown. Note that the rates integrate over different time scales. For conversion of units ($\text{t km}^{-2} \text{ y}^{-1}$ to mm ky^{-1}), a density of 2.6 g cm^{-3} was used.

The chemical weathering rates comprise only about 5 to 10% of $D_{\text{in situ}}$ for Lysina and Na Zeleném and about 20% for Pluhův Bor, respectively. In comparison with D_{meteo} , the contribution of chemical weathering comprises only about 10% of the total denudation in all three catchments. This low contribution is surprising, at least in granitic lithologies where transport-limited weathering usually leads to a solute loss (CDF) of typically 50% (Dixon and Riebe, 2014; Dixon and von Blanckenburg, 2012; West et al., 2005). In the case of the mafic and the ultramafic catchments, a higher degree of weathering is further indicated by their high $(f_{\text{reac}}^{9\text{Be}} + f_{\text{diss}}^{9\text{Be}})$ of 0.62 at Na Zeleném and 0.54 at Pluhův Bor. For this apparent inconsistency, I offer the following explanations: (1) a methodological bias, (2) spatial heterogeneity on the small scale investigated here or (3) different integration time scales. Regarding (1) a systematic underestimation of modern river loads as stated by several authors (Kirchner et al., 2001; Schaller et al., 2001) is only valid for suspended loads and cannot be transferred to dissolved chemical weathering fluxes. Volumetrically high-magnitude events affect only the transport of suspended sediments and have only a negligible effect on the dissolved load (see Figure 2.25; Hovius and von Blanckenburg (2007)).

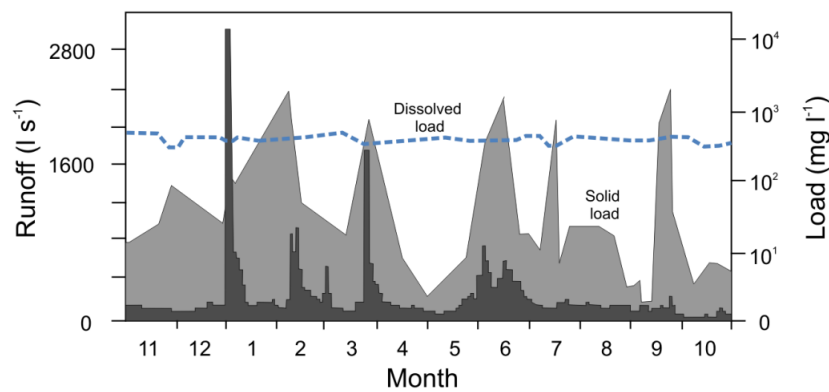


Figure 2.25: Hydrometric record showing that the concentration of dissolved material (dotted blue line) is virtually invariant with time and that there are only minor dissolution effects during high water runoff (shaded in dark grey). In contrast, the suspended sediment concentration (shaded in light grey) is highly dependent on precipitation and water runoff. Figure adapted from *Hovius and von Blanckenburg (2007)*.

Considering (2), a characteristic spatial scale has to be achieved to balance the fluxes in and out of the weathering system in order for the derived weathering and denudation rates to be representative. This spatial scale implies that through homogenization of sediment and waters all variations (laterally and vertically on the soil column and stream profile scales) are averaged out. Aside from variations in the water chemistry, episodic and spatially not-uniform erosion (e.g. linear dissection) or selective tapping of deeper sediment could occur (Schaller et al., 2001) that is not averaged out on the small scale considered in this study. This deep sediment would have both lower meteoric and lower *in situ* ^{10}Be nuclide concentrations and thus would lead to overestimations of both ^{10}Be derived denudation rates. As there is no such deep dissection from field observation, I regard this possibility as unlikely. Another aspect to consider is that in low mountain areas of central Europe Pleistocene periglacial conditions and processes, like gelifluction and cryoturbation, have led to the formation of cover beds (Semmel and Terhorst, 2010). These periglacial slope deposits are widely distributed in non-glaciated mid-latitude regions of Europe (Raab et al., 2007). The basal layer of cover beds is composed of bedrock material from surrounding slopes, followed by an intermediate and upper layer that are characterized by aeolian input (Semmel and Terhorst, 2010). Mixing processes and addition of allochthonous material due to cover bed formation potentially altered the cosmogenic nuclide record in a soil profile and thus bias the cosmogenic beryllium concentrations measured in soil and bedload sediments (Schaller et al., 2002a).

Explanation (3) suggest different integration times scales of the methods over which the rates actually change as cause for the observed chemical weathering rates being low in proportion to the cosmogenic derived denudation. Dissolved loads usually integrate over a few decades only. At Lysina and Pluhův Bor periodic sampling of dissolved fluxes started in 1991 and at Na Zeleném in 2001, yielding short-term weathering fluxes integrating over about 10 to 20 years. In contrast, the

integration time scales for the cosmogenic nuclide methods are in the order of 10^4 years. $D_{in situ}$ integrates over 14 ky for Lysina, 16 ky for Na Zeleném and 32 ky for Pluhův Bor, respectively (see Table 2.9). At Lysina and Na Zeleném these rates thus integrate over the Holocene and the transition from the late Pleistocene to Holocene. In the case of D_{meteo} I assessed integration times of 60 ky for Lysina, 24 ky for Na Zeleném, and 27 ky for Pluhův Bor, respectively (see Section 2.8.2) covering the Last Glacial Maximum (LGM) and the Holocene. At Lysina the integration time scale extend further back into the last glacial period (Weichselian glaciation). Considering the much longer integration time scales of the cosmogenic derived denudation rates, it is possible that an inherited higher denudation rate signal from the Late Pleistocene characterized by post-LGM conditions still influences the present-day measured nuclide concentrations (Granger and Schaller, 2014). In a very recent study carried out on $^{10}\text{Be}(\text{meteoric})/^{9}\text{Be}$ ratios in marine sediment records, von Blanckenburg et al. (2015) did not find any evidence for a shift in global weathering fluxes to the ocean between glacial and interglacial periods. They explained this lack of variation with minor shifts in runoff between glacials and interglacials that did not result in changes in weathering fluxes. However, on a local scale, both erosion and weathering might have been elevated during and at the termination of the LGM in upland catchments that were exposed to periglacial environmental conditions and Pleistocene permafrost like the studied catchments (Czudek, 1993). At the end of the LGM rapid chemical weathering was initiated, triggered by high physical erosion rates, and increased sediment delivery. This proposed higher sediment flux and increased chemical weathering during deglaciation (Crocket et al., 2012) could tentatively explain the observed inconsistency between the long-term denudation and the short-term weathering rates. Areas affected by permafrost have high rock to water ratios and high rock/water contact times in their active layers that lead to maximized chemical weathering (Tranter, 2003). Climate warming leads to an increase in river discharge and to permafrost thaw with a subsequent increase of the unfrozen layer thickness that in turn likely leads to an increase in dissolved elemental fluxes (Zakharova et al., 2007). Increased melt-water and wetter post-glacial conditions deliver fresh and unweathered fine-grained material that is highly reactive to chemical weathering agents. A study in Siberian streams revealed that if permafrost disappears total inorganic solutes would increase by about 60% (Frey et al., 2007).

To summarize, I suggest that it is possible that high chemical weathering fluxes at the end of the LGM prevailed in the studied area, but this signal could not have been preserved until present times given that the weathering zone is transport-limited and soluble cations had been removed before the present day. Paleo-denudation rates from terrace sediments in Middle Europe show a strong decrease from the Pleistocene to the Holocene (Schaller et al., 2002b) showing that the peak in sediment erosion and chemical weathering initiated at the end of the LGM is not sustained over long time periods. Still, the ^{10}Be concentration record is reduced due to the long lag time of the cosmogenic nuclide method (Dosseto and Schaller, 2016; von Blanckenburg, 2005; Willenbring and von Blanckenburg, 2010b).

2.9 Conclusion Slavkov Forest

In this study I explored the potential of the $^{10}\text{Be}(\text{meteoric})/^9\text{Be}$ isotope system in small headwater catchments underlain by different lithologies. $(^{10}\text{Be}/^9\text{Be})_{\text{reac}}$ and $(^{10}\text{Be}/^9\text{Be})_{\text{diss}}$ measured on fine-grained bedload sediment and in stream water, respectively, agree within a factor of two for each catchment. The dissolved phase seems to equilibrate preferably with the amorphous oxide phase, as shown by a better agreement of $(^{10}\text{Be}/^9\text{Be})_{\text{am-ox}}$ and $(^{10}\text{Be}/^9\text{Be})_{\text{diss}}$, an observation that I attribute to the nature of oxide formation. A seasonal variability is observed in $(^{10}\text{Be}/^9\text{Be})_{\text{diss}}$, reflecting most likely short-term changes in precipitation and hydrological conditions. In the Lysina catchment runoff generation can be described in detail and a beryllium depth profile was measured. $(^{10}\text{Be}/^9\text{Be})_{\text{reac}}$ decreases with increasing soil profile depth, such that $(^{10}\text{Be}/^9\text{Be})_{\text{diss}}$ in stream water is most likely governed by the depth of fluid flow paths through the different compartments of the catchment (groundwater, (sub-) surface water flow). $(^{10}\text{Be}/^9\text{Be})_{\text{reac}}$ in the uppermost soil sample of the depth profile corresponds to $(^{10}\text{Be}/^9\text{Be})_{\text{reac}}$ measured in the bedload sediment. Due to the variability in $(^{10}\text{Be}/^9\text{Be})_{\text{diss}}$, I concluded that $(^{10}\text{Be}/^9\text{Be})_{\text{reac}}$ more suitably reflects the long-term state of denudation in the catchments.

In the studied Lysina catchment, that is characterized by an ongoing effect of acid rain and where e.g. buffering of acids through weathering processes fails, a mass flux balance based on ^{10}Be concentrations shows that the dissolved fluxes of ^{10}Be are elevated compared to steady state conditions. Still, the long-term reactive pool of meteoric ^{10}Be is most likely unaffected by this temporary disturbance of the system. Nonetheless, in naturally acidic environments, erosion or denudation rates calculated with meteoric ^{10}Be or $^{10}\text{Be}/^9\text{Be}$, respectively, still have to be corrected for the loss of beryllium in the dissolved phase due to low K_d values; otherwise these rates will be overestimates.

The fraction of ^9Be that is mobilized from primary minerals through weathering can be either calculated using measured ^9Be concentrations or dissolved and particulate ^9Be fluxes. In the case of the acidic Lysina catchment the use of the second approach leads to an overestimation of this fraction due to an increased dissolved ^9Be flux induced by the acidic environmental conditions, whereas in the neutral catchments both estimates are the same.

A substantial requirement for the application of the new meteoric isotope system on the small basin scale is the exact knowledge of the parent bedrock ^9Be concentration. The type of bedrock prevailing in a catchment plays a critical role in deriving a denudation rate. The catchments studied here are highly heterogeneous regarding their lithologies and reveal high variations in beryllium concentration among the single bedrock types. Since the areal distribution of these bedrock types in each catchment and their contribution to weathering is unknown, I can only estimate an integrating bedrock

concentration for each of the catchments that is based on an element regression approach. This bedrock heterogeneity introduces an uncertainty on the validity of the determined denudation rates.

Denudation rates derived from $(^{10}\text{Be}/^9\text{Be})_{\text{reac}}$ measured on fine-grained bedload sediments are about $65 \text{ t km}^{-2} \text{ y}^{-1}$ in the granitic catchment (LYS), and $99 \text{ t km}^{-2} \text{ y}^{-1}$ (NAZ) and $116 \text{ t km}^{-2} \text{ y}^{-1}$ (PLB) in the two (ultra-)mafic catchments, respectively. Due to the presence of quartz in all three catchments, *in situ*-derived denudation rates could be determined on sand-sized bedload sediment. These $D_{\text{in situ}}$ are $108 \text{ t km}^{-2} \text{ y}^{-1}$ in Lysina, $97 \text{ t km}^{-2} \text{ y}^{-1}$ in Na Zeleném, and $49 \text{ t km}^{-2} \text{ y}^{-1}$ in Pluhův Bor, respectively. I observe an inconsistency between these cosmogenic derived denudation rates and weathering rates derived from dissolved river loads. Amongst three possible explanations for this inconsistency, being (1) a methodological bias, (2) spatial heterogeneity on the small scale investigated here or (3) different integration time scales, I favour the changes in chemical weathering and physical erosion due to environmental changes at the transition from the last glacial into the contemporary interglacial phase as explanation. Most likely, higher post-LGM weathering rates cannot be sustained up to the present day, whereas cosmogenic denudation rates integrate and average over this period, resulting in overall higher values. However, both cosmogenic derived denudation rate estimates are in the range of *in situ* ^{10}Be - derived denudation rates determined for stream catchments in middle Europe. Accordingly, the denudation rates derived from the $^{10}\text{Be}(\text{meteoric})/^9\text{Be}$ system are most likely reliable for the small catchments of the Slavkov Forest despite the uncertainties that are linked to the application of this new proxy.

These promising results indicate that the $^{10}\text{Be}(\text{meteoric})/^9\text{Be}$ system is an adequate and integrated approach that can now be applied in small scale catchments with variable lithology, provided that the bedrock ^9Be concentration can be assessed. Further, the $^{10}\text{Be}(\text{meteoric})/^9\text{Be}$ isotope ratio can be used to constrain the natural background denudation rate ($\sim 10^4$ years) in areas strongly affected by recent anthropogenic acidification. Besides a study from Gayer et al. (2008) who used cosmogenic helium to quantify basin-wide erosion rates in tholeiitic rocks in Hawaii, the $^{10}\text{Be}(\text{meteoric})/^9\text{Be}$ derived denudation rates presented here are the first ones derived from cosmogenic nuclides in catchments that were formed by (ultra)mafic bedrock. In contrast to the *in situ* ^{10}Be method, whose application is dependent on the presence of quartz minerals, only a small amount of soil or sediment ($< 1\text{g}$) is needed to quantify a meteoric ^{10}Be derived denudation rate. Hence, this method offers a large potential to study a wide range of geological settings to quantify Late Pleistocene and Holocene Earth's surface processes.

3 $^{10}\text{Be}(\text{meteoric})/^{9}\text{Be}$ isotope ratios and denudation rates measured in a small headwater catchment in the Southern Sierra Nevada, California

3.1 Introduction

Regolith covers large parts of the Earth's surface and acts as a dynamic interface between the atmosphere, the biosphere, and the lithosphere. The regolith is subdivided into a mobile and an immobile part. The immobile part, the saprolite is produced by chemical alteration and dissolution of bedrock but retains the structure of the parent rock material. The upper part of the regolith is defined as the physically mobile soil layer that is produced by physical and chemical alteration of the underlying saprolite or bedrock. While mineralogical changes and alterations occur throughout the whole saprolite column, much of the chemical loss occurs at a discrete weathering front at the bedrock-saprolite boundary (Buss et al., 2008; Fletcher et al., 2006; Lebedeva et al., 2007). Several studies suggest that saprolite weathering plays an important role in landscape evolution as it may exceed rates of soil weathering in upland landscapes (Anderson et al., 2002; Dixon et al., 2009a). In such landscapes, complications in the application of *in situ* cosmogenic nuclides arise when overlying soil shields the build-up of cosmogenic nuclides in parts of the regolith where weathering occurs. In such a case cosmogenic ^{10}Be may only record a fraction of the total denudation in deeply weathered landscapes (Dixon et al., 2009b; Riebe and Granger, 2013). $^{10}\text{Be}(\text{meteoric})/^{9}\text{Be}$ determined on stream bedload sediment and along a regolith depth profile can serve to quantify catchment-wide denudation rates and the degree of ^{9}Be weathering within a regolith (von Blanckenburg et al., 2012).

In this part of my study I used the $^{10}\text{Be}(\text{meteoric})/^{9}\text{Be}$ isotope system to explore a small headwater catchment in the Southern Sierra Nevada, California, United States, which belongs to the Southern Sierra Critical Zone Observation. I measured meteoric ^{10}Be and stable ^{9}Be concentrations along depth profiles throughout a deep regolith (0-800 cm) and a shallow soil profile (0-120 cm), respectively, and on bedload sediment and stream water sampled within the upland and soil-mantled Providence Creek catchment. Using the total $^{10}\text{Be}(\text{meteoric})/^{9}\text{Be}$ ratio determined in bedload sediment, I calculated a catchment-wide denudation rate. An erosion rate for the regolith profile was calculated from the total meteoric ^{10}Be inventory. Combining this erosion rate with the chemical depletion fraction of the soil, a local soil denudation rate can be derived.

3.2 Study Sites and Samples

The Southern Sierra Critical Zone Observatory (Southern Sierra CZO) is located SE of Shaver Lake on the western slope of the Sierra Nevada Range near the divide between the San Joaquin and Kings rivers. Within the Southern Sierra CZO, the Providence Creek catchment is situated, which is part of the Kings River Experimental Catchments (KREW). KREW is a U.S. Forest Service catchment-level, integrated ecosystem project for long-term research in headwater catchments in the Sierra National Forest. The Providence Creek catchment covers an area of 4.6 km² and is divided in three small adjacent subcatchment areas termed P301 (0.99 km²), P303 (1.32 km²), and P304 (0.49 km²) which lie on an elevation range of 1660 to 2100 m (for location see Figure 3.2 and Table 3.1).

Table 3.1: Location of sample sites

Study Site	Location	Sample types	Coordinates	Elevation (m)
BP	Southern Sierra Nevada	regolith profile	37°09.221' N, 119°15.709' W	1927
PIG	Providence Creek	bedload sediment, stream water	37°03.221' N, 119°12.272' W	1680
P301	Providence Creek	soil profile, stream water	37°03.670' N, 119°12.322' W	1817
P303	Providence Creek	stream water	37°03.545' N, 119°11.413' W	1732
P304	Providence Creek	stream water	37°03.029' N, 119°11.183' W	1780
D102	Duff Creek	stream water	37°02.506' N, 119°11.644' W	1488

The landscape of the Sierra Nevada mountain range of California is characterized by a sequence of parallel ridges and valleys with alternating steep and gentle areas that are actively eroding (Jessup et al., 2011). At the surface granitic rocks of the Sierra Nevada batholith are exposed. The lithology of the studied sites mainly comprises the so-called “Dinky Creek Granodiorite”. This rock type is composed of strongly foliated biotite-hornblende granodiorite with titanite, plagioclase and opaque minerals. An additionally occurring rock is quartz-rich tonalite with hornblende prisms and biotite plates (“Bass Lake Tonalite”; Bateman and Wones (1972), Hahm et al. (2014)). Based on topography, field observations, US Geological Survey geomorphology maps, and the presence of thick saprolite layers, glaciation of the study sites can be excluded (Dixon et al., 2009b). Paleoclimate records for the Sierra Nevada suggest roughly uniform climatic conditions during the Holocene (Riebe et al., 2001a). The average annual temperature of the area is 11.3 °C and the mean annual precipitation is about 1000 mm y⁻¹ (50 y record; Bales et al. (2011)). The Providence Creek catchment is located in the rain-snow transition zone such that most of the precipitation is received in the winters in the form of snow (average effective winter snow line at around 1600 m (Dahlgren et al., 1997)) and the water runoff is maximized during snowmelt in spring. The studied sites are covered to about 76-99% by a mixed conifer forest (pine species, cedar, and fir; Bales et al. (2011)).

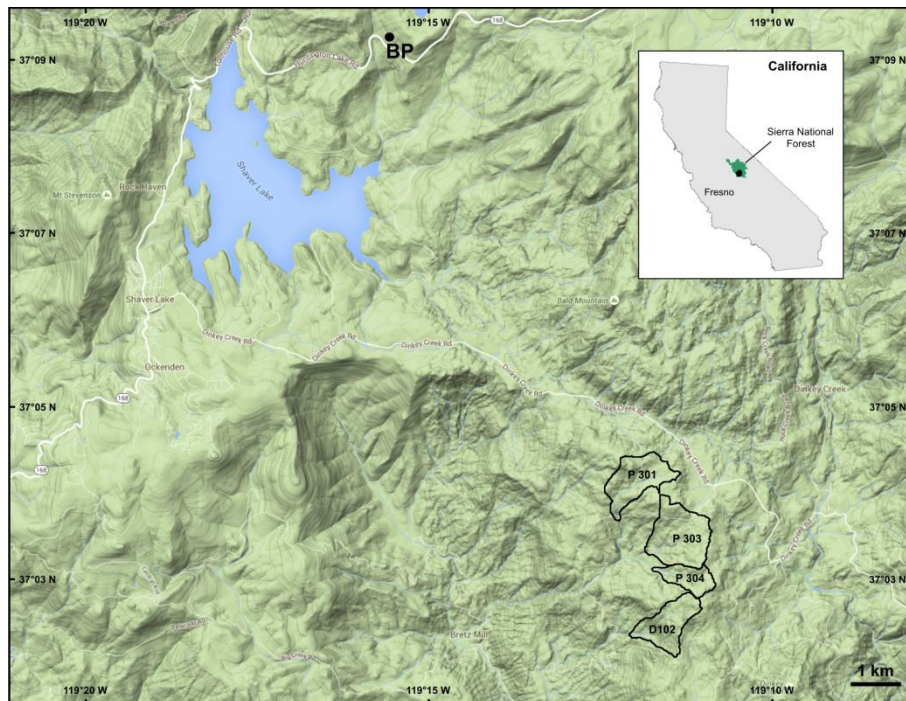


Figure 3.1: Hillshade map showing the location of the Providence Creek subcatchments P301, P303, P304, and D102, and the location of the Balsam Profile (“BP”) NE of Shaver Lake along the Tollhouse Road (Road 168). The inset shows a map of California, USA, with the Sierra National Forest indicated.

Prevailing soil types are weakly developed inceptisols and entisols that are attributed to the Gerle-Cagwin (USDA-NRCS taxonomy; *Gerle*: coarse-loamy, mixed, frigid typic dystoxerepts; *Cagwin*: mixed, frigid dystric xeropsamments) and Shaver soil families (coarse-loamy, mixed, mesic humic dystoxerepts; Johnson et al. (2011)). The soil pH determined on surface soil samples is 5.7 in Cagwin and 5.6 in Shaver soils; these soils have an average soil thickness of about 65 cm and a bulk density of 1.4 g cm^{-3} (Johnson et al., 2011). Saprolite is developed locally to more than 10 m in thickness (Holbrook et al., 2014; Riebe and Granger, 2013). The prevailing environmental conditions (e.g. melting of the winter snow pack each spring) lead to intense weathering of feldspars, especially plagioclase, and the subsequent formation of kaolinite and hydroxy-interlayered vermiculite (Graham and O'Geen, 2010). Dahlgren et al. (1997) showed in a previous study across a Sierra Nevada elevation transect that the highest clay contents occur at mean elevation sites. Soil transport was observed in the field to take place mainly by overland flow and soil creep like processes (Dixon et al., 2009b; Riebe et al., 2001b). Denudation rates based on cosmogenic *in situ* ^{10}Be concentrations measured in soils combined with chemical analyses of soil, saprolite, and rock are on average $220 \text{ t km}^{-2} \text{ y}^{-1}$ in the Providence Creek catchment (Dixon et al., 2009b). These authors attribute about half of the denudation in the studied area to chemical weathering of the saprolite (Dixon et al., 2009b). Denudation rate estimates derived from *in situ* ^{10}Be concentrations measured in stream sediment are, however, much lower with an average value of about $150 \text{ t km}^{-2} \text{ y}^{-1}$ for soil-mantle slopes and an average value of about $65 \text{ t km}^{-2} \text{ y}^{-1}$ for bare-bedrock slopes (Hahm et al., 2014).

Accordingly, bedrock that is covered by regolith is weathered more extensively and eroded faster than bedrock exposed at the surface, shaping the characteristic topography of the western Sierra Nevada slope (Hahm et al., 2014; Jessup et al., 2011; Wahrhaftig, 1965).

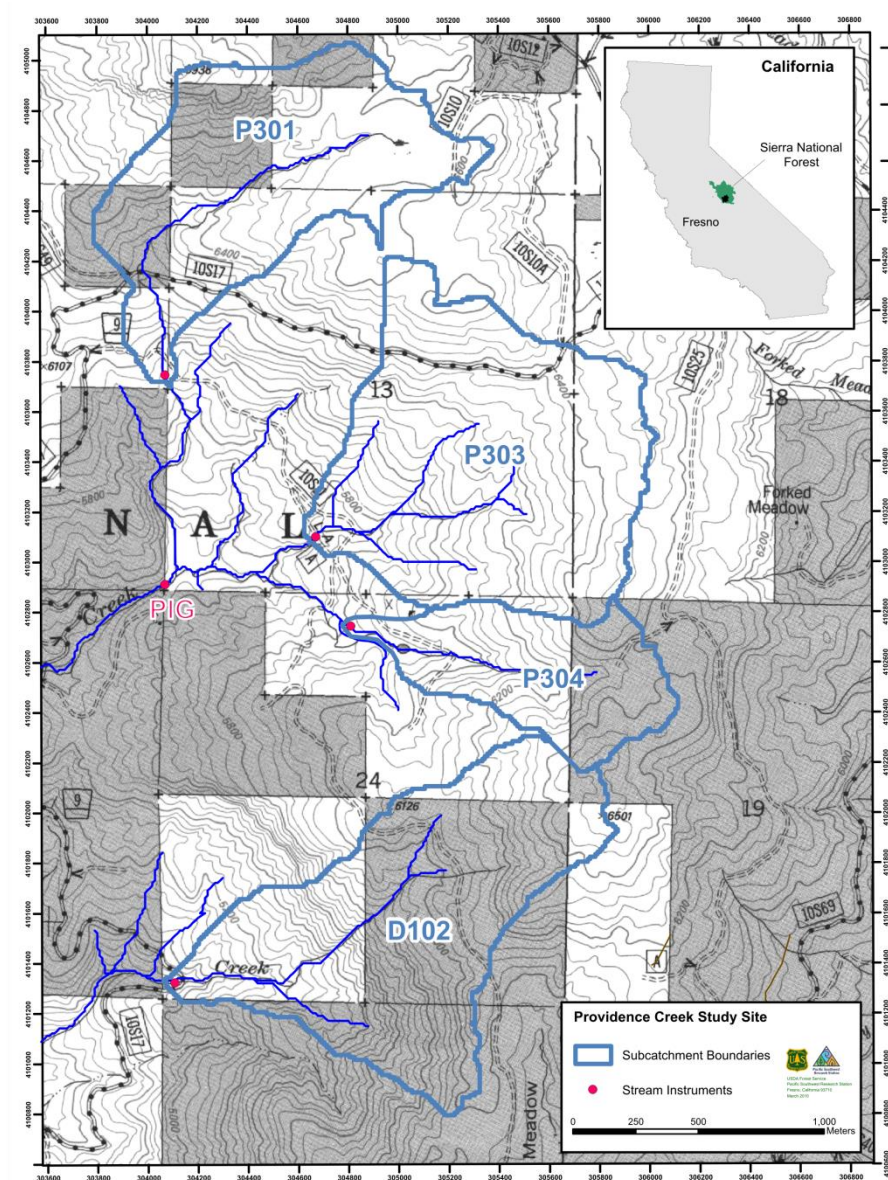


Figure 3.2: Topographic map of the Providence Creek study site with the subcatchments P301, P303, P304, and D102. Modified from <http://www.fs.fed.us/psw/topics/water/kingsriver/>. Topographic lines are in 40 ft steps, corresponding to about 12 m steps. The inset shows the map of California, USA, with the Sierra National Forest indicated.

In May 2010 a field campaign was organized during which the majority of the soil, sediment, and water samples were taken. The studied soil profile was sampled within one of the subcatchments at Providence Creek (catchment code P301; SN1 to SN10). Bulk soil samples were taken with a soil corer in the shallow soil horizons and an auger in the deeper soil horizons. In addition to the soil profile, a regolith profile (Balsam Profile, “BP”) was sampled in a distance of about 10 km from

Providence Creek on a road cut along the Tollhouse Road (Road 168) NE of Shaver Lake (see Figure 3.1 and Table 3.1). The Balsam saprolite profile was sampled over a depth from about 800 to about 180 cm below the surface (samples SN13 to SN20; see Figure 3.3). Besides these soil and saprolite samples, bedload sediment was sampled in the stream draining the entire Providence Creek catchment (“Providence integrated”, PIG; sample SN28). Additionally, stream water samples were taken at the outflow of the whole Providence Creek catchment (“PIG”), each subcatchment, and the south of Providence Creek adjacent Duff Creek catchment (stream water samples: SNW48 to SNW52). Bedrock material was sampled in the form of rock fragments that were exposed at the surface. In summer 2014 the overlying soil of the Balsam profile was sampled from the surface to a depth of 120 cm (samples SN59 to SN62).

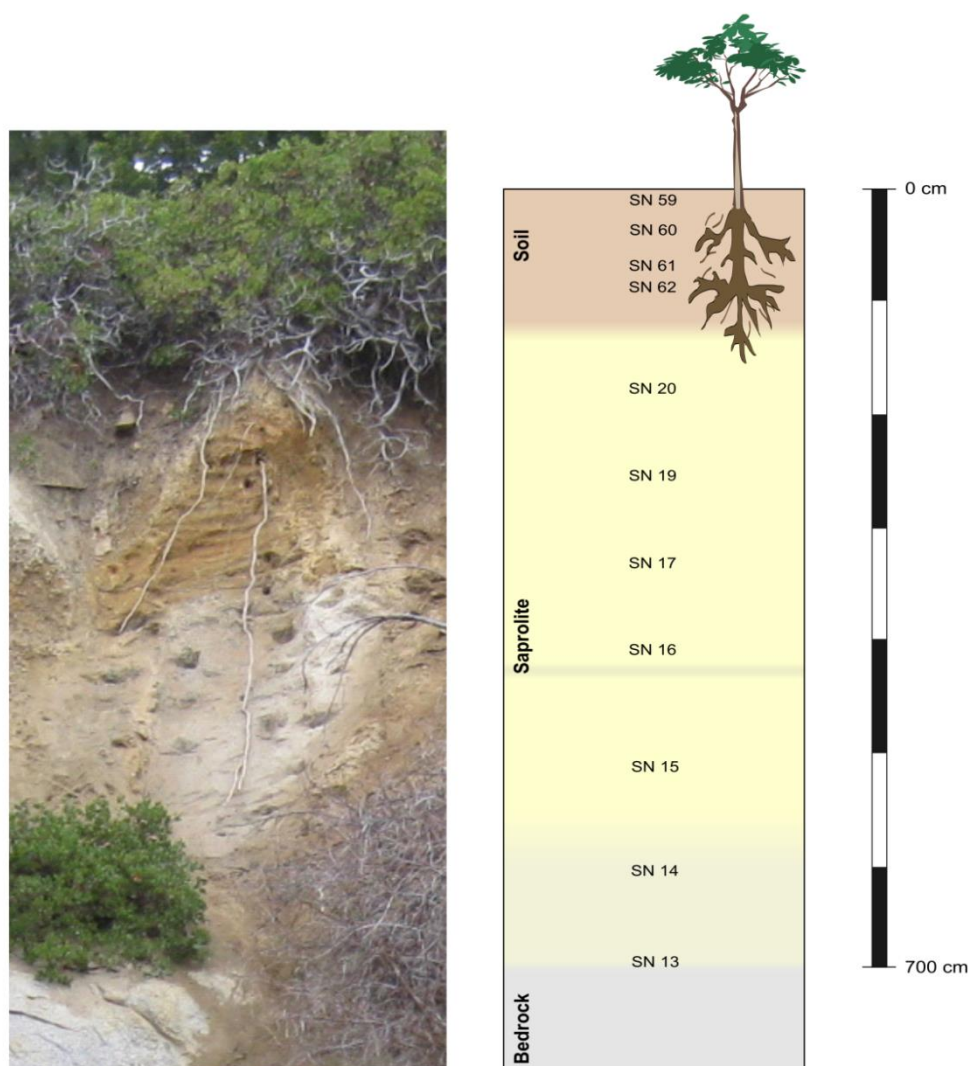


Figure 3.3: Photo of the Balsam Profile (left) with scale and depth locations of soil and saprolite samples indicated (right).

3.3 Methods

3.3.1 Soil, saprolite, and bedload sediment samples

I determined reactive and total $^{10}\text{Be}/^9\text{Be}$ ratios on bedload sediment of the PIG stream, on the soil and saprolite samples of the Balsam Profile, and on four soil samples of the soil profile sampled in the P301 catchment. All soil and sediment samples were sieved < 2 mm to remove larger grains or pebbles. I used about 0.5 – 1 g of sample material for the sequential extraction procedure described in Section 1.3.1. The residual silicate fraction was completely dissolved with HF and aqua regia digestion. Meteoric ^{10}Be and ^9Be concentrations were measured separately and the $^{10}\text{Be}/^9\text{Be}$ ratios were calculated. ^9Be concentration measurements were done on an ICP-OES and cosmogenic ^{10}Be measurements at the CologneAMS facility (for detailed sample preparation see Section 1.3.3).

The upper four soil samples of the Balsam regolith profile were processed by *D.Uhlig, GFZ Potsdam*, in 2015, applying the same sequential extraction method described in Section 1.3.1.

3.3.2 Stream water samples

In the field directly following sampling, the stream water samples have been filtered through a 0.2 μm membrane filter and acidified with nitric acid to a pH of about 2. The dissolved $^{10}\text{Be}/^9\text{Be}$ ratios in these waters were calculated from individually measured ^{10}Be and ^9Be concentrations. I processed about 500 ml of stream water spiked with about 200 μg ^9Be carrier using the method that is described in Section 1.3.2 in order to measure meteoric ^{10}Be at the CologneAMS facility. The natural ^9Be concentration of the stream water samples was measured on a HR-ICP-MS (see Section 1.3.2). Due to low concentrations, the samples had to be pre-concentrated. Hence, I evaporated about 50 ml of stream water that were taken up again in 0.3M HNO_3 for measurement. I simultaneously processed a reference stream water (SRM 1640a, see also Section 1.3.2) in order to monitor the accuracy of the measurements.

3.3.3 Bedrock samples

Beryllium concentrations in the granitic parent bedrock were determined on sampled fragments of bedrock, in total six bedrock samples from the P301, P303, and Balsam sites. About 75 mg of crushed and pulverized bedrock material was dissolved by combining HF and aqua regia digestion steps. After complete dissolution the samples were measured in 3M HNO_3 on an ICP-OES. I simultaneously

processed two standard reference materials (Geostandard GA and RGM-1; see Section 1.3.1) to have an independent control on the accuracy of the measurements.

3.3.4 Chemical depletion fraction and elemental loss

A large data set of measured elemental concentrations already exists for the soil and saprolite profiles (data set *GFZ Potsdam*, Sec 3.3; see also Appendix A.3.5), and can be used to quantify the weathering regime of this environment. The fraction of total denudation that is accounted for by chemical weathering can be assessed by the chemical depletion fraction (CDF; Riebe et al. (2001b)). The CDF is calculated by quantifying the enrichment of an immobile element (e.g. zirconium, Zr) in the weathered soil or saprolite relative to the parent bedrock material (Dixon et al., 2009b; Riebe et al., 2001b):

$$CDF = 1 - \frac{[Zr]_{rock}}{[Zr]_{weathered}} \quad \text{Equation 3.1}$$

$[Zr]_{rock}$ and $[Zr]_{weathered}$ are the concentrations of zirconium (in ppm) in the parent bedrock material and in the weathered soil or saprolite material, respectively. In the case of $CDF = 0$ no material is weathered and transported in the dissolved form, whereas if $CDF = 1$ all material is lost by chemical weathering from the soil or saprolite. However, in most lithologies the CDF will be < 0.5 as in many continental bedrock types quartz is present that is hardly soluble (Dixon and von Blanckenburg, 2012).

In addition to the total chemical depletion fraction, the mass loss of an individual element in the soil or saprolite relative to the parent bedrock can be quantified. This mass change is defined as the element-mass-transfer coefficient $\tau(x)$ (Brantley and White, 2009):

$$\tau(x) = \frac{[x]_{weathered}}{[x]_{rock}} - \frac{[Zr]_{rock}}{[Zr]_{weathered}} - 1 \quad \text{Equation 3.2}$$

$[x]_{rock}$ and $[x]_{weathered}$ represent the concentrations of an element x (in ppm or %) in the parent bedrock material and in the weathered soil or saprolite material, respectively. If $\tau(x) = 0$ no mobilization of the weatherable element x occurs relative to the parent bedrock (conservative behaviour). If $\tau(x) < 0$ or $\tau(x) > 0$, the element x was lost or enriched during chemical weathering processes, respectively (Brantley and White, 2009).

3.4 Results

3.4.1 $[^9\text{Be}]$, $[^{10}\text{Be}]$, and $(^{10}\text{Be}/^9\text{Be})$ measured on the Balsam Profile (BP)

The total ^9Be concentrations are with values of about 1.3 to 1.4 ppm roughly constant over the whole Balsam regolith profile (see Figure 3.5 A and Table 3.2). $[^9\text{Be}]_{\text{am-ox}}$ measured in the HCl-leachable fraction is also roughly uniform over the whole regolith being between 0.16 ± 0.01 and 0.25 ± 0.01 ppm (see Figure 3.4 A and Table 3.2). In contrast, $[^9\text{Be}]_{\text{x-ox}}$ shows a different pattern between the saprolite and the soil. In the saprolite $[^9\text{Be}]_{\text{x-ox}}$ decreases with increasing depth from a value of 0.50 ± 0.03 ppm in the uppermost saprolite sample (SN 20) to a value of 0.15 ± 0.01 ppm (SN 13) at the saprolite-bedrock boundary. In the upper four soil samples $[^9\text{Be}]_{\text{x-ox}}$ is markedly lower with about 0.06 to 0.09 ppm (SN 59 to 62). The calculated sum of reactive beryllium concentrations ($[^9\text{Be}]_{\text{reac}} = [^9\text{Be}]_{\text{am-ox}} + [^9\text{Be}]_{\text{x-ox}}$) is thus decreasing with increasing saprolite depth from about 0.7 ppm to about 0.4 ppm. In the soil $[^9\text{Be}]_{\text{reac}}$ is similar to the values in the lower saprolite (about 0.3 to 0.5 ppm; see Figure 3.4 B). The beryllium concentration measured in the silicate min fraction shows an opposed trend to $[^9\text{Be}]_{\text{x-ox}}$. In the soil $[^9\text{Be}]_{\text{min}}$ is about 1.0 ppm. In the top saprolite, $[^9\text{Be}]_{\text{min}}$ is only about 0.6 ppm but increases then with increasing depth to a value of about 1.0 ppm. The fraction of $[^9\text{Be}]_{\text{reac}}$ compared to $[^9\text{Be}]_{\text{total}}$ is constant with only about 25% in the soil but is decreasing in the saprolite towards the saprolite-bedrock boundary from about 55 to 30%.

Both, meteoric $[^{10}\text{Be}]_{\text{total}}$ and $[^{10}\text{Be}]_{\text{reac}}$ decrease from the top soil to the saprolite-bedrock boundary (see Figure 3.5 B and Table 3.3). $[^{10}\text{Be}]_{\text{total}}$ decreases from about 220×10^6 atoms g^{-1} in the uppermost soil sample to about 1×10^6 atoms g^{-1} in the lower saprolite, and $[^{10}\text{Be}]_{\text{reac}}$ decreases from ca. 100×10^6 atoms g^{-1} to 0.5×10^6 atoms g^{-1} . In the saprolite samples $[^{10}\text{Be}]_{\text{am-ox}}$ and $[^{10}\text{Be}]_{\text{x-ox}}$ range in the same order of magnitude, but in the soil samples $[^{10}\text{Be}]_{\text{am-ox}}$ is distinctly higher than $[^{10}\text{Be}]_{\text{x-ox}}$ (see Figure 3.5 A). While $[^{10}\text{Be}]_{\text{am-ox}}$ shows a clear offset from lower concentrations in the saprolite to higher concentrations in the soil, the distribution of $[^{10}\text{Be}]_{\text{x-ox}}$ across this boundary is uniform. The residual min fraction also contains significant amounts of meteoric ^{10}Be . Starting from a concentration of about 110×10^6 atoms g^{-1} in the uppermost samples, $[^{10}\text{Be}]_{\text{min}}$ decreases to about 0.3×10^6 atoms g^{-1} with increasing profile depth. This $[^{10}\text{Be}]_{\text{min}}$ comprises about 25 to 35% of $[^{10}\text{Be}]_{\text{total}}$ in the saprolite and even about 55% in the soil (see Figure 3.5 B and Table 3.3).

These ^9Be and ^{10}Be concentrations were used to calculate $^{10}\text{Be}/^9\text{Be}$ ratios (see Figure 3.6 and Table 3.4). The overall trend is described by an decreasing $(^{10}\text{Be}/^9\text{Be})_{\text{total}}$ and $(^{10}\text{Be}/^9\text{Be})_{\text{reac}}$ from the surface of the regolith to the bottom of the profile (see Figure 3.6 B). A similar trend is found for the ratios of the single fractions (see Figure 3.6 A).

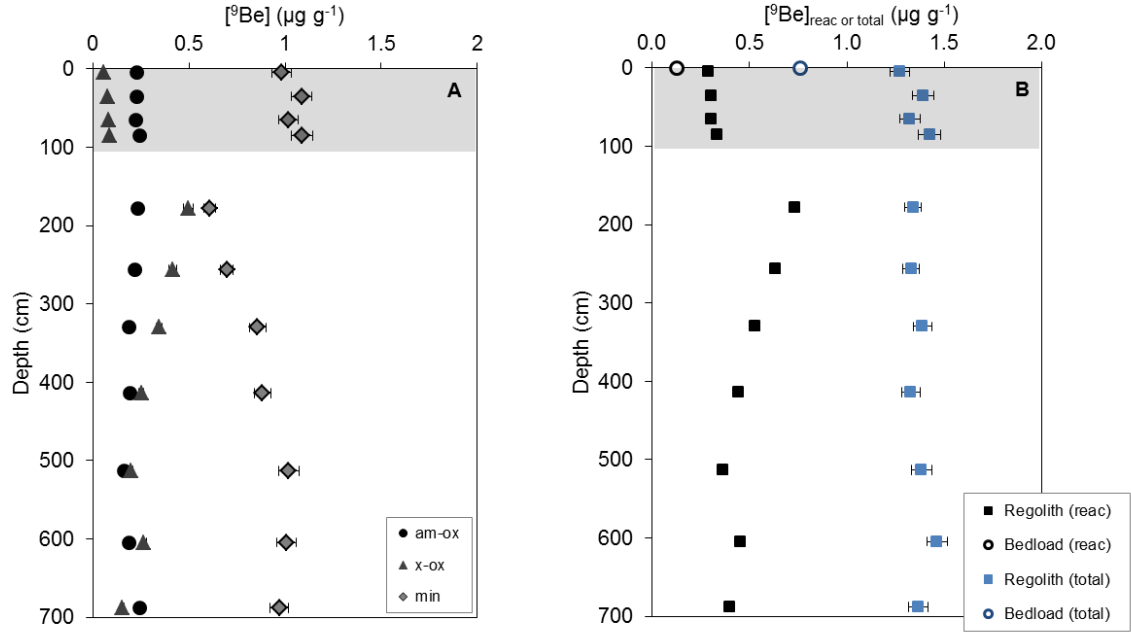


Figure 3.4: **A:** ^9Be concentrations (in $\mu\text{g g}^{-1}$) measured on the individually extracted fractions am-ox, x-ox, and the residual min fraction of the soil, and saprolite Balsam Profile samples. **B:** $^9\text{Be}_{\text{react}}$ (black symbols) and $^9\text{Be}_{\text{total}}$ (blue symbols; in $\mu\text{g g}^{-1}$) determined on the soil and saprolite Balsam Profile samples and on a bedload sample (PIG; circles). Soil samples are shaded in grey. Where error bars are not visible, they are smaller than displayed symbols.

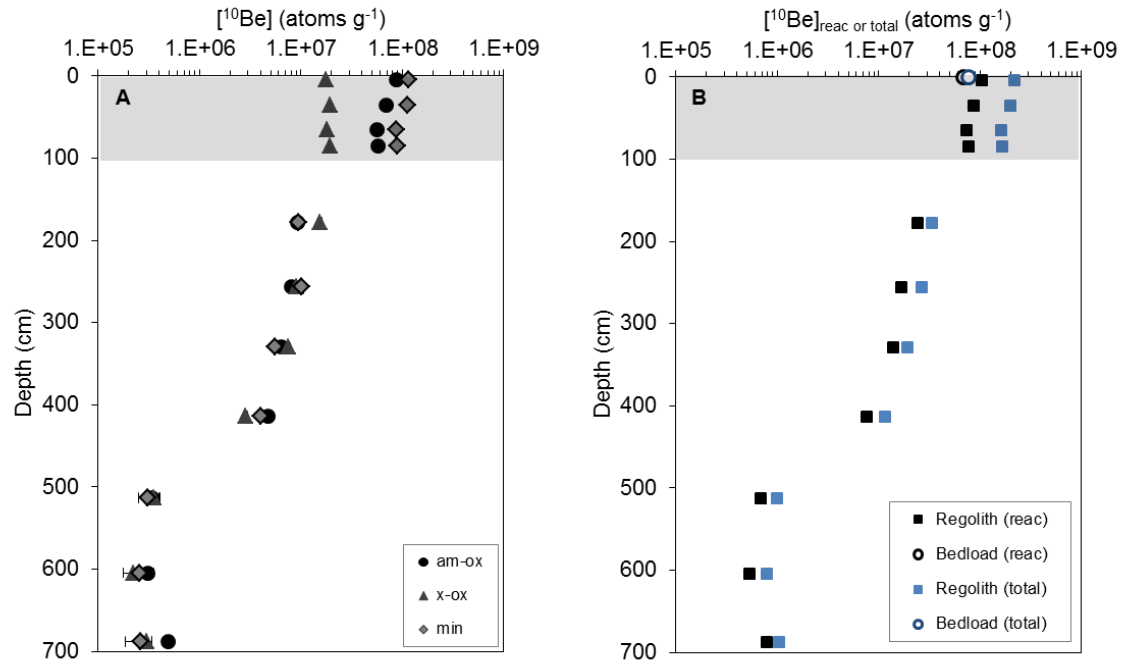


Figure 3.5: **A:** Meteoric ^{10}Be concentrations (in atoms g^{-1}) measured on the individually extracted fractions am-ox, x-ox, and the residual min fraction of the soil, and saprolite Balsam Profile samples. **B:** $^{10}\text{Be}_{\text{react}}$ (black symbols) and $^{10}\text{Be}_{\text{total}}$ (blue symbols; in atoms g^{-1}) determined on the soil and saprolite Balsam Profile samples and on a bedload sample (PIG; circles). Soil samples are shaded in grey. Where error bars are not visible, they are smaller than displayed symbols.

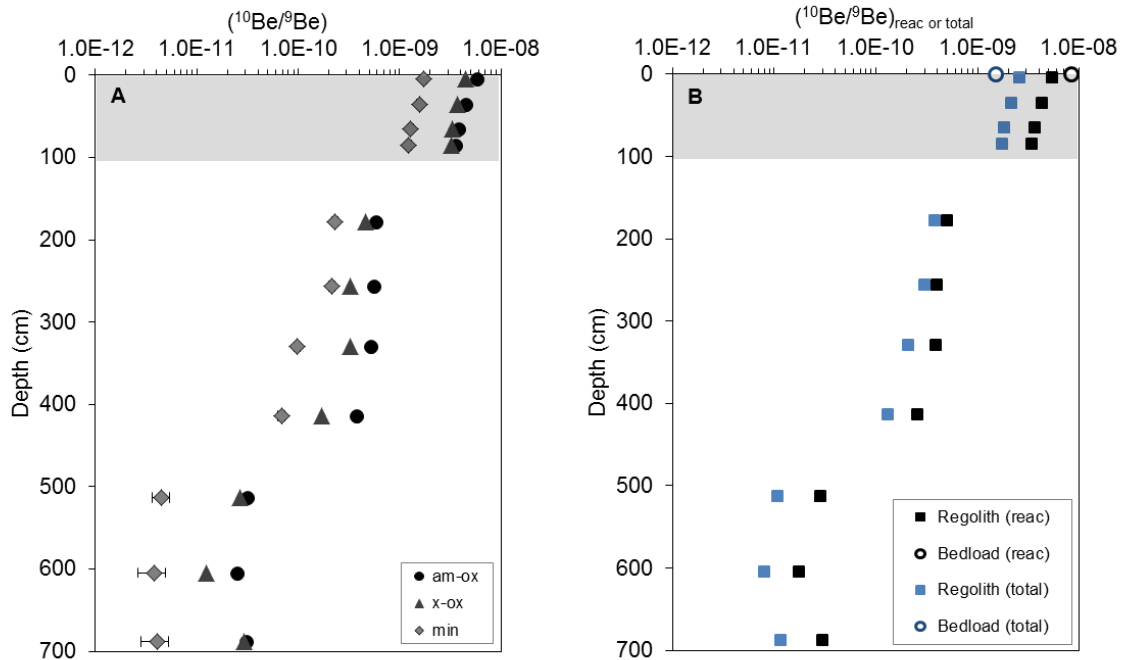


Figure 3.6: **A:** $^{10}\text{Be}/^9\text{Be}$ ratios determined on the individually extracted fractions am-ox, x-ox, and the residual min fraction of the soil, and saprolite Balsam Profile samples. **B:** $(^{10}\text{Be}/^9\text{Be})_{\text{reac}}$ (black symbols) and $(^{10}\text{Be}/^9\text{Be})_{\text{reac}}$ (blue symbols) determined in the soil and saprolite Balsam Profile samples and on a bedload sample (PIG; circles). Soil samples are shaded in grey. Where error bars are not visible, they are smaller than displayed symbols.

3.4.2 $[^9\text{Be}]$, $[^{10}\text{Be}]$, and $(^{10}\text{Be}/^9\text{Be})$ measured on the soil profile P301

$[^9\text{Be}]_{\text{total}}$ varies between about 1.2 and 1.4 ppm in the soil profile P301 but shows no trend (see Figure 3.8 A and Table 3.2). Considering the single extracted fractions separately, $[^9\text{Be}]_{\text{am-ox}}$ is also roughly uniform with values between ca. 0.14 and 0.16 ppm. $[^9\text{Be}]_{\text{x-ox}}$ reveals lower concentrations on the profile surface (see Figure 3.7 A). $[^9\text{Be}]_{\text{reac}}$ thus indicate a slight increase with increasing depth from about 0.33 to 0.45 ppm in the upper samples (see Figure 3.8 A). In contrast, $[^9\text{Be}]_{\text{min}}$ decreases from about 1.10 to 0.80 ppm with increasing soil depth (see Figure 3.7 A).

In comparison, meteoric $[^{10}\text{Be}]_{\text{total}}$ and $[^{10}\text{Be}]_{\text{reac}}$ exhibit no trend throughout the soil (see Figure 3.8B). $[^{10}\text{Be}]_{\text{total}}$ is about $470 \times 10^6 \text{ atoms g}^{-1}$. $[^{10}\text{Be}]_{\text{am-ox}}$ slightly decreases while $[^{10}\text{Be}]_{\text{x-ox}}$ slightly increases with increasing soil depth (see Figure 3.7 B). The amount of $[^{10}\text{Be}]_{\text{min}}$ that is measured in these samples is about 11 to 15% of $[^{10}\text{Be}]_{\text{total}}$.

Considering the $^{10}\text{Be}/^9\text{Be}$ ratios for each fraction there are only slight trends visible over the soil depth (see Figure 3.9 and Table 3.4). $(^{10}\text{Be}/^9\text{Be})_{\text{reac}}$ decreases from $184 \pm 8 \times 10^{-10}$ to $131 \pm 6 \times 10^{-10}$ with increasing soil depth, while $(^{10}\text{Be}/^9\text{Be})_{\text{total}}$ varies from 50 to $58 \pm 2 \times 10^{-10}$ (see Figure 3.9 B).

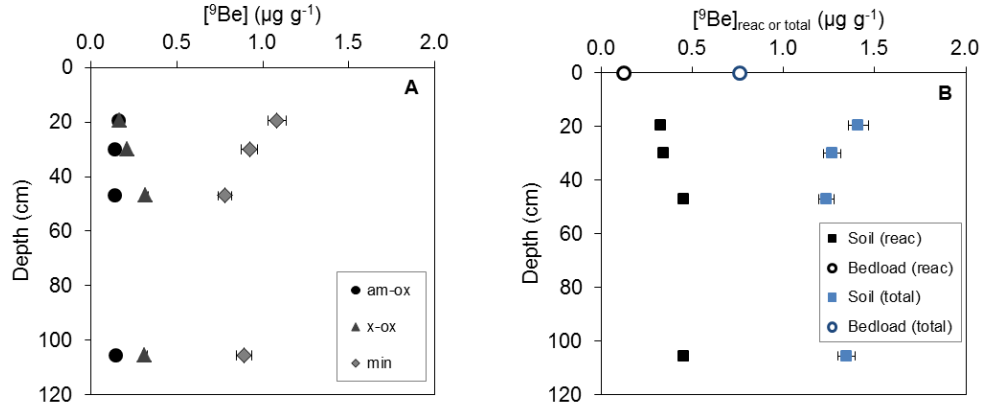


Figure 3.7: **A:** ^9Be (in $\mu\text{g g}^{-1}$) measured on the individually extracted fractions am-ox, x-ox, and the residual min fraction of the soil profile P301. **B:** $^9\text{Be}_{\text{reac}}$ (black symbols) and $^9\text{Be}_{\text{total}}$ (blue symbols; in $\mu\text{g g}^{-1}$) determined on the soil profile P301 and on a bedload sample (PIG; circles). Where error bars are not visible, they are smaller than displayed symbols.

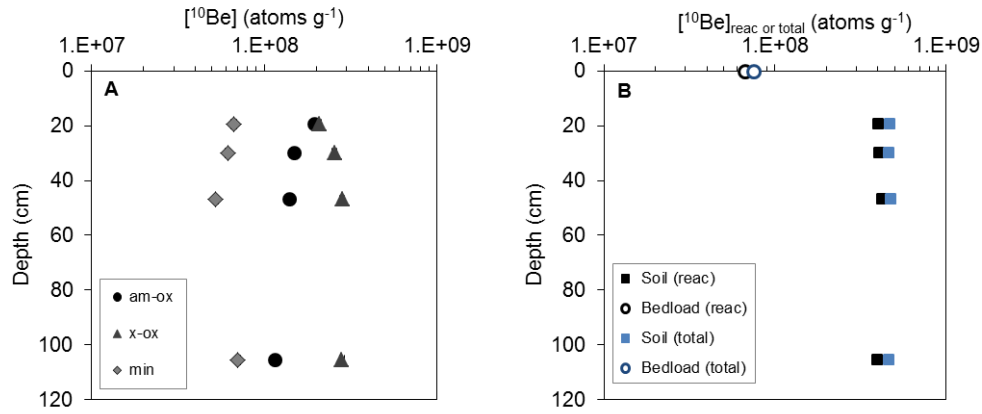


Figure 3.8: **A:** ^{10}Be (in atoms g^{-1}) measured on the individually extracted fractions am-ox, x-ox, and the residual min fraction of the soil profile P301. **B:** $^{10}\text{Be}_{\text{reac}}$ (black symbols) and $^{10}\text{Be}_{\text{total}}$ (blue symbols; in atoms g^{-1}) measured on the soil profile P301 and a bedload sample (PIG; circles). Where error bars are not visible, they are smaller than displayed symbols.

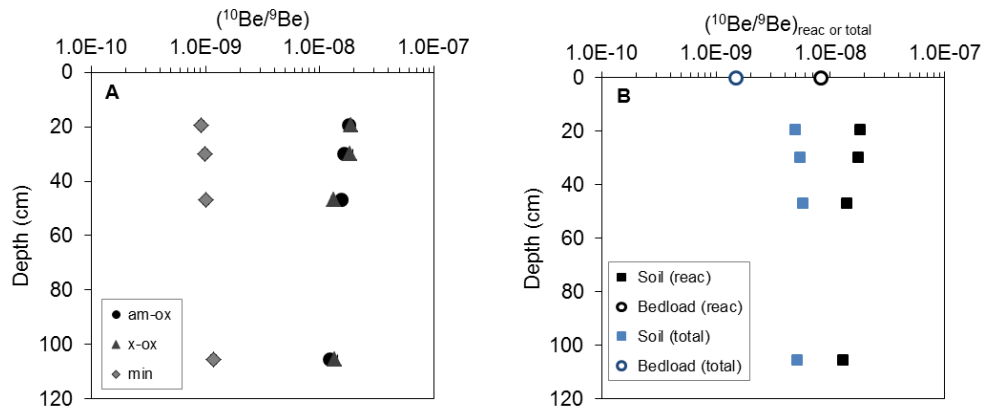


Figure 3.9: **A:** $^{10}\text{Be}/^9\text{Be}$ ratios determined on the individually extracted fractions am-ox, x-ox, and the residual min fraction of the soil profile P301. **B:** $^{10}\text{Be}/^9\text{Be}_{\text{reac}}$ (black symbols) and $^{10}\text{Be}/^9\text{Be}_{\text{total}}$ (blue symbols) determined on soil profile P301 and on a bedload sample (PIG; circles). Where error bars are not visible, they are smaller than displayed symbols.

Table 3.2: ^9Be concentrations measured in the single extracted compartments (am-ox, x-ox, min) and sums of reactive and total ^9Be in the studied soil, saprolite, and bedload samples

Lab ID	Sample name	Sample type	Mid depth (cm)	$[^9\text{Be}]_{\text{am-ox}}$ ($\mu\text{g g}^{-1}$)	$[^9\text{Be}]_{\text{x-ox}}$ ($\mu\text{g g}^{-1}$)	$[^9\text{Be}]_{\text{min}}$ ($\mu\text{g g}^{-1}$)	$[^9\text{Be}]_{\text{reac}}$ ($\mu\text{g g}^{-1}$)	$[^9\text{Be}]_{\text{total}}$ ($\mu\text{g g}^{-1}$)
<u><i>P 301</i></u>								
SN 2	P301	Soil (Core)	19.5	0.1605 ± 0.0080	0.1677 ± 0.0084	1.082 ± 0.054	0.328 ± 0.012	1.410 ± 0.055
SN 3	P301	Soil (Core)	30.0	0.1369 ± 0.0068	0.207 ± 0.010	0.923 ± 0.046	0.344 ± 0.012	1.267 ± 0.048
SN 4	P301	Soil (Auger)	47.0	0.1352 ± 0.0068	0.318 ± 0.016	0.781 ± 0.039	0.453 ± 0.017	1.234 ± 0.043
SN 9	P301	Soil (Auger)	105.5	0.1411 ± 0.0071	0.313 ± 0.016	0.893 ± 0.045	0.454 ± 0.017	1.347 ± 0.048
<u><i>Balsam Profile</i></u>								
SN 59	BP 0-10 cm	Soil	5	0.230 ± 0.011	0.0589 ± 0.0029	0.983 ± 0.049	0.289 ± 0.012	1.272 ± 0.051
SN 60	BP 30-40 cm	Soil	35	0.229 ± 0.011	0.0775 ± 0.0039	1.086 ± 0.054	0.306 ± 0.012	1.393 ± 0.056
SN 61	BP 60-70 cm	Soil	65	0.222 ± 0.011	0.0815 ± 0.0041	1.019 ± 0.051	0.304 ± 0.012	1.322 ± 0.052
SN 62	BP 80-90 cm	Soil	85	0.245 ± 0.012	0.0890 ± 0.0045	1.090 ± 0.054	0.334 ± 0.013	1.424 ± 0.056
SN 20	BP 204	Saprolite	178	0.235 ± 0.012	0.496 ± 0.025	0.608 ± 0.030	0.731 ± 0.027	1.339 ± 0.041
SN 19	BP 173	Saprolite	257	0.217 ± 0.011	0.416 ± 0.021	0.697 ± 0.035	0.633 ± 0.023	1.330 ± 0.042
SN 17	BP 144	Saprolite	330	0.1863 ± 0.0093	0.345 ± 0.017	0.857 ± 0.043	0.531 ± 0.020	1.388 ± 0.047
SN 16	BP 111	Saprolite	414	0.193 ± 0.010	0.252 ± 0.013	0.882 ± 0.044	0.445 ± 0.016	1.327 ± 0.047
SN 15	BP 72	Saprolite	513	0.1635 ± 0.0082	0.200 ± 0.010	1.020 ± 0.051	0.364 ± 0.013	1.384 ± 0.053
SN 14	BP 36	Saprolite	605	0.1870 ± 0.0093	0.266 ± 0.013	1.009 ± 0.050	0.453 ± 0.016	1.463 ± 0.053
SN 13	BP 3	Saprolite	688	0.244 ± 0.012	0.1540 ± 0.0077	0.970 ± 0.048	0.398 ± 0.014	1.367 ± 0.051
<u><i>Bedload Sediment</i></u>								
SN 28	PIG	Bedload		0.0681 ± 0.0034	0.0544 ± 0.0027	0.637 ± 0.032	0.1225 ± 0.0044	0.759 ± 0.032

Samples displayed in grey are processed by D.Uhlig, GFZ Potsdam in 2015

Table 3.3: ^{10}Be concentrations measured in the single extracted compartments (am-ox, x-ox, min) and sums of reactive and total ^{10}Be in the studied soil, saprolite, and bedload samples

Lab ID	Sample name	Sample type	Mid depth (cm)	$[^{10}\text{Be}]_{\text{am-ox}}$ (10^6 atoms g^{-1})	$[^{10}\text{Be}]_{\text{x-ox}}$ (10^6 atoms g^{-1})	$[^{10}\text{Be}]_{\text{min}}$ (10^6 atoms g^{-1})	$[^{10}\text{Be}]_{\text{reac}}$ (10^6 atoms g^{-1})	$[^{10}\text{Be}]_{\text{total}}$ (10^6 atoms g^{-1})
<u><i>P 301</i></u>								
SN 2	P301	Soil (Core)	19.5	194.5 ± 6.2	208.4 ± 6.7	66.6 ± 2.2	402.9 ± 9.1	469.5 ± 9.4
SN 3	P301	Soil (Core)	30.0	150.1 ± 4.8	255.8 ± 8.2	61.4 ± 2.1	405.9 ± 9.5	467.3 ± 9.7
SN 4	P301	Soil (Auger)	47.0	141.0 ± 4.5	282.7 ± 9.0	52.5 ± 1.8	424 ± 10	476 ± 10
SN 9	P301	Soil (Auger)	105.5	115.3 ± 3.7	281.5 ± 9.0	70.5 ± 2.3	396.9 ± 9.7	467 ± 10
<u><i>Balsam Profile</i></u>								
SN 59	BP 0-10 cm	Soil	5	87.7 ± 2.8	17.73 ± 0.61	114.0 ± 3.7	105.4 ± 2.9	219.4 ± 4.7
SN 60	BP 30-40 cm	Soil	35	68.4 ± 2.2	19.37 ± 0.66	113.3 ± 3.7	87.8 ± 2.3	201.1 ± 4.4
SN 61	BP 60-70 cm	Soil	65	56.1 ± 1.8	18.05 ± 0.62	87.4 ± 2.8	74.2 ± 1.9	161.6 ± 3.4
SN 62	BP 80-90 cm	Soil	85	57.6 ± 1.9	19.26 ± 0.66	89.3 ± 2.9	76.8 ± 2.0	166.1 ± 3.5
SN 20	BP 204	Soil	178	9.18 ± 0.34	15.41 ± 0.54	9.42 ± 0.51	24.59 ± 0.64	34.01 ± 0.82
SN 19	BP 173	Soil	257	7.97 ± 0.33	9.04 ± 0.50	10.02 ± 0.48	17.00 ± 0.60	27.03 ± 0.77
SN 17	BP 144	Saprolite	330	6.41 ± 0.30	7.57 ± 0.33	5.59 ± 0.26	13.98 ± 0.44	19.58 ± 0.51
SN 16	BP 111	Saprolite	414	4.77 ± 0.20	2.84 ± 0.14	4.05 ± 0.23	7.62 ± 0.24	11.66 ± 0.34
SN 15	BP 72	Saprolite	513	0.34 ± 0.05	0.352 ± 0.053	0.305 ± 0.057	0.692 ± 0.075	0.998 ± 0.094
SN 14	BP 36	Saprolite	605	0.309 ± 0.048	0.221 ± 0.043	0.255 ± 0.078	0.530 ± 0.064	0.78 ± 0.10
SN 13	BP 3	Saprolite	688	0.493 ± 0.046	0.300 ± 0.037	0.261 ± 0.076	0.793 ± 0.060	1.05 ± 0.10
<u><i>Bedload Sediment</i></u>								
SN 28	PIG	Bedload		38.3 ± 1.3	28.70 ± 0.94	8.12 ± 0.32	67.0 ± 1.6	75.1 ± 1.6

Samples displayed in grey are processed by D.Uhlig, GFZ Potsdam in 2015

Table 3.4: $^{10}\text{Be}/^9\text{Be}$ ratios determined on the single extracted compartments (am-ox, x-ox, min) and sums of reactive and total $^{10}\text{Be}/^9\text{Be}$ in the studied soil, saprolite, and bedload samples

Lab ID	Sample name	Sample type	Mid depth (cm)	$(^{10}\text{Be}/^9\text{Be})_{\text{am-ox}}$ ($\times 10^{-10}$)	$(^{10}\text{Be}/^9\text{Be})_{\text{x-ox}}$ ($\times 10^{-10}$)	$(^{10}\text{Be}/^9\text{Be})_{\text{min}}$ ($\times 10^{-10}$)	$(^{10}\text{Be}/^9\text{Be})_{\text{reac}}$ ($\times 10^{-10}$)	$(^{10}\text{Be}/^9\text{Be})_{\text{total}}$ ($\times 10^{-10}$)
<u><i>P 301</i></u>								
SN 2	P301	Soil (Core)	19.5	181 \pm 11	186 \pm 11	9.22 \pm 0.55	183.7 \pm 7.7	49.8 \pm 2.2
SN 3	P301	Soil (Core)	30.0	164 \pm 10	185 \pm 11	9.96 \pm 0.60	176.4 \pm 7.6	55.2 \pm 2.4
SN 4	P301	Soil (Auger)	47.0	156.1 \pm 9.3	132.9 \pm 7.9	10.06 \pm 0.61	139.8 \pm 6.3	57.7 \pm 2.4
SN 9	P301	Soil (Auger)	105.5	122.4 \pm 7.3	134.8 \pm 8.0	11.82 \pm 0.71	130.9 \pm 5.9	51.9 \pm 2.2
<u><i>Balsam Profile</i></u>								
SN 59	BP 0-10 cm	Soil	5	57.1 \pm 3.4	45.0 \pm 2.7	17.36 \pm 1.04	54.6 \pm 2.7	25.8 \pm 1.4
SN 60	BP 30-40 cm	Soil	35	44.8 \pm 2.7	37.4 \pm 2.3	15.61 \pm 0.93	42.9 \pm 2.0	21.6 \pm 1.2
SN 61	BP 60-70 cm	Soil	65	37.8 \pm 2.3	33.1 \pm 2.0	12.85 \pm 0.77	36.5 \pm 1.7	18.3 \pm 1.0
SN 62	BP 80-90 cm	Soil	85	35.2 \pm 2.1	32.4 \pm 2.0	12.26 \pm 0.73	34.4 \pm 1.6	17.46 \pm 0.95
SN 20	BP 204	Saprolite	178	5.84 \pm 0.36	4.65 \pm 0.28	2.32 \pm 0.17	5.03 \pm 0.23	3.80 \pm 0.15
SN 19	BP 173	Saprolite	257	5.48 \pm 0.36	3.25 \pm 0.24	2.15 \pm 0.15	4.02 \pm 0.21	3.04 \pm 0.13
SN 17	BP 144	Saprolite	330	5.15 \pm 0.35	3.29 \pm 0.22	0.977 \pm 0.066	3.94 \pm 0.19	2.111 \pm 0.091
SN 16	BP 111	Saprolite	414	3.70 \pm 0.24	1.69 \pm 0.12	0.687 \pm 0.052	2.56 \pm 0.12	1.316 \pm 0.060
SN 15	BP 72	Saprolite	513	0.311 \pm 0.050	0.264 \pm 0.042	0.0448 \pm 0.0087	0.285 \pm 0.032	0.108 \pm 0.011
SN 14	BP 36	Saprolite	605	0.248 \pm 0.040	0.124 \pm 0.025	0.038 \pm 0.012	0.175 \pm 0.022	0.080 \pm 0.011
SN 13	BP 3	Saprolite	688	0.303 \pm 0.032	0.292 \pm 0.039	0.040 \pm 0.012	0.299 \pm 0.025	0.115 \pm 0.011
<u><i>Bedload Sediment</i></u>								
SN 28	PIG	Bedload		84.3 \pm 5.0	79.0 \pm 4.7	1.91 \pm 0.12	81.9 \pm 3.5	14.81 \pm 0.70

Samples displayed in grey are processed by D.Uhlig, GFZ Potsdam in 2015

3.4.3 [^9Be], [^{10}Be], and ($^{10}\text{Be}/^9\text{Be}$) measured on stream bedload sediment

Concentrations of ^9Be and meteoric ^{10}Be were further measured on bedload sediment of the main Providence Creek stream (PIG; see Table 3.2 and Table 3.3). [^9Be]_{reac} is 0.12 ± 0.01 ppm and [^9Be]_{total} is 0.79 ± 0.03 ppm, respectively (see Figure 3.5 A). [^9Be] of the individual fractions am-ox, x-ox, and min are overall similar in the river sediment. Meteoric [^{10}Be]_{reac} is $67 \pm 2 \times 10^6$ atoms g^{-1} , being the sum of [^{10}Be]_{am-ox} of $38.3 \pm 1.3 \times 10^6$ atoms g^{-1} and [^{10}Be]_{x-ox} of $28.7 \pm 0.9 \times 10^6$ atoms g^{-1} , respectively. A concentration of $8.1 \pm 0.3 \times 10^6$ atoms g^{-1} is still present in the mineral-bound fraction, contributing about 11% to [^{10}Be]_{total}. Calculated ($^{10}\text{Be}/^9\text{Be}$)_{reac} and ($^{10}\text{Be}/^9\text{Be}$)_{total} result to about 82×10^{-10} and 15×10^{-10} , respectively (see Table 3.4).

3.4.4 San Joaquin Soil (Reference Material)

Simultaneously to the samples I processed a soil reference material “SRM 2709” (see Section 1.3.1). In the case of the first extraction step, using 0.5M HCl, [^9Be]_{am-ox} is 0.32 ± 0.02 ppm ($n = 6$; see Appendix A.3.2). For the second extraction step, using $\text{NH}_2\text{OH} \cdot \text{HCl}$, the resulting [^9Be]_{x-ox} are 0.12 ± 0.01 and 0.21 ± 0.01 ppm ($n = 2$). For the sample batch processed in 2015 by *D. Uhlig, GFZ Potsdam*, a [^9Be]_{x-ox} of only 0.065 ± 0.003 ppm is measured. Note that the certified value for the summed leach steps (treated using USEPA methods 200.7 and 3050B) is 0.61 ppm (see Section 1.3.1).

3.4.5 [^9Be], [^{10}Be], and ($^{10}\text{Be}/^9\text{Be}$) measured on stream water

Dissolved ^9Be concentrations in the stream waters vary between the individual subcatchments (see Table 3.5). P301 reveals with about 5.3 ng l^{-1} the highest [^9Be]_{diss} and P303 and P304 with ca. 2.1 and 2.6 ng l^{-1} , respectively, the lowest concentrations. The PIG stream water sample that averages over these three subcatchments has a [^9Be]_{diss} of about 3.5 ng l^{-1} . [^9Be]_{diss} in the stream water of the D102 catchment, that is located outside Providence Creek, is 4.9 ng l^{-1} . Meteoric [^{10}Be]_{diss} is also highest at P301 with $3240 \text{ atoms g}^{-1}$ and lowest at P303 and P304 with 910 and 1100 atoms g^{-1} , respectively. In the PIG stream water [^{10}Be]_{diss} is $2100 \text{ atoms g}^{-1}$ and the D102 stream water has a [^{10}Be]_{diss} of $1670 \text{ atoms g}^{-1}$. ($^{10}\text{Be}/^9\text{Be}$)_{diss} calculated using these concentrations show a similar pattern in variability. P301 and PIG stream waters show the highest ($^{10}\text{Be}/^9\text{Be}$)_{diss} with $92 \pm 8 \times 10^{-10}$ and $89 \pm 8 \times 10^{-10}$, respectively (see Table 3.5). ($^{10}\text{Be}/^9\text{Be}$)_{diss} of the P303 and P304 stream waters are

$66 \pm 7 \times 10^{-10}$ and $34 \pm 6 \times 10^{-10}$, respectively. The lowest ($^{10}\text{Be}/^9\text{Be}$)_{diss} of $52 \pm 5 \times 10^{-10}$ is obtained for the D102 stream water.

Table 3.5: ^{10}Be and ^9Be concentration measured in stream water and calculated dissolved $^{10}\text{Be}/^9\text{Be}$ ratio

Sample name	Sample type	Elevation range	Catchment area	Discharge ¹	Stream water pH	[^9Be]	[^{10}Be]	($^{10}\text{Be}/^9\text{Be}$) _{diss}
		(m)	(km ²)	(l s ⁻¹)		(ng l ⁻¹)	(atoms g ⁻¹)	(x 10 ⁻¹⁰)
P301	Stream Water	1790-2115	0.99	36	6.5	5.26 ± 0.41	3240 ± 140	92.1 ± 8.2
P303	Stream Water	1730-1990	1.32	36	6.7	2.07 ± 0.16	914 ± 60	66.1 ± 6.7
P304	Stream Water	1770-1970	0.49	17	7.3	2.58 ± 0.20	1100 ± 70	63.7 ± 6.3
PIG	Stream Water	1660-2100	4.60	219	7.2	3.51 ± 0.27	2090 ± 110	89.1 ± 8.4
D102	Stream Water	1485-1980	1.21	17	7.4	4.85 ± 0.37	1670 ± 90	51.6 ± 4.9

¹ Discharge averaged over a time span of 30 days around date of sampling in spring. Discharge data are from the Southern Sierra CZO dataset (provided by Dr. C. Hunsaker; <http://criticalzone.org/sierra/data/datasets/>).

3.4.6 [^9Be]_{parent} in the bedrock

The ^9Be concentration from six parent bedrock samples is on average about 1.1 ± 0.1 ppm, ranging between 0.91 and 1.22 ppm Be (see Appendix A.3.2).

3.5 Discussion

3.5.1 Weathering indices (Balsam Profile)

Considering the chemical weathering indices, the CDF and the element-mass-transfer coefficient τ , for the Balsam regolith profile, there is a distinct difference between the saprolite and the soil visible (see Figure 3.10). The soil is weathered more intensively than the saprolite, indicated by higher CDF values of about 0.5 in the soil compared to values of about 0.3 in the saprolite (see Figure 3.10 A). Throughout the saprolite profile itself no trend in CDF is resolved. There is one group of elements that stays at constantly depleted τ -values throughout the saprolite but reveals slightly more negative values in the soil. This group comprises besides Be also Al, Mg, Si, and K (see Figure 3.10 B, C). These constant τ -values throughout the saprolite suggest that the depletion of these elements has occurred at the weathering front beneath the profile and no significant additional depletion takes place within the saprolite. The loss of beryllium from its τ -values is reflecting the CDF, meaning that beryllium is lost proportional to the total chemical loss of the major elements. In forest soils the

presence of organic ligands leads to the dissolution of oxides and minerals, providing a mechanism for the lowest τ -values for some elements in the uppermost soil (Brantley and White, 2009). The pattern of τ_{Fe} shows that Fe is enriched in the upper saprolite, suggesting increased formation of e.g. Fe-oxides in this part of the profile. The elements Na, Ca, and Sr comprise another group that is in general markedly more depleted and are continuously lost throughout the saprolite profile (see Figure 3.10 B) due to e.g. weathering of feldspars. Given the relatively high denudation rates, the studied profile is a “kinetically limited” weathering system such that e.g. plagioclase that releases Na and Ca is not fully weathered and leaching of these cations is not complete (Dixon and von Blanckenburg, 2012; West et al., 2005).

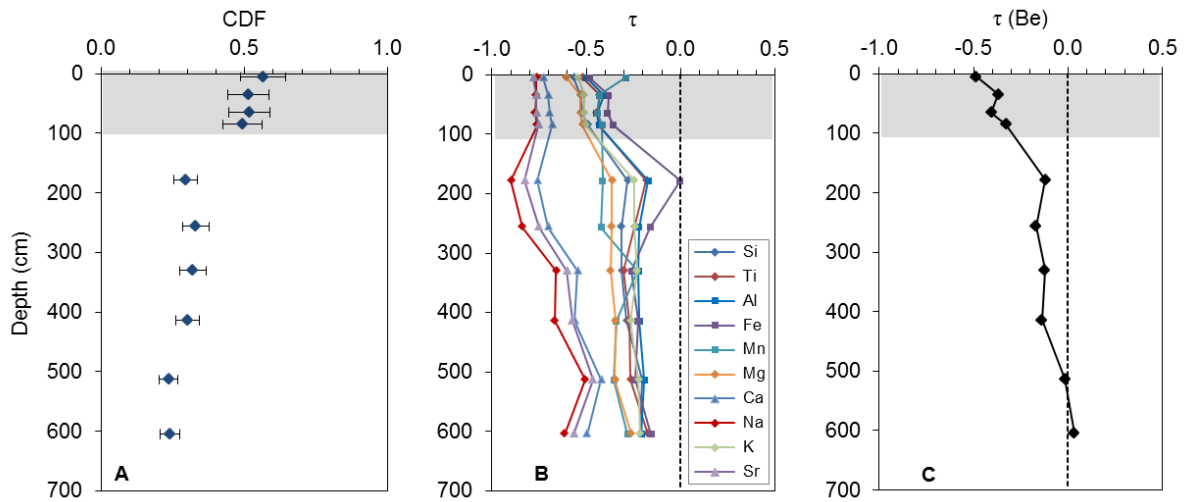


Figure 3.10: A: CDF (chemical depletion fraction), B: τ plots (element-mass transfer coefficient) for major elements, C: τ_{Be} , all determined on the samples of the Balsam regolith profile. CDF and τ for the major elements were calculated from XRF data (*Data Set GFZ Potsdam, Sec. 3.3*) and τ_{Be} is calculated from total beryllium concentrations measured on an ICP-OES. Shaded in grey are the soil samples.

3.5.2 Characterisation of the extracted phases

The concentration of reactive meteoric ^{10}Be is gradually decreasing from surface to depth throughout the Balsam regolith profile. This general profile shape is expected as ^{10}Be is deposited at the Earth’s surface where it is highly particle reactive in neutral environments and is directly adsorbed to surfaces of secondary oxides and clay minerals (Willenbring and von Blanckenburg, 2010b). Although intensively weathered, the soil profiles are only weakly developed with regard to soil horizons (Johnson et al., 2011). This lack of distinct soil horizons is reflected in ^{10}Be concentrations of the reactive phase that are continuously decreasing within the soil. For example, the translocation of clays and the formation of clay-rich horizons would lead to a “bulge” shaped profile with certain maxima in

[^{10}Be] (e.g. Bacon et al. (2012); Ebert et al. (2012); Graly et al. (2010); Jagercikova et al. (2015)) that is not observed here. The depth distribution of [^9Be]_{reac} is more complex. While [^9Be]_{total} and [^9Be]_{am-ox} are constant throughout the whole regolith, there is a clear offset from roughly uniform lower [^9Be]_{reac} in the soil towards much higher [^9Be]_{reac} in the upper saprolite, from where [^9Be]_{reac} again decreases with increasing depth. This increase from the soil to the saprolite is induced by [^9Be]_{x-ox} that is highest in the upper saprolite samples but markedly lower in the overlying soil. To assess whether this change in beryllium concentrations is reflected in the elemental composition of the extracted phases, I characterized these by normalizing the major elemental concentrations in the am-ox phase, the x-ox phase, and the reactive phase to total element concentrations (see Figure 3.11). From this characterisation, specific patterns are observed. (1) Within the saprolite and the soil, respectively, the distribution of the individual elements in the reactive phases is roughly uniform. Only Be and Fe are increasing with decreasing saprolite depth, which is potentially a result of increased formation of Fe-oxides in the upper saprolite. (2) Considering the upper four soil samples (SN59 to SN62), Fe, Mn and Be are the main components of the leached phases in these samples, suggesting that mainly authigenic phases such as Fe- and Mn- (hydro)oxides were extracted. (3) The elemental distribution in the amorphous oxide phase of the saprolite samples is similar. In the x-ox phase of these saprolite samples (SN14 to SN20), however, occur besides Fe, Mn, Ti, and Be exceptionally high amounts of Mg and K. As these elements do not occur in crystalline oxide phases their sources are most probably highly weathered or hydrated biotite or poorly developed clay minerals like vermiculite that were potentially partially dissolved in this hydroxylamine-hydrochloride step. A second observation that can be made is that while most elements of the x-ox phase comprise less than 10% of the total in soil samples, overall proportions are much larger in the saprolite samples compared (see Figure 3.11). In the soil samples all extractable elements are higher concentrated in the am-ox phase than in the x-ox phase; this distribution is reversed for the saprolite samples. (4) Both the normalized distribution and the actual concentration of the major elements (see Table 3.6) and of ^9Be are higher in the mineral-bound phase of the soil than the saprolite samples. However, it is not clear, whether these observations at the soil-saprolite transition are actually real or if they are caused by uncertainties in the reproducibility of the applied sequential extraction procedure (see Section 3.4.4). If the observed pattern are real, a possible explanation could be the dissolution of secondary oxides and minerals in the soil horizons from weathering in such a way that primary minerals (accessed by the “min” fraction) are concentrated. This explanation is supported by evaluating the τ -values of elements present in secondary phases (see Section 3.5.1). These values decrease at the transition from the saprolite into the soil, indicating further depletion of those elements (see Figure 3.10). A second explanation might be potential external input from e.g. aeolian material or soil material that is not *in situ* formed but laterally translocated by e.g. soil creep processes (Dixon et al., 2009b; Riebe et al., 2001b).

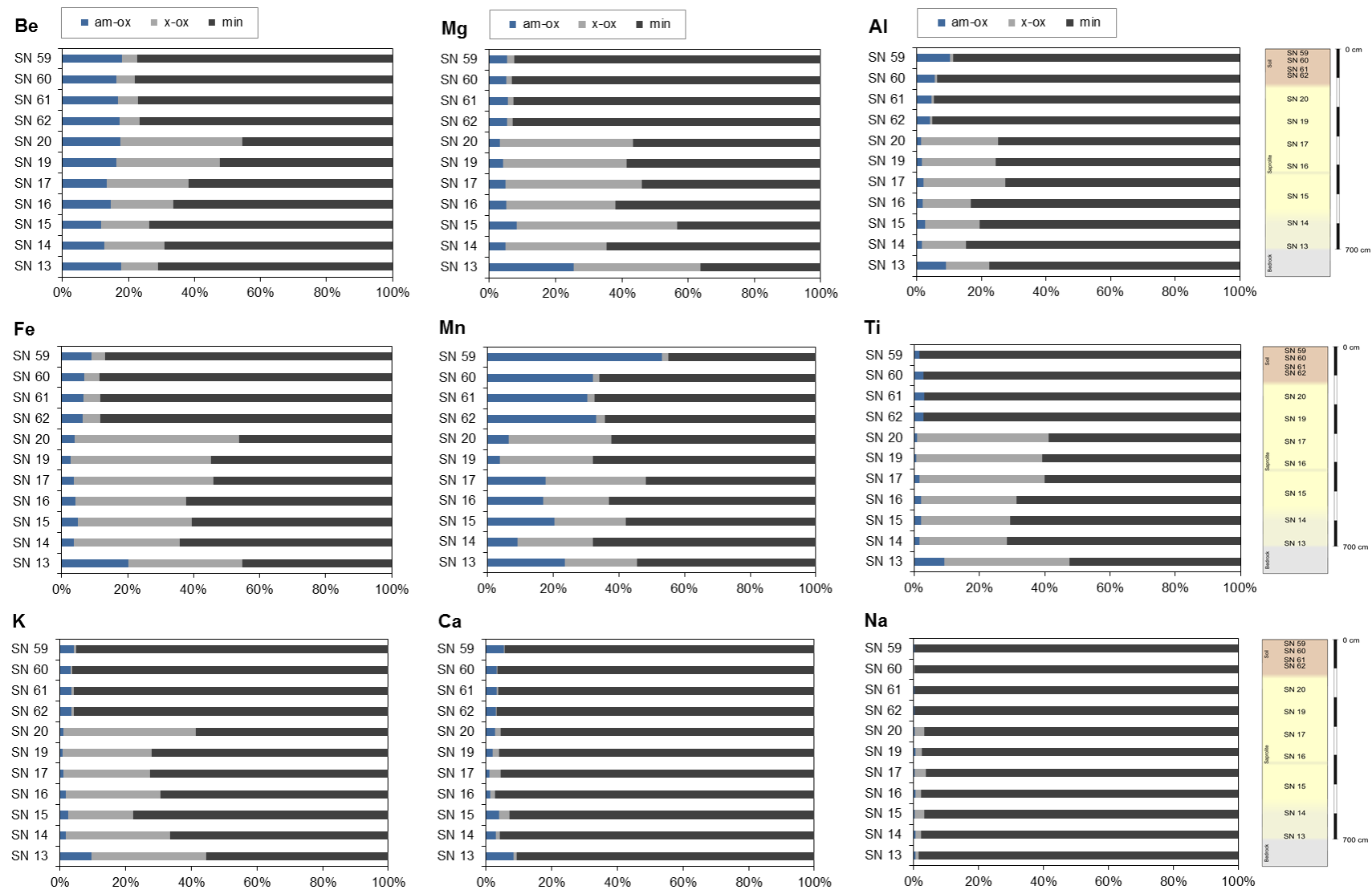


Figure 3.11: Distribution (normalized to 100%) of an element (Be, Fe, Al, Mg, K, Ca) between the extracted fractions (am-ox and x-ox), and the residual min fraction in the BP profile.

Table 3.6: Element concentration measured in the single extracted phases and the residual fraction of the Balsam regolith profile BP (in $\mu\text{g g}^{-1}$)

Lab ID	Sample type	Depth (cm)	(Extracted) fraction	Fe ($\mu\text{g g}^{-1}$)	Mn ($\mu\text{g g}^{-1}$)	Al ($\mu\text{g g}^{-1}$)	Ca ($\mu\text{g g}^{-1}$)	Na ($\mu\text{g g}^{-1}$)	Ti ($\mu\text{g g}^{-1}$)	K ($\mu\text{g g}^{-1}$)	Mg ($\mu\text{g g}^{-1}$)
SN 59	Soil	20	am-ox	4370 \pm 230	532 \pm 28	8370 \pm 440	1130 \pm 60	24.0 \pm 1.2	54.0 \pm 2.8	646 \pm 34	780 \pm 41
			x-ox	2040 \pm 110	19.4 \pm 1.0	767 \pm 40	57 \pm 3	11.22 \pm 0.58	1.070 \pm 0.056	105 \pm 5	308 \pm 16
			min	42350 \pm 2200	449 \pm 23	72560 \pm 3770	19700 \pm 1020	10170 \pm 530	3220 \pm 170	14820 \pm 770	13240 \pm 690
SN 60	Soil	30	am-ox	3860 \pm 200	248 \pm 13	5210 \pm 270	777 \pm 40	23.4 \pm 1.2	96.5 \pm 5.0	501 \pm 26	859 \pm 45
			x-ox	2660 \pm 140	15.2 \pm 0.8	759 \pm 39	69 \pm 4	11.51 \pm 0.60	0.877 \pm 0.046	79 \pm 4	277 \pm 14
			min	50290 \pm 2620	513 \pm 27	88070 \pm 4580	23850 \pm 1240	11160 \pm 580	3500 \pm 180	15040 \pm 780	15500 \pm 810
SN 61	Soil	47	am-ox	3840 \pm 200	225 \pm 12	4000 \pm 210	747 \pm 39	23.8 \pm 1.2	111.6 \pm 5.8	557 \pm 29	898 \pm 47
			x-ox	2800 \pm 150	16.7 \pm 0.9	682 \pm 35	66 \pm 3	8.93 \pm 0.46	0.867 \pm 0.045	94 \pm 5	275 \pm 14
			min	50550 \pm 2630	502 \pm 26	82730 \pm 4300	21550 \pm 1120	9700 \pm 500	3500 \pm 180	15280 \pm 790	15070 \pm 780
SN 62	Soil	106	am-ox	3540 \pm 180	245 \pm 13	3950 \pm 210	712 \pm 37	25.8 \pm 1.3	99.0 \pm 5.2	575 \pm 30	852 \pm 44
			x-ox	2910 \pm 150	19.9 \pm 1.0	700 \pm 36	60 \pm 3	13.17 \pm 0.68	0.828 \pm 0.043	95 \pm 5	272 \pm 14
			min	48410 \pm 2520	476 \pm 25	91350 \pm 4750	23370 \pm 1220	11770 \pm 610	3360 \pm 170	15350 \pm 800	14700 \pm 760
SN 20	Saprolite	178	am-ox	2590 \pm 130	51.4 \pm 2.7	1488 \pm 77	456 \pm 24	24.1 \pm 1.3	57.3 \pm 3.0	241 \pm 13	546 \pm 28
			x-ox	33310 \pm 1730	248 \pm 13	25160 \pm 1310	254 \pm 13	171.7 \pm 8.9	2590 \pm 130	8440 \pm 440	6890 \pm 360
			min	30970 \pm 1610	493 \pm 26	79300 \pm 4120	15510 \pm 810	5540 \pm 290	3780 \pm 200	12349 \pm 640	9660 \pm 500
SN 19	Saprolite	257	am-ox	1710 \pm 90	32.7 \pm 1.7	1637 \pm 85	453 \pm 24	39.5 \pm 2.1	44.0 \pm 2.3	186 \pm 10	816 \pm 42
			x-ox	26280 \pm 1370	248 \pm 13	23970 \pm 1250	421 \pm 22	173.3 \pm 9.0	2410 \pm 130	5660 \pm 290	7270 \pm 380
			min	33850 \pm 1760	595 \pm 31	78860 \pm 4100	20680 \pm 1080	7990 \pm 420	3810 \pm 200	15190 \pm 790	11460 \pm 600
SN 17	Saprolite	330	am-ox	1820 \pm 90	186 \pm 10	2080 \pm 110	360 \pm 19	47.3 \pm 2.5	80.8 \pm 4.2	181 \pm 9	853 \pm 44
			x-ox	20840 \pm 1080	324 \pm 17	25560 \pm 1330	1074 \pm 56	535.6 \pm 27.8	2100 \pm 110	5260 \pm 270	7140 \pm 370
			min	26600 \pm 1380	547 \pm 28	73120 \pm 3800	30170 \pm 1570	14810 \pm 770	3280 \pm 170	14350 \pm 750	9360 \pm 490
SN 16	Saprolite	414	am-ox	1950 \pm 100	145.7 \pm 7.6	1950 \pm 100	420 \pm 22	75.2 \pm 3.9	104.8 \pm 5.4	341 \pm 18	795 \pm 41
			x-ox	15410 \pm 800	169.8 \pm 8.8	14690 \pm 760	427 \pm 22	284.3 \pm 14.8	1480 \pm 77.0	5400 \pm 280	5190 \pm 270
			min	28540 \pm 1480	541 \pm 28	83400 \pm 4340	29570 \pm 1540	15450 \pm 800	3480 \pm 180	13010 \pm 680	9760 \pm 510
SN 15	Saprolite	513	am-ox	1980 \pm 100	139.7 \pm 7.3	2090 \pm 110	1213 \pm 63	55.1 \pm 2.9	91.2 \pm 4.7	398 \pm 21	814 \pm 42
			x-ox	13590 \pm 710	150 \pm 8	14320 \pm 740	979 \pm 51	516.5 \pm 26.9	1260 \pm 65.4	3320 \pm 170	4830 \pm 250
			min	23990 \pm 1250	399 \pm 21	67540 \pm 3510	28810 \pm 1500	16100 \pm 840	3230 \pm 170	12950 \pm 670	4300 \pm 220
SN 14	Saprolite	605	am-ox	1810 \pm 90	84.4 \pm 4.4	1650 \pm 86	1082 \pm 56	99.9 \pm 5.2	88.1 \pm 4.6	294 \pm 15	880 \pm 46
			x-ox	16170 \pm 840	214 \pm 11	13180 \pm 690	502 \pm 26	321.5 \pm 16.7	1475.6 \pm 76.7	5600 \pm 290	5400 \pm 280
			min	32240 \pm 1680	635 \pm 33	82760 \pm 4300	35100 \pm 1830	17200 \pm 890	3970 \pm 210	11710 \pm 610	11430 \pm 590
SN 13	Saprolite	688	am-ox	10280 \pm 530	192 \pm 10	7170 \pm 370	3160 \pm 160	100.6 \pm 5.2	514.5 \pm 26.8	1389 \pm 72	4040 \pm 210
			x-ox	17450 \pm 910	180.1 \pm 9.4	10830 \pm 560	347 \pm 18	211.1 \pm 11.0	2190 \pm 110	5070 \pm 260	6100 \pm 320
			min	23010 \pm 1200	446 \pm 23	62400 \pm 3240	34130 \pm 1770	18230 \pm 950	2970 \pm 150	8080 \pm 420	5760 \pm 300

3.5.3 (^{10}Be)_{meteoric} in the mineral-bound phase

In the mineral-bound residual fraction of the soil and saprolite samples high concentrations of meteoric ^{10}Be were measured (see Section 3.4.1 and 3.4.2). However, by definition there is no mineral-bound meteoric ^{10}Be present in the residual fraction (von Blanckenburg et al., 2012). I offer four possible explanations why $[^{10}\text{Be}]_{\text{min}}$ is still present in this phase: (1) The measured beryllium concentration is governed by *in situ*-produced ^{10}Be present in quartz minerals. Dixon et al. (2009b) measured *in situ* ^{10}Be concentrations of about 1 to 3×10^5 atoms g^{-1} in soil samples at depths of 60 to 110 cm at Providence Creek. The absorption depth scale in soils is commonly about 140 cm meaning that at this depth the cosmic ray intensity is reduced by a factor of $1/e$. Although $[^{10}\text{Be}]_{\text{min}}$ measured in the lower three samples in the saprolite is in the order of *in situ* $[^{10}\text{Be}]$ it is thus unlikely that these concentrations reflect *in situ* ^{10}Be nuclides as the samples are from depths deeper than 400 cm. (2) A methodological explanation could be that the sequential extraction procedure applied here to extract beryllium was not complete such that not all secondary oxides were dissolved by the hydroxylamine-hydrochloride step. (3) Alternatively, ^{10}Be is built into the structure of the secondary clay mineral phases that are not attacked by the extraction steps but were destroyed in the final HF digestion. (4) Depending on their weathering degree, primary minerals like biotite, and additionally (intermediate) weathering products, like vermiculite, were potentially attacked to varying degrees by the applied leaching procedure. Considering possibilities (3) and (4), it is essential that beryllium is not only present in the reactive but is also incorporated into the residual phase while it is forming. During initial weathering of the prevailing biotite-bearing granitic bedrock, ion exchange occurs within the interlayer of the biotite that leads to partial alteration and expansion of the mineral (Graham et al., 2010; Wahrhaftig, 1965). At this early stage of biotite alteration commonly hydrobiotite or vermiculite are formed by oxidation of Fe^{2+} to Fe^{3+} , depletion of K^+ from interlayer sites, and retention and incorporation of Mg^{2+} (Blum et al., 1994). The expansion of the mineral structure shatters the granitic bedrock and new pathways for water percolation are generated such that the surface area for weathering reactions is increased and hydrolysis becomes an important weathering process (Graham et al., 2010; Wahrhaftig, 1965). Prevailing feldspars are less altered and only plagioclase is weathered preferentially to clay minerals, such as kaolinite, and gibbsite (Graham and O'Geen, 2010; Wahrhaftig, 1965). Because of the chemical similarity beryllium can e.g. undergo isomorphic substitution with Al or Si in tetrahedral positions of secondary clay minerals (Romney and Childress, 1965; Veselý et al., 2002). Summarized beryllium isotopes are potentially not only adsorbed to exchange sites but also incorporated into the structure of some of the weathering products (Sudo et al., 1981).

The ^9Be concentrations measured in the x-ox phase of the San Joaquin Reference Soil (see Section 3.4.4) vary highly, revealing a rather low reproducibility of this leach step with regard to soil material. Wilson et al. (2013) found in sequential acid-reductive leaching experiments that the extraction with hydroxylamine is highly sensitive to time; becoming apparent by significant increases in Fe and Al concentrations with time. This uncertainty regarding the reproducibility and the completeness of the applied sequential leaching procedure leads to unreliable concentrations of the reactive and the mineral-bound phase. For that reason, further calculations using these concentration values are not carried out here. These calculations would encompass the calculation of the denudation rate using Equation 1.16 that requires the knowledge of $(^{10}\text{Be}/^9\text{Be})_{\text{reac}}$ but also of $[^9\text{Be}]_{\text{min}}$ and $[^9\text{Be}]_{\text{reac}}$, and the calculation of $f_{\text{reac}}^{^9\text{Be}} + f_{\text{diss}}^{^9\text{Be}}$ within the regolith profile. For example, $f_{\text{reac}}^{^9\text{Be}} + f_{\text{diss}}^{^9\text{Be}}$ that describes the degree to which ^9Be is released from primary minerals and that is calculated from $[^9\text{Be}]_{\text{reac}}$ and $[^9\text{Be}]_{\text{min}}$ (see Section 1.2.2) would be biased towards lower values if $[^9\text{Be}]_{\text{reac}}$ is underestimated and $[^9\text{Be}]_{\text{min}}$ overestimated. Similarly, the calculated $(^{10}\text{Be}/^9\text{Be})_{\text{reac}}$ ratios would be biased and do not present actual ratios. However, provided that the sequential extraction procedure was incomplete, the mineral-bound phase was not attacked. In that case, both $[^{10}\text{Be}]_{\text{x-ox}}$ and $[^9\text{Be}]_{\text{x-ox}}$, and hence $[^{10}\text{Be}]_{\text{reac}}$ and $[^9\text{Be}]_{\text{reac}}$ were measured too low. On the assumption that any fractionation between ^{10}Be and ^9Be is negligible, the reactive ratios calculated from these concentration values should then still be real.

3.5.4 Equilibrium between dissolved and reactive phases

The overall low dissolved ^{10}Be and ^9Be concentrations in the stream waters are ascribed to neutral stream water pH values of about 6.5 to 7.4 in the studied catchments. Considering the dissolved concentrations in the PIG stream water, which covers the whole Providence Creek catchment by integrating all subcatchments, these seem to reflect a proportional mixture of all three subcatchment streams (see Table 3.5). In the case of the PIG stream where I determined $(^{10}\text{Be}/^9\text{Be})$ in the dissolved form in stream water and in the reactive fraction of bedload sediment, I am able to discuss whether these phases are in equilibrium. Accordingly, $(^{10}\text{Be}/^9\text{Be})_{\text{reac/am-ox/x-ox}}$ were plotted versus $(^{10}\text{Be}/^9\text{Be})_{\text{diss}}$ in Figure 3.12. $(^{10}\text{Be}/^9\text{Be})_{\text{reac}}$ agrees with $(^{10}\text{Be}/^9\text{Be})_{\text{diss}}$ within uncertainty. Regarding the individually extracted phases, the amorphous oxide phase is in equilibrium with the dissolved phase, and also the “crystalline oxide phase” can be considered in equilibrium with the dissolved phase, all within uncertainty. This equilibrium between all phases is supported by the observation that both ratios, $(^{10}\text{Be}/^9\text{Be})_{\text{am-ox}}$ and $(^{10}\text{Be}/^9\text{Be})_{\text{x-ox}}$, are the same at certain depths of the regolith and the soil profile (see Section 3.4.1 and 3.4.2).

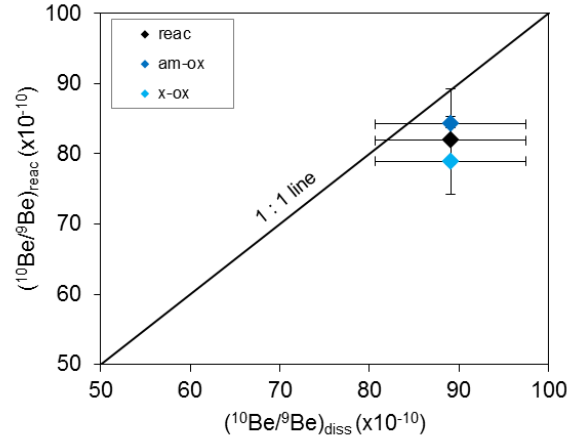


Figure 3.12: $(^{10}\text{Be}/^9\text{Be})_{\text{am-ox}}$, $(^{10}\text{Be}/^9\text{Be})_{\text{x-ox}}$, and $(^{10}\text{Be}/^9\text{Be})_{\text{reac}}$ determined on bedload sediment of the Providence Creek catchment versus $(^{10}\text{Be}/^9\text{Be})_{\text{diss}}$ measured in stream water of this catchment (sample name “PIG”). Error bars display the uncertainty of the concentration measurements.

3.5.5 Balance of meteoric ^{10}Be input and output fluxes

To test whether meteoric ^{10}Be fluxes are in steady state considering the Providence Creek catchment, I balanced the atmospheric flux of meteoric ^{10}Be deposited at the surface area of the catchment ($J_{\text{atm}}^{10\text{Be}}$) with the flux of ^{10}Be that is transported in the dissolved and particulate form in the PIG stream ($J_{\text{stream}}^{10\text{Be}}$; see Table 3.7). The depositional flux of meteoric ^{10}Be is $1.20 \pm 0.41 \times 10^6 \text{ atoms cm}^{-2} \text{ y}^{-1}$ (Heikkilä and von Blanckenburg, 2015) for Sierra Nevada sites (see Section 1.1.2). $J_{\text{atm}}^{10\text{Be}}$ is calculated using Equation 1.1 and the calculation of $J_{\text{stream}}^{10\text{Be}}$ is done by using Equation 1.2. To calculate the particulate flux I used $[^{10}\text{Be}]_{\text{total}}$ and an erosion rate of $91 \pm 13 \text{ mm ky}^{-1}$ from Dixon et al. (2009b). The resulting fluxes are given in Table 3.7. Since $J_{\text{stream}}^{10\text{Be}}/J_{\text{atm}}^{10\text{Be}}$ is about 0.8 ± 0.3 , the meteoric ^{10}Be fluxes are in steady state within in the uncertainty, meaning that the summed particulate and dissolved exported ^{10}Be fluxes agree with the depositional atmospheric ^{10}Be flux.

Table 3.7: Catchment-wide ^{10}Be mass balance fluxes

Sample name	$J_{\text{atm}}^{10\text{Be}}$ ¹	$J_{\text{diss}}^{10\text{Be}}$ ²	$J_{\text{reac}}^{10\text{Be}}$ ^{2, 3}	$J_{\text{stream}}^{10\text{Be}}$ ⁴	$J_{\text{stream}}^{10\text{Be}}/J_{\text{atm}}^{10\text{Be}}$
	($10^{15} \text{ atoms y}^{-1}$)	($10^{15} \text{ atoms y}^{-1}$)	($10^{15} \text{ atoms y}^{-1}$)	($10^{15} \text{ atoms y}^{-1}$)	
PIG	55 ± 19	14.42 ± 0.79	31.8 ± 4.7	46.2 ± 4.7	0.83 ± 0.29

¹ Depositional ^{10}Be flux normalized to the surface area of each catchment calculated with Equation 1.1.

² Dissolved and particulate flux calculated with Equation 1.3.

³ Particulate flux calculated with $[^{10}\text{Be}]_{\text{total}}$ and an erosion rate of $91.1 \pm 13.4 \text{ mm ky}^{-1}$ (from Dixon et al. (2009b)).

⁴ Total exported ^{10}Be flux calculated with Equation 1.2.

3.5.6 Denudation and erosion rates

As the fluxes of meteoric ^{10}Be into and out of the Providence Creek catchment are at steady state (see Section 3.5.5), I am able to calculate a catchment-wide denudation rate D . A total denudation rate that integrates over a whole catchment can be calculated with the total $^{10}\text{Be}/^9\text{Be}$ ratio measured on the bulk solid material exported from a weathering system (see Equation 1.18; von Blanckenburg et al. (2012)). I determined a denudation rate with $(^{10}\text{Be}/^9\text{Be})_{\text{total}}$ measured on bedload sediment ($< 2 \text{ mm}$) of the Providence Creek catchment at sampling point PIG $((^{10}\text{Be}/^9\text{Be})_{\text{total}} = 14.8 \times 10^{-10}$; see Section 3.4.3), a depositional meteoric ^{10}Be flux of $1.20 \pm 0.41 \times 10^6 \text{ atoms cm}^{-2} \text{ y}^{-1}$ (see Section 1.1.2), and a $[^9\text{Be}]_{\text{parent}}$ of 1.1 ppm (see Section 3.4.6). The resulting catchment-wide denudation rate is about $113 \pm 41 \text{ t km}^{-2} \text{ y}^{-1}$ for the Providence Creek catchment, integrating over a time scale of about 150 ky assuming a adsorption depth of meteoric ^{10}Be of 700 cm. This rate is within the range of denudation rates of 99 and $124 \text{ t km}^{-2} \text{ y}^{-1}$ determined from *in situ* ^{10}Be concentrations measured on stream sediment of the three soil-mantled subcatchments (P301, P303, P304) of Providence Creek (Hahm et al., 2014). These *in situ* ^{10}Be -derived denudation rates were corrected for the chemical erosion factor (CEF; Hahm et al. (2014)) that corrects for biases introduced from deep chemical weathering in saprolite (Riebe and Granger, 2013). For comparison, an erosion rate calculated with a $[^{10}\text{Be}]_{\text{total}}$ of $75.1 \times 10^6 \text{ atoms g}^{-1}$ measured on bedload of the Providence Creek at PIG (Equation 1.13) is about $160 \text{ t km}^{-2} \text{ y}^{-1}$. However, this erosion rate is considered to be most likely not representative due to grain-size dependent particle sorting of bedload sediment, which causes erosion rates to be too high, i.e. higher than respective denudation rates (Wittmann et al., 2015).

In the case of the Balsam regolith profile, I calculated a total meteoric ^{10}Be inventory as $[^{10}\text{Be}]_{\text{total}}$ decreases to less than 1% of the surface concentration at the saprolite to bedrock boundary (see Figure 3.5 B; Willenbring and von Blanckenburg (2010b)):

$$I_{^{10}\text{Be}} = \int_{z=0}^z [^{10}\text{Be}]_{\text{total}} * \rho * dz \quad \text{Equation 3.3}$$

The inventory is about $5 \times 10^{10} \text{ atoms cm}^{-2}$ when using a saprolite bulk density of 2.2 g cm^{-3} (Dixon et al., 2009b) and a soil density of 1.4 g cm^{-3} (Johnson et al., 2011). Although, loss of ^{10}Be in the dissolved form is assumed to be low because of soil and stream water pH values of above six such that most ^{10}Be should be retained on the secondary phases in the regolith, this inventory is only a minimum estimate.

Regarding the presence of a steadily eroding setting where the depositional meteoric ^{10}Be flux equals the flux of ^{10}Be exported from the system (see Section 3.5.5), a soil erosion rate can be calculated from a ^{10}Be inventory and a surface ^{10}Be concentration (Willenbring and von Blanckenburg, 2010b):

$$E = \frac{(F_{met}^{10Be} - \lambda * I)}{[^{10}Be]_{surf}} \quad \text{Equation 3.4}$$

where E is the erosion rate ($\text{g cm}^{-2} \text{ y}^{-1}$), F_{met}^{10Be} the depositional ^{10}Be flux ($\text{atoms cm}^{-2} \text{ y}^{-1}$), λ the decay constant (y^{-1}), I the total ^{10}Be inventory (atoms cm^{-2}), and $[^{10}\text{Be}]_{surf}$ the ^{10}Be concentration measured at the soil surface (atoms g^{-1}). To be consistent in units this rate is multiplied with 10^4 to obtain an erosion rate in $\text{t km}^{-2} \text{ y}^{-1}$. Accordingly, a local erosion rate of $54 \pm 18 \text{ t km}^{-2} \text{ y}^{-1}$ is derived from the ^{10}Be inventory for the Balsam profile site. This rate agrees within lower boundaries with erosion rates ranging between 59 and $132 \text{ t km}^{-2} \text{ y}^{-1}$ that were determined on soil profiles of the Providence Creek catchment from *in situ* ^{10}Be -derived soil production rates coupled with soil weathering fractions (Dixon et al., 2009b). Average soil CDF values determined for the Balsam profile site are about 0.52 (see Section 3.5.1), meaning that 52% of the total denudation is attained by chemical weathering and the remaining 48% by physical erosion. At steady state it is assumed that the regolith thickness stays constant and a denudation rate can be derived from the erosion rate and the CDF. This soil denudation rate is then $112 \pm 38 \text{ t km}^{-2} \text{ y}^{-1}$ when taking the inventory-based erosion rate combined with a soil CDF value of 0.52.

Table 3.8: Summary of this study's and published erosion and denudation rates

Site	Balsam Profile/ Providence Creek	Providence Creek
Description	Regolith profiles	Bedload sediment (catchment-wide)
$E_{meteo} (\text{t km}^{-2} \text{ y}^{-1})$	54 ± 18 ¹	160 ± 54 ^{4, 5}
$D_{meteo} (\text{t km}^{-2} \text{ y}^{-1})$	112 ± 38 ²	113 ± 41 ⁶
$D_{in situ} (\text{t km}^{-2} \text{ y}^{-1})$	$220 (140 - 295)$ ³	$112 (99 - 124)$ ⁷

¹ Calculated with Equation 3.4 using the surface ^{10}Be concentration and the ^{10}Be inventory measured for the Balsam Profile.

² Calculated by combining E_{meteo} determined on the regolith profile with a soil CDF value of 0.52.

³ From Dixon et al. (2009b); determined on soil profiles within the Providence Creek catchment by combining *in situ* ^{10}Be -derived soil production rates with CDF values. Average value with range given in parentheses.

⁴ Calculated using Equation 1.13 using $[^{10}\text{Be}]_{total}$ measured on bedload sediment.

⁵ Value is most likely overestimated due to particle sorting and concomitant grain size distribution.

⁶ Calculated using Equation 1.18 and $(^{10}\text{Be}/^9\text{Be})_{total}$ measured on bedload sediment.

⁷ From Hahm et al. (2014); determined on bedload sediment of the three subcatchments of Providence Creek (corrected for CEF). Average value with range given in parentheses.

Published denudation rates determined on regolith profiles of the Providence Creek catchment are however higher, ranging between 140 and $295 \text{ t km}^{-2} \text{ y}^{-1}$ (Dixon et al. (2009b); see Table 3.8). These authors calculated total denudation rates using a mass balance approach that combines *in situ* ^{10}Be -

derived soil production rates with [Zr] in rock, soil, and saprolite. They calculated soil and saprolite weathering rates and determined that about 50% of the total denudation originates from saprolite weathering, apparent by saprolite CDF values of 0.47 to 0.60. In contrast, the saprolite CDF values derived in this study are distinctly lower, on average being 0.29 for the Balsam saprolite. Although Zr is a conservative element generally retained in sediment or rock, its concentration may still vary spatially in the parent bedrock of the study area. I tried to cover this spatial variability and derive a spatially representative [Zr] by using the *GFZ Potsdam* dataset that combines bedrock concentration data from different authors (see Appendix A.3.5). If the CDF values in the previous study by Dixon et al. (2009b) were overestimated due to an unrepresentative bedrock concentration, the denudation rates would be likewise overestimated. Thus, the difference in the denudation rates could potentially arise from the natural variability in [Zr] that is found for the studied sites when considering a larger dataset, or it could be an artefact from spatially-limited sampling. Whatever the cause, I conclude from the fact that the rates derived in this study with meteoric [^{10}Be] and $(^{10}\text{Be}/^9\text{Be})_{\text{total}}$, respectively, agree within (lower) bounds with published rates (see Table 3.8) that my denudation rates provide a reliable estimate of Earth surface denudation. Furthermore, comparing the denudation rate derived for the regolith profile that may be representative for a single hillslope with the catchment-wide denudation rate obtained for the Providence Creek catchment, excellent agreement is observed (see Table 3.8). This leads me to conclude that this method is well suitable to representatively estimate steady state denudation processes from the soil column to the small catchment scale, always provided that geomorphological steady state has been attained.

3.6 Conclusion Sierra Nevada

The Balsam regolith profile located in the Southern Sierra CZO is characterized by a relatively constant weathering degree in the saprolite and the overlying soil, respectively. CDF and τ -values are similar within the soil and the saprolite, respectively, but show a distinct change at the soil-saprolite boundary. This may indicate a change in the mineralogy or weathering degree of the soil material. The transition from the saprolite to the soil is also pronounced in the stable ^9Be data, while meteoric ^{10}Be concentrations and $^{10}\text{Be}/^9\text{Be}$ ratios are consistently decreasing with increasing profile depth. Measured ^{10}Be concentrations and $^{10}\text{Be}/^9\text{Be}$ ratios in the nearby soil profile P301 are constant throughout the soil and higher than at the Balsam profile site. However, it is not clear whether the offset in ^9Be concentrations at the soil-saprolite boundary of the regolith profile is real and (1) originates from e.g. changes in the occurrence of mineral phases or from input of laterally transported soil material or (2) if it is caused by a lack in reproducibility of the applied sequential extraction procedure. Nevertheless, I was able to calculate a total meteoric ^{10}Be inventory measured in the Balsam Profile that is used to calculate an erosion rate of about $54 \text{ t km}^{-2} \text{ y}^{-1}$. When coupled to a soil CDF value of 0.52, a total denudation rate of about $112 \text{ t km}^{-2} \text{ y}^{-1}$ is derived for this regolith site.

The results obtained for the bedload sediment of the Providence Creek catchment that integrates over the analysed soil and saprolite profiles potentially reflect the natural variability in $^{10}\text{Be}/^9\text{Be}$ ratios distributed in the catchment that is also visible when comparing the Balsam to the P301 profile. $^{10}\text{Be}/^9\text{Be}$ ratios determined on the reactive phase of the bedload sediment that are in equilibrium with those of the dissolved phase in stream water, indicated by $(^{10}\text{Be}/^9\text{Be})_{\text{reac}}$ that equals $(^{10}\text{Be}/^9\text{Be})_{\text{diss}}$. Moreover, the flux of meteoric ^{10}Be deposited at the surface area of the catchment and the flux of ^{10}Be exported in the dissolved and particulate form via the streams are balanced. Hence, it is valid to determine a catchment-wide denudation rate with $(^{10}\text{Be}/^9\text{Be})_{\text{total}}$ measured on bedload sediment. This denudation rate is about $113 \text{ t km}^{-2} \text{ y}^{-1}$ which agrees well with that from the regolith profile and is similar to catchment-wide *in situ*-derived denudation rates provided by other authors. This consistence between these rates leads me to the conclusion that the $^{10}\text{Be}(\text{meteoric})/^9\text{Be}$ isotope system can be applied on the hillslope scale in creek scale headwater catchments. To exploit the potential of this proxy on the soil column scale, future studies should include reactive transport models as these will quantitatively establish the mixing of ^{10}Be and ^9Be and will improve our quantitative understanding of environmental processes in the Critical Zone.

Bibliography

- Aldahan, A., Ye, H.P., Possnert, G., 1999. Distribution of beryllium between solution and minerals (biotite and albite) under atmospheric conditions and variable pH. *Chemical Geology*, 156(1-4): 209-229.
- Anderson, S.P., Dietrich, W.E., Brimhall, G.H., 2002. Weathering profiles, mass-balance analysis, and rates of solute loss: Linkages between weathering and erosion in a small, steep catchment. *Geological Society of America Bulletin*, 114(9): 1143-1158.
- Anderson, S.P., von Blanckenburg, F., White, A.F., 2007. Physical and Chemical Controls on the Critical Zone. *Elements*, 3(5): 315-319.
- Bacon, A.R., Richter, D.d., Bierman, P.R., Rood, D.H., 2012. Coupling meteoric ^{10}Be with pedogenic losses of ^9Be to improve soil residence time estimates on an ancient North American interfluvium. *Geology*, 40(9): 847-850.
- Bales, R.C. et al., 2011. Soil Moisture Response to Snowmelt and Rainfall in a Sierra Nevada Mixed-Conifer Forest All rights reserved. No part of this periodical may be reproduced or transmitted in any form or by any means, electronic or mechanical, including photocopying, recording, or any information storage and retrieval system, without permission in writing from the publisher. *gsvadzone*, 10(3): 786-799.
- Banwart, S. et al., 2011. Soil Processes and Functions in Critical Zone Observatories: Hypotheses and Experimental Design. *Vadose Zone Journal*, 10(3): 974-987.
- Barg, E., Lal, D., Pavich, M.J., Caffee, M.W., Southon, J.R., 1997. Beryllium geochemistry in soils: evaluation of $^{10}\text{Be}/^9\text{Be}$ ratios in authigenic minerals as a basis for age models. *Chemical Geology*, 140(3-4): 237-258.
- Bateman, P.C., Wones, D.R., 1972. Geologic map of the Huntington Lake quadrangle, central Sierra Nevada, California. In: Series, U.N. (Editor).
- Bea, F., Montero, P., 1999. Behavior of accessory phases and redistribution of Zr, REE, Y, Th, and U during metamorphism and partial melting of metapelites in the lower crust: an example from the Kinzigite Formation of Ivrea-Verbano, NW Italy. *Geochimica et Cosmochimica Acta*, 63(7-8): 1133-1153.

- Bebout, G.E., Ryan, J.G., Leeman, W.P., 1993. B - Be systematics in subduction-related metamorphic rocks: Characterization of the subducted component. *Geochimica Et Cosmochimica Acta*, 57(10): 2227-2237.
- Bierman, P.R., Nichols, K.K., 2004. Rock to sediment - Slope to sea with Be-10 - Rates of landscape change. *Annual Review of Earth and Planetary Sciences*, 32: 215-255.
- Blecha, V., Stempok, M., 2012. Petrophysical and geochemical characteristics of late Variscan granites in the Karlovy Vary Massif (Czech Republic) - implications for gravity and magnetic interpretation in shallow depths. *Journal of Geosciences*, 57(2): 65-85.
- Blum, J.D., Erel, Y., Brown, K., 1994. $^{87}\text{Sr}/^{86}\text{Sr}$ ratios of Sierra Nevada stream waters: Implications for relative mineral weathering rates. *Geochimica et Cosmochimica Acta*, 57(21-22): 5019-5025.
- Bourlès, D., Raisbeck, G.M., Yiou, F., 1989. ^{10}Be and ^9Be in marine sediments and their potential for dating. *Geochimica Et Cosmochimica Acta*, 53(2): 443-452.
- Brantley, S.L., White, A.F., 2009. Approaches to Modeling Weathered Regolith. *Reviews in Mineralogy and Geochemistry*, 70(1): 435-484.
- Brown, E.T. et al., 1992. Beryllium isotope geochemistry in tropical river basins. *Geochimica Et Cosmochimica Acta*, 56: 1607-1624.
- Brown, L., 1987. ^{10}Be as a tracer of erosion and sediment transport. *Chemical Geology: Isotope Geoscience section*, 65(3-4): 189-196.
- Brown, L., Pavich, M.J., Hickman, R.E., Klein, J., Middleton, R., 1988. Erosion of the eastern United States observed with ^{10}Be . *Earth Surface Processes and Landforms*, 13(5): 441-457.
- Bulmer, C.E., Lavkulich, L.M., 1994. Pedogenic and geochemical processes of ultramafic soils along a climatic gradient in southwestern British Columbia. *Canadian Journal of Soil Science*, 74(2): 165-177.
- Buss, H.L., Sak, P.B., Webb, S.M., Brantley, S.L., 2008. Weathering of the Rio Blanco quartz diorite, Luquillo Mountains, Puerto Rico: Coupling oxidation, dissolution, and fracturing. *Geochimica et Cosmochimica Acta*, 72(18): 4488-4507.
- Büttcher, H., 2001. Random variability or reproducible spatial patterns? Investigating sulphate dynamics in forested catchments with a coupled transport sorption model, Universität Bayreuth.

- Buzek, F., Hruška, J., Krám, P., 1995. Three-component model of runoff generation, Lysina catchment, Czech Republic. *Water, Air, & Soil Pollution*, 79(1): 391-408.
- Caillaud, J., Proust, D., Righi, D., 2006. Weathering sequences of rock-forming minerals in a serpentinite: Influence of microsystems on clay mineralogy. *Clays and Clay Minerals*, 54(1): 87-100.
- Caillaud, J., Proust, D., Righi, D., Martin, F., 2004. Fe-rich clays in a weathering profile developed from serpentinite. *Clays and Clay Minerals*, 52(6): 779-791.
- Chadwick, O.A., Chorover, J., 2001. The chemistry of pedogenic thresholds. *Geoderma*, 100(3-4): 321-353.
- Chmieleff, J., von Blanckenburg, F., Kossert, K., Jakob, D., 2010. Determination of the ^{10}Be half-life by multicollector ICP-MS and liquid scintillation counting. *NIM-B: Beam Interactions with Materials and Atoms*, 268(2): 192-199.
- Cleaves, E.T., Fisher, D.W., Bricker, O.P., 1974. Chemical Weathering of Serpentinite in the Eastern Piedmont of Maryland. *Geological Society of America Bulletin*, 85(3): 437-444.
- Codilean, A.T., Fenton, C.R., Fabel, D., Bishop, P., Xu, S., 2014. Discordance between cosmogenic nuclide concentrations in amalgamated sands and individual fluvial pebbles in an arid zone catchment. *Quaternary Geochronology*, 19: 173-180.
- Cosby, B.J., Ferrier, R.C., Jenkins, A., Wright, R.F., 2001. Modelling the effects of acid deposition: refinements, adjustments and inclusion of nitrogen dynamics in the MAGIC model. *Hydrol. Earth Syst. Sci.*, 5(3): 499-518.
- Cosby, B.J., Hornberger, G.M., Galloway, J.N., Wright, R.F., 1985. Modeling the Effects of Acid Deposition: Assessment of a Lumped Parameter Model of Soil Water and Streamwater Chemistry. *Water Resour. Res.*, 21(1): 51-63.
- Crocket, K.C., Vance, D., Foster, G.L., Richards, D.A., Tranter, M., 2012. Continental weathering fluxes during the last glacial/interglacial cycle: insights from the marine sedimentary Pb isotope record at Orphan Knoll, NW Atlantic. *Quaternary Science Reviews*, 38: 89-99.
- Cudennec, Y., Lecerf, A., 2006. The transformation of ferrihydrite into goethite or hematite, revisited. *Journal of Solid State Chemistry*, 179(3): 716-722.
- Czudek, T., 1993. Pleistocene periglacial structures and landforms in Western Czechoslovakia. *Permafrost and Periglacial Processes*, 4(1): 65-75.

- Dahlgren, R.A., Boettinger, J.L., Huntington, G.L., Amundson, R.G., 1997. Soil development along an elevational transect in the western Sierra Nevada, California. *Geoderma*, 78(3–4): 207-236.
- Dickin, A.P., 2005. *Radiogenic Isotope Geology*, 2. Cambridge University Press, Cambridge.
- Dixon, J.L., Heimsath, A., Kaste, J., Amundson, R., 2009a. Climate-driven processes of hillslope weathering. *Geology*, 37(11): 975-978.
- Dixon, J.L., Heimsath, A.M., Amundson, R., 2009b. The critical role of climate and saprolite weathering in landscape evolution. *Earth Surface Processes and Landforms*, 34(11): 1507-1521.
- Dixon, J.L., Riebe, C.S., 2014. Tracing and Pacing Soil Across Slopes. *Elements*, 10(5): 363-368.
- Dixon, J.L., von Blanckenburg, F., 2012. Soils as pacemakers and limiters of global silicate weathering. *Comptes Rendus Geoscience*, 344(11–12): 597-609.
- Dosseto, A., Schaller, M., 2016. The erosion response to Quaternary climate change quantified using uranium isotopes and in situ-produced cosmogenic nuclides. *Earth-Science Reviews*, 155: 60-81.
- Drever, J.I., 1997. *The geochemistry of natural waters: surface and groundwater environments*, 3rd ed. Englewood Cliffs, N.J. : Prentice-Hall 436 pp.
- Dunai, T.J., 2000. Scaling factors for production rates of in situ produced cosmogenic nuclides: a critical reevaluation. *Earth and Planetary Science Letters*, 176(1): 157-169.
- Ebert, K., Willenbring, J., Norton, K.P., Hall, A., Hattestrand, C., 2012. Meteoric Be-10 concentrations from saprolite and till in northern Sweden: Implications for glacial erosion and age. *Quaternary Geochronology*, 12: 11-22.
- Faure, G., Mensing, M.M., 2004. *Isotopes: Principles and Applications*, 3. John Wiley & Sons, Inc., New Jersey, 896 pp.
- Field, C.V., Schmidt, G.A., Koch, D., Salyk, C., 2006. Modeling production and climate-related impacts on Be-10 concentration in ice cores. *Journal of Geophysical Research-Atmospheres*, 111(D15).
- Finkel, R.C., Nishiizumi, K., 1997. Beryllium 10 concentrations in the Greenland Ice Sheet Project 2 ice core from 3-40 ka. *J. Geophys. Res.*, 102(C12): 26699-26706.

- Fletcher, R.C., Buss, H.L., Brantley, S.L., 2006. A spheroidal weathering model coupling porewater chemistry to soil thicknesses during steady-state denudation. *Earth and Planetary Science Letters*, 244(1–2): 444–457.
- Foster, M.A., Anderson, R.S., Wyshnytzky, C.E., Ouimet, W.B., Dethier, D.P., 2015. Hillslope lowering rates and mobile-regolith residence times from in situ and meteoric ^{10}Be analysis, Boulder Creek Critical Zone Observatory, Colorado. *Geological Society of America Bulletin*.
- Frank, M. et al., 2008. Beryllium isotopes in central Arctic Ocean sediments over the past 12.3 million years: Stratigraphic and paleoclimatic implications. *Paleoceanography*, 23(1): PA1S02.
- Frank, M. et al., 2009. The dissolved Beryllium isotope composition of the Arctic Ocean. *Geochimica Et Cosmochimica Acta*, 73(20): 6114–6133.
- Frey, K.E., Siegel, D.I., Smith, L.C., 2007. Geochemistry of west Siberian streams and their potential response to permafrost degradation. *Water Resources Research*, 43(3): W03406.
- Freyssinet, P., Farah, A.S.d., 2000. Geochemical mass balance and weathering rates of ultramafic schists in Amazonia. *Chemical Geology*, 170(1–4): 133–151.
- Galy, A., France-Lanord, C., 1999. Weathering processes in the Ganges-Brahmaputra basin and the riverine alkalinity budget. *Chemical Geology*, 159(1–4): 31–60.
- Gao, S. et al., 1998. Chemical composition of the continental crust as revealed by studies in East China. *Geochimica et Cosmochimica Acta*, 62(11): 1959–1975.
- Gayer, E., Mukhopadhyay, S., Meade, B.J., 2008. Spatial variability of erosion rates inferred from the frequency distribution of cosmogenic ^3He in olivines from Hawaiian river sediments. *Earth and Planetary Science Letters*, 266(3–4): 303–315.
- Georg, R.B., Reynolds, B.C., Frank, M., Halliday, A.N., 2006. New sample preparation techniques for the determination of Si isotopic compositions using MC-ICPMS. *Chemical Geology*, 235(1–2): 95–104.
- Godsey, S.E., Kirchner, J.W., Clow, D.W., 2009. Concentration–discharge relationships reflect chemostatic characteristics of US catchments. *Hydrological Processes*, 23(13): 1844–1864.
- Gosse, J.C., Phillips, F.M., 2001. Terrestrial in situ cosmogenic nuclides: theory and application. *Quaternary Science Reviews*, 20(14): 1475–1560.

- Govindaraju, K., 1994. Compilation of working values and sample description for 383 Geostandards. *Geostandards Newsletter*, 18: 1-158.
- Govindaraju, K., 1995. Working values with confidence limits for twenty-six CRPG, ANRT and IWG-GIT Geostandards. *Geostandards Newsletter*, 19: 1-32.
- Graham, R.C., O'Geen, A.T., 2010. Soil mineralogy trends in California landscapes. *Geoderma*, 154(3-4): 418-437.
- Graham, w.C., Rossi, A.M., Hubbert, K.R., 2010. Rock to regolith conversion: Producing hospitable substrates for terrestrial ecosystems. *GSA Today*, 20(2): 4-9.
- Graly, J.A., Bierman, P.R., Reusser, L.J., Pavich, M.J., 2010. Meteoric ^{10}Be in soil profiles – A global meta-analysis. *Geochimica Et Cosmochimica Acta*, 74(23): 6814-6829.
- Graly, J.A., Reusser, L.J., Bierman, P.R., 2011. Short and long-term delivery rates of meteoric ^{10}Be to terrestrial soils. *Earth and Planetary Science Letters*, 302(3-4): 329-336.
- Granger, D.E., Riebe, C.S., 2007. Cosmogenic nuclides in weathering and erosion. In: Drever, J.I. (Ed.), *Treatise on Geochemistry. Surface and Ground Water, Weathering, and Soils*. Elsevier, London.
- Granger, D.E., Schaller, M., 2014. Cosmogenic Nuclides and Erosion at the Watershed Scale. *Elements*, 10(5): 369-373.
- Grew, E.S., 2002. Beryllium in Metamorphic Environments (emphasis on aluminous compositions). *Reviews in Mineralogy and Geochemistry*, 50(1): 487-549.
- Grigor'yev, N.A., 1986a. Distribution of Beryllium at the Surface of the Earth. *International Geology Review*, 28(3): 327-371.
- Grigor'yev, N.A., 1986b. Distribution of Beryllium at the Surface of the Earth. *International Geology Review*, 28(2): 127-179.
- Guelke, M., von Blanckenburg, F., Schoenberg, R., Staubwasser, M., Stuetzel, H., 2010. Determining the stable Fe isotope signature of plant-available iron in soils. *Chemical Geology*, 277(3-4): 269-280.
- Haase, D. et al., 2007. Loess in Europe—its spatial distribution based on a European Loess Map, scale 1:2,500,000. *Quaternary Science Reviews*, 26(9-10): 1301-1312.

- Hahm, W.J., Riebe, C.S., Lukens, C.E., Araki, S., 2014. Bedrock composition regulates mountain ecosystems and landscape evolution. *Proceedings of the National Academy of Sciences*, 111(9).
- Heikkilä, U., 2007. Modeling of the atmospheric transport of the cosmogenic radionuclides ^{10}Be and ^7Be using the ECHAM5-HAM General Circulation Model, ETH Zuerich, 148 pp.
- Heikkilä, U., Beer, J., Abreu, J.A., Steinhilber, F., 2013a. On the Atmospheric Transport and Deposition of the Cosmogenic Radionuclides (^{10}Be): A Review. *Space Science Reviews*, 176(1-4): 321-332.
- Heikkilä, U., Phipps, S.J., Smith, A.M., 2013b. ^{10}Be in late deglacial climate simulated by ECHAM5-HAM - Part 1: Climatological influences on ^{10}Be deposition. *Clim. Past*, 9(6): 2641-2649.
- Heikkilä, U., Smith, A.M., 2013. Production rate and climate influences on the variability of ^{10}Be deposition simulated by ECHAM5-HAM: Globally, in Greenland, and in Antarctica. *Journal of Geophysical Research: Atmospheres*, 118(6): 2506-2520.
- Heikkilä, U., von Blanckenburg, F., 2015. The global distribution of Holocene meteoric ^{10}Be fluxes from atmospheric models. Distribution maps for terrestrial Earth surface applications, GFZ Data Services.
- Helz, G.R., Valette-Silver, N., 1992. Beryllium-10 in Chesapeake Bay sediments: An indicator of sediment provenance. *Estuarine, Coastal and Shelf Science*, 34(5): 459-469.
- Holbrook, W.S. et al., 2014. Geophysical constraints on deep weathering and water storage potential in the Southern Sierra Critical Zone Observatory. *Earth Surface Processes and Landforms*, 39(3): 366-380.
- Hovius, N., von Blanckenburg, F., 2007. Constraining the denudational response to faulting. *The Dynamics of Fault Zones*. MIT Press, Cambridge, USA, 231-273 pp.
- Hruška, J., Kram, P., 2003. Modelling long-term changes in stream water and soil chemistry in catchments with contrasting vulnerability to acidification (Lysina and Pluhuv Bor, Czech Republic). *Hydrology and Earth System Sciences*, 7(4): 525-539.
- Jagercikova, M. et al., 2015. Understanding long-term soil processes using meteoric ^{10}Be : A first attempt on loessic deposits. *Quaternary Geochronology*, 27: 11-21.
- Jeandel, C., 1993. Concentration and isotopic composition of Nd in the South Atlantic Ocean. *Earth and Planetary Science Letters*, 117(3-4): 581-591.

- Jelínek, E., Štědrá, V., 1997. Petrology and geochemistry of the Mariánské Lázně Complex. In: Vrána, S., Štědrá, V. (Eds.), Geological model of Western Bohemia related to the KTB borehole in Germany. Czech Geological Survey, Prague, pp. 63-65.
- Jelínek, E., Štědrá, V., Cháb, J., 1997. The Mariánské Lázně complex. In: Vrána, S., Štědrá, V. (Eds.), Geological model of western Bohemia related to the KTB borehole in Germany. Czech Geological Survey, Prague, pp. 61.
- Jessup, B.S., Jesse Hahm, W., Miller, S.N., Kirchner, J.W., Riebe, C.S., 2011. Landscape response to tipping points in granite weathering: The case of stepped topography in the Southern Sierra Critical Zone Observatory. *Applied Geochemistry*, 26, Supplement: S48-S50.
- Johnson, D.W., Hunsaker, C.T., Glass, D.W., Rau, B.M., Roath, B.A., 2011. Carbon and nutrient contents in soils from the Kings River Experimental Watersheds, Sierra Nevada Mountains, California. *Geoderma*, 160(3-4): 490-502.
- Jungers, M.C. et al., 2009. Tracing hillslope sediment production and transport with in situ and meteoric ^{10}Be . *Journal of Geophysical Research*, 114.
- Kirchner, J.W. et al., 2001. Mountain erosion over 10 yr, 10 k.y., and 10 m.y. time scales. *Geology*, 29(7): 591-594.
- Korschinek, G. et al., 2010. A new value for the half-life of ^{10}Be by heavy-ion elastic recoil detection and liquid scintillation counting. *Nuclear Instruments & Methods in Physics Research Section B-Beam Interactions with Materials and Atoms*, 268(2): 187-191.
- Krám, P., Hruška, J., 1994. Influence Of Bedrock Geology On Elemental Fluxes In Two Forested Catchments Affected By High Acidic Deposition. *Hydrogeology Journal*, 2(2): 50-58.
- Krám, P., Hruška, J., Driscoll, C.T., 1998. Beryllium Chemistry in the Lysina Catchment, Czech Republic. *Water, Air, & Soil Pollution*, 105(1): 409-415.
- Krám, P., Hruška, J., Shanley, J.B., 2012. Streamwater chemistry in three contrasting monolithologic Czech catchments. *Applied Geochemistry*, 27(9): 1854-1863.
- Krám, P., Myška, O., Čuřík, J., Veselovský, F., Hruška, J., 2013. Drainage water chemistry in geochemically contrasting catchments. In: R. Stojanov, Z.Ž., P. Cudlín, A. Farda, O. Urban, M. Trnka (Ed.), *Global change and resilience, from impacts to responses*, Global Change Research Centre AS CR. Brno.

- Krám, P. et al., 2009. Geoecology of a Forest Watershed Underlain by Serpentine in Central Europe. *Northeastern Naturalist*, 16(sp5): 309-328.
- Kubik, P.W., Christl, M., 2010. ^{10}Be and ^{26}Al measurements at the Zurich 6 MV Tandem AMS facility. *Nuclear Instruments and Methods in Physics Research Section B- Beam Interactions with Materials and Atoms*, 268: 880-883.
- Lal, D., 1991. Cosmic ray labeling of erosion surfaces: in situ nuclide production rates and erosion models. *Earth and Planetary Science Letters*, 104(2-4): 424-439.
- Lal, D., Peters, B., 1967. Cosmic ray-produced radioactivity on the Earth. In: Fluegge, S. (Ed.), *Handbuch der Physik*. Springer Verlag.
- Lebatard, A.-E. et al., 2010. Application of the authigenic $^{10}\text{Be}/^9\text{Be}$ dating method to continental sediments: Reconstruction of the Mio-Pleistocene sedimentary sequence in the early hominid fossiliferous areas of the northern Chad Basin. *Earth and Planetary Science Letters*, 297(1-2): 57-70.
- Lebedeva, M.I., Fletcher, R.C., Balashov, V.N., Brantley, S.L., 2007. A reactive diffusion model describing transformation of bedrock to saprolite. *Chemical Geology*, 244(3-4): 624-645.
- Lischeid, G., Kram, P., Weyer, C., 2010. Tracing Biogeochemical Processes in Small Catchments Using Non-linear Methods. In: Müller, F., Baessler, C., Schubert, H., Klotz, S. (Ed.), *Long-term Ecological Research - between Theory and Application*. Springer Berlin, pp. 221-242.
- Maher, K., 2011. The role of fluid residence time and topographic scales in determining chemical fluxes from landscapes. *Earth and Planetary Science Letters*, 312(1-2): 48-58.
- Masarik, J., Beer, J., 2009. An updated simulation of particle fluxes and cosmogenic nuclide production in the Earth's atmosphere. *J. Geophys. Res.*, 114.
- McHargue, L.R., Damon, P.E., 1991. The global Beryllium-10 cycle. *Reviews of Geophysics*, 29(2): 141-158.
- Menon, M. et al., 2014. SoilTrEC: a global initiative on critical zone research and integration. *Environmental Science and Pollution Research*, 21(4): 3191-3195.
- Meybeck, M., 1987. Global chemical weathering of surficial rocks estimated from river dissolved loads. *American Journal of Science*, 287(5): 401-428.

- Morel, P., Von Blanckenburg, F., Schaller, M., Kubik, P.W., Hinderer, M., 2003. Lithology, landscape dissection and glaciation controls on catchment erosion as determined by cosmogenic nuclides in river sediment (the Wutach Gorge, Black Forest). *Terra Nova*, 15(6): 398-404.
- Muscheler, R., Beer, J., Vonmoos, M., 2004. Causes and timing of the 8200 yr BP event inferred from the comparison of the GRIP ^{10}Be and the tree ring $\Delta^{14}\text{C}$ record. *Quaternary Science Reviews*, 23(20–22): 2101-2111.
- Muzikar, P., Elmore, D., Granger, D.E., 2003. Accelerator mass spectrometry in geologic research. *Geological Society of America Bulletin*, 115(6): 643-654.
- Navrátil, T., 2000. Beryllium in Waters of Czech Forested Ecosystems and the Release of Beryllium from Granites. *GeoLines*, 12: 18-40.
- Navrátil, T., Kurz, D., Krám, P., Hofmeister, J., Hruška, J., 2007. Acidification and recovery of soil at a heavily impacted forest catchment (Lysina, Czech Republic)—SAFE modeling and field results. *Ecological Modelling*, 205(3–4): 464-474.
- Navrátil, T., Skřivan, P., Minařík, L., Žigová, A., 2002. Beryllium Geochemistry in the Lesní Potok Catchment (Czech Republic), 7 Years of Systematic Study. *Aquatic Geochemistry*, 8(2): 121-133.
- Nishiizumi, K. et al., 2007. Absolute calibration of ^{10}Be AMS standards. *Nuclear Instruments & Methods in Physics Research Section B- Beam Interactions with Materials and Atoms*, 258(2): 403-413.
- Nyffeler, U.P., Li, Y.-H., Santschi, P.H., 1984. A kinetic approach to describe trace-element distribution between particles and solution in natural aquatic systems. *Geochimica Et Cosmochimica Acta*, 48(7): 1513-1522.
- Oliva, P., Viers, J., Dupré, B., 2003. Chemical weathering in granitic environments. *Chemical Geology*, 202(3–4): 225-256.
- Oulehle, F. et al., 2008. Long-Term Trends in Stream Nitrate Concentrations and Losses Across Watersheds Undergoing Recovery from Acidification in the Czech Republic. *Ecosystems*, 11(3): 410-425.
- Paces, T., 1985. Sources of acidification in Central Europe estimated from elemental budgets in small basins. *Nature*, 315(6014): 31-36.

- Paces, T., 1986. Rates of Weathering and Erosion Derived from Mass Balance in Small Drainage Basins. In: Colman, S.M., Dethier, D.P. (Ed.), Rates of Chemical Weathering of Rocks and Minerals. Academic Press, INC. , Orlando, pp. 603.
- Pavich, M.J., Brown, L., Harden, J., Klein, J., Middleton, R., 1986. ^{10}Be distribution in soils from Merced River terraces, California. *Geochimica Et Cosmochimica Acta*, 50(8): 1727-1735.
- Pavich, M.J., Brown, L., Klein, J., Middleton, R., 1984. ^{10}Be accumulation in a soil chronosequence. *Earth and Planetary Science Letters*, 68(2): 198-204.
- Pelletier, L., Müntener, O., Kalt, A., Vennemann, T.W., Belgia, T., 2008. Emplacement of ultramafic rocks into the continental crust monitored by light and other trace elements: An example from the Geisspfad body (Swiss-Italian Alps). *Chemical Geology*, 255(1–2): 143-159.
- Phillips, F.M. et al., 2016. The CRONUS-Earth Project: A synthesis. *Quaternary Geochronology*, 31: 119-154.
- Probst, A., Dambrine, E., Viville, D., Fritz, B., 1990. Influence of acid atmospheric inputs on surface-water chemistry and mineral fluxes in a declining spruce stand within a small granitic catchment (Vosges Massif, France). *Journal of Hydrology*, 116(1-4): 101-124.
- Raab, T., Leopold, M., Völkel, J., 2007. Character, Age, and Ecological Significance of Pleistocene Periglacial Slope Deposits in Germany. *Physical Geography*, 28(6): 451-473.
- Raisbeck, G.M. et al., 1981. Cosmogenic $^{10}\text{Be}/^7\text{Be}$ as a probe of atmospheric transport processes. *Geophysical Research Letters*, 8(9): 1015-1018.
- Regelink, I.C. et al., 2015. Linkages between aggregate formation, porosity and soil chemical properties. *Geoderma*, 247–248: 24-37.
- Regelink, I.C., Weng, L., van Riemsdijk, W.H., 2011. The contribution of organic and mineral colloidal nanoparticles to element transport in a podzol soil. *Applied Geochemistry*, 26: S241-S244.
- Reuss, J.O., Cosby, B.J., Wright, R.F., 1987. Chemical processes governing soil and water acidification. *Nature*, 329(6134): 27-32.
- Reusser, L., Graly, J., Bierman, P., Rood, D., 2010. Calibrating a long-term meteoric ^{10}Be accumulation rate in soil. *Geophysical Research Letters*, 37(19): L19403.

- Riebe, C.S., Granger, D.E., 2013. Quantifying effects of deep and near-surface chemical erosion on cosmogenic nuclides in soils, saprolite, and sediment. *Earth Surface Processes and Landforms*, 38(5): 523-533.
- Riebe, C.S., Kirchner, J.W., Granger, D.E., Finkel, R.C., 2001a. Minimal climatic control on erosion rates in the Sierra Nevada, California. *Geology*, 29(5): 447-450.
- Riebe, C.S., Kirchner, J.W., Granger, D.E., Finkel, R.C., 2001b. Strong tectonic and weak climatic control of long-term chemical weathering rates. *Geology*, 29(6): 511-514.
- Romney, E.M., Childress, J.D., 1965. Effects of beryllium in plants and soils. *Soil Science*, 100(3): 210-217.
- Rudnick, R.L., Gao, S., Heinrich, D.H., Karl, K.T., 2003. Composition of the Continental Crust, *Treatise on Geochemistry*. Pergamon, Oxford, pp. 1-64.
- Ryan, J.G., Langmuir, C.H., 1988. Beryllium systematics in young volcanic rocks: Implications for ^{10}Be . *Geochimica et Cosmochimica Acta*, 52(1): 237-244.
- Schaller, M., von Blanckenburg, F., Hovius, N., Kubik, P.W., 2001. Large-scale erosion rates from in situ-produced cosmogenic nuclides in European river sediments. *Earth and Planetary Science Letters*, 188(3-4): 441-458.
- Schaller, M., von Blanckenburg, F., Veit, H., Kubik, P.W., 2002a. Influence of periglacial cover beds on in situ-produced cosmogenic ^{10}Be in soil sections. *Geomorphology*, 49(3-4): 255-267.
- Schaller, M. et al., 2002b. A 30 000 yr record of erosion rates from cosmogenic Be-10 in Middle European river terraces. *Earth and Planetary Science Letters*, 204(1-2): 307-320.
- Schwertmann, U., Friedl, J., Stanjek, H., 1999. From Fe(III) Ions to Ferrihydrite and then to Hematite. *Journal of Colloid and Interface Science*, 209(1): 215-223.
- Semmel, A., Terhorst, B., 2010. The concept of the Pleistocene periglacial cover beds in central Europe: A review. *Quaternary International*, 222(1-2): 120-128.
- Shen, C. et al., 2004. Grain size distribution, ^{10}Be content and magnetic susceptibility of micrometer-nanometer loess materials. *Nuclear Instruments and Methods in Physics Research Section B: Beam Interactions with Materials and Atoms*, 223-224: 613-617.

- Štědrá, V., Krám, P., Farkaš, J., 2014. Petrology and whole-rock geochemistry of metabasites from borehole cores in the Na Zeleném and Pluhův Bor catchments in the Slavkov Forest, western Bohemia. *Bulletin of Geosciences*, 2014.
- Steinhilber, F. et al., 2012. 9,400 years of cosmic radiation and solar activity from ice cores and tree rings. *Proceedings of the National Academy of Sciences*, 109(16): 5967-5971.
- Stone, J., 1998. A Rapid Fusion Method for Separation of Beryllium-10 From Soils and Silicates. *Geochimica Et Cosmochimica Acta*, 62(3): 555-561.
- Sudo, T., Shimoda, S., Yotsumoto, H., Aita, S., 1981. Crystal morphology and structure of clay minerals, *Electron micrographs of clay minerals*. Elsevier.
- Takahashi, Y., Minai, Y., Ambe, S., Makide, Y., Ambe, F., 1999. Comparison of adsorption behavior of multiple inorganic ions on kaolinite and silica in the presence of humic acid using the multitracer technique. *Geochimica Et Cosmochimica Acta*, 63(6): 815-836.
- Tessier, A., Campbell, P.G.C., Bisson, M., 1979. Sequential extraction procedure for the speciation of particulate trace metals. *Analytical Chemistry*, 51(7): 844-851.
- Tranter, M., 2003. 5.07 - Geochemical Weathering in Glacial and Proglacial Environments. In: Turekian, H.D.H.K. (Ed.), *Treatise on Geochemistry*. Pergamon, Oxford, pp. 189-205.
- Vanmaercke, M., Poesen, J., Verstraeten, G., de Vente, J., Ocakoglu, F., 2011. Sediment yield in Europe: Spatial patterns and scale dependency. *Geomorphology*, 130(3–4): 142-161.
- Vanmaercke, M., Poesen, J., Verstraeten, G., Maetens, W., 2010. Regional differences and scale dependency of sediment yield in Europe, 2nd Joint Federal Interagency Conference, Las Vegas, NV.
- Velbel, M.A., 1992. Geochemical mass balances and weathering rates in forested watersheds of the southern Blue Ridge; III, Cation budgets and the weathering rate of amphibole. *American Journal of Science*, 292(1): 58-78.
- Veselý, J. et al., 2002. Environmental Chemistry of Beryllium. *Reviews in Mineralogy and Geochemistry*, 50(1): 291-317.
- Vils, F., Pelletier, L., Kalt, A., Müntener, O., Ludwig, T., 2008. The Lithium, Boron and Beryllium content of serpentinized peridotites from ODP Leg 209 (Sites 1272A and 1274A): Implications for lithium and boron budgets of oceanic lithosphere. *Geochimica Et Cosmochimica Acta*, 72(22): 5475-5504.

- Viville, D., Chabaux, F., Stille, P., Pierret, M.C., Gangloff, S., 2012. Erosion and weathering fluxes in granitic basins: The example of the Strengbach catchment (Vosges massif, eastern France). *CATENA*, 92: 122-129.
- von Blanckenburg, F., 2005. The control mechanisms of erosion and weathering at basin scale from cosmogenic nuclides in river sediment. *Earth and Planetary Science Letters*, 237(3-4): 462-479.
- von Blanckenburg, F., Belshaw, N.S., O'Nions, R.K., 1996a. Separation of ^9Be and cosmogenic ^{10}Be from environmental materials and SIMS isotope dilution analysis. *Chemical Geology*, 129(1-2): 93-99.
- von Blanckenburg, F., Bouchez, J., 2014. River fluxes to the sea from the ocean's $^{10}\text{Be}/^9\text{Be}$ ratio. *Earth and Planetary Science Letters*, 387: 34-43.
- von Blanckenburg, F., Bouchez, J., Ibarra, D.E., Maher, K., 2015. Stable runoff and weathering fluxes into the oceans over Quaternary climate cycles. *Nature Geosci*, advance online publication.
- von Blanckenburg, F., Bouchez, J., Wittmann, H., 2012. Earth surface erosion and weathering from the ^{10}Be (meteoric)/ ^9Be ratio. *Earth and Planetary Science Letters*, 351–352: 295-305.
- von Blanckenburg, F., Hewawasam, T., Kubik, P.W., 2004. Cosmogenic nuclide evidence for low weathering and denudation in the wet, tropical highlands of Sri Lanka. *Journal of Geophysical Research-Earth Surface*, 109(F3).
- von Blanckenburg, F., O'Nions, R.K., Belshaw, N.S., Gibb, A., Hein, J.R., 1996b. Global distribution of beryllium isotopes in deep ocean water as derived from Fe---Mn crusts. *Earth and Planetary Science Letters*, 141(1-4): 213-226.
- von Blanckenburg, F., Willenbring, J.K., 2014. Cosmogenic Nuclides: Dates and Rates of Earth-Surface Change. *Elements*, 10(5): 341-346.
- Vonmoos, M., Beer, J., Muscheler, R., 2006. Large variations in Holocene solar activity: Constraints from ^{10}Be in the Greenland Ice Core Project ice core. *Journal of Geophysical Research*, 111(A10105).
- Wahrhaftig, C., 1965. Stepped Topography of the Southern Sierra Nevada, California. *Geological Society of America Bulletin*, 76(10): 1165-1190.
- Waychunas, G.A., Kim, C.S., Banfield, J.F., 2005. Nanoparticulate iron oxide minerals in soils and sediments: unique properties and contaminant scavenging mechanisms. *Journal of Nanoparticle Research*, 7(4-5): 409-433.

- West, A.J., Galy, A., Bickle, M., 2005. Tectonic and climatic controls on silicate weathering. *Earth and Planetary Science Letters*, 235(1-2): 211-228.
- West, N. et al., 2013. Regolith production and transport at the Susquehanna Shale Hills Critical Zone Observatory, Part 2: Insights from meteoric ^{10}Be . *Journal of Geophysical Research: Earth Surface*, 118: 1877–1896.
- Willenbring, J.K., von Blanckenburg, F., 2010a. Long-term stability of global erosion rates and weathering during late-Cenozoic cooling. *Nature*, 465: 211-214.
- Willenbring, J.K., von Blanckenburg, F., 2010b. Meteoric cosmogenic Beryllium-10 adsorbed to river sediment and soil: Applications for Earth-surface dynamics. *Earth-Science Reviews*, 98(1-2): 105-122.
- Wilson, D.J., Piotrowski, A.M., Galy, A., Clegg, J.A., 2013. Reactivity of neodymium carriers in deep sea sediments: Implications for boundary exchange and paleoceanography. *Geochimica et Cosmochimica Acta*, 109: 197-221.
- Wilson, M.J., 2004. Weathering of the primary rock-forming minerals: processes, products and rates. *Clay Minerals*, 39(3): 233-266.
- Wittmann, H. et al., 2015. A test of the cosmogenic $^{10}\text{Be}(\text{meteoric})/^{9}\text{Be}$ proxy for simultaneously determining basin-wide erosion rates, denudation rates, and the degree of weathering in the Amazon basin. *J. Geophys. Res. Earth Surf.*, 120: 2498–2528.
- Wittmann, H. et al., 2012. The dependence of meteoric ^{10}Be concentrations on particle size in Amazon River bed sediment and the extraction of reactive $^{10}\text{Be}/^{9}\text{Be}$ ratios. *Chemical Geology*, 318–319(0): 126-138.
- You, C.-F., Lee, T., Li, Y.-H., 1989. The partition of Be between soil and water. *Chemical Geology*, 77(2): 105-118.
- You, C.F., Lee, T., Brown, L., Shen, J.J., Chen, J.C., 1988. ^{10}Be study of rapid erosion in Taiwan. *Geochimica Et Cosmochimica Acta*, 52(11): 2687-2691.
- Zakharova, E.A., Pokrovsky, O.S., Dupré, B., Gaillardet, J., Efimova, L.E., 2007. Chemical weathering of silicate rocks in Karelia region and Kola peninsula, NW Russia: Assessing the effect of rock composition, wetlands and vegetation. *Chemical Geology*, 242(1–2): 255-277.

A Appendix

A	Appendix	117
A.1	Sample preparation and laboratory methodology	118
A.1.1	Detailed description of the sequential extraction procedure	118
A.1.2	Ion exchange chromatography	120
A.1.3	Reference Materials.....	122
A.2	Detailed data set and additional information for the Slavkov Forest sites	126
A.2.1	Detailed results of sequential extraction procedure	126
A.2.2	^{10}Be data (AMS results).....	127
A.2.3	Element concentrations in bedload sediment (XRF analysis).....	132
A.2.4	$(^{10}\text{Be}/^9\text{Be})_{\text{reac}}$ ratio measured on different grain sizes.....	134
A.2.5	Stable $[^9\text{Be}]_{\text{am-ox}}$ measured on bedrock core samples.....	135
A.2.6	Bedrock data set	136
A.2.7	Stream water chemistry	144
A.2.8	^{10}Be inventory at Lysina	144
A.3	Detailed data set and additional information for the Sierra Nevada sites	145
A.3.1	AMS Results	145
A.3.2	$[^9\text{Be}]_{\text{parent}}$ for the Sierra Nevada Sites	152
A.3.3	Reproducibility of the sequential extraction procedure for the Balsam Profile	152
A.3.4	Comparison of meteoric $[^{10}\text{Be}]$ measured in the Providence Creek Catchment.....	156
A.3.5	Background data for chemical weathering indices	156

A.1 Sample preparation and laboratory methodology

A.1.1 Detailed description of the sequential extraction procedure

1. Step: Exchangeable Beryllium (Be)_{ex}

- Weighted about 0.5 to 1 g of sediment or soil to centrifuge tube
- Volumetric addition of 10 ml 1 M $MgCl_2$
- Mild mixing for 12 hours @ room temperature (using a “Hot-Dog Roller”)
- Centrifugation of solution (15 min @ 4000 rpm)
- Pipetting of supernatant and transfer to Teflon beaker (*Savillex*®)
- Evaporation of the supernatant @ 110° C on hotplate
- Redissolving evaporated residue in 1 ml 3 M HNO_3 (QD)
- Transfer to new centrifuge tube and taking weight
- Gravimetric dilution with MilliQ®-H₂O to 10 ml (resulting in 10 ml 0.3 M HNO_3)

2. Step: Amorphous oxides (Be)_{am-ox}

- Volumetric addition of 10 ml 0.5 M HCl
- Mixing for 24 hours @ room temperature
- Centrifugation of solution (15 min @ 4000 rpm)
- Pipetting of supernatant and transfer to Teflon beaker (*Savillex*®)
- Evaporation of the supernatant @ 110° C on hotplate
- Redissolving evaporated residue in 1 ml 3 M HNO_3 (QD)
- Transfer to new centrifuge tube and taking weight
- Gravimetric dilution with MilliQ®-H₂O to 10 ml (resulting in 10 ml 0.3 M HNO_3)

3. Step: Crystalline oxides (Be)_{x-ox}

- Volumetric addition of 10 ml 1 M hydroxylamine-hydrochloride solution in 1 M HCl
- 4 hours @ 70° C in ultrasonic bath with manual overhead shaking every 10 minutes
- Centrifugation of solution (15 min @ 4000 rpm)
- Pipetting of supernatant and transfer to Teflon beaker (*Savillex*®)
- Evaporation of the supernatant @ 110° C on hotplate
- Addition of concentrated HNO_3 and H_2O_2 (30 %, Suprapur®)
- Heating until solution was clear and free of any crystal build up from hydroxylamine solution
- Alternative: Microwave application
 - Transferring supernatant into QS-50 quartz glass vials and evaporate
 - Adding 10 ml MilliQ®- H₂O to sample
 - Placing the QS-50 quartz glass vial in MPV-100 microwave beaker
 - Filling MPV-100 beaker with concentrated HNO_3 (10 ml; surrounding QS-50 quartz glass vial)
 - Run of microwave application
- Transfer sample back to Teflon beaker and evaporation @ 110° C on hotplate
- Redissolving evaporated residue in 1 ml 3 M HNO_3
- Transferring to new centrifuge tube and taking weight
- Gravimetric dilution with MilliQ®-H₂O to 10 ml (resulting in 10 ml 0.3 M HNO_3)

4. Step: Organic-bound beryllium (Be)_{org}

- Volumetric addition of 2 ml 0.01 M HNO₃ and 5 ml H₂O₂ (30 %)
- Homogenization
- 2 hours @ 80° C (in ultrasonic bath, only heat)
- Volumetric addition of 1 ml H₂O₂ (30 %)
- 1 hour @ 80° C
- Volumetric addition of 2 ml 0.01 M HNO₃
- 1 hour @ 80° C
- Centrifugation of solution (15 min @ 4000 rpm)
- Pipetting of supernatant and transfer to Teflon beaker (Savillex®)
- Evaporation of the supernatant @ 110° C on hotplate
- Redissolving evaporated residue in 1 ml 3 M HNO₃ (QD)
- Transfer to new centrifuge tube and taking weight
- Gravimetric dilution with MilliQ®-H₂O to 10 ml (resulting in 10 ml 0.3 M HNO₃)

5. Step: Silicate residue and clay minerals (Be)_{min}

- Transfer of whole sediment residue into Teflon beaker (Savillex®)
- Evaporation of any water left from rinsing the sample sediment
- Volumetric addition of HF (48 %, trace elements) and concentrated HNO₃
- Leaving closed on hotplate @ 120° C until sample is dissolved
- Evaporation @ max. 110° C (Al becomes volatile at higher T)
- Volumetric addition of aqua regia to destroy any fluorides
- Evaporation @ max. 110° C
- Alternative: Microwave application
 - Adding „aqua regia“ (1 HNO₃ : 1 HCl)
 - Run of microwave application:
 - 6 min to reach T of 160° C
 - 4 min to reach T of 210° C
 - 20 min @ 210° C
 - Cool down (25 min)
- Evaporation @ max. 110° C
- Repetition until all left material is completely dissolved
- Redissolving evaporated residue in 1 ml 3 M HNO₃
- Transfer to new centrifuge tube and taking weight
- Gravimetric dilution with MilliQ®-H₂O to 10 ml (resulting in 10 ml 0.3 M HNO₃)

The dilution of all samples was done gravimetrically to determine the dilution factors. The original sediment sample in the initial centrifuge tube (left over from previous dissolution step) was washed twice with MilliQ®- H₂O between single extraction steps. This wash solution was discarded.

A.1.2 Ion exchange chromatography

A.1.2.1 Anion column chemistry

- Cleaning of resin
 - 7.5 ml 0.3M HCl
 - 7.5 ml 0.3M HCl
- Conditioning of resin
 - 3 ml 6 M HCl
 - 3 ml 6 M HCl
 - 3 ml 6 M HCl
- Loading sample in 6 M HCl
 - 5 ml 6 M HCl
 - 3 ml 6 M HCl
 - 3 ml 6 M HCl
- Cleaning of resin
 - 3 ml 0.3 M HCl
 - 7.5 ml 0.3 M HCl
 - 7.5 ml 0.3 M HCl
- Store in MilliQ[®]-H₂O

The samples in 6 M HCl were evaporated and redissolved in 0.4 M oxalic acid for following cation column.

A.1.2.2 Cation column chemistry

Following, a chromatographic separation of beryllium from the remaining sample matrix was carried out on a cation exchange column using Bio-Rad AG 50W-X8 resin (200-400 mesh). The sample is in 4 or 20 ml 0.4 M oxalic acid, depending on the cation load (meq). This was determined by measuring a 100 µl sample aliquot with ICP-OES. In some cases I used more than one column per sample, then adapting the amount of oxalic acid. The samples were warmed up for at least two hours at 60° C and then centrifuged in case some calcium oxalate precipitated. The 1 M HNO₃ was titrated to avoid early elution of beryllium.

Small columns (1 ml resin):

- Cleaning of resin
 - 2 ml 5 M HNO₃
 - 3 ml 5 M HNO₃
 - 2 ml MilliQ[®]-H₂O
 - 3 ml MilliQ[®]-H₂O
- Conditioning of resin
 - 2 ml 0.4 M oxalic acid
 - 3 ml 0.4 M oxalic acid
- Load sample in 0.4 M oxalic acid

- 1 ml 0.4 M oxalic acid collect Al, Ti
- 1 ml 0.4 M oxalic acid collect Al, Ti
- 5 ml 0.4 M oxalic acid collect Al, Ti
- 5 ml 0.4 M oxalic acid collect Al, Ti
- 1 ml MilliQ®-H₂O
- 2 ml MilliQ®-H₂O
- 2 ml 0.5 M HNO₃ collect Na, Mg
- 2 ml 0.5 M HNO₃ collect Na, Mg
- 4 ml 0.5 M HNO₃ collect Na, Mg
- 3 ml 1 M HNO₃ collect Be
- 3 ml 1 M HNO₃ collect Be
- 5 ml 1 M HNO₃ collect Be
- Cleaning of resin
 - 5 ml 5 M HNO₃
 - 5 ml 5 M HNO₃
 - 5 ml MilliQ®-H₂O
- Store in MilliQ®-H₂O

Large columns (5 ml resin):

- Cleaning of resin
 - 10 ml 5 M HNO₃
 - 15 ml 5 M HNO₃
 - 10 ml MilliQ®-H₂O
 - 15 ml MilliQ®-H₂O
- Conditioning of resin
 - 10 ml 0.4 M oxalic acid
 - 15 ml 0.4 M oxalic acid
- Load sample in 0.4 M oxalic acid
 - 5 ml 0.4 M oxalic acid collect Al, Ti
 - 5 ml 0.4 M oxalic acid collect Al, Ti
 - 25 ml 0.4 M oxalic acid collect Al, Ti
 - 25 ml 0.4 M oxalic acid collect Al, Ti
 - 5 ml MilliQ®-H₂O
 - 10 ml MilliQ®-H₂O
 - 15 ml 0.5 M HNO₃ collect Na, Mg
 - 25 ml 0.5 M HNO₃ collect Na, Mg
 - 10 ml 1 M HNO₃
 - 20 ml 1 M HNO₃ collect Be
 - 10 ml 1 M HNO₃ collect Be
 - 10 ml 1 M HNO₃ collect Be
- Cleaning of resin
 - 20 ml 5 M HNO₃
 - 20 ml 5 M HNO₃
 - 5 ml MilliQ®-H₂O
 - 5 ml MilliQ®-H₂O
- Store in MilliQ®-H₂O

A.1.3 Reference Materials

A.1.3.1 Reproducibility of HR-ICP-MS stream water measurements

In order to check the reproducibility of the HR-ICP-MS (*Element XR Thermo Fischer*) measurements of dissolved ^9Be concentration in stream water samples, a natural water (acidified spring water, “SRM 1640a”, *National Institute of Standards & Technology NIST*) was measured (Table A.1).

Table A.1: Measurement of SRM 1640a with HR-ICP-MS

Date of measurement	[Be] (ng g ⁻¹)
Dez 2011	2.90
Dez 2011	2.86
Dez 2011	3.15
Dez 2011	2.99
Dez 2011	2.85
Mar 2012	2.78
Mar 2012	2.94
Mar 2012	3.09
Mar 2012	3.28
Sept 2012	3.35
Sept 2012	3.22
Nov 2012	3.43
Jan 2013	3.56
Juni 2014	3.28
Average (n = 14)	3.12
SD (n = 14)	0.23
SE (n = 14)	0.062
Relative uncertainty (%)	7.4
Accuracy (%)	3.9
Certified Concentration (ng g ⁻¹)	3.002
SE (ng g ⁻¹)	0.027

A.1.3.2 Reproducibility the ICP-OES measurements

In order to check the reproducibility of the ICP-OES measurements of stable beryllium concentrations, reference materials of a granitic (“Geostandard GA”, *Centre de Recherches Pétrographiques et Géochimiques CRPG – CNRS*; Govindaraju (1995)) and a rhyolitic composition (“RGM-1”, *United States Geological Survey USGS*; Govindaraju (1994)) were measured together with samples (see Table A.2) over a time of several months. These rock standards were dissolved with a mixture of HF, HNO₃, and aqua regia and diluted to Be concentrations of 50 ppb (GA) and 30 ppb (RGM-1), respectively.

Table A.2: Concentration measurements of the “Geostandard GA” and the “RGM-1” standard on the ICP-OES

Sample Labels	Al (ppm)	Ba (ppm)	Be (ppm)	Ca (ppm)	Cr (ppm)	Fe (ppm)	K (ppm)	Mg (ppm)	Mn (ppm)	Na (ppm)	Ni (ppm)	Sr (ppm)	Ti (ppm)	Zn (ppm)	Zr (ppm)
GA (50ppb Be)	n.d.	n.d.	0.046	n.d.	n.d.	n.d.	n.d.	68.1	8.5	n.d.	n.d.	n.d.	27.4	n.d.	n.d.
GA (50ppb Be)	n.d.	n.d.	0.046	n.d.	n.d.	n.d.	n.d.	70.3	8.5	n.d.	n.d.	n.d.	27.1	n.d.	n.d.
GA (50ppb Be)	n.d.	n.d.	0.046	n.d.	n.d.	n.d.	n.d.	72.2	8.6	n.d.	n.d.	n.d.	27.2	n.d.	n.d.
GA (50ppb Be)	n.d.	10.6	0.042	n.d.	0.13	n.d.	n.d.	n.d.	8.4	n.d.	0.04	3.53	n.d.	0.84	1.02
GA (50ppb Be)	n.d.	10.3	0.040	n.d.	0.14	n.d.	n.d.	n.d.	8.7	n.d.	0.04	3.64	n.d.	0.82	1.07
GA (50ppb Be)	n.d.	10.2	0.039	n.d.	0.14	n.d.	n.d.	n.d.	8.9	n.d.	0.04	3.54	n.d.	0.81	1.02
GA (50ppb Be)	n.d.	10.7	0.041	n.d.	0.12	n.d.	n.d.	n.d.	9.0	n.d.	0.04	3.73	n.d.	0.85	1.04
GA (50ppb Be)	n.d.	n.d.	0.045	n.d.	n.d.	n.d.	n.d.	68.6	8.6	n.d.	n.d.	n.d.	28.0	n.d.	n.d.
GA (50ppb Be)	n.d.	10.8	0.040	n.d.	0.13	n.d.	n.d.	n.d.	8.4	n.d.	0.04	3.74	n.d.	0.81	1.02
GA (50ppb Be)	n.d.	11.2	0.042	n.d.	0.13	n.d.	n.d.	n.d.	8.6	n.d.	0.04	4.11	n.d.	0.81	1.05
GA (50ppb Be)	n.d.	10.2	0.040	n.d.	0.13	n.d.	n.d.	n.d.	8.4	n.d.	0.04	4.02	n.d.	0.84	1.02
Average		10.6	0.042		0.13			69.8	8.6		0.04	3.76	27.4	0.83	1.03
1 SD		0.4	0.002		0.01			1.6	0.2		0.00	0.21	0.3	0.01	0.02
Rel. Error (%)		3.3	5.9		4.50			2.3	2.3		4.36	5.55	1.2	1.78	1.98
Certified value	1053	12	0.049	240	0.16	272	459	79	9.6	361	0.10	4.3	31	1.1	2.1
Accuracy (%)		-8	-14		-21			-11	-10		-57	-12	-12	-25	-50
RGM -1 (30ppb)	n.d.	n.d.	0.028	92.67	n.d.	n.d.	n.d.	20.87	3.23	n.d.	n.d.	n.d.	18.16	n.d.	n.d.
RGM -1 (30ppb)	n.d.	9.76	0.026	n.d.	0.02	n.d.	n.d.	n.d.	3.25	n.d.	0.02	1.17	n.d.	0.43	2.37
RGM -1 (30ppb)	n.d.	n.d.	0.027	n.d.	n.d.	n.d.	n.d.	18.63	3.19	n.d.	n.d.	n.d.	18.38	n.d.	n.d.
RGM -1 (30ppb)	n.d.	10.63	0.027	n.d.	0.02	n.d.	n.d.	n.d.	3.34	n.d.	0.02	1.35	n.d.	n.d.	n.d.
RGM -1 (30ppb)	n.d.	9.45	0.025	n.d.	0.02	n.d.	n.d.	n.d.	3.29	n.d.	0.02	1.35	n.d.	0.45	2.33
Average		9.94	0.027	92.7	0.02			19.8	3.26		0.02	1.29	18.27	0.44	2.35
1 SD		0.50	0.001	0.00	0.00			1.12	0.05		0.00	0.08	0.11	0.01	0.02
Rel. Error (%)		5.0	3.4	0.0	4.6			5.7	1.6		3.6	6.5	0.6	1.9	0.9
Certified value	905	10	0.030	103	0.046	162			3.5	377		1.4		0.40	2.7
Accuracy (%)		-2	-11	-10	-51				-7			-6		9	-14

"n.d.": not determined. In case of major elements the concentrations were above the standard calibration line.

A.1.3.3 Recovery of co-precipitation method for water samples

Dissolved cosmogenic ^{10}Be is concentrated in a water sample by co-precipitation with iron(III)-hydroxide (see main text). The recovery of this method was tested by adding a known amount of ^9Be and in some cases oxalic acid to simulate a organic matrix to artificial samples (see Table A.3).

Table A.3: Recovery test of beryllium precipitation from an artificial water sample with FeCl_3

	^9Be added ¹	^9Be measured ²	Be recovery (rel. to 100%)
	(μg)	(μg)	(%)
<i>Sample without organic matrix</i>			
Sample 1	94	88.8 \pm 4.4	94.4
Sample 2	190	170.5 \pm 8.5	89.8
Sample 3	195	174.6 \pm 8.7	89.5
Sample 4	197	184.8 \pm 9.2	93.7
Sample 5	215	195.4 \pm 9.8	91.0
Average Recovery ³			91.7 \pm 2.3
<i>Sample spiked with oxalic acid</i>			
Sample 6	~ 200 ⁴	168 \pm 8.4	84
Sample 7	~ 200 ⁴	176 \pm 8.8	88
Average Recovery ³			85.8 \pm 2.9

¹ Amount of added beryllium given with balance uncertainty of 1d.

² Amount of measured beryllium given with uncertainty of ICP-OES measurement (5%).

³ Average recovery given with 1SD uncertainty..

⁴ Only volumetrically added.

A.1.3.4 Rock standards processed along with samples

The rock reference materials “GA” and “RGM-1”, and an additional basaltic rock (“BHVO”, *United States Geological Survey* USGS, Govindaraju (1994)) were processed together with bedrock samples during acid decomposition and fusion in several batches (see Table A.4) such that treatment of samples and reference materials can be considered identical.

Table A.4: Concentrations of the rock reference materials “GA”, “RGM-1”, and “BHVO” that were processed together with bedrock samples during acid decomposition and fusion

Sample Labels	Al (ppm)	Ba (ppm)	Be (ppm)	Ca (ppm)	Cr (ppm)	Fe (ppm)	K (ppm)	Mg (ppm)	Mn (ppm)	Na (ppm)	Ni (ppm)	Sr (ppm)	Ti (ppm)	Zn (ppm)	Zr (ppm)
GA	79887	863	3.0	18291	14	20122	10897	5481	762	23128	4	250	2228	68	84
GA	81649	883	2.8	18537	7	19955	10671	5735	709	22296	2	227	2274	67	76
GA	n.d.	n.d.	3.3	n.d.	n.d.	n.d.	n.d.	5616	n.d.	n.d.	n.d.	n.d.	2017	n.d.	n.d.
GA	n.d.	n.d.	3.1	n.d.	n.d.	n.d.	n.d.	n.d.	n.d.	n.d.	n.d.	n.d.	n.d.	n.d.	112
GA	n.d.	796.55	3.0	n.d.	7	n.d.	n.d.	n.d.	n.d.	n.d.	4	n.d.	n.d.	70	117
GA	n.d.	770.3	3.1	n.d.	8	n.d.	n.d.	n.d.	624	n.d.	3	279	n.d.	67	72
GA	n.d.	n.d.	3.1	n.d.	n.d.	n.d.	n.d.	n.d.	n.d.	n.d.	n.d.	n.d.	n.d.	n.d.	n.d.
Average	80768	828	3.1	18414	9	20038	10784	5611	698	22712	3	252	2173	68	92
SD	881	46	0.1	123	3	84	113	104	57	416	1	21	112	1	19
Rel. Error (%)	1	6	3.9	1	33	0	1	2	8	2	19	8	5	2	20
Certified value	76743	840	3.6	17510	12	19773	33455	5729	697	26336	7	310	2278	80	150
Accuracy (%)	5	-1	-15	5	-26	1	-68	-2	0	-14	-54	-19	-5	-15	-39
RGM-1	75353	866	2.2	8884	1.7	13166	11689	1567	250.1	26832	1.2	94.4	1646	35.1	188.8
Certified value	72514	810	2.4	8214		13369	35694	1688	279	30195		110	1619	32	220
Accuracy (%)	4	7	-10	8		-2	-67	-7	-10	-11		-14	2	10	-14
BHVO	76090	87.1	0.6	86726	178.0	89933	1582	46660	1469	15447	72.8	n.d.	17706	58.2	109.1
Certified value	73043			81430		86416	4317	43597	1317	16767			16246		
Accuracy (%)	4			7		4	-63	7	12	-8			9		

"n.d.": not determined. In case of major elements the concentrations were above the standard calibration line.

A.2 Detailed data set and additional information for the Slavkov Forest sites

A.2.1 Detailed results of sequential extraction procedure

I applied the complete sequential extraction procedure (described above in Appendix A.1.1) only to the fine-grained bedload sediment samples of the Slavkov Forest. The results show that [^9Be] in the exchangeable and the organic fraction is negligible (Table A.5). For that reason only step 2, step 3, and the final dissolution step 5 were applied to sediment or soil samples.

Table A.5: ^9Be concentrations measured on the different extracted phases in ng g^{-1}

Sample name ¹	Extracted fraction ²	Initial Sample Weight (g)	^9Be concentration (ng g^{-1})	Percentage of total Be (%)
LYS	ex	0.5069	b.d.l.	
	am-ox	0.5069	1124 \pm 58	20
	x-ox	0.5069	325 \pm 17	5.9
	org	0.5069	6.48 \pm 0.34	0.1
	min	0.5069	4039 \pm 210	74
	total		5495 \pm 219	
NAZ	ex	0.5092	2.00 \pm 0.10	0.1
	am-ox	0.5092	1395 \pm 72	40
	x-ox	0.5092	759 \pm 39	22
	org	0.5092	12.75 \pm 0.66	0.4
	min	0.5092	1294 \pm 67	37
	total		3463 \pm 106	
NAZ (1)	ex ³		-	
	am-ox	0.5220	1327 \pm 69	47
	x-ox	0.5220	202 \pm 11	7.1
	min	0.5220	1312 \pm 68	46
	org ³		-	
	total		2841 \pm 98	
PLB	ex	0.5649	b.d.l.	
	am-ox	0.5649	249 \pm 13	43
	x-ox	0.5649	62.1 \pm 3.2	11
	org	0.5649	b.d.l.	
	min	0.5649	267 \pm 14	46
	total		579 \pm 19	

"b.d.l.": below detection limit

¹ NAZ and NAZ(1) are two independently processed sample aliquots (newly weighted)

² "ex" = exchangeable fraction, "am-ox" = amorphous oxides, "x-ox" = crystalline oxides,

"org" = organic-bound, "min" = mineral-bound, "total" = sum of all extraction steps

³ "ex" and "org" not measured

A.2.2 ^{10}Be data (AMS results)

This page is intentionally left blank

Table A.6: Detailed report of meteoric ^{10}Be results from ETH AMS for bedload sediment samples from the Slavkov Forest

ETH Code ¹	Sample name ²	Sample type	Grain Size	Extracted fraction ³	Initial sample weight	^9Be Carrier ⁴	$(^{10}\text{Be}/^9\text{Be})_{\text{AMS}}$ ⁵	Relative analytical uncertainty	Absolute ^{10}Be amount	^{10}Be concentration ⁶
			(μm)		(g)	(μg)	($\times 10^{-12}$)	(%)	($\times 10^6$ atoms)	($\times 10^6$ atoms g^{-1})
ZB8699	LYS	Bedload sediment	< 63	Am-Ox	0.5069	519	1.39	3.3	77.0 ± 2.7	151.9 ± 5.2
ZB8693	LYS	Bedload sediment	< 63	X-Ox	0.5069	499	0.23	4.2	12.5 ± 0.55	24.6 ± 1.1
ZB8686	LYS	Bedload sediment	< 63	Min	0.5069	223	0.34	4.6	7.8 ± 0.38	15.31 ± 0.75
ZB8702	NAZ	Bedload sediment	< 63	Am-Ox	0.5092	520	3.36	3.0	180.3 ± 5.7	354 ± 11
ZB8696	NAZ	Bedload sediment	< 63	X-Ox	0.5092	498	0.45	3.8	23.16 ± 0.92	45.5 ± 1.8
ZB8689	NAZ	Bedload sediment	< 63	Min	0.5092	223	0.19	4.9	4.31 ± 0.23	8.46 ± 0.46
ZB8703	NAZ (1)	Bedload sediment	< 63	Am-Ox	0.5220	532	3.58	3.0	183.3 ± 5.8	351 ± 11
ZB8697	NAZ (1)	Bedload sediment	< 63	X-Ox	0.5220	532	0.48	3.6	24.60 ± 0.93	47.1 ± 1.8
ZB8690	NAZ (1)	Bedload sediment	< 63	Min	0.5220	219	0.26	7.0	5.45 ± 0.40	10.43 ± 0.76
ZB8701	PLB	Bedload sediment	< 63	Am-Ox	0.5649	518	3.62	3.0	193.7 ± 6.1	343 ± 11
ZB8695	PLB	Bedload sediment	< 63	X-Ox	0.5649	498	0.66	3.7	34.1 ± 1.3	60.3 ± 2.3
ZB8688	PLB	Bedload sediment	< 63	Min	0.5649	223	0.25	4.6	5.71 ± 0.28	10.12 ± 0.50
TB1350	LYS 125	Bedload sediment	125-250	Reac	0.7531	205	10.13	1.5	21.70 ± 0.64	50.3 ± 1.6
TB1349	NAZ 125	Bedload sediment	125-250	Reac	0.7533	206	9.79	1.3	134.7 ± 1.7	310.4 ± 5.1
TB1348	PLB 125	Bedload sediment	125-250	Reac	1.0059	206	1.59	2.9	139.1 ± 2.1	242.1 ± 4.4

¹ ZB: samples measured at the 6 MV Tandem facility at the ETH Zurich; TB: samples measured at the 0.5 MV Tandy facility at the ETH Zurich

² NAZ and NAZ(1) are two independently processed sample aliquots (newly weighted)

³ HCl leachable fraction (am-ox) and hydroxylamine-hydrochloride leachable fraction (x-ox) were extracted separately. For samples with TB code, these fractions were then combined to one reactive fraction for AMS measurement

⁴ Concentration of ^9Be carrier is 372.5 ± 3.5 ppm

⁵ Ratio as measured on AMS

⁶ Calculated from AMS ratio using the sum of ^9Be carrier and natural ^9Be content, with combined analytical and blank error (all uncertainties 1SD), relative to initial solid sample weight. The blank ratio of ^{10}Be measurement is $3.10 \pm 1.27 \times 10^{-15}$ ($n = 5$) for samples with ZB Code and $6.51 \pm 0.08 \times 10^{-15}$ ($n = 2$) for samples with TB code.

Table A.7: Detailed report of *in situ* ^{10}Be results from ETH AMS for bedload sediment samples from the Slavkov Forest

ETH Code ¹	Sample name	Sample type	Grain Size (μm)	Extracted fraction	Initial sample weight (g)	^9Be Carrier ² (μg)	$(^{10}\text{Be}/^9\text{Be})_{\text{AMS}}$ ³ ($\times 10^{-12}$)	Relative analytical uncertainty (%)	Absolute ^{10}Be amount ($\times 10^6$ atoms)	^{10}Be concentration ⁴ ($\times 10^6$ atoms g^{-1})
ZB8705	LYS 250	Bedload sediment	125-250	<i>in situ</i>	5.894	220	0.076	6.1	1.038 ± 0.082	0.176 ± 0.014
ZB8706	LYS 500	Bedload sediment	250-500	<i>in situ</i>	24.121	484	0.135	5.0	4.27 ± 0.22	0.177 ± 0.009
ZB9468	NAZ	Bedload sediment	125-800	<i>in situ</i>	7.622	152	0.142	8.2	1.36 ± 0.13	0.179 ± 0.015
ZB9469	PLB	Bedload sediment	125-800	<i>in situ</i>	2.9191	152	0.105	7.5	0.986 ± 0.092	0.338 ± 0.026

¹ ZB: samples measured at the 6 MV Tandem facility at the ETH Zurich

² Concentration of ^9Be carrier is 372.5 ± 3.5 ppm

³ Ratio as measured on AMS

⁴ Calculated from AMS ratio using the sum of ^9Be carrier, with combined analytical and blank error (all uncertainties 1SD), relative to initial solid sample weight.
The blank ratio of ^{10}Be measurement is $3.10 \pm 1.27 \times 10^{-15}$ (n = 5).

Table A.8: Detailed report of meteoric ^{10}Be results from CologneAMS for soil and sediment samples of the bedrock core at Lysina

CologneAMS Code	Sample name	Sample type	Sampled depth (cm)	Grain Size (mm)	Extracted fraction ¹	Initial sample weight (g)	^9Be Carrier ² (μg)	$(^{10}\text{Be}/^9\text{Be})_{\text{AMS}}$ ³	Relative analytical uncertainty (%)	Absolute ^{10}Be amount ($\times 10^6$ atoms)	^{10}Be concentration ⁴ ($\times 10^6$ atoms g^{-1})
s03635	LYS C	sandy soil	60	< 2	Reac	0.7577	153	1.8	3.16	53.2 ± 1.7	70.3 ± 2.3
s03636	LYS 1	sandy soil	115	< 2	Reac	0.7503	153	2.1	3.15	61.8 ± 1.9	82.3 ± 2.7
s03637	LYS 2	sandy residuum	160	< 2	Reac	0.7525	153	2.5	3.14	73.0 ± 2.3	97.0 ± 3.2
s03638	LYS 4	sandy residuum	218	< 2	Reac	0.7562	153	0.77	3.31	22.81 ± 0.76	30.2 ± 1.0
s03639	LYS 6	sandy residuum	320	< 2	Reac	0.7528	153	0.63	3.38	18.51 ± 0.63	24.59 ± 0.87
s03640	LYS 8	rock fragment	440	< 2	Reac	0.7762	153	0.43	3.54	12.96 ± 0.46	16.69 ± 0.62

¹ HCl leachable fraction (am-ox) and hydroxylamine-hydrochloride leachable fraction (x-ox) were extracted separately and then combined to one reactive fraction for AMS measurement

² Concentration of ^9Be carrier is 372.5 ± 3.5 ppm

³ Ratio as measured on AMS

⁴ Calculated from AMS ratio using the sum of ^9Be carrier and natural ^9Be content, with combined analytical and blank uncertainty (all uncertainties 1SD), relative to the initial solid sample weight. The blank ratio of ^{10}Be measurement is $1.48 \pm 1.30 \times 10^{-15}$ (n = 9).

Table A.9: Detailed report of meteoric ^{10}Be results from ETH AMS for stream water samples

ETH Code ¹	Sample ID ²	Sampling date	Initial sample weight (g)	^9Be Carrier (μg)	$(^{10}\text{Be}/^9\text{Be})_{\text{AMS}}$ ³ ($\times 10^{-12}$)	Relative analytical uncertainty (%)	Absolute ^{10}Be amount ($\times 10^6$ atoms)	^{10}Be concentration ⁴ (10^4 atoms g^{-1})
ZB8736	LYS 1 S (1108)	03/08/2011	203	411	0.87	4.2	24.0 ± 1.0	11.82 ± 0.51
ZB8939	LYS 1204	30/04/2012	200	267	1.40	3.8	24.9 ± 1.0	12.35 ± 0.49
ZB9179	LYS 1206	27/06/2012	199	245	1.26	4.4	20.51 ± 0.91	10.32 ± 0.47
ZB9180	LYS 1207	01/08/2012	198	245	1.26	3.3	20.64 ± 0.68	10.42 ± 0.36
ZB9181	LYS 1208	29/08/2012	202	246	1.25	4.0	20.50 ± 0.82	10.13 ± 0.42
ZB9182	LYS 1209	01/10/2012	202	224	1.33	6.8	19.8 ± 1.4	9.80 ± 0.68
ZB9183	LYS 1210	01/11/2012	203	223	1.85	6.5	27.5 ± 1.8	13.52 ± 0.89
ZB9196	LYS 1211	28/11/2012	204	224	2.13	3.0	31.9 ± 1.0	15.6 ± 1.0
TB1345	LYS 1301	08/01/2013	225	204	1.98	3.8	26.9 ± 1.0	11.98 ± 0.48
TB1346	LYS 1302	05/02/2013	230	204	2.01	2.9	27.33 ± 0.81	11.91 ± 0.37
ZB8737	LYS 2 S (groundwater)	03/08/2011	483	390	2.47	3.0	64.6 ± 1.9	13.36 ± 0.40
ZB8740	NAZ S (1108)	03/08/2011	601	411	0.13	7.7	3.48 ± 0.25	0.579 ± 0.046
ZB8941	NAZ 1204	30/04/2012	503	267	0.42	6.2	7.33 ± 0.97	1.410 ± 0.089
ZB9167	NAZ 1206	27/06/2012	349	246	0.13	9.9	2.00 ± 0.21	0.574 ± 0.060
ZB9168	NAZ 1207	01/08/2012	370	245	0.12	9.9	1.99 ± 0.21	0.537 ± 0.056
ZB9169	NAZ 1208	29/08/2012	364	246	0.11	9.3	1.72 ± 0.17	0.473 ± 0.046
ZB9170	NAZ 1209	01/10/2012	394	223	0.10	13.1	1.41 ± 0.20	0.358 ± 0.050
ZB9171	NAZ 1210	01/11/2012	397	224	0.21	9.1	3.02 ± 0.28	0.761 ± 0.072
ZB9172	NAZ 1211	28/11/2012	401	223	0.19	8.4	2.83 ± 0.25	0.706 ± 0.062
TB1343	NAZ 1301	07/01/2013	399	204	0.78	3.3	10.52 ± 0.35	2.633 ± 0.092
TB1344	NAZ 1302	05/02/2013	399	204	0.64	4.9	8.58 ± 0.43	2.15 ± 0.11

Table A.9: continued

ETH Code ¹	Sample ID ²	Sampling date	Initial sample weight (g)	⁹ Be Carrier (μg)	(¹⁰ Be/ ⁹ Be) _{AMS} ³ (x 10 ⁻¹²)	Relative analytical uncertainty (%)	Absolute ¹⁰ Be amount (x 10 ⁶ atoms)	¹⁰ Be concentration ⁴ (10 ⁴ atoms g ⁻¹)
ZB8739	PLB S (1108)	03/08/2011	477	411	0.22	4.1	6.1 ± 1.3	1.274 ± 0.054
ZB8940	PLB 1204	30/04/2012	221	267	0.23	6.0	3.85 ± 0.29	1.635 ± 0.099
ZB9173	PLB 1206	27/06/2012	253	246	0.09	13.3	1.44 ± 0.20	0.567 ± 0.080
ZB9174	PLB 1207	01/08/2012	264	246	0.31	8.9	5.05 ± 0.46	1.91 ± 0.17
ZB9175	PLB 1208	29/08/2012	273	246	0.07	12.9	1.14 ± 0.16	0.418 ± 0.058
ZB9176	PLB 1209	01/10/2012	317	224	0.06	15.0	0.82 ± 0.14	0.258 ± 0.043
ZB9177	PLB 1210	01/11/2012	298	224	0.47	6.4	6.93 ± 0.45	2.32 ± 0.15
ZB9178	PLB 1211	28/11/2012	297	224	0.41	8.5	6.03 ± 0.52	2.03 ± 0.18
TB1341	PLB 1301	07/01/2013	387	204	1.49	2.7	20.17 ± 0.56	5.21 ± 0.15
TB1342	PLB 1302	06/02/2013	395	204	1.63	3.5	22.15 ± 0.78	5.60 ± 0.20

¹ ETH code: ZB, ¹⁰Be measurement with the AMS at ETH Zurich; TB, ¹⁰Be measurement with the Tandy facility at ETH Zurich

² Sample ID made up of year and month.

³ Ratio as measured on AMS

⁴ Calculated from AMS ratio using the sum of ⁹Be carrier, with combined analytical and blank error (all uncertainties 1SD), relative to initial solid sample weight.
The blank ratio of ¹⁰Be measurement is $1.75 \pm 0.07 \times 10^{-15}$ (n = 2) for samples with ZB Code 8xxx, $2.75 \pm 3.04 \times 10^{-15}$ (n = 2) for samples with ZB code 9xxxx, and $6.51 \pm 0.08 \times 10^{-15}$ (n = 2) for samples with TB code

A.2.3 Element concentrations in bedload sediment (XRF analysis)

This page is intentionally left blank

Table A.10: XRF data for the fine-grained bedload sediment (grain size < 63 µm, split of samples on which the sequential extraction procedure was applied)

Sample name	SiO ₂ (%)	TiO ₂ (%)	Al ₂ O ₃ (%)	Fe ₂ O ₃ (%)	MnO (%)	MgO (%)	CaO (%)	Na ₂ O (%)	K ₂ O (%)	P ₂ O ₅ (%)	LOI (%)	Sum (%)	Ba (ppm)	Cr (ppm)	Nb (ppm)	Ni (ppm)	Rb (ppm)	Sr (ppm)	V (ppm)	Y (ppm)	Zn (ppm)	Zr (ppm)
LYS (< 63 µm)	62.5	0.398	14.3	2.51	0.042	0.58	1.38	2.18	2.80	0.372	12.25	99.30	231	38	33	26	436	64	28	19	105	255
NAZ (< 63 µm)	54.1	1.061	15.6	8.75	0.750	3.30	3.10	0.92	1.94	0.267	17.23	99.28	794	146	30	88	190	229	177	38	266	312
PLB (< 63 µm)	47.0	0.652	7.9	8.87	0.292	12.15	4.00	0.46	0.58	0.152	9.91	99.71	190	1922	15	1269	76	78	117	20	111	233

Table A.11: XRF data for bulk bedload sediment

Sample name	SiO ₂ (%)	TiO ₂ (%)	Al ₂ O ₃ (%)	Fe ₂ O ₃ (%)	MnO (%)	MgO (%)	CaO (%)	Na ₂ O (%)	K ₂ O (%)	P ₂ O ₅ (%)	LOI (%)	Sum (%)	Ba (ppm)	Cr (ppm)	Nb (ppm)	Ni (ppm)	Rb (ppm)	Sr (ppm)	V (ppm)	Y (ppm)	Zn (ppm)	Zr (ppm)
LYS (bulk)	71.1	0.096	13.1	1.55	0.025	0.10	0.21	2.43	4.23	0.230	6.25	99.35	121	10	12	<10	777	38	<10	<10	51	57
NAZ (bulk)	66.1	0.573	13.9	5.44	0.322	2.20	3.48	2.92	1.59	0.162	2.99	99.71	605	81	<10	33	84	373	110	15	121	133
PLB (bulk)	49.6	0.535	9.4	11.37	0.223	15.67	4.41	1.23	0.73	0.086	5.93	99.17	298	3120	<10	1185	35	156	140	10	86	113

A.2.4 ($^{10}\text{Be}/^9\text{Be}$)_{reac} ratio measured on different grain sizes

Whereas [^9Be]_{reac} was measured on four grain size fractions (< 63 μm , 63-125 μm , 125-250 μm , 250-500 μm), I measured [^{10}Be]_{reac} only on two individual grain size fractions (see Table A.12). As ($^{10}\text{Be}/^9\text{Be}$)_{reac} is the same for all grain sizes (within the analytical uncertainty; see Table A.12), I used an average ratio to calculate [^{10}Be]_{reac} for all grain size fractions using the measured [^9Be]_{reac} (see Table A.12). Additionally, I determined the portion of each grain size fraction on the bulk samples by taking the initial weights of these. A “bulk” [^{10}Be]_{reac} was then calculated by multiplying these fractional amounts with the [^{10}Be]_{reac} calculated for the individual grain size fractions (see Table A.12). These calculations were carried out to correct for the ^{10}Be contained in the unidentified coarse-grained and bulk sample fractions. However, I do not know the associated uncertainties of this approach and a large portion of this ^{10}Be is most likely still missing in these fractions. Hence I will use the fine-grained fraction for calculations in the main text.

Table A.12: Calculation of ^{10}Be and ^9Be concentrations for “bulk” samples

Sample Labels	Grain Size	Fractional amount of grain size (rel. to total)	Measured ^{10}Be concentration	^9Be concentration	($^{10}\text{Be}/^9\text{Be}$) _{reac}	Recalculated ^{10}Be concentration
	(μm)		(10^6 atoms g^{-1})	(ppm)		(10^6 atoms g^{-1})
LYS	< 63	0.05	191.9 ± 5.4	1.449 ± 0.061	19.82 ± 1.00	190 ± 14
LYS 63	63-125	0.07		1.067 ± 0.041		140 ± 10
LYS 125	125-250	0.21	50.3 ± 1.6	0.387 ± 0.015	19.44 ± 0.98	50.8 ± 3.6
LYS 250	250-500	0.66		0.320 ± 0.013		42.0 ± 3.0
LYS "Bulk" ¹	< 500			0.447 ± 0.010		58.7 ± 2.4
LYS Average ²					19.6 ± 1.4	
NAZ	< 63	0.10	409 ± 11	2.087 ± 0.080	29.3 ± 1.4	435 ± 28
NAZ 63	63-125	0.12		1.696 ± 0.067		354 ± 23
NAZ 125	125-250	0.25	310.4 ± 5.1	1.403 ± 0.055	33.1 ± 1.4	293 ± 19
NAZ 250	250-500	0.53		1.055 ± 0.042		220 ± 14
NAZ "Bulk" ¹	< 500			1.322 ± 0.028		276 ± 10
NAZ Average ²					31.2 ± 2.0	
PLB	< 63	0.04	413 ± 11	0.31 ± 0.013	199 ± 10	446 ± 31
PLB 63	63-125	0.07		0.2167 ± 0.0093		310 ± 21
PLB 125	125-250	0.23	242.1 ± 4.4	0.1578 ± 0.0068	230 ± 11	226 ± 16
PLB 250	250-500	0.66		0.1415 ± 0.0060		203 ± 14
PLB "Bulk" ¹	< 500			0.1574 ± 0.0043		225 ± 10
PLB Average ²					214 ± 15	

¹ All concentrations are recalculated by multiplying the weighted grain size fraction with the corresponding [Be].

² Averaged $^{10}\text{Be}/^9\text{Be}$ used for recalculation of [^{10}Be]_{bulk} and [^9Be]_{bulk}.

A.2.5 Stable [^9Be]_{am-ox} measured on bedrock core samples

From the Lysina and the Pluhův Bor site available soil and sediment samples from the bedrock core that cover the whole regolith (from the top of the soil to the bedrock border; from P. Kram, Czech Geological Survey). These samples were only treated with the HCl extraction step to acquire the amorphous phase. Since this phase constitutes the main fraction of leached ^9Be and is in exchange with the dissolved phase, the distribution of ^9Be with depth can be assessed. Whereas in the acidic Lysina catchment [^9Be]_{am-ox} shows a bulge shaped profile with about the same concentration in the uppermost and the lowest sample, [^9Be]_{am-ox} distinctly declines in the neutral to slightly alkaline catchments (see Table A.13).

Table A.13: [^9Be]_{Am-Ox} determined on depth profile samples

Sample name	Sampled depth ¹ (cm)	Extracted fraction ²	Initial sample weight (g)	[^9Be] _{Am-Ox} (ng g ⁻¹)
LYS C	60	am-ox	0.7577	297 ± 15
LYS D	90	am-ox	0.764	285 ± 15
LYS 1	115	am-ox	0.7503	404 ± 21
LYS 2	160	am-ox	0.7525	430 ± 22
LYS 3	190	am-ox	0.7509	431 ± 22
LYS 4	218	am-ox	0.7562	329 ± 17
LYS 5	270	am-ox	0.7521	333 ± 17
LYS 6	320	am-ox	0.7528	306 ± 16
LYS 7	370	am-ox	0.7578	351 ± 18
LYS 8	440	am-ox	0.7762	291 ± 15
LYS 9	490	am-ox	0.7671	284 ± 15
PLB C	70	am-ox	0.7538	66.1 ± 3.4
PLB D	95	am-ox	0.7556	23.0 ± 1.2
PLB 1	120	am-ox	0.7561	17.77 ± 0.92
PLB 2	160	am-ox	1.0037	9.27 ± 0.48
PLB 3	195	am-ox	1.0121	4.07 ± 0.21
PLB 4	215	am-ox	1.0159	5.92 ± 0.31
PLB 5	255	am-ox	1.0084	6.13 ± 0.32

¹ Mean depth at which samples were taken from the core.

² am-ox: HCl-leachable fraction.

A.2.6 Bedrock data set

The parent bedrock of the studied catchments is highly variable (see Table A.14 to Table A.16): (1) the granites at Lysina reveal a median [Be] of 3.5 ppm, but in some samples peak concentrations are >10 ppm Be; (2) at Na Zeleném the bedrock types are amphibolite and other mafic rocks that differ widely in their [Be]; (3) the ultramafic serpentinite at Pluhův Bor has exceptionally low [Be] but is accompanied by mafic rocks with distinctly higher [Be].

The variation in the [Be] in the Lysina granites could be due to a “nugget effect” caused by beryllium minerals like beryl or bertrandite. However, imaging a thin section from this granite and analysing it with a femto-second laser ablation system coupled to an iCAP Q ICP-MS, no accessory minerals with exceptional high beryllium concentrations could be detected (see Figure A.2.1). The typical beryllium concentration in feldspar and mica minerals is about 4 to 10 ppm, with some mica minerals phases exhibiting the highest beryllium concentrations (see Figure A.2.1), possibly indicating zinwaldite (Navrátil, 2000). In the quartz phase beryllium is below the limit of detection. The distribution of quartz, feldspar, and mica within the granite and different weathering degrees of the rock could potentially result in the observed variation in the beryllium concentration.

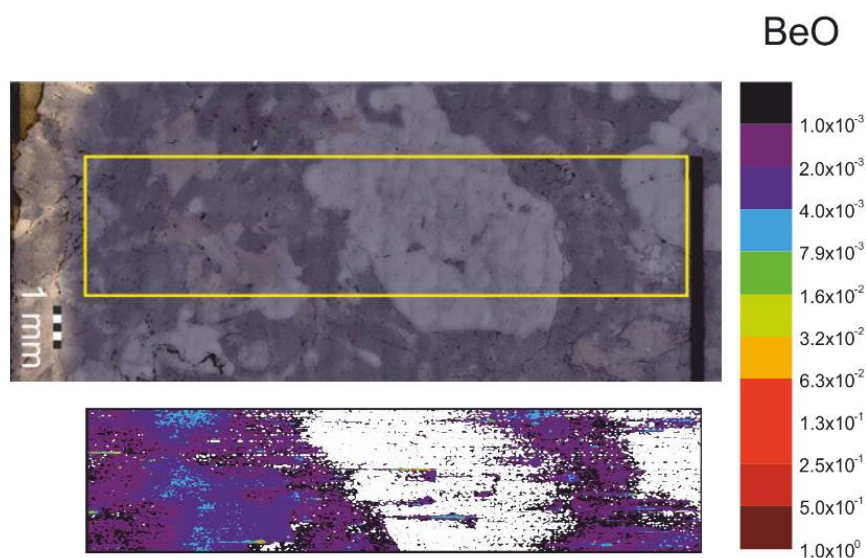


Figure A.2.1: Beryllium oxide (BeO) map (in wt%) using a logarithmic scale imaged with a femto-second laser ablation system coupled to an iCAP Q ICP-MS (quadro-pole mass spectrometer). White areas are area with BeO below the detection limit, indicating quartz mineral phase. The measurement was done by *D. Frick, GFZ Potsdam*.

Table A.14: Detailed description of bedrock types prevailing in the bedrock cores taken at Lysina, Na Zeleném, and Pluhův Bor (pers. comm. *P. Kram, Czech Geological Survey*). Further are given beryllium concentrations measured on bedrock sampled from different types of bedrock and depth in the cores (in ppm; *own data*).

<i>Lysina Bedrock Core</i>						
Depth		Thickness	Description	Bedrock type ¹	Sample depth	Average [Be] ²
(m)		(m)			(cm)	(ppm)
min	max					
0.0	0.3	0.3	soil	Q		
0.3	1.5	1.2	soil with granite fragments	Q		
1.5	3.4	1.9	sandy residuum, loose granite	G		
3.4	5.3	1.9	fine grained granite, porphyric	Gp	465	11.46 ± 0.60
5.3	6.1	0.8	tectonized	Gp		
6.1	6.5	0.4	fine grained granite, porphyric	Gp		
6.5	8.0	1.5	medium grained granite	G	695	3.32 ± 0.17
8.0	11.0	3.0	medium grained granite, altered	G	850	3.18 ± 0.17
					983	3.40 ± 0.18
11.0	12.7	1.7	granite, altered KFsp	G	1195	3.43 ± 0.18
12.7	14.0	1.3	light granite	G	1354	3.58 ± 0.19
14.0	15.0	1.0	tectonized, weak alteration	G		
15.0	18.3	3.3	solid granite	G	1518	3.61 ± 0.19
					1810	4.24 ± 0.22
18.3	19.4	1.1	solid medium grained granite	G		
19.4	19.4	0.0	crack fille dwith Qtz			
19.4	20.3	0.9	medium grained granite, haematite		1990	5.20 ± 0.27
20.3	21.2	0.9	mylonitized zone with haematite			
21.2	21.5	0.3	solid fine grained granite	G		
21.5	25.2	3.8	solid fine grained granite, pinkish	G	2241	3.22 ± 0.17
					2395	2.83 ± 0.15
25.2	27.0	1.8	fine grained granite, porphyric	Gp	2600	3.95 ± 0.21
27.0	28.4	1.4	fine to medium grained granite		2725	3.48 ± 0.18
28.4	30.3	1.9	medium grained granite (LYS type)	G	2955	20.3 ± 1.06
<i>Na Zeleném Bedrock Core</i>						
Depth		Thickness	Description	Bedrock type ¹	Sample depth	Average [Be] ²
(m)		(m)			(cm)	(ppm)
min	max					
0.0	0.2	0.2	soil, O horizon	Q		
0.2	0.5	0.3	rusty soil	Q		
0.5	0.9	0.4	amphibolite fragments	Amf		
0.9	1.8	0.9	residual rocks, AMF fragments	Amf		
1.8	2.0	0.2	sandy residuum			
2.0	2.7	0.7	AMF blocks	Amf	273	0.426 ± 0.022
2.7	3.0	0.3	medium grained AMF	Amf		
3.0	3.1	0.1	epidot amphibolite	Amf		
3.1	3.5	0.4	coarse grained AMF	Amf		
3.5	3.6	0.1	heterogenous AMF	Amf		
3.6	3.7	0.1	mafic AMF	Amf		
3.7	3.9	0.2	weakly banded AMF	Amf		
3.9	4.4	0.5	altered dark AMF	Amf		
4.4	4.9	0.4	deformed AMF	Amf		
4.9	5.0	0.2	altered melt AMF-Fs	Amf		
5.0	5.2	0.2	tectonic clay, actinolite			

Table A.14: continued

Depth	Thickness	Description	Bedrock type ¹	Sample depth	Average [Be] ²
(m)	(m)			(cm)	(ppm)
min max					
5.2 5.4	0.2	fragmented AMF	Amf		
5.4 5.8	0.4	massiv, banded AMF	Amf	560	0.993 ± 0.052
5.8 6.1	0.3	limonitizeds cracks			
6.1 6.4	0.3	fine grained granate AMF	Amf		
6.4 7.1	0.7	altered, fine grained AMF	Amf	695	1.174 ± 0.061
7.1 8.1	1.0	epidotized AMF	Amf	752	0.757 ± 0.039
8.1 8.2	0.1	Ep/Pl melt			
8.2 9.1	0.9	epidotized coarse grained AMF	Amf		
9.1 9.8	0.8	fine grained AMF	Amf	930	0.621 ± 0.032
9.8 10.4	0.6	coarse grained AMF, granate	Amf		
10.4 11.3	0.9	AMF	Amf	1098	0.634 ± 0.033
11.3 12.7	1.4	coarse grained grt AMF	Amf	1143	0.443 ± 0.023
12.7 13.2	0.5	grt AMF			
13.2 13.5	0.3	nodular metabazite	Metabaz		
13.5 13.8	0.3	fine grained bt. Metadolerite	Metadol		
13.8 14.0	0.3	lithological transition			
14.0 14.6	0.6	ep metabazite	Metabaz	1458	2.55 ± 0.13
14.6 14.9	0.3	contact metabazite and metadolerite			
14.9 15.5	0.7	fine grained bt metadolerite	Metadol		
15.5 16.3	0.8	fine grained bt metadolerite, Qtz	Metadol		
16.3 21.1	4.9	fine grained bt metadolerite	Metadol	1684	2.29 ± 0.12
				1759	2.08 ± 0.11
				1953	2.47 ± 0.13
21.1 21.4	0.3	crack, Ep-Ab-Act			
21.4 21.5	0.1	sulfide traces			
21.5 21.8	0.4	homogenous black AMF	Amf	2163	0.536 ± 0.028
21.8 22.1	0.3	heterogenous AMF	Amf		
22.1 23.4	1.3	fine grained bt metadolerite	Metadol	2320	2.89 ± 0.15
23.4 23.6	0.2	bt metadolerite	Metadol		
23.6 23.9	0.3	altered AMF	Amf		
23.9 24.5	0.6	AMF	Amf	2426	0.644 ± 0.033
24.5 25.0	0.5	Fs-Qtz-Act melt			
25.0 25.6	0.6	amphibole gneiss	Gn		
25.6 25.9	0.3	deformed Ep AMF	Amf		
25.9 26.1	0.2	fine grained Ep AMF	Amf		

Pluhův Bor Bedrock Core

Thickness	Description	Bedrock type ¹	Sample depth	Average [Be] ²
(m)			(cm)	(ppm)
min max				
0.0 0.1	0.1	soil, O horizon	Q	
0.1 1.2	1.1	soil + serpentinite	Q	
1.2 1.9	0.7	clayey serpentinite + residual		
1.9 3.6	1.7	stony resium of serpentinite	Serp	259
				259
				b.d.l.
3.6 5	1.4	serpentinized peridotite, sec magnetite	Pdt	404
				b.d.l.
5 5.2	0.2	altered Serp in fragments	Serp	
5.2 5.65	0.5	serpentinite	Serp	537
				b.d.l.

Table A.14: continued

Depth		Thickness	Description	Bedrock type ¹	Sample depth	Average [Be] ²
(m)		(m)			(cm)	(ppm)
min	max					
5.65	5.8	0.1	shear zone			
5.8	6.1	0.3	serpentinite	Serp	597	b.d.l.
6.1	6.4	0.3	Fs melt			
6.4	7	0.6	serpentinite	Serp	671	b.d.l.
7	7.65	0.7	amphibolite	Amf	720	0.727 ± 0.038
7.65	8	0.4	tremolite shist (Mg-rich)	Trem		
8	8.15	0.2	amphibolite	Amf		
8.15	8.8	0.7	ultrabasite	Ultrabazite	850	0.102 ± 0.0053
8.8	8.9	0.1	homogenous dark ultrabasite			
8.9	9.3	0.4	shear zone			
9.3	10.1	0.8	AMF	Amf	951	0.368 ± 0.019
10.1	10.2	0.1	tremolite shist (metabazite)	Trem		
10.2	11.7	1.5	actinolite shist (metabazite)	Shist	1060	0.249 ± 0.013
11.7	15.2	3.5	metabazite + def	Metabazite	1345	0.225 ± 0.012
15.2	16.1	0.9	tremolite shist	Trem		
16.1	16.2	0.1	intermediate AMF	Amf		
16.2	16.9	0.7	shear zone			
16.9	17.2	0.3	actinolite shist (metabazite)	Shist		
17.2	17.2	0.0	Fs melt			
17.2	17.9	0.7	AMF or metagabbro	Amf	1758	0.452 ± 0.024
17.9	18.2	0.3	shear zone			
18.2	18.9	0.7	ultra/metabazite	Ultrabaz		
18.9	19.2	0.3	AMF	Amf		
19.2	19.5	0.3	laminated AMF	Amf		
19.5	19.6	0.1	tremolite shist	Trem		
19.6	20.1	0.5	ultra/metabazite	Ultrabaz		
20.1	20.6	0.5	coarse grained AMF rich melt			
20.6	20.9	0.3	Metabazite	Metabaz		
20.9	21.9	1.0	fine grained banded AMF	Amf		
21.9	22.3	0.4	ultra/metabazite	Ultrabaz		
22.3	22.3	0.0	discontinuity!			
22.3	22.7	0.4	metabasite	Metabaz		
22.7	23.2	0.5	metapyroxenite, tremolite-chlorite shist			
23.2	23.5	0.3	talc rich serpentinite with Mg amphibole	Serp/Amf	2317	0.01673 ± 0.00087
23.5	24.2	0.7	metapyroxenite	Pyrox	2362	b.d.l.
24.2	24.6	0.4	AMF	Amf		
24.6	24.7	0.1	talc rich AMF	Amf		
24.7	25	0.3	shear zone			
25	25.2	0.2	talc rich tremolite shist (hornblendit)	Amf		
25.2	25.4	0.2	shear zone			
25.4	28	2.6	amphibolite	Amf	2670	0.482 ± 0.025
					2758	0.445 ± 0.023

b.d.l.: below detection limit (detection limit of measurements is 10 ppb of Be in the bedrock)

¹ Q = Quaternary soil and sediments, G = Granite, Gp = porphyric Granite, Amf = Amphibolite, Metabaz = Metabazite, Metadol = Metadolerite, Gn = Gneiss, Serp = Serpentinite, Pdt = Peridotite, Pyrox = Pyroxenite

² value given with 5% uncertainty for ICP-OES measurement

Table A.15: Minerals occurring in selected bedrock samples from each core (only qualitative determined with XRD)

Sample Name	Sample Depth (cm)	Bedrock description ¹	Minerals ²
<u><i>Lysina</i></u>			
LYS 9.83	983	<i>granite</i>	qtz, plag, microcline, musc, biotite, topaz, (illite?)
LYS 15.18	1518	<i>granite</i>	qtz, plag, microcline, musc, biotite, (illite?)
LYS 18.10	1810	<i>granite</i>	qtz, plag, microcline, musc, biotite, topaz, (illite?)
LYS 22.41	2241	<i>granite</i>	qtz, plag, microcline, musc, biotite, topaz, (illite?)
LYS 29.55	2960	<i>granite</i>	qtz, plag, microcline, musc, biotite
<u><i>Na Zeleném</i></u>			
NAZ 2.73	273	<i>amphibolite</i>	Mg-hornbl, tremolite, albite, anorthite, chlorite, illmenite, qtz, biotite
NAZ 11.44	1143	<i>grt amphibolite</i>	Mg-hornbl, tremolite, albite, anorthite, chlorite, illmenite, qtz, biotite, calc
NAZ 14.68	1458	<i>ep metabazite</i>	Mg-hornbl, albite, anorthite, orthoclase, chlorite, musc, qtz, biotite, calc
NAZ 17.59	1759	<i>bt metadolerite</i>	Mg-hornbl, albite, anorthite, orthoclase, chlorite, musc, qtz, biotite, calc
NAZ 23.20	2320	<i>bt metadolerite</i>	Mg-hornbl, albite, anorthite, orthoclase, chlorite, qtz, biotite, calc
<u><i>Pluhův Bor</i></u>			
PLB 2.59	259	<i>serpentinite</i>	Lizardite (serpentine), antigorite, chlorite, vermiculite, chromite
PLB 4.04	404	<i>peridotite</i>	Lizardite (serpentine), antigorite, chlorite, vermiculite, chromite
PLB 10.60	1060	<i>tremolite shist</i>	Mg-hornbl, tremolite, albite, anorthite, chlorite, actinolite
PLB 17.58	1758	<i>amphibolite</i>	Mg-hornbl, tremolite, albite, anorthite, chlorite, actinolite
PLB 23.62	2362	<i>metapyroxenite</i>	Mg-hornbl, tremolite, Ca-amphibole, chlorite, actinolite, talc
PLB 27.58	2758	<i>amphibolite</i>	Mg-hornbl, tremolite, albite, anorthite, chlorite, actinolite

¹ Pers. comm. P. Kram, Czech Geological Survey.

² qtz = quartz, plag = plagioclase, musc = muscovite, hornbl = hornblende, calc = calcite

Table A.16: XRF data for bedrock samples from the drilled bedrock cores taken in each catchment

Sample name ¹	SiO ₂ (%)	TiO ₂ (%)	Al ₂ O ₃ (%)	Fe ₂ O ₃ (%)	MnO (%)	MgO (%)	CaO (%)	Na ₂ O (%)	K ₂ O (%)	P ₂ O ₅ (%)	LOI (%)	Sum (%)
<i>Lysina bedrock core</i>												
LYS 4.65	74.0	0.095	14.4	1.30	0.040	0.11	0.45	3.35	4.79	0.314	0.52	99.35
LYS 6.95	74.4	0.063	14.1	1.22	0.043	0.07	0.34	2.90	4.75	0.337	0.94	99.15
LYS 8.50	74.7	0.068	14.3	1.01	0.030	0.05	0.33	3.52	4.43	0.360	0.30	99.15
LYS 9.83	75.3	0.049	13.8	0.84	0.027	0.06	0.33	3.25	4.25	0.355	0.04	99.29
LYS 10.95	74.9	0.064	14.2	1.12	0.038	0.08	0.40	3.18	4.35	0.406	0.43	99.15
LYS 13.54	75.3	0.055	14.0	0.89	0.035	0.10	0.41	3.14	4.35	0.406	0.57	99.26
LYS 15.18	74.6	0.053	14.2	0.91	0.035	0.07	0.42	3.23	4.22	0.415	0.05	99.12
LYS 16.40	72.9	0.050	15.2	0.93	0.038	0.15	0.46	2.98	4.89	0.416	1.42	99.39
LYS 18.10	73.9	0.038	14.4	1.07	0.050	0.19	0.50	2.62	4.34	0.457	0.06	99.40
LYS 19.90	77.8	0.035	12.2	0.85	0.039	0.11	1.33	2.08	3.15	0.323	1.32	99.14
LYS 22.41	74.7	0.039	14.0	0.93	0.045	0.10	0.54	2.79	4.70	0.388	0.07	99.49
LYS 23.95	74.3	0.035	14.8	0.75	0.032	0.04	0.50	3.53	3.94	0.392	0.69	99.05
LYS 26.00	70.6	0.085	16.1	1.12	0.054	0.14	0.48	2.50	6.81	0.434	0.90	99.20
LYS 27.25	73.9	0.149	14.0	2.22	0.071	0.15	0.44	2.37	4.57	0.367	0.74	98.91
LYS 29.55	73.0	0.068	14.5	0.95	0.053	0.11	0.47	2.68	6.02	0.471	0.04	99.38
<i>Na Zeleném bedrock core</i>												
NAZ 2.73	53.2	0.379	6.8	15.24	0.302	11.70	7.63	0.54	0.20	0.085	0.08	98.49
NAZ 5.60	47.2	1.112	15.2	11.91	0.165	9.74	9.07	2.14	0.75	0.278	1.92	99.55
NAZ 6.95	69.6	0.552	14.4	4.59	0.038	1.75	0.33	5.32	1.28	0.122	1.53	99.51
NAZ 7.52	59.7	1.106	18.7	4.67	0.070	2.88	3.79	5.45	1.18	0.235	1.58	99.32
NAZ 9.30	43.9	1.954	13.2	12.37	0.213	8.34	10.28	1.61	0.55	0.630	6.50	99.59
NAZ 10.20	49.3	1.762	15.7	11.71	0.202	6.99	9.49	2.37	0.75	0.356	0.71	99.41
NAZ 10.98	44.9	3.030	15.6	13.57	0.238	7.98	9.88	2.27	0.63	0.364	1.02	99.47
NAZ 11.44	48.4	3.016	13.2	13.30	0.236	7.57	9.00	2.19	0.41	0.149	0.10	99.52
NAZ 12.00	47.3	2.468	15.4	12.20	0.201	7.23	10.11	2.66	0.44	0.816	0.74	99.61
NAZ 12.87	47.1	0.928	17.1	11.65	0.174	8.38	8.99	2.01	1.13	0.243	2.00	99.66
NAZ 14.68	53.0	1.426	15.5	7.76	0.117	6.59	6.04	2.74	3.66	0.657	0.04	99.24
NAZ 16.84	52.1	1.508	15.6	8.03	0.119	6.99	6.21	2.60	4.07	0.694	1.09	99.01
NAZ 17.59	51.0	1.431	14.8	8.17	0.131	8.02	6.46	2.38	3.69	0.624	0.11	99.09
NAZ 19.53	52.3	1.458	15.5	8.39	0.123	7.19	6.11	2.69	3.80	0.679	1.06	99.23
NAZ 21.63	38.4	2.561	12.9	11.22	0.222	3.74	6.32	2.99	0.88	1.142	18.87	99.15
NAZ 22.27	53.2	1.382	15.3	9.40	0.113	6.59	6.05	3.07	2.80	0.631	0.78	99.35
NAZ 23.20	53.7	1.369	15.5	7.82	0.121	6.23	5.79	3.14	2.34	0.626	0.12	99.41
NAZ 24.26	52.1	1.064	16.1	9.02	0.156	7.61	6.84	3.64	1.53	0.036	1.45	99.58
<i>Pluhův Bor bedrock core</i>												
PLB 2.59	39.2	0.035	1.8	8.89	0.078	37.17	0.01	<0.01	<0.01	0.010	0.08	99.14
PLB 4.04	39.3	0.016	0.3	10.04	0.103	37.24	0.01	<0.01	<0.01	0.014	0.08	99.09
PLB 5.37	41.0	0.031	0.7	7.87	0.131	36.72	0.05	<0.01	<0.01	0.013	12.84	99.39
PLB 5.97	29.4	0.798	18.1	10.20	0.072	29.92	0.11	<0.01	<0.01	0.076	11.07	99.78
PLB 6.71	50.6	0.050	3.3	8.51	0.098	27.36	2.48	<0.01	<0.01	0.010	6.74	99.12
PLB 7.20	42.2	0.613	16.5	9.39	0.165	14.07	11.24	2.41	0.36	0.113	2.53	99.61
PLB 8.50	47.4	0.462	14.4	9.06	0.148	13.70	9.08	2.81	0.29	0.040	2.23	99.64
PLB 9.51	51.8	0.648	16.1	7.02	0.101	9.48	7.58	4.31	0.32	0.103	2.27	99.66
PLB 10.60	48.8	0.676	16.2	7.93	0.113	9.88	8.19	3.68	0.30	0.105	0.90	99.78
PLB 12.37	48.9	0.621	16.7	8.41	0.112	8.53	6.35	4.04	0.58	0.135	5.25	99.60
PLB 13.45	49.9	0.499	13.3	9.79	0.122	12.91	7.51	2.83	0.21	0.062	2.55	99.67
PLB 17.58	49.7	0.650	16.4	8.18	0.099	10.47	7.06	3.96	0.39	0.024	0.06	99.80
PLB 18.48	52.0	0.634	16.3	8.00	0.121	8.66	8.04	4.24	0.24	0.053	1.49	99.79
PLB 23.17	52.9	0.065	3.4	5.14	0.088	24.49	10.04	0.12	0.01	0.014	3.36	99.62
PLB 23.62	51.9	0.037	3.6	5.73	0.102	25.96	7.30	0.03	<0.01	<0.01	0.11	99.54
PLB 26.70	55.8	0.608	17.5	6.56	0.091	6.49	3.86	6.38	0.42	0.098	2.08	99.79
PLB 27.58	57.2	0.639	16.3	5.80	0.085	5.64	4.73	6.56	0.27	0.095	0.10	99.81

Table A.16: continued

Sample name ¹	Ba (ppm)	Cr (ppm)	Ga (ppm)	Nb (ppm)	Ni (ppm)	Rb (ppm)	Sr (ppm)	V (ppm)	Y (ppm)	Zn (ppm)	Zr (ppm)
<i>Lysina bedrock core</i>											
LYS 4.65	48	<10	29	21	<10	1008	20	<10	<10	71	74
LYS 6.95	53	<10	36	28	<10	1165	15	<10	<10	76	58
LYS 8.50	28	<10	29	26	<10	1035	18	<10	13	63	41
LYS 9.83	16	<10	28	18	<10	904	18	<10	<10	54	44
LYS 10.95	27	<10	31	27	<10	1044	21	<10	<10	68	44
LYS 13.54	30	<10	29	21	<10	981	21	<10	<10	58	48
LYS 15.18	39	12	30	25	<10	937	21	<10	<10	59	43
LYS 16.40	34	<10	33	25	<10	1060	22	<10	<10	63	49
LYS 18.10	35	<10	32	11	<10	967	15	<10	<10	84	12
LYS 19.90	16	<10	26	17	<10	720	20	<10	<10	51	40
LYS 22.41	38	<10	29	18	<10	955	23	<10	<10	68	43
LYS 23.95	32	<10	29	10	<10	867	22	<10	<10	56	33
LYS 26.00	440	<10	31	20	<10	1346	53	<10	<10	99	53
LYS 27.25	63	<10	34	44	<10	1444	25	<10	<10	145	79
LYS 29.55	77	<10	24	16	<10	1188	33	<10	<10	81	46
<i>Na Zeleném bedrock core</i>											
NAZ 2.73	99	305	10	<10	394	15	43	133	53	147	829
NAZ 5.60	206	437	21	<10	127	30	191	191	29	133	1032
NAZ 6.95	233	24	10	<10	<10	66	147	70	11	66	131
NAZ 7.52	284	174	15	<10	139	59	320	138	13	113	46
NAZ 9.30	226	336	17	<10	90	30	127	324	52	96	100
NAZ 10.20	279	305	15	<10	142	41	204	244	44	73	75
NAZ 10.98	294	196	17	11	131	31	162	275	49	102	101
NAZ 11.44	242	380	14	<10	151	20	95	368	26	97	106
NAZ 12.00	357	221	18	<10	114	25	201	259	52	90	102
NAZ 12.87	377	394	24	<10	139	52	260	220	37	104	80
NAZ 14.68	2196	318	18	29	180	177	523	147	24	89	332
NAZ 16.84	2387	382	18	30	168	197	581	149	28	84	395
NAZ 17.59	2253	402	18	26	163	172	517	149	21	88	363
NAZ 19.53	2427	345	18	30	136	197	559	141	25	88	407
NAZ 21.63	594	82	23	14	36	45	198	234	70	130	692
NAZ 22.27	1695	356	16	29	142	152	479	137	22	88	377
NAZ 23.20	1753	290	18	27	116	119	471	137	24	87	364
NAZ 24.26	628	501	16	<10	162	68	218	267	22	113	60
<i>Pluhův Bor bedrock core</i>											
PLB 2.59	<10	3633	<10	<10	2319	11	<10	44	<10	40	12
PLB 4.04	18	4222	<10	<10	2313	11	<10	31	<10	35	12
PLB 5.37	19	2217	<10	<10	1857	10	<10	30	<10	34	15
PLB 5.97	57	885	16	<10	443	15	<10	164	<10	60	34
PLB 6.71	<10	4462	<10	<10	2052	<10	10	78	<10	49	11
PLB 7.20	389	993	19	<10	498	24	93	195	19	46	38
PLB 8.50	123	1099	12	<10	413	18	237	210	17	58	29
PLB 9.51	168	344	17	<10	170	20	428	217	31	26	106
PLB 10.60	118	235	14	<10	103	21	382	242	19	35	97
PLB 12.37	162	201	19	<10	95	25	466	217	22	24	110
PLB 13.45	115	405	15	<10	451	15	253	222	15	40	93
PLB 17.58	175	74	13	<10	143	20	507	190	15	29	124
PLB 18.48	204	301	15	<10	121	20	418	228	19	35	68
PLB 23.17	<10	1180	<10	<10	1263	11	26	67	<10	24	15
PLB 23.62	<10	1796	<10	<10	1550	10	17	53	<10	30	12
PLB 26.70	487	21	17	<10	43	24	408	225	17	21	118
PLB 27.58	209	15	14	<10	25	23	377	192	15	19	113

¹ Sample name includes depth in m from drilled bedrock core

Table A.17: Beryllium concentrations measured on hand pieces of weathered rocks sampled at outcrops (in ppm). Data are excluded from further evaluation because of unknown/variable stage of weathering.

Sample name	Be concentration ¹ (ppm)
<u>Lysina</u>	
<i>weathered hand pieces of rock</i>	
LYS Rx 11.01.1	4.12 ± 0.21
LYS Rx 11.01.2	3.30 ± 0.17
LYS Rx 11.02	19.1 ± 0.2
LYS Rx 11.04	4.72 ± 0.7
LYS RX 12.01.1	3.40 ± 0.5
LYS RX 12.01.2	3.30 ± 0.0
LYS Rx 12.02	3.97 ± 0.6
LYS Rx 12.03	14.07 ± 6.7
LYS RX 12.04.1	3.45 ± 0.1
LYS Rx 12.04.2	6.14 ± 0.7
LYS Rx 12.04.3	20.8 ± 0.0
LYS Rx 12.05	3.64 ± 0.3
LYS Rx 12.06	5.56 ± 0.29
LYS Rx 12.07	10.91 ± 0.5
LYS Rx 12.08	17.24 ± 3.2
<u>Na Zeleném</u>	
<i>weathered hand pieces of rock</i>	
NAZ Rx 11.01	0.427 ± 0.022
NAZ Rx 11.02	0.361 ± 0.019
NAZ Rx 12.01	0.250 ± 0.013
NAZ Rx 12.02	0.265 ± 0.014
NAZ Rx 12.03.1	0.300 ± 0.026
NAZ Rx 12.03.2	0.297 ± 0.015
NAZ Rx 12.04.1	0.296 ± 0.015
NAZ Rx 12.04.2	0.294 ± 0.015
NAZ Rx 12.05	1.152 ± 0.082
NAZ RX 12.07	1.425 ± 0.011
NAZ Rx 12.08	1.026 ± 0.053
NAZ Rx 12.17	0.856 ± 0.044
NAZ Rx 12.19	0.886 ± 0.046
NAZ Rx 12.20	0.472 ± 0.048
NAZ RX 12.22	0.323 ± 0.062
NAZ RX 12.24	0.092 ± 0.035
<u>Pluhův Bor</u>	
<i>weathered hand pieces of rock</i>	
PLB Rx 11.01	b.d.l.
PLB Rx 11.02	b.d.l.
PLB Rx 12.01	0.0236 ± 0.0081
PLB RX 12.05	0.0274 ± 0.0014
PLB Rx 12.07	0.0488 ± 0.0025
PLB Rx 12.08	0.0565 ± 0.0089
PLB Rx 12.09	0.030 ± 0.015
PLB Rx 12.10	0.0480 ± 0.0077
PLB Rx 12.11	0.0452 ± 0.0023
PLB Rx 12.12	0.0341 ± 0.0018
PLB Rx 12.14	0.195 ± 0.010
PLB RX 12.13	0.770 ± 0.030

¹ Value given with 5% uncertainty for ICP-OES measurement; in cases where more than one measurement was done on one individual sample the 1SD uncertainty is given (in grey).

b.d.l.: below detection limit (detection limit of measurements is 10 ppb of Be in the bedrock).

A.2.7 Stream water chemistry

Table A.18: Average dissolved element concentrations in the stream waters (in mg l⁻¹ and µg l⁻¹) measured on a HR-ICP-MS (*Element XR Thermo Fischer*) for the period from April 2012 to February 2013

Element concentration	Lysina	Na Zeleném	Pluhův Bor
<i>Major Elements (mg l⁻¹)</i>			
Mg	0.51	3.50	17.48
Si	9.82	7.34	8.49
Ca	2.29	7.86	4.13
Na	3.44	4.26	1.27
K	0.60	0.85	0.41
<i>Trace Elements (µg l⁻¹)</i>			
Al	500.5	25.53	16.82
Cr	0.69	0.32	6.01
Cu	0.88	1.22	1.41
Fe	475.6	25.27	57.29
Li	19.77	2.96	1.75
Mn	114.6	15.46	5.76
Ni	1.31	1.73	62.13
Sr	8.18	58.63	12.11
Ti	2.19	0.27	0.77
Zr	1.07	0.07	0.09

A.2.8 ¹⁰Be inventory at Lysina

Table A.19: Calculation of the ¹⁰Be inventory by means of [¹⁰Be]_{reac} measured on samples from the Lysina bedrock core

Sample ID	Sample type	Sampling depth	Depth interval	Assumed density	[¹⁰ Be] _{reac}	Inventory
		(cm)	(cm)		(atoms g ⁻¹)	(atoms cm ⁻²)
LYS	measured bedload, < 63µm (1) ¹	stream	30	1.5	1.92 × 10 ⁰⁸	8.6 × 10 ⁰⁹
	"recalculated" bulk bedload (2) ²	stream	30	1.5	5.87 × 10 ⁰⁷	2.6 × 10 ⁰⁹
LYS C	soil	60	58	1.8	7.0 × 10 ⁰⁷	7.3 × 10 ⁰⁹
LYS 1	soil	115	50	1.8	8.2 × 10 ⁰⁷	7.4 × 10 ⁰⁹
LYS 2	soil	160	52	1.8	9.7 × 10 ⁰⁷	9.0 × 10 ⁰⁹
LYS 4	sediment	218	80	1.8	3.0 × 10 ⁰⁷	4.3 × 10 ⁰⁹
LYS 6	sediment	320	71	1.8	2.5 × 10 ⁰⁷	3.1 × 10 ⁰⁹
Total Inventory (1)						4.2 × 10 ¹⁰
Total Inventory (2)						3.6 × 10 ¹⁰

¹ [¹⁰Be] measured on fine-grained bedload sediment used for calculation of inventory (1).

² [¹⁰Be] recalculated for a bulk bedload sediment sample (see Appendix A.2.4) used for calculation of inventory (2).

A.3 Detailed data set and additional information for the Sierra Nevada sites

A.3.1 AMS Results

This page is intentionally left blank

Table A.20: Detailed report of meteoric ^{10}Be results from CologneAMS for the different solid sample types measured at the Sierra Nevada site (soil, saprolite, bedload)

CologneAMS Code	Lab ID	Sample name	Sample type	Mid depth	Grain Size	(Extracted) fraction	Initial sample weight	^9Be carrier weight ¹	$(^{10}\text{Be}/^9\text{Be})_{\text{AMS}}$ ²	Relative analytical uncertainty	Absolute ^{10}Be concentration	^{10}Be concentration ³
				(cm)	(mm)		(g)	(mg)		(%)	(10^6 atoms)	(10^6 atoms g ⁻¹)
s03677	SN 2	P301	Soil	20	< 2	am-ox	0.5069	0.248	3.83×10^{-12}	3.04	98.6 ± 3.0	194.5 ± 6.2
s03693						x-ox	0.5069	0.246	4.10×10^{-12}	3.05	105.7 ± 3.2	208.4 ± 6.7
s03661 *						min	0.5069	0.151	1.64×10^{-12}	3.19	33.8 ± 1.1	66.6 ± 2.2
						reac	0.5069				204.2 ± 4.4	402.9 ± 9.1
						total	0.5069				238.0 ± 4.5	469.5 ± 9.4
s03678	SN 3	P301	Soil	30	< 2	am-ox	0.4847	0.246	2.69×10^{-12}	3.05	72.7 ± 2.2	150.1 ± 4.8
s03694						x-ox	0.4847	0.246	4.90×10^{-12}	3.04	124.0 ± 3.8	255.8 ± 8.2
s03662 *						min	0.4847	0.151	1.40×10^{-12}	3.22	29.8 ± 1.0	61.4 ± 2.1
						reac	0.4847				196.7 ± 4.4	405.9 ± 9.5
						total	0.4847				226.5 ± 4.5	467.3 ± 9.7
s03679	SN 4	P301	Soil	47	< 2	am-ox	0.5037	0.246	2.78×10^{-12}	3.05	71.0 ± 2.2	141.0 ± 4.5
s03695						x-ox	0.5037	0.246	5.64×10^{-12}	3.04	142.4 ± 4.3	282.7 ± 9.0
s03663 *						min	0.5037	0.152	1.24×10^{-12}	3.23	26.5 ± 0.9	52.5 ± 1.8
						reac	0.5037				213.4 ± 4.8	424 ± 10
						total	0.5037				239.9 ± 4.9	476 ± 10
s03680	SN 9	P301	Soil	106	< 2	am-ox	0.5095	0.246	2.17×10^{-12}	3.06	58.8 ± 1.8	115.3 ± 3.7
s03696						x-ox	0.5095	0.246	5.66×10^{-12}	3.04	143.4 ± 4.4	281.5 ± 9.0
s03664 *						min	0.5095	0.151	1.67×10^{-12}	3.16	35.9 ± 1.1	70.5 ± 2.3
						reac	0.5095				202.2 ± 4.7	396.9 ± 9.7
						total	0.5095				238.1 ± 4.9	467 ± 10
s06941	SN 59	BP 0-10 cm	Soil	5	< 2	am-ox	0.5910	0.206	3.767×10^{-12}	3.11	51.8 ± 1.7	87.69 ± 2.8
s06950						x-ox	0.5910	0.151	1.043×10^{-12}	3.28	10.5 ± 0.4	17.73 ± 0.6
s07806						min	0.5910	0.151	6.656×10^{-12}	3.11	67.4 ± 2.2	113.99 ± 3.7
						reac	0.5910				62.3 ± 1.7	105.4 ± 2.9
						total	0.5910				129.7 ± 2.8	219.4 ± 4.7

Table A.20: continued

CologneAMS Code	Lab ID	Sample name	Sample type	Mid depth	Grain Size	(Extracted) fraction	Initial sample weight	⁹ Be carrier weight ¹	(¹⁰ Be/ ⁹ Be) _{AMS} ²	Relative analytical uncertainty	¹⁰ Be	¹⁰ Be concentration ³
				(cm)	(mm)		(g)	(mg)		(%)	(10 ⁶ atoms)	(10 ⁶ atoms g ⁻¹)
s06942	SN 60	BP 30-40 cm	Soil	35	< 2	am-ox	0.5888	0.206	2.923 × 10 ⁻¹²	3.12	40.3 ± 1.3	68.41 ± 2.2
s06951						x-ox	0.5888	0.151	1.138 × 10 ⁻¹²	3.25	11.4 ± 0.4	19.37 ± 0.7
s07807						min	0.5888	0.151	6.587 × 10 ⁻¹²	3.12	66.7 ± 2.2	113.29 ± 3.7
						reac	0.5888				51.7 ± 1.4	87.8 ± 2.3
						total	0.5888				118.4 ± 2.6	201.1 ± 4.4
s06943	SN 61	BP 60-70 cm	Soil	65	< 2	am-ox	0.5774	0.206	2.354 × 10 ⁻¹²	3.13	32.4 ± 1.1	56.11 ± 1.8
s06952						x-ox	0.5774	0.151	1.038 × 10 ⁻¹²	3.26	10.4 ± 0.4	18.05 ± 0.6
s07808						min	0.5774	0.151	4.980 × 10 ⁻¹²	3.12	50.5 ± 1.6	87.43 ± 2.8
						reac	0.5774				42.8 ± 1.1	74.2 ± 1.9
						total	0.5774				93.3 ± 2.0	161.6 ± 3.4
s06944	SN 62	BP 80-90 cm	Soil	85	< 2	am-ox	0.5766	0.206	2.409 × 10 ⁻¹²	3.13	33.2 ± 1.1	57.57 ± 1.9
s06953						x-ox	0.5766	0.151	1.108 × 10 ⁻¹²	3.26	11.1 ± 0.4	19.26 ± 0.7
s07809						min	0.5766	0.151	5.088 × 10 ⁻¹²	3.11	51.5 ± 1.7	89.30 ± 2.9
						reac	0.5766				44.3 ± 1.2	76.8 ± 2.0
						total	0.5766				95.8 ± 2.0	166.1 ± 3.5
s03687	SN 20	BP 204	Saprolite	178	< 2	am-ox	0.509	0.206	2.23 × 10 ⁻¹³	3.58	4.67 ± 0.17	9.18 ± 0.34
s03703						x-ox	0.509	0.206	3.84 × 10 ⁻¹³	3.37	7.85 ± 0.27	15.41 ± 0.54
s03633						min	0.509	0.144	2.56 × 10 ⁻¹³	5.27	4.80 ± 0.26	9.42 ± 0.51
						reac	0.509				12.52 ± 0.31	24.59 ± 0.64
						total	0.509				17.31 ± 0.41	34.01 ± 0.82
s03686	SN 19	BP 173	Saprolite	257	< 2	am-ox	0.5015	0.152	1.70 × 10 ⁻¹³	3.95	4.00 ± 0.16	7.97 ± 0.33
s03702						x-ox	0.5015	0.152	2.05 × 10 ⁻¹³	5.43	4.53 ± 0.25	9.04 ± 0.50
s03632						min	0.5015	0.153	2.56 × 10 ⁻¹³	4.67	5.03 ± 0.24	10.02 ± 0.48
						reac	0.5015				8.53 ± 0.30	17.00 ± 0.60
						total	0.5015				13.55 ± 0.38	27.03 ± 0.77

Table A.20: continued

CologneAMS Code	Lab ID	Sample name	Sample type	Mid depth	Grain Size	(Extracted) fraction	Initial sample weight	⁹ Be carrier weight ¹	(¹⁰ Be/ ⁹ Be) _{AMS} ²	Relative analytical uncertainty	¹⁰ Be	¹⁰ Be concentration ³
				(cm)	(mm)		(g)	(mg)		(%)	(10 ⁶ atoms)	(10 ⁶ atoms g ⁻¹)
s03685	SN 17	BP 144	Saprolite	330	< 2	am-ox	0.5195	0.152	1.24 × 10 ⁻¹³	4.43	3.33 ± 0.15	6.41 ± 0.30
s03701						x-ox	0.5195	0.152	1.63 × 10 ⁻¹³	4.13	3.93 ± 0.17	7.57 ± 0.33
s03631						min	0.5195	0.153	1.55 × 10 ⁻¹³	4.36	2.91 ± 0.13	5.59 ± 0.26
						reac	0.5195				7.26 ± 0.23	13.98 ± 0.44
						total	0.5195				10.17 ± 0.26	19.58 ± 0.51
s03684	SN 16	BP 111	Saprolite	414	< 2	am-ox	0.4982	0.206	1.15 × 10 ⁻¹³	3.96	2.377 ± 0.096	4.77 ± 0.20
s03700						x-ox	0.4982	0.206	6.87 × 10 ⁻¹⁴	4.66	1.417 ± 0.069	2.84 ± 0.14
s03630						min	0.4982	0.153	1.08 × 10 ⁻¹³	5.48	2.02 ± 0.11	4.05 ± 0.23
						reac	0.4982				3.79 ± 0.12	7.62 ± 0.24
						total	0.4982				5.81 ± 0.16	11.66 ± 0.34
s03683	SN 15	BP 72	Saprolite	513	< 2	am-ox	0.7476	0.152	1.17 × 10 ⁻¹⁴	9.8	0.254 ± 0.039	0.340 ± 0.052
s03699						x-ox	0.7476	0.152	1.25 × 10 ⁻¹⁴	10.21	0.263 ± 0.040	0.352 ± 0.053
s03629						min	0.7476	0.153	1.36 × 10 ⁻¹⁴	14.75	0.228 ± 0.043	0.305 ± 0.057
						reac	0.7476				0.518 ± 0.056	0.692 ± 0.075
						total	0.7476				0.746 ± 0.070	0.998 ± 0.094
s03682	SN 14	BP 36	Saprolite	605	< 2	am-ox	0.5131	0.206	8.95 × 10 ⁻¹⁵	10.17	0.159 ± 0.024	0.309 ± 0.048
s03698						x-ox	0.5131	0.206	6.87 × 10 ⁻¹⁵	11.65	0.113 ± 0.022	0.221 ± 0.043
s03628						min	0.5131	0.153	8.26 × 10 ⁻¹⁵	21.54	0.131 ± 0.040	0.255 ± 0.078
						reac	0.5131				0.272 ± 0.033	0.530 ± 0.064
						total	0.5131				0.403 ± 0.052	0.78 ± 0.10
s03681	SN 13	BP 3	Saprolite	688	< 2	am-ox	0.7491	0.206	1.90 × 10 ⁻¹⁴	7.79	0.369 ± 0.035	0.493 ± 0.046
s03697						x-ox	0.7491	0.206	1.22 × 10 ⁻¹⁴	9.21	0.225 ± 0.028	0.300 ± 0.037
s03627						min	0.7491	0.153	1.19 × 10 ⁻¹⁴	23.77	0.196 ± 0.057	0.261 ± 0.076
						reac	0.7491				0.594 ± 0.044	0.793 ± 0.060
						total	0.7491				0.790 ± 0.072	1.05 ± 0.10

Table A.20: continued

CologneAMS Code	Lab ID	Sample name	Sample type	Mid depth	Grain Size	(Extracted) fraction	Initial sample weight	⁹ Be carrier weight ¹	(¹⁰ Be/ ⁹ Be) _{AMS} ²	Relative analytical uncertainty	¹⁰ Be	¹⁰ Be concentration ³
				(cm)	(mm)		(g)	(mg)		(%)	(10 ⁶ atoms)	(10 ⁶ atoms g ⁻¹)
s03689	SN 28	PIG	Bedload		< 2	am-ox	0.9776	0.185	1.60×10^{-12}	3.13	37.5 ± 1.2	38.3 ± 1.3
s03705						x-ox	0.9776	0.185	1.43×10^{-12}	3.12	28.06 ± 0.88	28.70 ± 0.94
s03666 *						min	0.9776	0.152	3.71×10^{-13}	3.8	7.94 ± 0.30	8.12 ± 0.32
						reac	0.9776				65.5 ± 1.5	67.0 ± 1.6
						total	0.9776				73.5 ± 1.5	75.1 ± 1.6
s02444	PC 39	PC 39	Soil	5	< 1	am-ox	0.5133	0.203	1.268×10^{-12}	3.3	28.0 ± 0.9	14.1 ± 1.9
s02439						x-ox	0.5133	0.203	2.891×10^{-12}	3.19	65.0 ± 2.1	126.7 ± 4.2
s02434						min	0.5133	0.201	3.322×10^{-13}	3.55	7.25 ± 0.26	14.12 ± 0.52
						reac	0.5133				93.0 ± 2.3	140.8 ± 4.6
						total	0.5133				100.3 ± 2.3	154.9 ± 4.7

Samples displayed in grey are processed by *D.Uhlig, GFZ Potsdam*, in 2015

¹ Concentration of ⁹Be carrier is 372.5 ± 3.5 ppm

² Ratio as measured on AMS

³ Calculated from AMS ratio using the sum of ⁹Be carrier and natural ⁹Be content, with combined analytical and blank error (all uncertainties 1SD), relative to the initial solid sample weight.

The blank ratio of ¹⁰Be measurement is 1.48 ± 1.30 × 10⁻¹⁵ (n = 9).

* Samples were measured in the wrong order at the CologneAMS and are given here with the actual AMS Code.

Table A.21: Detailed report of meteoric ¹⁰Be results from the CologneAMS for the stream waters at the Sierra Nevada site

CologneAMS Code	Lab ID	Sample name	Sample type	"Fraction"	Initial sample weight	⁹ Be carrier weight ¹	(¹⁰ Be/ ⁹ Be) _{AMS} ²	Relative analytical uncertainty	Absolute ¹⁰ Be amount	¹⁰ Be concentration ³
					(g)	(mg)		(%)	(10 ⁴ atoms)	(10 ⁴ atoms g ⁻¹)
s02420	SNW48	P301 Stream	Stream Water	diss	489	0.202	1.18 × 10 ⁻¹³	4.3	158.2 ± 6.9	0.324 ± 0.014
s02421	SNW49	P303 Stream	Stream Water	diss	496	0.202	3.46 × 10 ⁻¹⁴	5.9	45.3 ± 3.0	0.0914 ± 0.0060
s02422	SNW50	P304 Stream	Stream Water	diss	497	0.202	4.15 × 10 ⁻¹⁴	5.7	54.6 ± 3.4	0.1098 ± 0.0068
s03624	SNW51	PIG Stream	Stream Water	diss	401	0.185	6.89 × 10 ⁻¹⁴	5.2	83.7 ± 4.5	0.209 ± 0.012
s02423	SNW52	D102 Stream	Stream Water	diss	424	0.203	5.34 × 10 ⁻¹⁴	5.2	71.0 ± 3.9	0.1674 ± 0.0094

¹ Concentration of ⁹Be carrier is 372.5 ± 3.5 ppm
² Ratio as measured on AMS
³ Calculated from AMS ratio using the amount of ⁹Be carrier, with combined analytical and blank uncertainty (all uncertainties 1SD), relative to initial solid sample weight.
The blank ratio of ¹⁰Be measurement is 0.98 ± 0.77 x10⁻¹⁵ (n = 6).

Table A.22: Detailed report of meteoric ^{10}Be results from CologneAMS for further measured soil and saprolite samples that were not considered in the data evaluation

CologneAMS Code	Lab ID ¹	Sample name	Sample type	Mid depth (cm)	Grain Size (mm)	(Extracted) fraction	Initial sample weight (g)	^9Be carrier weight ² (mg)	$(^{10}\text{Be}/^9\text{Be})_{\text{AMS}}$ ³	Relative analytical uncertainty (%)	Absolute ^{10}Be amount (10^6 atoms)	^{10}Be concentration ⁴ (10^6 atoms g^{-1})
s02429	SN 20	BP 204	Saprolite	178	< 5	am-ox	0.3506	0.204	1.454×10^{-13}	3.92	3.57 ± 0.14	10.18 ± 0.42
s02430	SN 16	BP 111	Saprolite	414	< 6	am-ox	0.4553	0.204	8.577×10^{-14}	4.39	2.13 ± 0.10	4.69 ± 0.22
s02431	SN 14	BP 36	Saprolite	605	< 7	am-ox	0.4635	0.205	4.939×10^{-15}	13.61	0.110 ± 0.028	0.237 ± 0.061
s02425	SN 20	BP 204	Saprolite	178	< 2	x-ox	0.3506	0.205	4.001×10^{-13}	3.46	10.03 ± 0.35	28.62 ± 1.03
s02426	SN 16	BP 111	Saprolite	414	< 3	x-ox	0.4553	0.203	1.337×10^{-13}	3.97	3.30 ± 0.13	7.25 ± 0.30
s02427	SN 14	BP 36	Saprolite	605	< 4	x-ox	0.4635	0.204	1.410×10^{-14}	8.41	0.329 ± 0.035	0.709 ± 0.077
s02443		WB 25	Soil	5	< 2	am-ox	0.5047	0.203	1.545×10^{-12}	3.22	34.6 ± 1.1	68.6 ± 2.3
s02438		WB 25	Soil			x-ox	0.5047	0.203	2.023×10^{-12}	3.21	46.3 ± 1.5	91.7 ± 3.1
s02433		WB 25	Soil			min	0.5047	0.204	2.549×10^{-13}	3.67	5.45 ± 0.20	10.81 ± 0.41
s02444		PC 39	Soil	5	< 1	am-ox	0.5133	0.203	1.268×10^{-12}	3.3	28.01 ± 0.93	54.6 ± 1.9
s02439		PC 39	Soil			x-ox	0.5133	0.203	2.891×10^{-12}	3.19	65.0 ± 2.1	126.7 ± 4.2
s02434		PC 39	Soil			min	0.5133	0.201	3.322×10^{-13}	3.55	7.25 ± 0.26	14.12 ± 0.52
s02446		BM 54	Soil	5	< 1	am-ox	0.5012	0.202	2.648×10^{-12}	3.19	61.2 ± 2.0	122.0 ± 4.1
s02441		BM 54	Soil			x-ox	0.5012	0.204	1.757×10^{-12}	3.21	41.3 ± 1.3	82.4 ± 2.8
s02436		BM 54	Soil			min	0.5012	0.203	1.459×10^{-12}	3.24	32.4 ± 1.1	64.7 ± 2.2
s02445		BM 53	Soil	15	< 1	am-ox	0.4908	0.203	2.656×10^{-12}	3.18	64.5 ± 2.1	131.5 ± 4.4
s02440		BM 53	Soil			x-ox	0.4908	0.203	2.054×10^{-12}	3.21	48.6 ± 1.6	99.0 ± 3.3
s02435		BM 53	Soil			min	0.4908	0.203	1.804×10^{-12}	3.2	38.6 ± 1.2	78.5 ± 2.6

¹ Same samples as in Table A.20, but processed in a different batch.² Concentration of ^9Be carrier is 372.5 ± 3.5 ppm.³ Ratio as measured on AMS⁴ Calculated from AMS ratio using the sum of ^9Be carrier and natural ^9Be content, with combined analytical and blank error (all uncertainties 1SD), relative to the initial solid sample weight.

A.3.2 [⁹Be]_{parent} for the Sierra Nevada Sites

Table A.23: ⁹Be concentration (in µg g⁻¹) of the parent bedrock (rock fragments)

Sample ID	Sample type	Location	Be concentration ¹ (µg g ⁻¹)
SN 31	bedrock	P 301	1.148 ± 0.060
SN 32	bedrock	P 301	0.991 ± 0.052
SN 35	bedrock	P 303	0.913 ± 0.047
SN 36	bedrock	P 303	0.985 ± 0.051
SN 41	bedrock	Balsam site	1.200 ± 0.062
SN 43	bedrock	Balsam site	1.220 ± 0.063
Average (with 1SD)			1.08 ± 0.12

¹ Concentration of sample is given with an uncertainty of 5% that denotes the long-term ICP-OES repeatability.

A.3.3 Reproducibility of the sequential extraction procedure for the Balsam Profile

In the case of the Balsam saprolite profile, sample aliquots of the same saprolite sample were processed and measured repeatedly at various times by the same operator. The results for the first extraction step using 0.5M HCl show that the reproducibility is given (see Table A.24). This reproducibility for the first extraction step is supported by measurements of the San Joaquin Soil reference material (“SRM 2709”, *National Institute of Standards & Technology* NIST). This reference material was processed along with different sample batches by different operators and at various times (see Table A.25). However, as already mentioned in the main text of this study, the reproducibility for the second extraction step (“X-Ox”) using a hydroxylamine-hydrochloride solution is relatively low. One possible reason could be a high temperature sensitivity of the leaching step.

Table A.24: [^9Be], [^{10}Be], and ($^{10}\text{Be}/^9\text{Be}$) measured in the individually extracted fractions (am-ox, x-ox, min) and sums of reactive and total ^9Be on two sampled aliquots of three saprolite samples, respectively, that were processed and measured at different times.

Lab ID	Sample name	Sample type	Mid depth (cm)	[^9Be] _{am-ox} (10^6 atoms g $^{-1}$)	[^9Be] _{x-ox} (10^6 atoms g $^{-1}$)	[^9Be] _{min} (10^6 atoms g $^{-1}$)	[^9Be] _{reac} (10^6 atoms g $^{-1}$)	[^9Be] _{total} (10^6 atoms g $^{-1}$)
<i><u>Balsam Profile</u></i>								
<i>Samples processed for AMS measurement in April 2013</i>								
SN 20	BP 204	Saprolite	178	0.248 \pm 0.012	0.937 \pm 0.047	0.252 \pm 0.013	1.185 \pm 0.059	1.437 \pm 0.072
SN 16	BP 111	Saprolite	414	0.200 \pm 0.010	0.540 \pm 0.027	0.606 \pm 0.030	0.739 \pm 0.037	1.345 \pm 0.067
SN 14	BP 36	Saprolite	605	0.200 \pm 0.010	0.568 \pm 0.028	0.759 \pm 0.038	0.769 \pm 0.038	1.528 \pm 0.076
<i>Samples processed for AMS measurement in Jan 2014</i>								
SN 20	BP 204	Saprolite	178	0.235 \pm 0.012	0.496 \pm 0.025	0.608 \pm 0.030	0.731 \pm 0.037	1.339 \pm 0.067
SN 16	BP 111	Saprolite	414	0.193 \pm 0.010	0.252 \pm 0.013	0.882 \pm 0.044	0.445 \pm 0.022	1.327 \pm 0.066
SN 14	BP 36	Saprolite	605	0.187 \pm 0.009	0.266 \pm 0.013	1.009 \pm 0.050	0.453 \pm 0.023	1.463 \pm 0.073
Lab ID	Sample name	Sample type	Mid depth (cm)	[^{10}Be] _{am-ox} (10^6 atoms g $^{-1}$)	[^{10}Be] _{x-ox} (10^6 atoms g $^{-1}$)	[^{10}Be] _{min} (10^6 atoms g $^{-1}$)	[^{10}Be] _{reac} (10^6 atoms g $^{-1}$)	[^{10}Be] _{total} (10^6 atoms g $^{-1}$)
<i><u>Balsam Profile</u></i>								
<i>Samples processed for AMS measurement in April 2013</i>								
SN 20	BP 204	Saprolite	178	10.18 \pm 0.42	28.6 \pm 1.0	n.d.	38.8 \pm 1.1	n.d.
SN 16	BP 111	Saprolite	414	4.69 \pm 0.22	7.25 \pm 0.30	n.d.	11.94 \pm 0.37	n.d.
SN 14	BP 36	Saprolite	605	0.237 \pm 0.061	0.709 \pm 0.077	n.d.	0.95 \pm 0.10	n.d.
<i>Samples processed for AMS measurement in Jan 2014</i>								
SN 20	BP 204	Saprolite	178	9.18 \pm 0.34	15.41 \pm 0.54	9.42 \pm 0.51	24.59 \pm 0.64	34.01 \pm 0.82
SN 16	BP 111	Saprolite	414	4.77 \pm 0.20	2.84 \pm 0.14	4.05 \pm 0.23	7.62 \pm 0.24	11.66 \pm 0.34
SN 14	BP 36	Saprolite	605	0.309 \pm 0.048	0.221 \pm 0.043	0.255 \pm 0.078	0.530 \pm 0.064	0.78 \pm 0.10

Table A.24: continued

Lab ID	Sample name	Sample type	Mid depth (cm)	$(^{10}\text{Be}/^9\text{Be})_{\text{am-ox}}$ ($\times 10^{-10}$)	$(^{10}\text{Be}/^9\text{Be})_{\text{x-ox}}$ ($\times 10^{-10}$)	$(^{10}\text{Be}/^9\text{Be})_{\text{min}}$ ($\times 10^{-10}$)	$(^{10}\text{Be}/^9\text{Be})_{\text{reac}}$ ($\times 10^{-10}$)	$(^{10}\text{Be}/^9\text{Be})_{\text{total}}$ ($\times 10^{-10}$)
<i><u>Balsam Profile</u></i>								
<i>Samples processed for AMS measurement in April 2013</i>								
SN 20	BP 204	Saprolite	178	6.14 \pm 0.40	4.57 \pm 0.28	n.d.	4.90 \pm 0.28	n.d.
SN 16	BP 111	Saprolite	414	3.52 \pm 0.24	2.01 \pm 0.13	n.d.	2.42 \pm 0.14	n.d.
SN 14	BP 36	Saprolite	605	0.177 \pm 0.046	0.187 \pm 0.022	n.d.	0.184 \pm 0.021	n.d.
<i>Samples processed for AMS measurement in Jan 2014</i>								
SN 20	BP 204	Saprolite	178	5.84 \pm 0.36	4.65 \pm 0.28	2.32 \pm 0.17	5.03 \pm 0.28	3.80 \pm 0.21
SN 16	BP 111	Saprolite	414	3.70 \pm 0.24	1.69 \pm 0.12	0.69 \pm 0.05	2.56 \pm 0.15	1.32 \pm 0.08
SN 14	BP 36	Saprolite	605	0.248 \pm 0.040	0.124 \pm 0.025	0.038 \pm 0.012	0.175 \pm 0.023	0.080 \pm 0.011

" n.d.": not determined

Table A.25: Compilation of the results from the sequential extraction procedure for the San Joaquin Soil reference material (“SRM 2709”)

Sample name	Al (ppm)	Ba (ppm)	Be (ppm)	Ca (ppm)	Cr (ppm)	Cu (ppm)	Fe (ppm)	K (ppm)	Mg (ppm)	Mn (ppm)	Na (ppm)	Ni (ppm)	Pb (ppm)	Sr (ppm)	Ti (ppm)	Zn (ppm)	Zr (ppm)	Operator
SRM2709a am-ox	4477	184	0.32	3579	10	12	n.d.	470	7429	261	90	25	5.8	30	11	22	<0.10	DU
SRM2709a am-ox	5141	264	0.31	12942	15	22	5804	942	4611	324	349	29	5.8	75	12	n.d.	0.74	ND
SRM2709a am-ox	5003	274	0.31	12826	15	14	6071	841	4890	336	295	29	5.7	12	14	0.8	0.00	ND
SRM2709a am-ox	5328	335	0.34	12490	16	14	6191	1091	4667	319	401	32	6.2	85	18	27	0.57	ND
SRM2709a am-ox	n.d.	329	0.36	n.d.	16	14	n.d.	n.d.	n.d.	n.d.	413	36	6.3	n.d.	14	30	0.59	ND
SRM2709a am-ox	n.d.	196	0.30	n.d.	12	12	n.d.	n.d.	n.d.	n.d.	n.d.	27	5.4	65	8	23	0.40	ND
SRM2709a am-ox	n.d.	272	0.33	n.d.	15	14	n.d.	n.d.	n.d.	n.d.	n.d.	30	6.0	72	13	27	0.52	ND
SRM2709a am-ox	5925	383	0.38	14413	17	16	7057	1421	5152	331	551	n.d.	n.d.	86	43	n.d.	n.d.	MO
SRM2709a am-ox	7339	375	0.40	14027	27	19	9714	1658	6619	362	422	n.d.	n.d.	95	249	n.d.	n.d.	MO
SRM2709a am-ox	7469	368	0.40	13657	24	17	7045	1710	5365	363	430	n.d.	n.d.	94	65	n.d.	n.d.	MO
Average (am-ox)	5812	298	0.35	11990	17	15	6980	1162	5533	328	369	30	5.9	68	45	22	0.47	
1SD (am-ox)	1083	68	0.04	3493	4.7	2.9	1311	422	997	32	126	3.4	0.3	27	70	10	0.23	
SRM2709a x-ox	515	36	0.07	378	1.6	3.0	4627	220	1987	47	68	16	2.7	12	<0.83	16	<0.10	DU
SRM2709a x-ox	9844	80	0.12	384	8.4	3.3	18783	3618	6547	183	69	2	1.2	5	1928	34	1.9	ND
SRM2709a x-ox	9561	80	0.21	630	37	16	19024	1377	6303	138	216	35	4.7	20	129	57	0.66	ND
SRM2709a x-ox	2197	36	0.11	406	9.1	5.4	8027	641	3435	n.d.	n.d.	n.d.	n.d.	14	n.d.	n.d.	n.d.	MO
SRM2709a x-ox	1887	27	0.09	338	6.7	9.2	7078	540	2298	62	67	n.d.	n.d.	12	1.9	n.d.	n.d.	MO
SRM2709a x-ox	1907	25	0.09	223	8.1	10	6852	530	2179	62	77	n.d.	n.d.	12	2.7	n.d.	n.d.	MO
Average (x-ox)	4318	48	0.12	393	12	7.9	10732	1154	3792	98	99	18	2.9	13	515	36	1.3	
1SD (x-ox)	3845	23	0.05	122	12	4.6	5868	1156	1920	53	59	14	1.5	4.3	817	17	0.6	
SRM2709a min	56095	n.d.	0.68	5287	74	3.3	7826	20094	3505	69	12613	9.1	3.9	134	3015	17	59	ND
SRM2709a min	52653	n.d.	0.63	4800	59	2.6	6509	17732	3126	63	11232	7.4	3.7	130	2746	14	49	ND
Average (min)	54374		0.65	5044	66	3.0	7167	18913	3315	66	11923	8.2	3.8	132	2880	16	54	
1SD (min)	1721		0.03	243	7.2	0.4	658	1181	189	3.3	691	0.9	0.1	2.0	135	1.7	4.8	

n.d.: not determined

A.3.4 Comparison of meteoric [^{10}Be] measured in the Providence Creek Catchment

In the Providence Creek catchment site meteoric ^{10}Be concentrations were measured on different profiles and by different operators. All samples were processed using the sequential extraction procedure described in this study. The total ^{10}Be concentration results are compiled in Figure A.3.1.

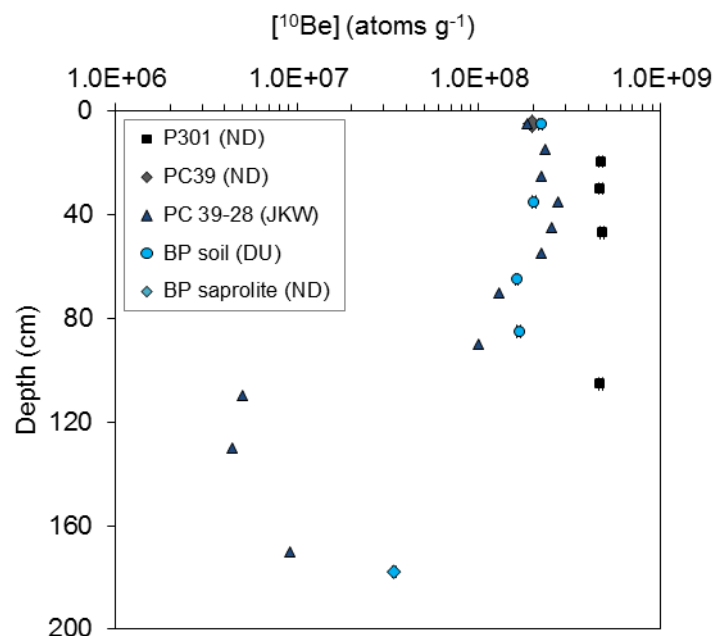


Figure A.3.1: Comparison of [^{10}Be] (in atoms g $^{-1}$) measured in this study by myself (ND; P301, grey symbols) and by David Uhlig (DU; BP soil, light blue symbols), and [^{10}Be] measured by Jane K. Willenbring (JKW) at the GFZ Potsdam in 2010 on a soil profile sampled at Providence Creek (PC, dark blue symbols). The uppermost sample of this soil profile - PC39 (grey diamond) - was processed by myself along with the soil samples from this study. Error bars are smaller than symbols.

[^{10}Be] determined on aliquots of the sample “PC39” in this study and by Jane K. Willenbring are about the same confirming reproducibility of the method in the case of these soil samples. The meteoric [^{10}Be] measured on different soil profiles in the catchment site are in the same order, showing that there is only a small variation within the studied area.

A.3.5 Background data for chemical weathering indices

To extend the bedrock data base in order to reduce potential inhomogeneity in the bedrock due to small sample numbers, the chemical bedrock concentrations measured at the *GFZ Potsdam* were combined with chemical concentration data published by Hahm et al. (2014) and Riebe and Granger (2013). The average concentrations values derived from these dataset were used to calculate CDF and τ values (see Table A.26, Table A.27, and Table A.28).

Table A.26: Major element concentrations determined with XRF, and average value from a data set from *Hahm et al. (2014)*, *Riebe and Granger (2013)*, and *GFZ Potsdam, Sec. 3.3*

sample ID	sample description	sample type	mean depth (cm)	LOI corrected data (major oxides)										
				LOI (wt%)	SiO ₂ (wt%)	TiO ₂ (wt%)	Al ₂ O ₃ (wt%)	Fe ₂ O ₃ (wt%)	MnO (wt%)	MgO (wt%)	CaO (wt%)	Na ₂ O (wt%)	K ₂ O (wt%)	P ₂ O ₅ (wt%)
P301 regolith depth profile														
SN01	P301 Core 0-13cm	soil	7	37.5	10.1	0.15	3.2	0.94	0.12	0.43	1.26	0.37	0.53	0.10
SN02	P301 Core 13-26cm	soil	20	20.3	63.4	0.91	19.2	6.27	0.21	2.46	4.12	2.50	2.82	0.34
SN03	P301 Core 26-34cm	soil	30	6.31	57.4	0.87	17.6	6.27	0.12	2.49	3.73	2.08	2.32	0.23
SN04	P301 Auger 30-47cm	soil	39	6.78	56.3	0.93	17.6	6.62	0.11	2.64	3.67	1.89	2.25	0.21
SN05	P301 Auger 47-58cm	soil	53	6.08	59.1	1.01	18.8	7.27	0.11	2.85	3.79	1.91	2.39	0.20
SN06	P301 Auger 58-71cm	soil	65	5.75	58.5	0.99	18.8	7.23	0.11	2.82	3.77	1.90	2.25	0.19
SN07	P301 Auger 71-83cm	soil	77	5.10	59.0	0.98	18.4	7.06	0.11	2.78	3.72	1.84	2.28	0.19
SN08	P301 Auger 83-95cm	soil	89	5.26	57.4	1.06	19.9	7.84	0.12	3.02	3.81	1.79	2.26	0.19
SN09	P301 Auger 95-105cm	soil	100	4.62	57.7	1.03	19.4	7.78	0.13	2.96	3.71	1.78	2.37	0.18
SN10	P301 Auger 105-116cm	soil	111	6.67	60.1	1.04	19.5	7.92	0.13	3.02	3.76	1.76	2.31	0.17
Balsam regolith depth profile														
SN59	BP 0-10cm	soil	5	9.08	59.1	1.07	19.8	8.47	0.21	2.91	3.86	1.69	2.27	0.30
SN60	BP 30-40cm	soil	35	5.60	57.6	1.14	20.9	9.09	0.15	3.10	3.78	1.49	2.17	0.18
SN61	BP 60-70cm	soil	65	6.27	58.7	1.12	19.8	9.06	0.15	3.13	3.92	1.48	2.18	0.14
SN62	BP 80-90cm	soil	85	4.83	59.6	1.08	19.2	9.05	0.15	3.03	3.86	1.47	2.12	0.13
SN20	BP 204	saprolite	178	7.95	60.5	1.13	20.1	10.07	0.11	2.89	2.11	0.45	2.30	0.06
SN19	BP 173	saprolite	257	6.88	60.7	1.10	20.0	8.92	0.11	3.04	2.73	0.74	2.44	0.04
SN18	BP 161	saprolite	287	6.37	57.0	1.25	20.0	9.88	0.15	3.94	4.13	1.23	2.03	0.04
SN17	BP 144	saprolite	330	5.59	60.1	1.00	19.6	7.76	0.15	2.97	4.10	1.56	2.45	0.04
SN16	BP 111	saprolite	414	5.19	60.7	1.01	19.2	7.91	0.12	3.01	3.87	1.49	2.28	0.07
SN15	BP 72	saprolite	513	3.89	61.7	0.93	18.1	7.10	0.11	2.74	4.66	2.01	2.20	0.17
SN14	BP 36	saprolite	605	4.62	61.6	1.06	17.9	7.93	0.12	3.11	4.07	1.57	2.23	0.12
SN13	BP rock piece	weathered Granodiorite	647	3.30	60.7	0.99	17.1	7.50	0.12	3.01	5.90	2.60	1.52	0.26
SN12	BP rock piece	weathered Granodiorite	692	1.99	60.1	0.98	16.7	7.59	0.12	3.08	5.87	2.66	2.38	0.23
SN11	BP rock	weathered Granodiorite	-	1.17	68.4	0.54	14.7	4.31	0.07	1.56	3.59	2.59	3.84	0.11
Creek sediment loads														
SN28	PIG bedload	bedload sediment	-	3.34	68.3	1.2	11.7	7.5	0.1	2.7	4.8	1.7	1.5	0.1
mean bedrock (data from Hahm et al. (2014), Riebe and Granger (2013), and GFZ Potsdam, Sec 3.3)														
mean bedrock after outlier removal					59.5	1.0	17.2	7.2	0.1	3.2	6.2	3.1	2.2	0.2
2 SD bedrock after outlier removal					8.7	0.4	1.8	3.4	0.1	2.0	2.5	0.4	0.9	0.1
2 SE bedrock after outlier removal					1.0	0.0	0.2	0.4	0.0	0.2	0.3	0.0	0.1	0.0

Table A.27: Trace element concentrations determined with XRF, and average value from a data set from *Hahm et al. (2014)*, *Riebe and Granger (2013)*, and *GFZ Potsdam, Sec. 3.3*

sample ID	sample description	sample type	mean depth (cm)	LOI corrected data (trace elements)										
				Ba (µg/g)	Cr (µg/g)	Ga (µg/g)	Nb (µg/g)	Ni (µg/g)	Rb (µg/g)	Sr (µg/g)	V (µg/g)	Y (µg/g)	Zn (µg/g)	Zr (µg/g)
P301 regolith depth profile														
SN01	P301 Core 0-13cm	soil	7	262	<16	<16	<16	<16	21	88	19	<16	24	30
SN02	P301 Core 13-26cm	soil	20	1014	38	21	16	21	120	369	112	26	103	192
SN03	P301 Core 26-34cm	soil	30	835	37	21	13	15	111	331	122	23	101	173
SN04	P301 Auger 30-47cm	soil	39	795	39	20	15	19	109	310	130	25	94	173
SN05	P301 Auger 47-58cm	soil	53	859	46	19	17	17	112	324	147	27	101	187
SN06	P301 Auger 58-71cm	soil	65	785	44	22	15	19	110	316	142	25	103	185
SN07	P301 Auger 71-83cm	soil	77	803	42	21	15	16	110	319	135	24	96	183
SN08	P301 Auger 83-95cm	soil	89	786	45	22	16	21	113	310	156	26	103	211
SN09	P301 Auger 95-105cm	soil	100	837	44	23	15	18	110	305	154	26	102	211
SN10	P301 Auger 105-116cm	soil	111	821	48	22	16	17	116	307	153	27	99	208
Balsam regolith depth profile														
SN59	BP 0-10cm	soil	5	788	25	21	15	<11	111	244	151	32	126	295
SN60	BP 30-40cm	soil	35	717	24	24	15	<11	120	235	160	30	124	264
SN61	BP 60-70cm	soil	65	712	21	21	16	<11	112	236	165	29	116	266
SN62	BP 80-90cm	soil	85	668	27	21	13	<11	113	234	170	30	107	252
SN20	BP 204	saprolite	178	707	36	25	16	13	112	118	187	27	89	181
SN19	BP 173	saprolite	257	799	33	21	15	13	110	179	154	28	92	191
SN18	BP 161	saprolite	287	553	38	22	18	15	111	215	187	35	113	187
SN17	BP 144	saprolite	330	798	30	22	15	12	109	283	142	26	90	189
SN16	BP 111	saprolite	414	788	35	22	18	14	127	294	143	31	83	184
SN15	BP 72	saprolite	513	764	28	21	15	10	95	337	131	25	82	168
SN14	BP 36	saprolite	605	643	29	22	15	12	116	275	148	26	89	169
SN13	BP rock piece	weathered Granodiorite	647	549	32	21	17	11	64	406	146	27	89	184
SN12	BP rock piece	weathered Granodiorite	692	776	29	17	13	13	95	410	147	23	89	195
SN11	BP rock	weathered Granodiorite	-	642	17	15	14	11	147	276	73	21	51	139
Creek sediment loads														
SN28	PIG bedload	bedload sediment	-	481	39	14	18	16	51	327	153	31	72	276
mean bedrock (data from Hahm et al. (2014), Riebe and Granger (2013), and GFZ Potsdam, Sec 3.3)														
mean bedrock after outlier removal				685	35	18	9	39	102	484	119	19	102	128
2 SD bedrock after outlier removal				325	48	6	4	109	83	121	71	11	43	46
2 SE bedrock after outlier removal				36	13	3	0	55	48	13	20	1	12	5

Table A.28: CDF and τ values for the studied soil and regolith profiles P301 and BP calculated according to Equation 3.1 and Equation 3.2 in the main text

sample ID	sample description	sample type	Mid depth (cm)	CDF _{total}	Mass transfer coefficients												
					τ _{Si}	τ _{Ti}	τ _{Al}	τ _{Fe}	τ _{Mn}	τ _{Mg}	τ _{Ca}	τ _{Na}	τ _K	τ _P	τ _{Sr}	τ _{Zn}	τ _{Be}
P301 soil profile																	
SN01	P301 core 0-13cm	soil	7	-3.22	-0.28	-0.33	-0.22	-0.44	2.84	-0.43	-0.13	-0.50	0.03	1.20	-0.23	-0.01	
SN02	P301 core 13-26cm	soil	20	0.33	-0.29	-0.37	-0.25	-0.41	0.11	-0.49	-0.55	-0.47	-0.13	0.15	-0.49	-0.33	-0.12
SN03	P301 core 26-34cm	soil	30	0.26	-0.28	-0.33	-0.24	-0.35	-0.33	-0.43	-0.55	-0.51	-0.21	-0.12	-0.49	-0.26	-0.13
SN04	P301 Auger 30-47cm	soil	47	0.26	-0.30	-0.29	-0.24	-0.31	-0.37	-0.39	-0.56	-0.55	-0.23	-0.19	-0.52	-0.31	-0.15
SN05	P301 Auger 47-58cm	soil	53	0.32	-0.32	-0.29	-0.25	-0.30	-0.41	-0.39	-0.58	-0.58	-0.25	-0.31	-0.54	-0.32	
SN06	P301 Auger 58-71cm	soil	65	0.30	-0.32	-0.29	-0.24	-0.30	-0.41	-0.39	-0.57	-0.58	-0.28	-0.32	-0.55	-0.30	
SN07	P301 Auger 71-83cm	soil	77	0.30	-0.31	-0.30	-0.25	-0.31	-0.41	-0.39	-0.58	-0.59	-0.26	-0.33	-0.54	-0.34	
SN08	P301 Auger 83-95cm	soil	89	0.39	-0.41	-0.34	-0.30	-0.33	-0.42	-0.43	-0.62	-0.65	-0.37	-0.41	-0.61	-0.38	
SN09	P301 Auger 95-105cm	soil	106	0.39	-0.41	-0.35	-0.31	-0.34	-0.40	-0.44	-0.63	-0.65	-0.33	-0.43	-0.62	-0.39	-0.24
SN10	P301 Auger 105-116cm	soil	111	0.38	-0.38	-0.34	-0.30	-0.32	-0.39	-0.42	-0.62	-0.65	-0.34	-0.47	-0.61	-0.40	
Balsam regolith profile																	
SN59	BP 0-10cm	soil	5	0.56	-0.57	-0.52	-0.50	-0.48	-0.29	-0.61	-0.73	-0.76	-0.54	-0.32	-0.78	-0.46	-0.49
SN60	BP 30-40cm	soil	35	0.51	-0.53	-0.43	-0.41	-0.38	-0.43	-0.53	-0.70	-0.77	-0.51	-0.56	-0.76	-0.41	-0.37
SN61	BP 60-70cm	soil	65	0.52	-0.52	-0.44	-0.44	-0.39	-0.44	-0.53	-0.69	-0.77	-0.51	-0.66	-0.76	-0.45	-0.41
SN62	BP 80-90cm	soil	85	0.49	-0.49	-0.43	-0.43	-0.36	-0.42	-0.52	-0.68	-0.76	-0.50	-0.66	-0.75	-0.47	-0.33
SN20	BP 204	saprolite	178	0.29	-0.28	-0.18	-0.17	0.00	-0.41	-0.36	-0.76	-0.90	-0.25	-0.80	-0.83	-0.38	-0.12
SN19	BP 173	saprolite	257	0.33	-0.32	-0.24	-0.22	-0.16	-0.42	-0.37	-0.70	-0.84	-0.24	-0.85	-0.75	-0.39	-0.17
SN18	BP 161	saprolite	287	0.31	-0.34	-0.12	-0.20	-0.05	-0.20	-0.16	-0.54	-0.73	-0.36	-0.86	-0.70	-0.24	
SN17	BP 144	saprolite	330	0.32	-0.31	-0.30	-0.22	-0.26	-0.23	-0.37	-0.55	-0.66	-0.23	-0.85	-0.60	-0.40	-0.12
SN16	BP 111	saprolite	414	0.30	-0.29	-0.27	-0.22	-0.23	-0.34	-0.35	-0.56	-0.67	-0.26	-0.76	-0.57	-0.43	-0.14
SN15	BP 72	saprolite	513	0.23	-0.21	-0.27	-0.19	-0.24	-0.35	-0.35	-0.42	-0.51	-0.22	-0.34	-0.47	-0.38	-0.01
SN14	BP 36	saprolite	605	0.24	-0.21	-0.17	-0.21	-0.16	-0.28	-0.26	-0.50	-0.62	-0.22	-0.54	-0.57	-0.34	0.03

